NAFION BASED HYBRID POLYMER ELECTROLYTES AND NANOCOMPOSITES: DESIGN AND ELECTROCHEMICAL INVESTIGATIONS

A THESIS

Submitted To The

UNIVERSITY OF PUNE

For The Degree Of

DOCTOR OF PHILOSOPHY
(IN CHEMISTRY)

By

P. MEERA

Dr. K. VIJAYAMOHANAN
(RESEARCH GUIDE)

PHYSICAL AND MATERIALS CHEMISTRY DIVISION
NATIONAL CHEMICAL LABORATORY
PUNE – 411 008
INDIA

MARCH 2009

DECLARATION

I, hereby declare that all the experiments embodied in this thesis entitled, **"NAFION BASED HYBRID POLYMER ELECTROLYTES AND NANOCOMPOSITES: DESIGN AND ELECTROCHEMICAL INVESTIGATIONS"**, submitted for the degree of Doctor of Philosophy in Chemistry, to the University of Pune have been carried out by me at the Physical and Materials Chemistry Division, National Chemical Laboratory, Pune, 411 008, India, under the supervision of Dr. K. Vijayamohanan. The work is original and has not been submitted in part or full by me, for any degree or diploma to this or to any other University.

Date: **P. MEERA**

Physical and Materials Chemistry Division
National Chemical Laboratory
Pune – 411 008

Dr. K. Vijayamohanan
Scientist

Physical and Materials
Chemistry Division
National Chemical Laboratory
Pune – 411 008
INDIA

Tel: 91-020-2590 2588
Res: 91-020-2587 0307
Fax: 91-020-2590 2636
Email: vk.pillai@ncl.res.in

CERTIFICATE

This is to certify that the work incorporated in the thesis entitled, "**NAFION BASED HYBRID POLYMER ELECTROLYTES AND NANOCOMPOSITES: DESIGN AND ELECTROCHEMICAL INVESTIGATIONS**" submitted by **Ms. P. Meera,** has been carried out by her under my supervision at the Physical and Materials Chemistry Division, National Chemical Laboratory, Pune, 411 008, India. All the materials from other sources have been duly acknowledged in the thesis.

Research Guide
(K. Vijayamohanan)

Date :
Place : Pune

Dedicated to
Amma, Cheechu
and
the loving memory
of Appa

Contents

Chapter 2

46-88

All-Solid-State Electrochemistry of Nafion Membranes

Acknowledgements

This dream of mine and the moments I cherish now are the fruits of a budding desire that lured me to taste the thrill of finding something new! It has been an adventurous expedition, sailing through different circumstances, people and stages of life. Now, standing at the summit of this memorable accomplishment, I gaze back to wonder what all have fetched me atop.

My deepest sense of gratitude and sincere thanks are due to my Research Supervisor, Dr. K, Vijayamohanan, for his constant encouragement, guidance and support throughout my Ph. D. I am especially indebted to him for providing me enormous freedom to pursue multi-disciplinary research. I am also thankful to him for teaching me the elements of modesty and concern for others. He has the rarest combination of humanity, professional skills and scientific knowledge. I always admire his excellent ability to locate the best quality in every student and adaptability to people of varying attitudes and temperament. This feat would have been definitely impossible without his vibrant guidance and moral support.

I would like to thank Dr. S. Sivaram, (Director, NCL), for providing me all the infrastructural facilities. I would extend my sincere thanks to Dr. Sourav Pal (Head, Physical Chemistry Division) for his persistent encouragement and support. Also, I am grateful to Dr. I. S. Mulla, Dr. Anil Kumar, Dr. P. A. Joy, Dr. B. L. V. Prasad and Dr. S. D. Prasad for their encouragement. Thanks are also due to our divisional staff, Shri. Dipak Jori and Shri. S. F. Punekar for their willing cooperation.

My special thanks to Dr. Sreekumar for his tremendous support in carrying out the fuel cell experiments and for his persistent encouragement. Also, I am highly thankful to Dr. Manjusha Shelke for her valuable discussions and support.

I devote my sincere acknowledgement to Dr. M. Islam Khan (Biochemical Sciences Division, NCL) for his invaluable guidance to carry out protein electrochemistry and electrophoresis experiments in his lab. I have always been inspired by his positive criticism and realistic views. I am also thankful to his students, Ansari and Shabab who helped me in experiments in addition to providing a friendly environment along with Madhurima, Avinash and Shashidhara.

I am highly thankful to Dr. Sulekha Hazra (Plant Tissue Culture Division, NCL) for her enormous support and encouragement to perform the SECM experiments on somatic embryo-derived

plantlets. I can never forget her student Shweta for her consistent support as a good friend and roommate, in addition to her dedicated role in tissue culture experiments.

I also acknowledge Dr. C. S. Gopinath, Dr. D. Srinivas (Catalysis division), Dr. Guruswamy, Dr. Ashish Lele and Dr. Neelima (CEPD) for fruitful scientific discussions.

I consider myself as the most privileged student to avail the guidance and moral support of some of the greatest teachers of the country. I would pay my humble tribute to my Guru, Prof. Goverdhan Mehta, who made me realize my abilities and appreciated my commitment, when I was working at IISc, Bangalore, in his supervision for my summer research project during my Bachelor's degree. He is one of my major inspirations, who has been constantly encouraging my scientific endeavors. Another great teacher was Prof. S. K. Rangarajan (late) who taught me the rigor in research and improved my confidence. I dedicate my present and all my future accomplishments to his memory. Also, I should never forget Prof. A. K. Shukla (Director, CECRI) for his consistent support, concern and good wishes. It was with his whole-hearted efforts and fatherly care that I could surmount my toughest times and complete my doctoral research. I am always grateful for the motivation, moral as well as financial support provided by my graduate teachers, Mrs. Jayalakshmi and Dr. Saraswathi.

I would like to express my sincere thanks to Dr. Santosh Haram (University of Pune) and Prof. Sampath (IISc) for their cheerful support. Also, I am thankful to my post-doctoral research guide, Prof. Cynthia Zoski (NMSU, US), with whom I will be working in the near future, for her enormous patience and encouragement to complete my Ph.D. thesis.

I am also thankful for the motherly care of Manju madam and will always remember my pleasant moments with Hari and Keshu.

Now I take the privilege of thanking all my friends who have been standing by my side in my tough times. I have been fortunate to get a collection of the best human souls as my friends for whom my happiness matters much more than my words of thanks. It gives me a great pleasure to mention some of them here – Ramesh anna, Nachiket (IISc), Kannan, Kishor Bhaiya, Ekta Bhabhi, Abhishek, Bhalchandra, Shraeddha, Nagesh, Deepti, Lallu, Tuhina, Indu, Maitri, Gitali and Manu. I would thank Kannan once again for his brilliant suggestions and support for my work. I always cherished my memorable moments with Viji, Venki's special sambhar, Dharma, Malli anna, Kamendra, Gowri's Doppler smile, Balaji's spritiual thoughts, Manasi and Ruby. I am overwhelmed by the friendly atmosphere and whole-hearted support provided by my beloved labmates, Bhaskar, Beena, Vinu,

Dhanu, Joy, Kuttu, Palani, Nilesh, Ranjith, Ashwini, Hussain and Vishal. I am also thankful to my seniors Nirmalya, Jadabji, Sneha, Mahima chechi for their valuable suggestions.

Above all, I find no words to express the love of my amma and cheechu, who have always given me the best of everything. They are the all-time champions of my every successful moment in life.

Finally, I acknowledge CSIR, India for granting research fellowship.

A second before the sunset. . . .
At the brim of silence. . . .
A moment before the dew
Could bid the grass adieu. . . .
With your helping hand
And soothing smile,
A free electron at the interface
Now tunnels to the next phase!

List of Abbreviations

PEM	Polymer Electrolyte Membrane
PEO	Polyethyleneoxide
NMR	Nuclear Magnetic Resonance
VTF	Vogel-Tamman-Fulcher
PEFC	Polymer Electrolyte Fuel Cell
MEA	Membrane-Electrode Assembly
IEC	Ion Exchange Capacity
PTFE	Poly(tetrafluoroethylene)
EQ	Equivalent Weight
SAXS	Small-Angle X-ray Scattering
SPEEK	Sulfonated Poly(etheretherketone)
RH	Relative Humidity
TEM	Transmission Electron Microscopy
SEM	Scanning Electron Microscopy
AFM	Atomic Force Microscopy
SECM	Scanning Electrochemical Microcopy
SANS	Small-Angle Neutron Scattering
SDS	Sodium Dodecyl Sulfate
PAGE	Polyacrylamide Gel Electrophoresis
PBI	Polybenzimidazole

UME	Ultramicroelectrode
CNT	Carbon Nanotube
SWCNT	Single-Walled Carbon Nanotube
MWCNT	Multi-Walled Carbon Nanotube
EXAFS	Extended X-ray Absorption Fine Structure
DRIFT	Diffuse Reflectance Infrared Fourier Transform Spectroscopy
FTIR	Fourier Transform Infrared Spectroscopy
XPS	X-ray Photoelectron Spectroscopy
LS	Langmuir-Schaefer
CV	Cyclic Voltammetry
ORR	Oxygen Reduction Reaction
PEDOT	Poly(ethylenedioxythiophene)
IAA	Indole-3-acetic acid
IBA	Indole-3-butyric acid
BAP	6-Benzylamino purine
CNLS	Complex Non-Linear Least Squares
RDE	Rotating Disk Electrode
LSV	Linear Sweep Voltammogram
PEC	Polyelectrolyte Complexes
OCP	Open Circuit Potential
EIS	Electrochemical Impedance Spectroscopy
SG/TC	Substrate Generation/Tip Collection

List of Symbols

$\boldsymbol{\sigma}$	Conductivity
T	Temperature
R	Universal gas constant
$\boldsymbol{R}$	Resistance
$\mathbf{T_g}$	Glass transition temperature
$\mathbf{T_m}$	Melting point
$\boldsymbol{R_p}$	Parallel resitance
$\boldsymbol{R_{ct}}$	Charge-transfer resistance
$\boldsymbol{R_f}$	Electrophoretic mobility
$\boldsymbol{k^o}$	Standard rate constant
$\boldsymbol{\alpha}$	Charge transfer coefficient
$\boldsymbol{E}$	Electrode potential
$E^{o'}$	Formal redox potential
$\boldsymbol{Z}$	Electrochemical impedance
$\boldsymbol{\%T}$	Gel concentration in PAGE
$\boldsymbol{\lambda}$	Water content
F	Faradays constant
$\boldsymbol{\upsilon}$	Potential scan rate
$\boldsymbol{\gamma}$	Surface tension
$\mathbf{M_o}$	Free electrophoretic mobility of proteins
$\mathbf{u_f}$	Electrophoretic mobility of tracking dye

K_R	Retardation coefficient
κ	Electrolytic conductivity
L	Dimensionless tip-substrate distance in SECM
i_T	SECM tip current
$i_{T,\infty}$	SECM tip current at infinite tip-substrate distance
ε_r	Relative permittivity
C	Capacitance
ω	Electrode rotation speed

Ionic Transport in Polymer Electrolytes

This chapter begins with a discussion of the fundamental aspects of the physical chemistry of polymer electrolytes to address several key questions: How does the presence of ions affect the properties of a polymer? How does the polymer alter the fate of the ions ensued in it? What are the methods of controlling transport properties of polymer electrolytes? How does ionic conductivity depend on microstructure and what are the critical parameters to modulate ion transport number? After discussing many of these issues, a general classification scheme of polymer electrolytes and the importance of Nafion as a proton conductor are lucidly brought out by emphasizing their unique structural and transport properties. This is followed by a critical survey of the current trends in polymer electrolyte research to locate the lacunae and to understand the limitations of Nafion. The scope and objectives set for this thesis based on the above framework are provided along with justifications toward the end of the chapter.

1.1 Introduction

Polymers, since time immemorial, have been considered as electrical insulators which can protect us from electric shocks and also for their other innumerable beneficial applications like water-repellant covering materials. However, this conventional perception about polymeric materials received an interesting revival with the brilliant discovery of ionic and electronic conduction in polymers by Grubbs and Shirakawa in 1957 and 1970 respectively [1]. Thanks to nanotechnology, it is now possible to design a plethora of polymers with ionic, electronic or mixed conduction using a variety of monomers with controllable features [2]. The increasing focus on conducting polymers could be mainly attributed to their remarkable applications in molecular electronics, solar photovoltaics and also in electrochemical power systems like batteries, fuel cells and supercapacitors, which are identified as a major means to harness energy from renewable sources.

The importance of ionically conducting polymers (polymer electrolytes) in electrochemical energy systems was realized when Thomas Grubb designed the first solid polymer electrolyte fuel cell for the Gemini space flights in 1957 using polystyrene sulfonic acid as the polymer electrolyte membrane [3]. Some of the key advantages of polymer electrolytes over liquid electrolytes are non-volatility, compactness, flexibility, ease of transportation without leakage problems in addition to better cycle life of devices as polymer electrolytes are least vulnerable to impurity adsorption and corrosion.

1.2 What are Polymer Electrolytes?

Polymer electrolytes can be broadly defined as organic/inorganic polymers capable of conducting ions either by virtue of ionic/ionizable functional groups present in the polymer chain or by the addition of a metal salt into a neutral polymer matrix. Sometimes they are referred to as ‘polyelectrolytes’, which in the broadest sense denote

any species (molecule/aggregate/particle/polymer) carrying a large number of charges. Here, we will stick to the term 'polymer electrolytes' to denote ionically conducting polymers, wherein the transport properties will be predominated by only one type of ion.

Ionic conduction can be achieved in polymers in one of the following ways.

- By introducing ionic/ionizable functional groups either along the backbone or in the side chains of the macromolecule (e.g., Nafion)
- By swelling a neutral polymer (crystalline/semicrystalline gel) with a salt solution, ionic liquid or a molten salt (e.g., phosphoric acid-doped polybenzimidazole)
- By dissolving a salt directly (without solvent) in a highly polar (but neutral) polymer medium (e.g., $LiClO_4$ in polyethylene oxide)

While these procedures can invoke ionic transport in the polymer, they do not essentially ensure the experimental realization of useful ionic conductivity values (i.e., higher transport numbers of the predominant ions) in these systems. There are many more structural and physico-chemical considerations with respect to the macromolecule practically applicable for polymer electrolytes. Some of the most important structural criteria for a polymeric material to be a good ionic conductor are

- The presence of a heteroatom (usually O, N, S) with lone pairs of electrons of donor power sufficient to bind protons and small cations
- Appropriate separation between the ionic functional groups to ensure hopping of charge carriers from one site to another
- Sufficient flexibility of polymer chain segments to facilitate the movement of ions

1.2.1. Physical Chemistry of Polymer Electrolytes

The ever-increasing thrust in polymer electrolytes is not only due to their technological significance but also their interesting deviations from the behavior of neutral polymers as well as from that of the conventional electrolytes, collectively known as the 'polyelectrolyte effect' [4]. The objective of this section is to address two important issues: How does an ionic group affect the properties of the polymer? How does the polymer affect the transport of ions?

First, let us consider the changes induced in the physical properties of the polymer matrix by the introduction of ionizable functional groups. The distinctive properties of polymer electrolytes arise mainly due to the long range nature of the electrostatic interactions between the charged polymer chains and counter ions, which introduce new length and time scales for ionic transport in addition to the dynamics of the neutral counterpart. Hence the basic description of a polymer electrolyte chain always begins with a quantification of its charge. A neutral, flexible polymer chain is normally characterized by at least three physical parameters viz., (i) the persistence length, l_p as a measure of chain stiffness, (ii) the contour length, *L,* as a measure of chain length and (iii) excluded volume strength, *v,* as a measure of segmental interactions. In the case of polymer electrolytes, a fourth parameter namely, the average axial spacing between the charges (*b*) characteristic of the linear charge density is required. Determination of the parameter, *b*, which is the inverse of the number of elementary charges of magnitude, *e* (1.602×10^{-19} C) per unit backbone length, depends on a number of assumptions such as (i) the electrostatic properties of the polymer electrolyte are independent of the dielectric properties of its backbone and (ii) the insignificance of tertiary structure, which may require a description of 'surface charge density' different from the simple 'linear charge density'. In reality, polymer electrolytes are more complex due to the structural flexibility offered by the subtle interactions between the charged polymer chains. Some of the

important physical properties of the polymer affected by the inclusion of ionizable functional groups are listed below [5].

- **Glass transition temperature (T_g)** – This is the temperature at which the segmental mobility of the polymer increases to create a rubber-like or glassy state. In an ionic polymer, the electrostatic forces between the bound ions in the polymer chain and the counter ions reduce the segmental mobility and increase the T_g. This behavior is very important for obtaining the polymer electrolyte in the form of 'membranes' for solid-state applications.
- **Melting point (T_m) –** Inclusion of ionic bonds lowers the melting point of the polymer mainly as a result of reduced crystallinity. In addition, the polymer melt has poor flow properties as the electrostatic forces lead to the formation of aggregates and clusters. Sometimes the ionizable group itself could decompose at a temperature below the melting point of the polymer.
- **Stiffness –** Similar to the effect of cross-linking, introduction of ionizable groups increases the stiffness of the polymer. For example, a simple exchange of protons with by sodium or potassium ions can make Nafion membranes stiffer.
- **Thermal expansion –** In accordance with the increase in mechanical strength, the ionizable groups reduce the coefficient of thermal expansion of the polymer matrix.

Having discussed the effect of ionic groups on the properties of the polymer matrix, it is equally important to appreciate the reverse case viz., the effect of the macromolecules on the dynamics of the constituent ions. The fate of the ionic groups immobilized on the polymer chain and that of their corresponding mobile counter ions dispersed in the polymer electrolyte, especially in terms of solvation and mobility is

dictated by various properties of the polymer chain like molecular structure, crystallinity and segmental mobility. For example, the solvation of protons in bulk water is quite different from that of protons in water entrapped in the hydrophilic domains of a proton exchange membrane. In aqueous solutions of acids, proton exists as hydronium ion, which itself is hydrated in two forms viz., $H_5O_2^+$ and $H_9O_4^+$ called the Eigen and Zundel ions respectively [6]. The main reason for the abnormally high mobility of protons (H_3O^+) compared to other ions of similar size is the rapid exchange of hydrogen bonds between the solvated forms [7]. On the other hand, in a proton exchange membrane like Nafion (a perfluorsulfonic acid polymer electrolyte), water exists in two different environments viz., surface water and bulk water. While the former refers to water molecules locally solvating the sulfonate groups of the pendant chains, the latter corresponds to those present in the middle of the hydrophilic pools. Interestingly, the dielectric constant of water entrapped in a proton exchange membrane is not the same as that of bulk water. As the water molecules forming the first two solvation shells of the sulfonate groups are more 'ordered' than those in the bulk of the pores, the dielectric constant decreases from the bulk of the pores toward the pore walls as demonstrated in Figure 1.1 [6]. This could be compared with the distribution in dielectric constant of a solvent at an electrode/electrolyte interface [8]. The electrified interface formed between the ionic charges immobilized in a polymer and the mobile counter-ions solvated in the hydrophilic domains of the polymer electrolyte may be considered to be qualitatively analogous to an electrode/electrolyte interface. The size of the hydrophilic domains increases as the water content (λ) of the membrane increases from 6 to 22.5. Similarly in the case of salt-containing polymer matrices like $LiPF_6$-Polyethylene oxide (PEO), partitioning of the solute and the orientation of solvent dipoles inside the membrane pore are immensely affected by the strong electric field created at the interface [9].

The polymer matrix not only affects the solvation of ions but also their mobility and renders their transport mechanism different from that in liquid electrolytes. Polymer

electrolytes also differ from ionically conducting framework solids like Ag_2HgI_4 due to the large scale translational freedom, softness and disorder in the polymer matrix [10

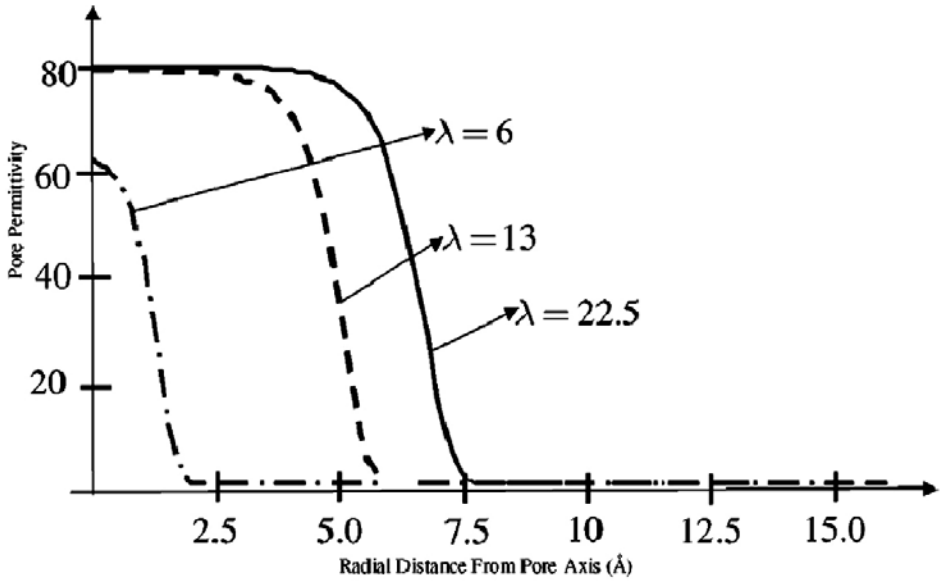

Figure 1.1. Radial dependence (computed) of dielectric constant of water in the pores of Nafion membranes with different levels of hydration (λ): 6, 13, 22.5 water molecules per sulfonate group. At low degree of hydration, even the water in the center of the pore has a dielectric constant substantially lower than that of bulk water. *Reproduced from Ref.*[*6*]

Also, the ionic conductivity of polymer electrolytes is a function of the crystallinity of the polymer matrix. For instance, Nuclear Magnetic Resonance (NMR) studies in the early 1980s had clearly shown that ionic conduction in PEO-based electrolytes takes place predominantly in the amorphous phase [11]. Most often, less crystalline polymer electrolytes exhibit a non-Arrhenius type of temperature dependent conductivity unlike that of the highly crystalline ones. The effect of crystallinity on ionic conduction can be explained in terms of the segmental mobility of the polymer chains coupled to ionic motion in the light of the 'dynamic bond percolation theory' and long-range ion transport mechanism proposed by Ratner [12]. Accordingly, Arrhenius-type ionic conduction in crystalline polymer electrolytes is due to the invariance of configurational entropy of the polymer chains with temperature. On the other hand, amorphous and partially crystalline

polymer electrolytes exhibit a temperature-dependent conductivity given by the Vogel-Tamman-Fulcher (VTF) expression as,

$$\sigma(T) = \sigma_o \exp\left[-\frac{B}{(T - T_o)}\right] \tag{1.1}$$

where, σ_o is the conductivity at a reference temperature, T_o, $B = E_a/R$ and E_a is the activation energy for ionic conduction and R is the universal gas constant (8.314 J/K/mol). Within the dynamic bond percolation theory, this is modified to describe ion transport by the semi-random motion of local polymer segments and the activation energy can be related to rotational barriers in the polymer chain [13]. On the other hand, theoretical treatment of polymer electrolytes with one of the charges immobilized on the chains requires further modifications to explain their ionic conductivity as discussed in Section 1.4 with Nafion as a specific example.

1.2.2. Classification of Polymer Electrolytes

With the rise of modern synthetic protocols and processing techniques, a number of polymers with ionic conduction under diverse categories have been developed. Although it is difficult to organize all of them under a single classification scheme, some of the most common schemes are based on:

i. Location of the ionic groups
ii. Degree of ionization
iii. Temperature of operation
iv. Nature of the mobile ion
v. Nature of the functional groups in the backbone and pendant chains
vi. Processable state of the material

A vast majority of polymer electrolytes can be classified based on the location of their ionic/ionizable groups. For example, some contain both cationic and anionic groups

in the macromolecule itself, called ampholytic polymers (or polyampholytes) and some others contain one type of charge localized in the macromolecule, while the other ion is completely mobile. The polyampholytes can be further classified depending on whether the opposite charges are present within the same pendant group or constitute the terminals of the main polymer chain. Similarly, polymer electrolytes with only one of the charges localized in the polymer chain can be classified based on whether the immobile ion is in the main chain or in the pendant chains of the polymer. Especially, when only a small proportion (< 10%) of the constitutional units has ionic groups, often there is phase separation of ionic domains from the continuous polymer phase with the ionic domains acting as physical crosslinks.

The next classification scheme is based on the degree of ionization as common to both liquid and polymer electrolytes governed by the Ostwald's law of electrolytic dissolution. Accordingly, polymer electrolytes can be classified as strong and weak. Strong polymer electrolytes are polysalts like Na-polystyrene sulfonate, which dissociate completely in the total pH range accessible by experiments. As the total charge and its specific distribution are 'fixed' during synthesis itself, they are also known as 'quenched' polymer electrolytes. On the other hand, the total charge on weak polymer electrolytes like polyacids and polybases, denoted as 'annealed' polymer electrolytes, can be tuned by changing the pH of the solution.

Polymer electrolytes can also be categorized based on their temperature of operation. Another broader scheme of classification is based on the nature of the mobile ions which can be cations (protons, alkali metal ions etc.,) or anions (Oxide, chloride ions etc.,) and on the nature of functional groups constituting the backbone and pendant chains of the polymers. Similarly, it is equally worth to classify them based on their physical state as solutions, gels and membranes. Although ionic conduction is common to all the three states, there are a number of differences in their properties like intrinsic viscosity and sensitivity to external stimuli. Gel polymer electrolytes are more advantageous than

the corresponding membranes especially for salt-dissolved polyethylene oxide systems in terms of enhanced proton conductivity, flexibility and adhesive properties. For example, the tunability of ionic conduction mechanism in crosslinked polyvinyl alcohol/poly acrylic acid hydrogel electrolytes has been demonstrated by absorbing solutions of $HClO_4$, NaOH and NaCl in the gel matrix [14].

1.2.3. Significance of Polymer Electrolytes

Polymer electrolytes have been actively investigated since several decades owing to their significance as ionic conductors for a number of applications. Research interest in natural polyelectrolytes like nucleic acids and proteins has been ever growing due to their pivotal role in maintaining and propagating life in the simplest as well as the most complex biological systems. Attempts to understand the organization and binding of these biological macromolecules to other ionic and molecular species under physiological conditions have been encouraged to get deeper insight into their impact on human life and health. On the other hand, the focus in the synthetic systems has been to investigate their properties as a function of solution pH, ionic strength, nature of ions, temperature etc. Also, the effect of introducing multivalent counter ions on the structure and dynamics is especially interesting. Thus the fact that polymer electrolytes' conformation and their interactions can be controlled by varying a number of parameters make them not only interesting candidates for the exploration of novel phenomena but also lead to new applications in a variety of fields. Current applications of polymer electrolytes are in the areas of waste water treatment, ion-exchange resin and ion/gas selective membranes for electrochemical devices. They are also used to prepare conductive coatings when complexed with conjugated polymers like polythiophenes and polyanilines.

Some of the important applications of polymer electrolytes are briefly discussed below.

- **Lithium Batteries –** Salt-containing polymer electrolytes in the form of membranes, gels and composites have found enormous application in secondary Lithium batteries [15]. Typical examples include polyethylene oxide based systems like PEO-LiBr, PEO-$LiAsF_6$ complexes. Although the excellent advantages of polymer electrolytes against the liquid systems like negligible internal shorting, leaks and corrosion are realized, not many commercial Lithium batteries with solid polymer electrolytes have been successful, mainly owing to their low conductivities ($< 10^{-3}$ S/cm).
- **Fuel cells –** Polymer electrolyte membranes, especially proton exchange membranes have been quite successfully deployed as electrolytes for fuel cell applications. Unlike those employed in Lithium batteries, these are polymers with one of the charges localized in their pendant chains with no added salt. e.g., Nafion
- **Electrochemical Capacitors –** Organic polymer gel electrolytes, which are prepared by the addition of a low molecular weight polar solvent to a polymer-salt system, have found extensive application in electrochemical double layer capacitors [16].
- **Electrolyzers –** Water electrolyzers based on solid polymer electrolytes are of great practical interest for on-board production of oxygen especially in submarines and extra-terrestrial applications. Nafion is the typical membrane material used in water electrolyzers as it can withstand high differential pressures without getting damaged in addition to other advantages like efficient separation of the gases and absence of leakage problems [17].
- **Electrochromic Devices –** Transparent films of polymer electrolytes are finding increasing application as electrolytes in smart windows. For example, quite recently, a diurea-cross linked poly(oxyethylene)/siloxane membrane has been used as a solid electrolyte in an electrochromic

smart window consisting of electronically conducting films of gallium doped Zinc oxide and an electrochromic layer of tungsten trioxide [18].

- **Chemical and Biological Sensors –** The sensitivity of the mechanical properties of polymer electrolyte membranes to an externally electric/magnetic field can be used to develop chemical and biological sensors [19].

1.3 Proton Exchange Membranes

Polymer Electrolyte Fuel Cells (PEFCs) involving a proton exchange membrane as the electrolyte (depicted in Figure 1.2) are considered as one of the major sustainable energy options to develop a hydrogen-based economy to reduce dependence on non-renewable energy sources and to minimize anthropogenic environmental pollution. Among its various components, the proton exchange membrane (PEM) plays a crucial role in determining the durability, operational life and performance of the fuel cell.

Characteristics of a good proton exchange membrane include [21],

i. High proton conductivity
ii. Negligible swelling
iii. Insignificant electronic conductivity
iv. Low permeability to fuel and oxidant
v. Low water transport through diffusion and electro-osmosis
vi. Oxidative and hydrolytic stability
vii. Good thermal stability
viii. Good mechanical stability in dry as well as in hydrated states
ix. Low cost

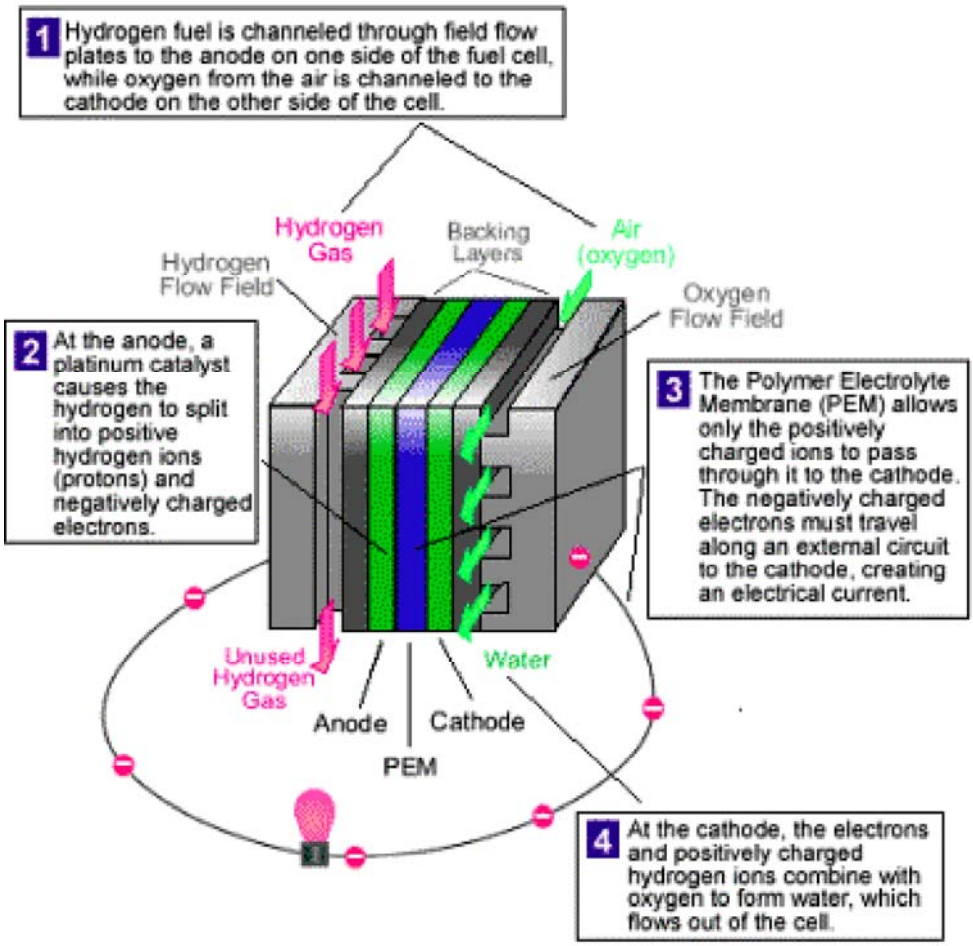

Figure 1.2. General operation of a Polymer Electrolyte Fuel cell (PEFC) with H_2 as the fuel and O_2 as the oxidant. The PEM sandwiched between the anode and the cathode together with the backing layers, constitutes the Membrane-Electrode Assembly (MEA). It should be noted that the flow channels for the fuel are designed perpendicular to those of the oxidant to prevent them from mixing. *Adapted from Ref* [*20*].

Although these criteria sound simple, each one of them is coupled in a complicated way to all others. For example, most of the currently used PEMs require water as the mobile phase for proton conduction. But the presence of more water reduces the mechanical stability of the membrane and may even reduce the proton conductivity of the membrane due to a decrease in the number of sulfonate groups per unit volume of the hydrophilic domains.

1.3.1. Classification of Proton Exchange Membranes

Since the introduction of Nafion® by DuPont in the late 1960s, a number of PEMs have emerged with different backbone structures and proton conducting functional groups. While Nafion comes under the class of perfluorinated sulfonic acid polymers, there are other sulfonic acid PEMs with perfluorinated backbones and aromatic side chains. On the other hand, a major class of non-fluorinated PEMs with partially aliphatic as well as aromatic backbones is also available. Similarly, functional groups other than sulfonic acid like imides, sulfonamides etc. have been investigated for proton conduction. Another way of classifying PEMs is based on their composition like copolymers, blends, composite/hybrid and bio-inspired membranes. Table 1.1 summarizes the major types of PEMs with different backbone and side chain functional groups.

1.3.2. Structural Considerations

One of the basic structural requirements of a PEM is the presence of an acidic functional group capable of generating protons and a strong hydrophobic backbone to provide mechanical stability. However there are many other structural aspects which need to be considered to design a PEM with desired properties and functions. Many of the bulk properties of the PEM can be controlled during synthesis itself by tailoring the functionality and hydrophobicity/hydrophilicity of the backbone and the pendant chains housing the proton-conducting moiety as summarized in Table 1.1.

Table 1.1. Classification of Proton Exchange Membranes based on the functional groups in the backbone and pendant chains

Proton conducting Moiety	**Backbone**	**Example**	**σ (S/cm) at 30 °C**	**Ref**
Sulfonic acid	a. PTFE	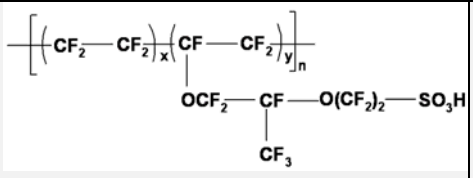	0.1	[22]
	b. Fluorinated Styrene	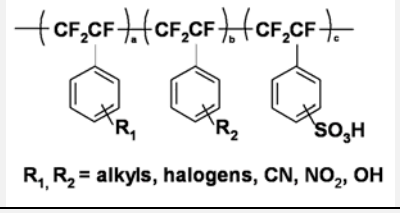	0.07-0.1	[23]
	Non-fluorinated systems c. Poly(arylene ether)	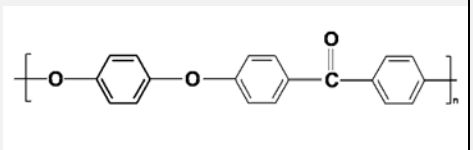	0.01	[24]
	d. Polyphosphazene	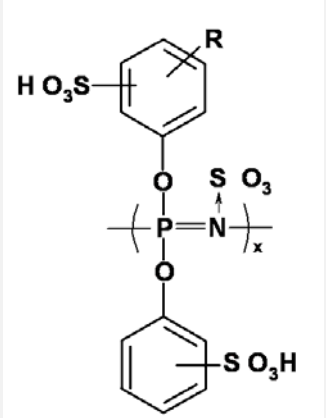	0.1	[25]
	e. PBI	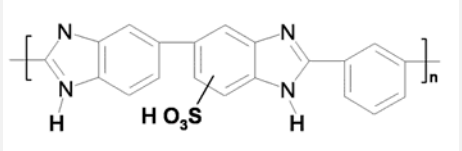	10^{-4}	[26]

Sulfonimide	a. Poly(arylene ether)	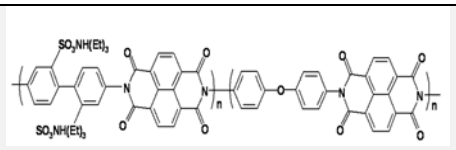	0.001	[27]
	b. Perfluoro alkyl	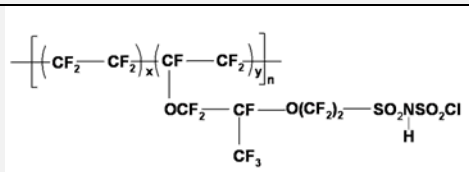	0.01	[28]
Phosphonic/ Phosphinic acid	a. Poly(arylene ether)	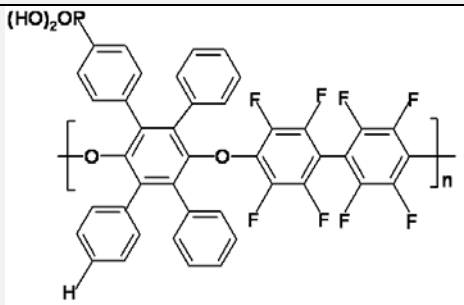	10^{-3}	[29]
Imidazole (doped with phosphoric acid)	a. Poly(alkyl ethers)	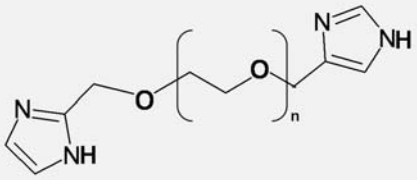	$7x10^{-4}$ at 200 ^{o}C	[30]
	b. PBI	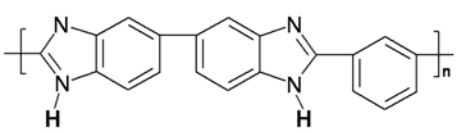	0.01	[26]

Most of the PEMs are amphiphilic in nature with distinct hydrophobic and hydrophilic domains. However, the presence of these domains is only a necessary condition for ionic conduction but is not a sufficient one. If the mere 'presence' of these domains is sufficient for proton transport, then why does the proton conductivity of a fluorinated PEM differs from that of its non-fluorinated analog? Why there are differences in conductivity within a given class, say fluorinated PEMs, with respect to

variations in equivalent weight of the polymer, degree of sulfonation and processing conditions? These questions are related to the microstructure of the PEMs which is described by the separation, distribution and sizes of the hydrophilic domains. For instance, sulfonated polyether ketones exhibit lower proton conductivity than that of fluorinated PEMs, mainly due to the poor microphase separation of the hydrophilic and the hydrophobic domains in the former [31] as depicted in Figure 1.3. Most of the synthetic methods currently adopted to prepare polymer electrolytes result in random or statistical placement of sulfonic acid units along the polymer chain although the distribution of sulfonic acid groups along the chain, as well as the acid strength and the nature of the moiety connecting them to the polymer backbone will have a considerable effect on the morphology and properties of the resulting membranes.

Water uptake is another property that strongly depends on the concentration of ionic groups in the PEM, characterized by the molar equivalents of ionic conductor per unit mass of the dry membrane expressed as the ion-exchange capacity (IEC) with units of milliequivalents per gram of the polymer. While it is desirable to maximize the conductivity of the membrane by increasing its ionic content, too many ionic groups will cause the membrane to swell excessively, which in turn would compromise mechanical integrity and durability. At the same time, the retention of an optimum amount of water is required as the mobile phase to maintain proton conductivity, which especially becomes critical at temperatures higher than 100 ^{o}C. Hence there is a critical need to improve

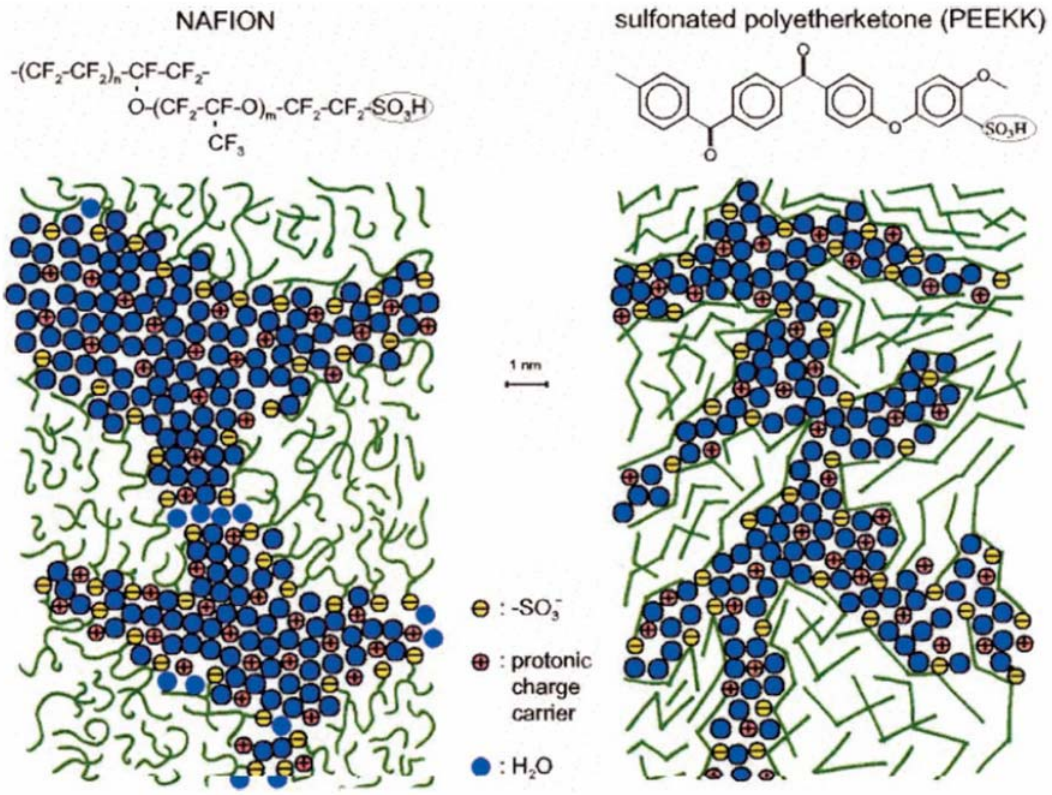

Figure 1.3. Schematic representation of nano-phase separation in hydrated Nafion and Poly (etheretherketone) derived from experiments and modeling. The scheme illustrates the sensitivity of various factors including the separation of hydrophilic and hydrophobic domains, connectivity of water and ionic domains and separation of the SO_3^- groups to the nature of the polymer backbone. *Reproduced from Ref.* [*31*].

water retention in PEMs at high temperatures and to improve performance at low water contents, while simultaneously giving special attention to chemical as well as morphological stability to resist excessive water swelling. Other membrane parameters which require critical attention include intrinsic viscosity, cross linking density and molecular weight and many of them are extensively being investigated in many parts of the world.

1.4 Nafion as a Proton Conductor

Nafion is a Teflon-based perfluorosulfonic acid polymer developed primarily as a permselective membrane in chlor-alkali electrolyzers [32]. The role of the membrane in this application is to separate Cl_2 and H_2 gases, allowing the transport of hydrated Na^+ ions from the anolyte (NaCl) chamber while preventing the back-migration of hydrated OH^- ions from the catholyte (NaOH/KOH) chamber. Since then Nafion has become a great commercial success and its use in fuel cells has been realized after the first use of a solid polymer electrolyte (polystyrene sulfonate) membrane in the Gemini space craft. Most of the commercial PEMs developed these days are based on Nafion. It also has the largest body of literature owing to its high, selective permeability to water and small cations, in particular protons [33], demonstrated industrial importance and commercial availability. This section provides an overview of the critical aspects of its molecular structure and physical properties.

Nafion is synthesized by the copolymerization of a perfluorinated vinyl ether comonomer with tetrafluoroethylene resulting in the chemical structure given below.

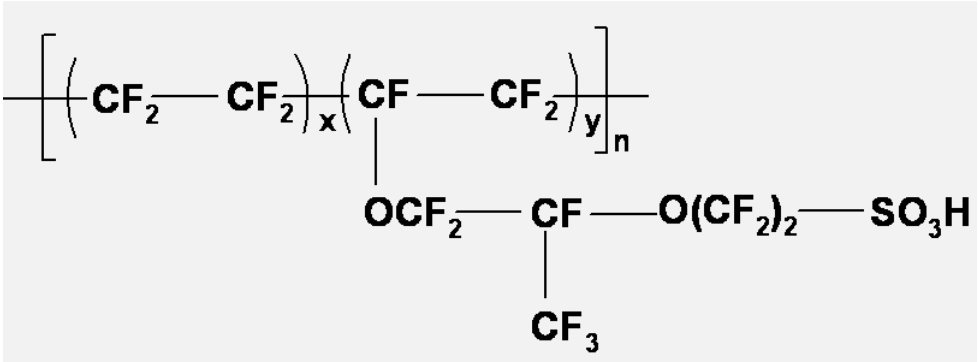

Also, Nafion membranes with carboxylate groups are reported although they exhibit very low proton conductivity compared to that of the sulfonic acid membranes [34].

These membranes are specified mainly using two parameters viz., the equivalent weight and membrane thickness, often expressed as a 3-4 digit number. For example, Nafion 115 refers to an equivalent weight of 1100 g/equiv (grams of dry Nafion per mole of sulfonic acid groups) and 5 refers to the thickness of the membrane in mills (1 mill = 25 μm). From the equivalent weight (EQ), the separation between the side chains, *m,* can be estimated using the expression [22],

$$EQ = 100m + 446 \tag{1.2}$$

Thus in a Nafion membrane of EQ 1100, the side chains are separated by 14 CF_2 units. The equivalent weight is related to the ion-exchange capacity (IEC) as,

$$IEC = 1000/EQ \tag{1.3}$$

The persistence length of the Nafion backbone is between 3 and 5 nm [35]. Nevertheless, the DuPont Nafion membranes are not entirely unique, since similar perfluorosulfonic acid ionomers have been developed by other manufacturers such as the Asahi chemical company (trade name: Aciplex) and the Asahi Glass company (Trade name: Flemion). The differences in the chemical structures of the co-monomers and properties of these related materials have been documented [36]. Once Dow Chemical company synthesized (but commercially unavailable now) a perfluorinated Nafion closely resembling Nafion, except that the length of the side chains of the former was shorter with one ether oxygen instead of two [37]. While a number of polymer electrolytes have been developed, Nafion is still being considered the benchmark material mainly due to the following structural characteristics [19].

i. The extremely hydrophobic, semi-crystalline polytetrafluoroethylene (PTFE) matrix, which provides excellent mechanical strength with

modulus greater than 100 MPa in the dry state and offers resistance to dissolution while swelling with hydrophilic agents.

ii. Microphase separation of the hydrophilic sulfonate functionalities, which serve as physical crosslinks in the dry state and channels for ion transport in the humidified state to achieve proton conductivities as high as 0.1 S/cm.

In addition, the perfluoro groups mitigate hydroperoxide formation, which reduces the durability of the non-fluorinated aliphatic analogues [21]. However, there are many more important properties including proton conductivity, water management, water retention at high temperatures and electro-osmotic drag, which require knowledge of the chemical microstructure and nanoscale morphology of Nafion.

1.4.1. Microstructure of Nafion

Following the discussion in Section 1.3.2 on the importance of the formation of hydrophilic and hydrophobic domains, their size, distribution and ordering in amphiphilic polymer electrolytes, in this section we focus more on the domain structure of Nafion. Since the past three decades, a number of experimental techniques have been employed to understand the morphology and ion distribution in Nafion and related systems. The techniques include, small – and wide – angle X-ray scattering, neutron scattering, differential scanning calorimetry, dielectric relaxation, dielectric spectroscopy, electrochemical impedance, scanning electrochemical microscopy, nuclear magnetic resonance, electron spin resonance, Raman, Mossbauer, Fluorescence probe spectroscopies, transmission and scanning electron microscopy and atomic force microscopy [31,33a,38]. However, the wealth of information gathered over the years using a variety of techniques is mostly indirect and are often based on simple morphological models that involve specific assumptions about the structure. Although the integrity and structural stability of the Nafion membranes are due to the PTFE backbone,

the hydrophilic clusters play a major role in transporting ions and water. The microstructure of these clusters or pores consists of an interfacial region of solvated perfluoroether side chains separating the polymer from more bulk-like water in the pores. The dimensions and shape of the water clusters are determined by the equilibrium reached between the internal osmotic pressure of the clusters and the counteracting elasticity of the organic matrix [39].

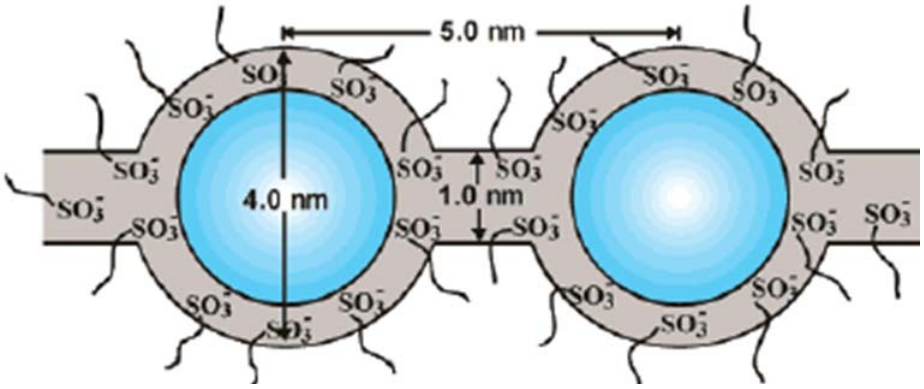

Figure 1.4. Gierke's Cluster-network model for the morphology of hydrated Nafion. *Adapted from Ref.*[*40*].

Based on Small Angle X-ray Scattering (SAXS) along with several other theoretical assumptions, Gierke in 1978 [40] proposed that there are 40 Å diameter clusters sulfonate-ended perfluoroalkyl ether groups that are organized as reverse micelles and arranged into a lattice (Fig. 1.4). These micelles are connected by pores or channels of 10 Å diameter. These $–SO_3^-$ coated ion channels account for inter-cluster ion hopping of positively charged species while preventing the transport of negative ions as in the case of chlor-alkali systems. Another early model of the microstructure of Nafion due to Yeager and Steck [41] based on studies of diffusion of various ions is slightly different. This is a three-phase model where according to which, the clusters do not have a strict geometrical definition as spherical clusters and cylindrical channels and their geometrical distribution are of lower order. Most importantly, the model proposes the presence of

transitional interphases between hydrophilic and hydrophobic regions, a concept that is being increasingly accepted nowadays.

These early models have been followed by many others according to some of which, the water clusters are non-spherical in shape and some others consider the water clusters to have a lamellar structure. A detailed review of all the classical models of Nafion has been provided by Paddison [39], who also proposed a model to describe the nature of water confined in the hydrophilic domains. More specifically, comparing the dielectric loss spectra of Nafion and Sulfonated Poly Ether Ether Ketone (SPEEK) [31, 38d, 42] (with water volume fraction, 0.40 and 0.41 respectively) reveals that due to the narrower hydrophilic channels in the latter, water has a lower dielectric constant i.e., more tightly bound than that in Nafion. Molecular dynamics simulations reveal that the sulfonate groups are preferentially hydrated over the ether functionalities present in the pendant chains [43]. Also it has been shown that each sulfonate group in Nafion is surrounded by four water molecules with a solvation enthalpy of -135 kJ/mol [44]. A further comparison of the enthalpies of mono-hydration of the sulfonate groups in Nafion 117 membrane (83 kJ/mol) with that of the sulfonic acid groups in trifluoromethane sulfonic acid (79 kJ/mol) and the enthalpy of monohydration of sulfuric acid in vapour phase (< 54 kJ/mol) reveals interesting insight into the impact of perfluorinated polymer backbone on the hydration enthalpies [45]. Despite the enormous research efforts, many properties of Nafion especially those related to water uptake and diffusion still remain elusive. For example, the famous Schroeder's paradox[*] of solvent uptake which was believed to be valid for Nafion as in the case of other polymer electrolyte membranes has been disproved quite recently [46].

[*] In 1903, Schroeder reported that gelatin has less water uptake from water vapor (100% RH) than from liquid water at the same temperature. This is a paradox, because according to thermodynamics, at equilibrium, the water content of gelatin should be the same in both the cases, as the chemical potential of liquid water is equal to that of water vapor at a given temperature [46].

Most recent models based on SAXS investigations of Nafion provide significant insights into its microstructure. Hydrated Nafion exhibits a typical SAXS signal, popularly called the 'ionomer peak' at around q (= 2π/(4 nm)), where, q (= 4π/λSinθ) is the scattering vector with the scattering angle 2θ and λ is the wavelength of the incident X-ray. This ionomer peak has been interpreted in different ways to represent the shape of the hydrophilic clusters in Nafion as spherical inverted micelle clusters [47a], layered structures [38b], channel networks [31, 47b] and polymer bundles [38a]. The most remarkable progress is the more general model for Nafion proposed recently based on SAXS simulations [48]. Accordingly, the water channels are parallel, like inverted-micelle cylinders of 4 nm diameter as depicted in Figure 1.5. This model is effective in explaining many dynamic aspects of Nafion membranes like why diffusion of water in Nafion at 20% hydration is only one order slower than that of bulk water? Why is the water self-diffusion coefficient in Nafion one order higher than that in other sulfonated polymers? How does its conductivity persist till – 50 ^{o}C although half of its water content freezes out at – 20 ^{o}C? To answer these questions, the authors have quantitatively analyzed the SAXS curves reported earlier [49] using the parallel water channel model. Interestingly Figure 1.5d shows how the scattering patterns of free-standing water cylinders and crystallites themselves in a structure-less matrix are correlated with the net pattern of the Nafion matrix in a log(I) versus log(q) plot while the inset of Figure 1.5d shows the ionomer peak alone in a linear I versus q plot.

1.4.2. Proton Conduction Mechanisms

Proton conduction in hydrated PEMs in general is assumed to occur in four important steps, viz.,

i. Dissociation of protons from the acidic site
ii. Subsequent transfer of the protons to the aqueous medium
iii. Screening of the proton from its conjugate base by water molecules

iv. Diffusion of protons in confined water

As a consequence of inadequate information about the microstructure, the proton conduction mechanism of Nafion also remains under debate. At present, it is widely

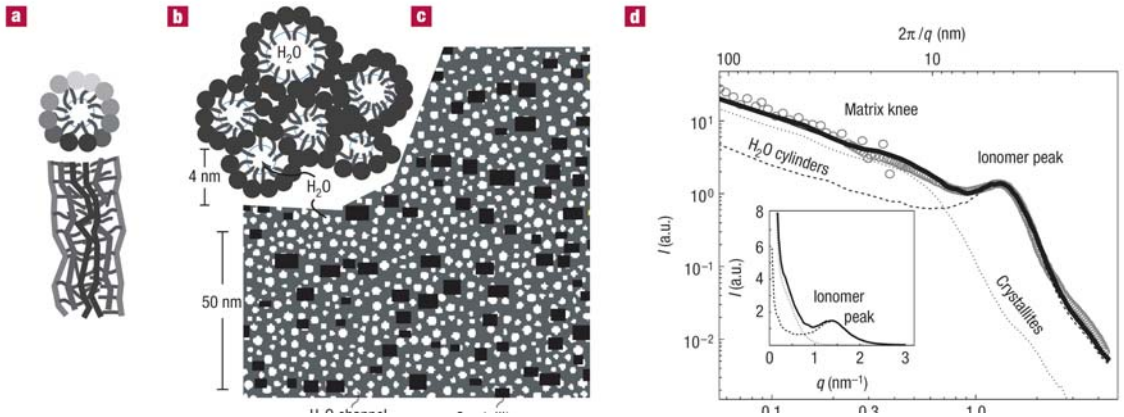

Figure 1.5. Parallel water channel (inverted-micelle cylinder) model of Nafion . a) Two views of an inverted-micelle cylinder with the polymer backbones on the outside and the ionic side groups lining the water channel. Polymer chains in the front and the back are distinguished by shading; b) Hexagonal packing of several such inverted-micelle cylinders; c) Cross sectional view in which the water channels are shown in white, crystallites in black and non-crystalline region in grey; d) Small angle X-ray scattering data simulated based on the model. *Reproduced from Ref.* [*48*].

accepted that the proton conductivity of Nafion strongly depends on its microstructure and water content. At low water content, the interaction between water molecules via hydrogen bonding is low and the sulfonic acid groups are not completely dissociated. This results in a low dielectric constant with the proton transport limited only to the surface leading to low conductivity. At higher water content, however, the properties of water in Nafion approach that of bulk water. Thus, two different water environments could be distinguished with water in the middle of the pores being referred to as ‘bulk water’, where proton transport is very fast and that in the pore surface close to the array of sulfonic acid groups is called ‘surface water’, where proton transport is slow. Thus the

measured proton conductivity of Nafion is a weighted average of the surface and the bulk conductivities which can vary by more than two orders of magnitude from a dry membrane to a fully humidified one. Accordingly, three major mechanisms of proton transport have been proposed for Nafion viz., surface diffusion, Grotthuss diffusion and *en masse* or vehicular transport as depicted in Figure 1.6 [7].

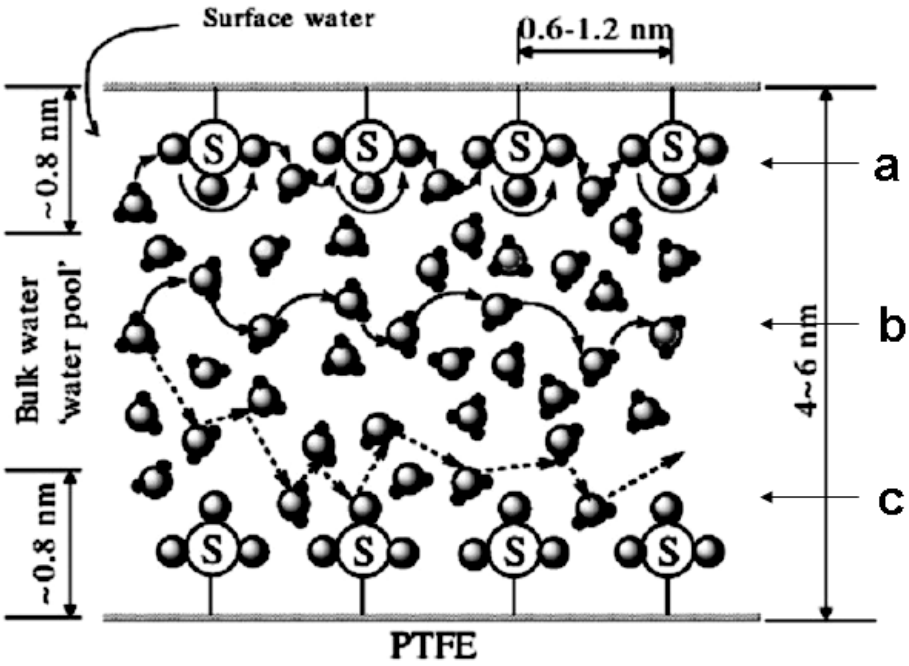

Figure 1.6. Proton transfer in Nafion in fully hydrated state by (a) surface diffusion, (b) Grotthuss mechanism and (c) vehicular mechanism. *Adapted from Ref.* [*6*].

In the **surface diffusion mechanism**, the proton hops between adjacent sulfonate sites [7]. As the distance between adjacent sulfonate groups is too large (0.6-1.2 nm) for a proton to step directly from one group to another, it hops via intermediate water molecules. The rate determining step in this process is to overcome the strong coulombic attraction between the SO_3^- and the H_3O^+ ions. The activation barrier for proton hopping may also involve contributions from conformational fluctuations of the pendant chains. The **Grotthuss or the "relay" mechanism** involves the conduction of protons along a chain of hydrogen bonded water molecules [50]. This 200 year-old mechanism

successfully explains the higher proton conductivity of ice than that of water (about 50 times higher than that of water) considering the more efficient hydrogen bonding in ice (four water molecules per hydronium ion) than that in liquid water (only three water molecules per hydronium ion) [14]. In the case of Nafion, the reorientation of the proton accepting water molecule is the rate-determining step for this mechanism [51]. On the other hand, **the *en masse* or vehicular mechanism** involves the diffusion of hydronium ions as a whole in a continuum of water, in which the diffusion process follows a simple Stokes-Einstein relationship,

$$D_{H^+} = \frac{k_B T}{6\pi\eta r} \tag{1.4}$$

where, k_B is the Boltzmann constant, η is the viscosity of the medium and r is the radius of the hydronium ion. An interesting comparison of the diffusion coefficient of protons for the three mechanisms calculated using molecular dynamics simulation using the assumptions discussed above is provided in Table 1.2. In addition, the table summarizes the critical time scales and length scales for proton transport calculated using the Einstein-Smoluchowski expression,

$$D_{H^+} = \frac{l^2}{\kappa\tau_D} \tag{1.5}$$

where, D is the diffusion coefficient of protons, l is the mean step distance, τ_D is the time lag between successive steps and κ could be an interger like 2,4,6 for a one-, two- or a three- dimensional walk respectively [7].

The mean step time is the smallest for the Grotthuss mechanism which indicates that it is the fastest mode of proton transport, while the smallest value for the surface diffusion mechanism implies that it does not contribute significantly to the overall proton

conductivity of Nafion except at low levels of hydration. This also explains the low proton conductivity of Nafion at low water contents, when protons transfer mostly via the surface diffusion mechanism. On the other hand, the kinetics of proton transfer has also been investigated since the past 60 years in the framework of transition state theory. While it has been assumed so far that the transition state occurs within the proton transfer coordinate, recent models have proved that it occurs within the solvent coordinate [52].

Table 1.2. Comparison of the three different mechanisms of proton transport in Nafion vide *Ref.* [*7*]

	Surface diffusion	**Grotthuss diffusion**	**Vehicular diffusion**
Proton Diffusion Coefficient (cm^2/s)	1.01×10^{-7}	7×10^{-5}	1.7×10^{-5}
Step time (τ_D) (s)	1.61×10^{-9}	1.5×10^{-12}	5.78×10^{-12}
Step distance, *l* (nm)	0.255	0.255	0.28

In the case of salt-containing polymer gel electrolytes, yet another mechanism of ion conduction, known as the segmental motion mechanism operates which involves ion transport assisted by the mobility of the polymer segments as depicted in Figure 1.7 [14].

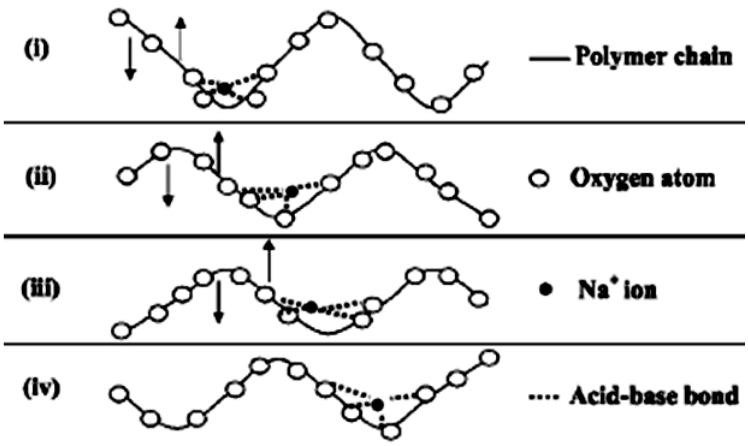

Figure 1.7. Ionic transport aided by segmental motion of the polymer chains in the case of salt-containing polymer electrolytes. *Reproduced from Ref.* [*14*].

The distribution of protons between the surface and the bulk of the pore is also important as this essentially depends upon the acid strength of the functional groups as well as on the nature of the polymer backbone. As the majority of proton transport occurs through the Grotthuss diffusion mechanism, the formation of a high fraction of hydronium ions in the pore bulk is important for high proton conductivity. This is one of the reasons for the success of Nafion, whose hydrophobic backbone facilitates the formation of bulk rather than surface water.

1.4.3. Limitations of Nafion

Before we proceed to engineer a material for a specific application, it is important to have a thorough knowledge of how its final properties are related to its molecular constitution. In this context, it is essential to understand the limitations of various experimental and theoretical procedures to understand Nafion, which has perhaps resulted in some misunderstanding. It is universally accepted that the transport properties and water content in a PEM depend on its morphology. But what is the morphology of Nafion? Every experimental technique used to study Nafion, has its own limitation which

precludes from examining the membrane in its 'active' state. For example, Transmission Electron Microscopy (TEM) is conducted in vacuum only for 'dry' membranes; Atomic Force Microscopy (AFM) probes the structure only near the surface; SAXS and Small Angle Neutron Scattering (SANS) show a single peak corresponding to the hydrophilic clusters and provide no information about the structure of the repeat units. With such uncertainties in understanding the morphology, how do we understand the water uptake behavior? An excellent example of this is the description of the misrepresentation of the famous Schroeder's paradox of water uptake in Nafion [46]. It has been reported frequently that at 30 ^{o}C, the liquid-equilibrated water content of Nafion (λ) is 22 mol H_2O/mol SO_3^- and 100 % RH-vapor equilibrated water content is 14 mol H_2O/mol SO_3^- [53]. A recent analysis has revealed that the paradox does not hold for Nafion and that the reported values were merely due to variations in water uptake in membranes of different thermal histories, morphology, uncertain experimental conditions, environmental effects and experiments conducted at non-equilibrium conditions. Similar errors have been noticed in proton conductivity measurements too [54].

In essence, the fundamental properties of Nafion which are still under debate include,

i. **Morphology of Nafion –** Experimental evidences show that the hydrophilic/hydrophobic interfaces are rough and 'fuzzy', while the models consider them as discrete phase discontinuities.
ii. **Structure of Confined Water in Nafion –** In sufficiently hydrated samples, water can form an extended phase and the clusters can become anisotropic and contiguous to form percolation pathways. The exact nature of the inter-domain water structure is under debate till date.
iii. **Chain Dynamics –** The long- and short-ranged motions in the backbone and side chains in Nafion have been interpreted differently by variously assigned transitions in dynamic mechanical studies.

iv. **Morphology-Mechanical Property Relationship –** With new methods of membrane preparation and drive toward thinner membranes for improved transport properties there is an immediate need for understanding critical morphology-mechanical property relationships.

v. **Failure of Mathematical models –** There has been no fundamental mathematical model for Nafion to predict new phenomena or to cause property improvements in a significant way. The shortcomings include an inability to sufficiently account for chemical identity, an inability to simulate and predict the long-range structure and the failure to simulate structure over different hierarchy levels.

From the above discussions, it is clear that the tuning of these materials for optimum performance requires a detailed knowledge of their chemical microstructure and nanoscale morphology. In particular, proton conductivity, water management, relative affinity of methanol and water in direct methanol fuel cells, hydration stability at high temperatures, electro-osmotic drag, mechanical, thermal and oxidative stability are important properties that must be controlled in the rational design of these membranes.

In addition, from a commercial viewpoint, Nafion suffers from a number of limitations like, poor oxidative stability of the perfluoro side chains in the presence of specific oxidants like peroxides, humidity-dependent proton conductivity, permeability to molecules/species of interest to fuel cells (viz., methanol, ethanol, hydrogen and borohydride), poor mechanical stability, high cost, environmental hazards and issues related to disposal. In addition, its inability to operate above 80 ^{o}C limits the performance of fuel cells using reformed hydrogen with possible CO contamination which poisons the Pt electrocatalyst. Although several approaches have been developed to address many of these issues, including attempts to replace Nafion with alternative polymer electrolytes and those involving chemical modifications of Nafion to achieve hybrid composite

electrolytes with desired properties, many aspects still remain unclear, necessitating more focused investigations in this system.

1.5. Current Trends in Polymer Electrolyte Research

As the number of primary variations in the chemical structure of Nafion membrane is very limited, research attempts are aimed at tuning its morphology and hence its properties for better performance either by varying the thermal/mechanical treatment procedures and solvent systems, or by adopting alternative strategies including composite/hybrid Nafion membranes, complexation with other polymer electrolytes and bio-inspired design. Extensive studies have been reported on the control of Nafion's properties by varying its intrinsic parameters such as treatment procedures and solvent systems [22]. Hence any further improvement in the properties of Nafion requires a radically different approach, which has been identified recently as the hybrid/composite membrane approach. There have been three broad categories of such 'multi-component' PEMs viz.,

- **Hybrid electrolytes –** Polymer blends, acid-base polymer electrolyte complexes and ionic liquids
- **Nanocomposites –** Composites of nanostructured oxides, Zeolites and Carbon nanotubes
- **Biocomposites –** Composites of biological entities and molecules

For example, various methods for converting thermally stable polymers into sulfonic acid-based PEMs are depicted in Figure 1.8.

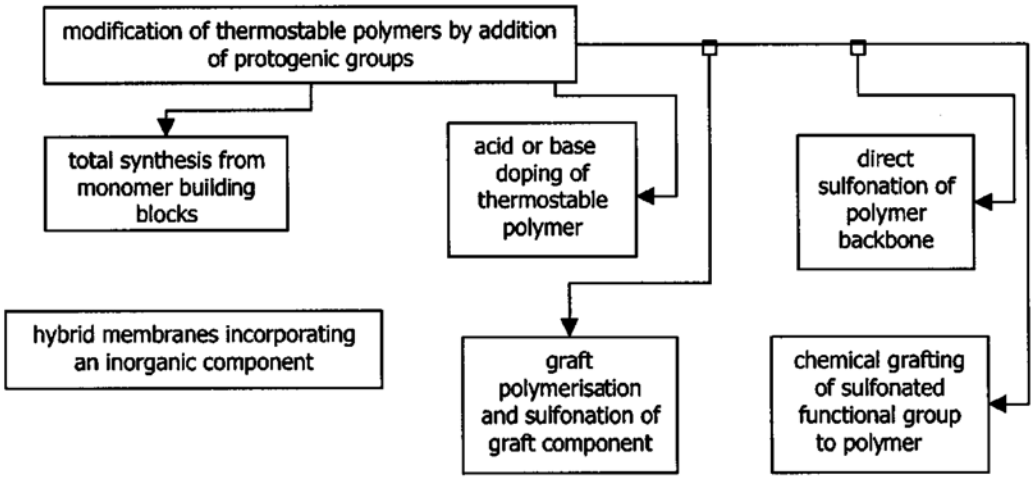

Figure 1.8. Development of proton conducting membranes by modifying thermally stable polymers in various ways. *Adapted from Ref* [*54*].

The concept of improving the properties of a polymer electrolyte using a foreign ingredient began with the synthesis of polymer blends. In this approach an existing polymer is combined with another polymer to achieve the requisite polymer properties by exploiting interfacial and geometrical (perhaps synergistic) effects of polymer-polymer interactions. For example, methanol permeability of Nafion can be reduced easily by introducing another polymer like poly (vinylidene fluoride), which changes its morphology without any significant loss in proton conductivity for application in direct methanol fuel cells [56]. This approach has been particularly effective when there is an acid-base interaction between the component polymers. More commonly, tethering of N-heterocycles to a polymer backbone followed by its blending with a sulfonic acid polymer is an attractive strategy to achieve high proton conduction through acid-base interactions involving the sulfonic acid groups in one polymer and the basic N-containing groups in the other polymer [57]. Another interesting example is the preparation of a rubbery gel electrolyte of Nafion by swelling it with 1-butyl-3-methyl-imidazolium (BMIM) based ionic liquids [58] following the strategy of 'polymer-in-salt' used in Lithium ion batteries [59].

Another approach to modify Nafion has been to prepare nanocomposites by introducing fillers such as montmorillonite, titanium dioxide, silica and hydroxyapetite often in nanostructured form [60], the main objectives being improved proton conductivity, water retention at high temperatures and better mechanical strength. These composites can be classified broadly into three types viz.,

- Both the polymer and the additive are ionically conductive
- Ionic polymer with a non-conducting additive for mechanical support
- Ionic polymer with a hygroscopic additive

The first attempt in this area was made by Savinell *et al* in 1994, who incorporated phosphoric acid in Nafion and achieved a conductivity of 0.05 Scm^{-1} at 150 ^{o}C [61]. Here, the phosphoric acid acts as a Bronsted base and solvates the proton from the strong sulfonic acid group in the same way as water does, the lower volatility of the former offering the advantage of extending the operating temperature upto 200 ^{o}C. Following this, several composites have been developed like phosphoric acid/ZrO_2 - doped poly(benzimidazole) (PBI) [62].

One of the more recent and highly appreciated approaches is the bio-inspired design of polymer electrolytes [63]. Unlike the fast translocation of protons in aqueous solution in PEFCs, most of the proton conduction phenomena in biological systems occur via a "hop-and-turn" or the Grotthuss mechanism, which involves chemical exchange of protons and reorganization among hydrogen bonded molecular networks. The controlled hydrogen-bonded network in biomolecules such as proteins, is essential for efficient energy transduction in living systems [64]. This approach has been especially successful to design anhydrous proton conductors in which proton transport occurs without the help of diffusible molecules such as the oxonium ions, phosphoric acid or sulfuric acid. A fairly recent example is the design of an anhydrous proton conductor employing

derivatives of Chitin (a mucopolysaccharide present in crab and shrimp) and Imidazole [65].

1.5.1. Electrochemical Imaging of Proton Transport

Real-time monitoring of proton transport along with its distribution in polymer electrolyte allows a correlation of the polymer morphology with its transport properties. This is achieved by electrochemical imaging of the polymer films using an ultramicroelectrode (UME) probe which is laterally rastered over the surface of the films. UME offers unique advantages over the conventional macroelectrodes owing to features like small currents, steady-state responses and short response times [66]. In addition, the application of UMEs offers very low ohmic drop at the electrode/electrolyte interface allowing investigations in highly resistive media and hence is especially suitable for un-supported systems like polymer electrolytes where electrochemical investigations can be carried out without an externally added supporting electrolyte [67]. Exploiting the unique features of UME, Bard and coworkers developed an elegant electrochemical imaging technique called Scanning Electrochemical Microscopy (SECM) [68], the importance of which for various investigations has been elegantly reviewed [69]. Typical types of polymer electrolyte studies using SECM involve;

i. Incorporation of inorganic complexes into the polymer electrolyte film [70]
ii. Following the injection of redox species dissolved in the electrolyte solution into the film [71]
iii. Investigations using the H^+/H_2 mediator systems to probe proton transport in the films without any externally added redox couple [72]
iv. Monitoring the transport of electroactive molecules in the polymer film [73]

In addition, SECM offers several advantages in studying processes in living cells and tissues over many other contemporary techniques [74]. For example, fluorescence imaging, which is a popular technique for real-time monitoring of processes at single cell level, is not suitable for long-term measurement due to photochemical decomposition of fluorescence staining agents [75]. Other indirect methods of studying cellular processes involve the monitoring of their metabolic activities through parameters like the rate of uptake of glucose and oxygen [76a], production of heat [76b] and pH changes [76c]. Thus SECM serves as a non-destructive tool for long-term monitoring of cellular activities. However, special attention is to be paid in discriminating artifacts arising from improper tip geometry and irregular morphology of the sample by imaging multiple regions often repeating the experiments with duplicate tips.

Based on the above discussion, it is obvious that a number of issues related to polymer electrolytes, in general and Nafion, in particular, require special attention necessitating further investigations including, the correlation of macroscopic (hydrodynamic) behavior with molecular scale properties, understanding critical factors affecting proton transport via experimental approaches in model systems and identifying molecular processes which are central to decide the performance of the final device. Accordingly, the scope and objectives of the present thesis have been identified as given below.

1.6 Scope and Objectives of the Thesis

The present thesis attempts to address some of the above challenges by designing different types of hybrid polymer electrolytes. More specifically, the objectives of the thesis are set as follows:

- To develop an all-solid-state electrochemical methodology for understanding the solid state transport properties of Nafion

- To understand the redox compatibility of Nafion with iron complexes like cyanoferrates and heme-proteins
- To tune the properties of Nafion by coupling it with oppositely charged polymer electrolytes
- To investigate the interaction of Nafion with selected molecules involved in proton transport processes in biology
- To interrogate the effect of incorporating one-dimensional nanostructures like carbon nanotubes in Nafion and similar systems like polyacrylamide
- To explore electrochemical imaging protocols using Scanning Electrochemical Microscopy for proton distribution and related phenomena in biological systems

1.7 Organization of the Thesis

First chapter represents a critical review of the state-of-the-art polymer electrolyte research. It begins by providing an overview of the physical chemistry of polymer electrolytes in general and their technological significance. This is followed by a discussion on the progress made so far in understanding various aspects of polymer electrolytes like ionic transport mechanism and microstructure with special emphasis on Nafion and related sulfonic acid based systems. After identifying the critical limitations, the objectives of the present study are explained with special relevance to understanding the proton conduction domains of Nafion using electrochemical techniques.

In **second chapter**, we demonstrate a unique methodology ('all-solid-state electrochemistry') to unravel the dynamical processes occurring at the interface of hydrophilic and hydrophobic domains in Nafion. A special three-electrode set up is designed, in which a film of the polymer electrolyte can be directly cast to form the electrode/ electrolyte interface. This differs from the conventional electrochemical cells

for polymer electrolyte investigations in that there is no need to dip the film-modified working electrode in an electrolyte. Thus the methodology avoids critical interruptions due to ion ingress/egress at the polymer/liquid electrolyte interface and allows a better understanding of its dynamical properties. This chapter specifically deals with the investigation of potassium ferro/ferri cyanide couple and hemoglobin entrapped in Nafion membrane.

In **third chapter**, we demonstrate the effect of molecular level electrostatic interactions between two oppositely charged polymer electrolytes on the dynamical behavior of either of the partners. More specifically, when Nafion is allowed to interact with polyoxyethylene bis (amine), the sulfonate groups of the former get electrostatically associated with the protonated amino groups of the latter. Physical, spectroscopic and electrochemical characterization of the hybrid materials in various compositions reveals the formation of polyelectrolyte complexes. The techniques include viscosity, capillarity, surface tension and contact angle measurements, UV-visible and fourier transform infrared spectroscopy and cyclic voltammetry with potassium ferro/ferri cyanide redox couple.

In **fourth chapter**, we explore the possibility of enhancing the performance of Nafion by incorporating molecules having a similar role in biological systems. More specifically, we have chosen a few nitrogenous compounds from two classes of plant hormones viz., the auxins and cytokinins to investigate the possibility. Dispersions and membranes of Nafion/hormone composites have been analyzed using UV-visible spectroscopy, diffuse reflectance infrared spectroscopy, solid-state cyclic voltammetry, and electrochemical impedance measurements. Subsequently, the hormones are introduced into the catalyst layer of H_2/O_2 polymer electrolyte fuel cells and the performance is tested with different loading of hormones. The respective membrane-electrode assemblies are studied using electrochemical impedance and kinetics of oxygen

reduction at the hormone-modified catalyst layer is followed using rotating disk voltammetry.

Fifth chapter discusses the synthesis and application of carbon nanotube (CNT)/polyacrylamide (PAM) composite gels for protein separation. Polyacrylamide is chosen because of its structural and functional similarities to Nafion such as amphiphilic structure, network formation and ability to conduct protons when acidified. Parameters like gel concentration and protein loading have been optimized to demonstrate how CNTs enhance the reliability of molecular weight determination of proteins by a commonly adapted technique called SDS-PAGE (sodium dodecyl sulfate- polyacrylamide gel electrophoresis). We also investigate the tunability of these composites by discriminating the efficiencies of single walled and multi walled carbon nanotubes and provide a rationale with a qualitative model to explain how the nanotubes affect the network topology of the polyacrylamide gel.

Sixth chapter deals with the development of various methodologies for imaging proton conductivity and proton coupled processes by Scanning Electrochemical Microscopy (SECM). Two modes of imaging viz., the 'Generation/Collection' and 'Feedback' modes have been optimized using different systems including Nafion membranes and platinized carbon incorporated in Nafion films. Then, the relevance of SECM in investigating specific biological phenomena has been demonstrated by studying the stomatal physiology and photosynthetic activity of peanut leaves. These results provide interesting insights into the relationship of stomatal movements to the transport of protons across the guard cells.

The last (**seventh**) chapter summarizes major conclusions realized from all the investigations of the thesis. It also outlines some of the limitations of these studies, including the lack of microscopic information on the distribution of hydrophilic and hydrophobic domains. Nevertheless, the results of these studies are believed to be useful

for the development of hybrid composite polymer electrolytes with tailor-made properties by incorporating key species and molecules that can effect critical changes in their microenvironments. The chapter finally indicates the future perspectives of polymer electrolytes with respect to major expectations in the following decades.

1.8 References

1. Scrosati, B. *Prog. Solid St. Chem.* **1988**, *18*, 1.
2. Brandon, N. P.; Skinner, S.; Steele, B. C. H. *Annu. Rev. Mater. Res.* **2003**, *33*, 183.
3. Agrawal, R. C.; Pandey, G. P. *J. Phys. D:Appl. Phys.* **2008**, *41*, 223001.
4. Drifford, M.; Dlabiez, J. P. *J. Phys. Chem.* **1984**, *88*, 5368.
5. Holliday, L. *Ed.,"Ionic Polymers"* Applied Science Publishers Ltd., London (1975).
6. Paddison, S. J. *Ann. Rev. Mater. Res.* **2003**, *33*, 289.
7. Choi, P.; Jalani, N. H.; Datte, R. *J. Electrochem. Soc.* **2005**, *152*, E123.
8. Bockris, J. O′ M; Reddy, A. K. N.; Aldeco, M. –G. *Modern Electrochemistry: Fundamentals of Electrodics, Vol. 2A, Second edition,* Kluwer Academic Publishers, New York (2000).
9. Bontha, J. R.; Pintauro, P. N. *Chem. Engg. Sci.,* **1994**, *49*, 3835.
10. Ratner, M. A. *Acc. Chem. Res.* **1982**, *15*, 355.
11. Berthier, C.; Gorecki, W.; Minnier, N.; Armand, M. B.; Chabagno, J. M.; Rigaud, P. *Solid State Ionics* **1983**, *11*, 91.
12. Druger, S. D.; Nitzan, A.; Ratner, M. A.; *J. Chem. Phys.* **1983**, *79*, 3133.
13. Bruce, P. G.; Vincent, C. A. *J. Chem . Soc. Farady Trans.* **1993**, *89*, 3187.
14. Choudhury, N. A.; Shukla, A. K.; Sampath, S.; Pitchumani, S. *J. Electrochem. Soc.* **2006**, *153*, A614.
15. Dias, F. B.; Plomp, L.; Veldhuis, J. B. J. *J. Power Sources* **2000**, *88*, 169.

16. Mitra, S.; Shukla, A. K.; Sampath, S. *J. Power Sources* **2001**, *101*, 213.
17. Millet, P.; Andolfatto, F.; Durand, R. *Int. J. Hydrogen Energy* **1996**, *21*, 87.
18. Nunes, S. C. *et al J. Mater. Chem.* **2007**, *17*, 4239.
19. Opekar, F. E.; Tulik, K. S. *Anal. Chim. Acta* **1999**, *385*, 151.
20. http://www.fueleconomy.gov/feg/fcv_pem.html
21. Hickner, M. A.; Ghassemi, H.; Kim, Y. S.; Einsla, B. R.; McGrath, J. E. *Chem. Rev.* **2004**, *104*, 4587.
22. Mauritz, K. A.; Moore, R. B. *Chem. Rev.* **2004**, *104*, 4535.
23. Wei, J.; Stone, C.; Stone, A. E., Ballard Power Systems Inc., June 6, 1995; U. S. Patent 5, 422, 411.
24. Xing, P.; Robertson, G. P.; Guiver, M. D.; Mikhailenko, S. D.; Wang, K.; Kaliaguine, S. *J. Membr. Sci.* **2004**, *229*, 95.
25. Wycisk, R.; Pintauro, P. N. *J. Membr. Sci.* **1996**, *119*, 155.
26. Chung, T. –S. *Polymer Reviews* **2008**, *37*, 277.
27. Genies, C.; Mercier, R.; Sillion, B.; Cornet, N.; Gebel, G.; Pineri, M. *Polymer* **2001**, *42*, 359.
28. Savett, S. C. *et al. J. Electrochem. Soc.* **2002**, *149*, A1527.
29. Miyatake, K.; Hay, A. S. *J. Polym. Sci., Part A: Polym. Chem.* **2001**, *39*, 3770.
30. Herz, H. G. ; Kreuer, K. D. ; Maier, J. ; Scharfenberger, G. ; Schuster, M. F. H.; Meyer, W. H. *Electrochim. Acta* **2003**, *48*, 2165.
31. Kreuer, K. D. *J. Membr. Sci.* **2001**, *185*, 29.
32. (a) Ibrahim, S. M.; Price, E. H.; Smith, R. A. of E. I. du Pont de Nemours and company, *Proc. Electrochem. Soc.* **1983**, 83. (b) Resnick, P. R.; Grot, W. G. of E. I. du Pont de Nemours and company, Wilmington, DE, Sept 12, 1978; U.S. Patent 4, 113, 585.
33. (a) Gierke, T. D.; Munn, G. E.; Wilson, F. C. *J. Polym. Sci. Polym. Phys. Edn.* **1981**, *19*, 1687. (b) Kreuer, K. D.; Paddison, S. J.; Spohr, E.; Schuster,

M. *Chem. Rev.* **2004,** *104*, 4637.

34. Robertson, M. A. F.; Yeager, H. L. *Macromolecules* **1996**, *29*, 5166.
35. (a) Chu, B.; Wu, C.; Buck, W. *Macromolecules* **1989**, *22*, 831. (b) Schwartz, B. –R.; Mitchell, G. R. *Polymer* **1996**, *37*, 1857.
36. Doyle, M.; Rajendran, G. *Handbook of Fuel Cells Fundamentals, Technology and Applications*; John Wiley & Sons: Chichester, U.K., 2003; Vol. 3, Part 3, Chapter 30, p. 351.
37. Xu, G. *Polymer* **1993**, *25*, 397.
38. (a) Rollet, A. -L. ; Diat, O. ; Gebel, G. *J. Phys. Chem. B* **2002**, *106*, 3033. (b) Starkweather, H. W. Jr. *Macromolecules*, **1982**, *15*, 320. (c) Mauritz, K. A.; Fu, R. -M. *Macromolecules*, **1988**, *21*, 1324. (d) Paddison, S. J.; Reagor, D. W.; Zawodzinski, T. A. Jr. *J. Electroanal. Chem.* **1998**, *459*, 91. (e) Ceynowa, J. *Polymer* **1978**, *19*, 73. (f) Zoppi, R. A.; Yoshida, I. V. P.; Nunes, S. P. *Polymer* **1998**, *39*, 1309. (g) Lehmani, A.; Vidal, S. –D.; Turq, P. *J. Appl. Polym. Sci.* **1998**, *68*, 503. (h) Bath, B. D.; Lee, R. S.; White, H. S.; Scout, E. R. *Anal. Chem.* **1998**, *70*, 1047. (i) Komoroski, R. A.; Mauritz, K. A. *J. Am. Chem. Soc.,* **1978**, *100*, 7487. (j) Amigo, M. G. –A.; Schlick, S. *J. Phys. Chem.* **1986**, *90*, 6353. (k) Wirguin, C. –H. *Polymer* **1979**, *20*, 371. (l) Martin, C. R.; Rubinstein, I.; Bard, A. J. *J. Am. Chem. Soc.* **1982**, *104*, 4817.
39. Paddison, S. J. *Ann. Rev. Mater. Res.* **2003**, *33*, 289.
40. Gierke, T. D. *J. Electrochem. Soc.* **1978**, *125*, 163C.
41. Yeager, H. L.; Steck, A. *J. Electrochem. Soc.* **1981**, *128*, 1880.
42. Paddison, S. J.; Bender, G.; Kreuer, K. D.; Nicoloso, N.; Zawodzinski, T. A. Jr. *J. New Mater. Electrochem. Syst.* **2000**, *3*, 291.
43. Seeliger, D.; Hartnig, C.; Spohr, E. *Electrochim. Acta* **2005**, *50*, 4234.
44. Marechal, M.; Souquet, J. –L.; Guindet, J.; Sanchez, J. –Y. *Electrochem. Commun.* **2007**, *9*, 1023.

45. Reucroft, P. J.; Rivin, D.; Schneider, N. S. *Polymer* **2002**, *43*, 5157.
46. Onishi, L. M.; Prausnitz, J. M.; Newman, J. *J. Phys. Chem. B* **2007**, *111*, 10166.
47. (a) Gebel, G.; Lambard, J. *Macromolecules*, **1997**, *30*, 7914. (b) Kim, M.-H.; Glinka, C. J.; Grot, S. A.; Trot, W. G. *Macromolecules*, **2006**, *39*, 4775.
48. Rohr, K. –S.; Chen, Q. *Nature Materials* **2007**, *7*, 75.
49. Rubatat, L.; Rollet, A. –L.; Gebel, G.; Diat, O. *Macromolecules* **2004**, *37*, 7772.
50. Mohammad, O. F.; Pines, D.; Dreyer, J.; Pines, E.; Nibbering, T. J. *Science* **2005**, *310*, 83.
51. (a) Bernal, J. D.; Fowler, R. H. *J. Chem. Phys.* **1933**, *1*, 515. (b) Conway, B. E.; Bockris, J. O' M.; Linton, H. *J. Chem. Phys.* **1956**, *24*, 834. (c) Agmon, N. *Chem. Phys. Lett.* **1995**, *244*, 456.
52. Peters, K. S. *Acc. Chem. Res.* **2009**, *42*, 89.
53. (a) Mooris, D. R.; Sun, X. *J. Appl. Polym. Sci.,* **1993**, *50*, 1445. (b) Zawodzinski, T. A.; Davey, J.; Valerio, J.; Gottesfeld, S. *Electrochim. Acta* **1995**, *40*, 297. (c) Weber, A. Z.; Newman, J. *J. Electrochem. Soc.* **2003**, *150*, A1008. (d) Weber, A. Z.; Newman, J. *J. Electrochem. Soc.* **2004**, *151*, A311.
54. Anantaraman, A. V.; Gardner, C. L. *J. Electroanal. Chem.* **1996**, *414*, 115.
55. Roziere, J.; Jones, D. J. *Annu. Rev. Mater. Sci.* **2003**, *33*, 503.
56. Wycisk, R.; Chisholm, J.; Lee, J.; Lin, J.; Pintauro, P. N. *J. Power Sources* **2006**, *163*, 9.
57. (a) Kerres, J. A. *J. Membr. Sci.* **2001**, *185*, 3. (b) Kerres, J. A. *Fuel Cells* **2005**, *5*, 230. (c) Fu, Y. –Z.; Manthiram, A.; Guiver, M. D. *Electrochem. Commun.* **2006**, *6*, 1386. (d) Jannasch, P. *Curr. Opin. Colloid Interface Sci.* **2003**, *8*, 96.
58. Doyle, M.; Choi, S. K.; Proulx. G. *J. Electrochem. Soc.* **2000**, *147*, 34.

59. Angell, C. A.; Liu, C.; Sanchez, E. *Nature* **1993**, *362*, 137.

60. (a) Silva, R. F.; Passerini, S.; Pozio, A. *Electrochim. Acta* **2005,** *50,* 2639. (b) Liu, J.; Wang, H. T.; Cheng, S. A.; Chan, K. Y. *J. Membr. Sci.* **2005**, *246*, 95. (c) Baglio, V. *et al J. New Mater. ELectrochem. Soc.* **2004**, *7*, 275. (d) Arico, A. S. *et al Solid State Ionics,* **2003***,161*, 255. (e) Mikaye, N.; Wainright, J. S.; Savinell, R. F. *J. Electrochem. Soc.* **2001**, *148*, A905. (f) Park, Y.; Yamazaki, Y. *Polym. Bull.* **2005**, *53*, 181.

61. Savinell, R, *et al., J. Electrochem. Soc.* **1994**, *141*, L46.

62. Jang, M. Y.; Yamazaki, Y. *Solid State Ionics* **2004**, *167*, 107.

63. (a) Iwata, K.; Sawadaishi, T.; Nishimura, S.; Tokura, S.; Nishi, N. *Int. J. Biol. Macromol.* **1996**, *18*, 149. (b) Kumar, M. N. V. R. *React. Funct. Polym.* **2000**, *46*, 1. (c) Suh, J. K. F.; Matthew, H. W. T. *Biomaterials* **2000**, *21*, 2589.

64. (a) Chernyshev, A.; Armstrong, K. M.; Cukierman, S. *Biophys. J.* **2003**, *84*, 238. (b) Pomes, R.; Roux, B. *Biophys. J.* **2002**, *82*, 2304.

65. Yamada, M.; Honma, I. *Angew Chem. Int. Ed.,* **2004**, *43,* 3688.

66. (a) Zoski, C. G. *Electroanalysis* **2002**, *14*, 1041. (b) Engstrom, R. C.; Wightman, R. M.; Kristensen, E. W. *Anal. Chem.* **1988**, *60*, 652. (c) Engstrom, R. S.; Weber, M.; Wunder, D. G.; Burgess, R.; Winquist, S. *Anal. Chem.* **1986**, *58*, 844. (c) Engstrom, R. C.; Meaney, T.; Tople, R.; Wightman, R. M. *Anal. Chem.* **1987**, *59*, 2005.

67. (a) Kwak, J.; Anson, F. C. *Anal. Chem.* **1992**, *64*, 250. (b) Lee, C.; Anson, F. C. *Anal. Chem.* **1992**, *64*, 528.

68. (a) Bard, A. J.; Fan, F. –R.; Kwak, J.; Lev, O' *Anal. Chem.* **1989**, *61*, 132. (b) Kwak, J.; Bard, A. J. *Anal. Chem.* **1989**, *61*, 1221. (c) Kwak, J.; Bard, A. J. *Anal. Chem.* **1989**, *61*, 1794.

69. (a) Lu, X.; Wang, Q.; Liu, X. *Anal. Chim. Acta* **2007**, *601*, 10. (b) Wittstock, G.; Burchardt, M.; Pust, S. E.; Shen, Y.; Zhao, C. *Angew. Chem.*

Int. Ed., **2007**, *46*, 1584.

70. Jeon, C.; Anson, F. C. *Anal. Chem.* **1992**, *64*, 2021.
71. Yang, N.; Zoski, C. G. *Langmuir* **2006**, *22*, 10338.
72. Kallio, T.; Slevin, C.; Sundholm, G.; Holmlund, P.; Kontturi, K. *Electrochem. Commun.* **2003**, *5*, 561.
73. Bath, B. D.; White, H. S. *Anal. Chem.* **2000**, *72*, 433.
74. (a) Liu, B.; Cheng, W.; Rotenberg, S. A.; Mirkin, M. V. *J. Electroanal. Chem.* **2001**, *500*, 590. (b) Amemiya, S.; Guo, J. D.; Xiong, H.; Gross, D. A. *Anal. Bioanal. Chem.* **2006**, *386*, 458. (c) Roberts, W. S.; Lonsdale, D. J.; Griffiths, J.; Hickson, S. P. J. *Biosens. Bioelectron.* **2007**, *23*, 301.
75. Roden, M. M.; Lee, K.; Panelli, M. C.; Marincola, F. M. *J. Immunol. Methods* **1999**, *226*, 29.
76. (a) Li, X. M.; Schwartz, R. M.; Cesar, E. Y.; Wang, H. Y. *Comput. Biol. Med.* **1988**, *18*, 367. (b) Hammerstedt, R. H.; Lovrein, R. E. *J. Exp. Zool.* **1983**, *228*, 459. (c) Hafner, F. *Biosens. Bioelectron.* **2000**, *15*, 149.

All-Solid-State Electrochemistry of Nafion Membranes

This chapter discusses the redox properties of ions entrapped in polymer electrolyte membranes, using an all-solid-state electrochemical cell developed in-house. Specifically, cyanoferrate (II), cyanoferrate (III) and hemoglobin are incorporated in Nafion membranes. While cyanoferrate (III) undergoes spontaneous reduction in Nafion matrix, the Iron center of hemoglobin is protected by the protein molecules covering the heme moiety. However, the polymer matrix affects the oxygen binding behavior of entrapped hemoglobin. The results of this investigation could be easily extended to study enzyme/substrate interactions and electron transfer processes of proteins in a biomimetic environment.

* The work discussed in this chapter has been published in: *Chem. Mater.* 2006, *18*, 5244 & *Biochem. Biophys. Res. Commun.* 2008, *364*, 86.

2.1 Introduction

Polymer electrolyte membranes form an important class of soft materials due to their increasing demand in modern energy generation and storage devices, like fuel cells, batteries and supercapacitors. Among the various polymer electrolytes, Nafion has a number of advantages like high proton conductivity at room temperature and excellent thermal/mechanical stability attributed mainly to its phase-separated microstructure as discussed in the first chapter.

A number of experimental and theoretical studies on the microstructure and ionic transport properties of Nafion have been performed till date [1]. Especially, ion fluxes in Nafion membranes have been extensively investigated using techniques like Scanning Electrochemical Microscopy [2], Extended X-ray Absorption Fine Structure (EXAFS) [3], Raman spectroscopy [3], NMR [4] and ESR [5]. One of the approaches to understand the crucial importance of its microstructure is to incorporate redox active/ionic entities into the polymer membrane and follow their dynamics and energetics as a function of parameters like temperature, humidity and equivalent weight of the polymer [6]. Another method to understand its microstructure is to introduce chromophore entities and surfactants in Nafion matrix [7,8]. However, a real time analysis of the membrane, incorporated in a fuel cell is unlikely, due to contributions from both dynamic and static variables like field, humidity, concentration and thermal gradients controlling the overall device performance. To circumvent this difficulty, it has been a common practice to study the electrochemical behavior of electrodes coated with the polymer film dipped in a liquid electrolyte, facilitating the extrapolation of the results to real device conditions [9]. Nevertheless, in this method, contribution arising from the interface between the solid membrane and the liquid electrolyte is unavoidable. A more relevant approach is to study the membrane in “an all-solid-state

configuration" related to which, a considerable number of reports are available with different solid electrolytes [10]. Especially, the impeded nature of the reactions in the solid state methods has been used advantageously to understand electrochemical phenomena, which are otherwise unperceivable in conventional electrochemistry. For example, a comparison of Ag and Pt electrodes coated with Nafion films using solid state electrochemistry has revealed that the Pt/Nafion interface catalyzes the hydrogen oxidation and oxygen reduction reactions while impeding the equilibration of water in the gas phase with the ions in the membrane [10a]. On the contrary, the Ag/Nafion interface is found to do the reverse viz., promoting better water equilibration and impeding the above electrochemical reactions. Thus solid-state electrochemistry can provide deeper insights into phenomena less spectacular in the conventional electrochemical experiments.

In the first chapter, the physical chemistry of polymer electrolytes has been critically reviewed and the current status of understanding the proton conducting polymer, Nafion has been analyzed thoroughly. Also, the limitations of various electroanalytical and spectroscopic tools in probing the properties of Nafion have been indicated. Subsequently, this chapter attempts to address one of the important questions raised therein: *How does the polymer matrix alter the fate of the ions ensued in it?* In this context, here we demonstrate critical phenomena at the interface of the hydrophobic and hydrophilic domains of Nafion and their effect on the redox behavior of ions incorporated in the membranes using "all-solid-state" electrochemistry.

First, the effect of the polymer electrolyte matrix on the redox behavior of a simple outer sphere couple viz., $[Fe(CN)_6]^{4-/3-}$ is studied. Critical insights into the effect of Nafion on the proton coupled electron transfer behavior and spectroscopic properties of cyanoferrate (II) and cyanoferrate (III) ions incorporated in it are obtained in this investigation. Techniques employed include Cyclic Voltammetry (CV), Zero current chronopotentiometry, electrochemical impedance, Diffuse Reflectance Infrared Fourier

Transform spectroscopy (DRIFT), UV-visible spectroscopy, X-ray Photoelectron Spectroscopy (XPS) and Electron Spin Resonance spectroscopy (ESR).

After analyzing the effect of the Nafion matrix on the redox behavior of $[Fe(CN)_6]^{4-/3-}$, electrochemistry of a heme protein viz., hemoglobin incorporated in Nafion matrix is investigated. The necessity of the all-solid-state methodology for protein electrochemistry can be appreciated from the following discussion. Direct electrochemistry of metallo-proteins is a very important tool to understand their electron transfer mechanism, catalytic activity in living cells and coupled chemical reactions, with the electrode playing the role of a biological redox partner [11]. But the experiments are often complicated by irreversible adsorption of proteins on the electrode surface, coupled with conformational changes, often leading to loss of activity. One of the most common means of performing direct electrochemistry has been to immobilize the proteins on the electrode surface by using Self-assembled Monolayers (SAM). For example, direct electrochemistry of cytochrome c has been achieved by attaching the protein on carboxyl terminated SAMs on gold electrodes [12]. However, this approach often presumes a prior knowledge about the SAM fabrication techniques, like the choice of a structurally defined monolayer for attaching specific metallo-enzymes to the electrode surface and optimizing the experimental conditions of self-assembly to ensure a proper orientation of the biomolecules. Yet another method is to adsorb the protein directly on a glassy carbon electrode, called Protein Film Voltammetry (PFV) [13], which again suffers from limitations arising due to lack of control over the conformation of the adsorbed protein. A simpler methodology is to incorporate the biomolecules into thin polymer films (either ionically or electronically conducting) cast on the electrode surface [14]. For example, Heller and coworkers attacked the problem by wiring redox enzymes to electrodes by 'electron relays' (sometimes redox polymers) and achieved a major leap in the field [15]. Among the diverse variety of polymers studied so far, Nafion, (a perfluoro sulfonic acid polyelectrolyte [2]) is one of the best polymers of choice for entrapping proteins due to

its phase-separated structure with hydrophilic pools, which preserve the biophysics of the protein molecules confining them in an environment similar to that in living cells [16,17].

Nevertheless, irrespective of whether the protein is attached to the electrode through a SAM or a polymer film, the method of electrochemical interrogation introduces a second interface in addition to the electrode/protein interface i.e., the electrode/electrolyte interface because the modified electrode needs to be dipped in a suitable electrolyte solution. For example, restrictions imposed by electro-neutrality requirements, often leads to ion ingress/egress at the polymer film/solution interface, especially when transient electrochemical techniques like cyclic voltammetry and chronoamperometry are used [18]. Though this problem can be overcome by using ultramicroelectrodes and ultrathin LS (Langmuir-Schaefer) films, fabrication of ultrathin films and optimization of film thickness demands extensive experimentation, which renders the method less feasible for routine analysis [19]. Moreover, in the LS technique, the subtle interaction between the substrate and the polymer film could result in extensive reorganization accompanying film formation/transfer based on the solvent nature in the sub phase.

In this connection, investigation of biological electron transfer in an all-solid-state configuration is free from these shortcomings and could offer considerable insight into the actual redox process as well as the chemical changes accompanying them. The importance of solid-state techniques is well explained recently in an interesting report on thermal and photo-initiated reduction of heme proteins in glasses derived from sugars like glucose, sucrose and trehalose [20]. In this report, we demonstrate the direct electrochemistry of hemoglobin entrapped in a recast Nafion membrane, achieved using an "all-solid-state" electrochemical cell. Hemoglobin is chosen because of its well-studied redox behavior (next to the cytochromes) and also due to its simpler biological pathways, easier to correlate with electrochemical data compared to other complicated

protein systems. One of the primary objectives of this work is to bring out the importance of protein-polymer interactions in tuning the function of the entrapped protein, different from earlier reports considering Nafion just as a physical matrix to freeze the proteins in a favorable configuration. In particular, the utility of solid-state voltammetry in characterizing biochemical interactions at a molecular level is demonstrated by a systematic analysis of the electrochemical and spectroscopic data.

2.2. Experimental Section

A 5 wt % dispersion of Nafion (1000 g/equiv) in a mixture of lower aliphatic alcohols and water was procured from Aldrich chemicals and potassium ferrocyanide trihydrate and potassium ferricyanide from Qualigens fine chemicals, Mumbai, India. Deionized water (Millipore 18 MΩ) was used for preparing the cyanoferrate solutions. Hemoglobin from bovine blood (in Methemoglobin form) (M.Wt. 64,500) was purchased from Sigma chemicals. Sodium hydroxide (Analytical Reagent grade) was obtained from Ranbaxy fine chemicals Ltd., New Delhi, India and Sodium dihydrogen phosphate ('Excelar' grade) from Qualigens fine chemicals Ltd., Mumbai, India. All solutions were prepared using deionized water (Millipore 18 MΩ). N_2, O_2 gases were of INOX grade (99.9% purity) and SO_2 (1% in N_2) was obtained from Deluxe trading company, Pune, India

Electrochemistry of Cyanoferrates

'All Solid State Cyclic Voltammetry' was carried out using a specially designed home - made electrochemical cell made of Teflon, shown in Figure 2.1. The cell was made of a cylindrical block of Teflon of 1.7 cm height and 0.8 cm diameter. In one end of the block, a shallow trough of 1mm depth was made. For housing the electrodes, three holes were drilled through the center of the trough to the other end of the cylinder, at appropriate positions such that the counter electrode (a 0.5 mm Pt wire) encircles the

working (a 0.140 mm Pt wire) and the reference electrodes (Ag/AgCl electrode obtained by chloridation of a 0.5 mm Ag wire) inserted in the middle holes. Provision

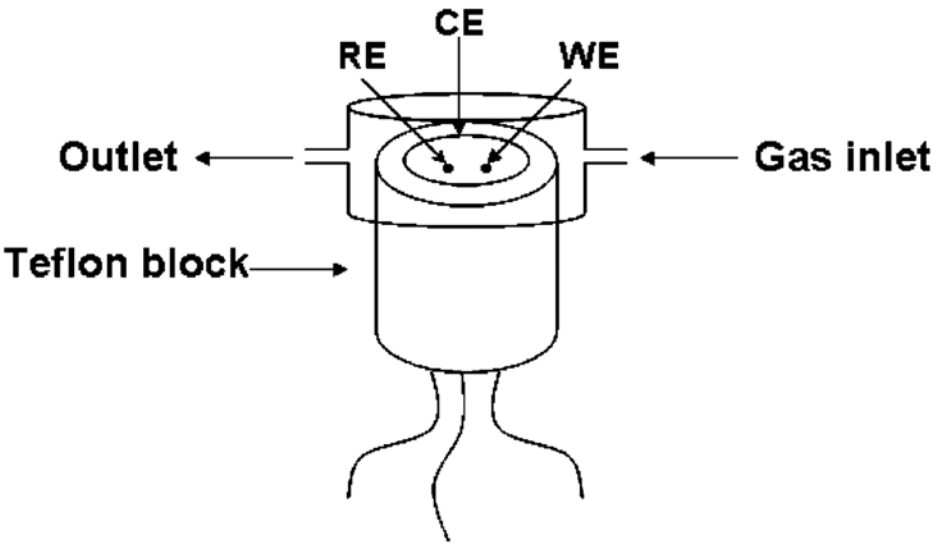

Figure 2.1. Electrochemical cell for "all-solid-state" investigations of polymer electrolyte membranes (WE: working electrode; CE: counter electrode; RE: Reference electrode).

for performing the experiments in different gaseous atmospheres was made by fabricating a two- way screw cap over the cylindrical Teflon block. OCV-time profiles were recorded for Nafion membranes with different concentrations of potassium ferricyanide (0.7, 1.3 and 2.6 mM) using the same instrument. Cyclic voltammetry with pristine Nafion membrane was conducted with an Autolab PGSTAT30 (ECO CHEMIE) instrument using a continuous film of Nafion (thickness 0.5 mm), cast over the electrodes fixed in the Teflon cell. Then 20 µl of a 0.5 M aqueous solution of $K_3[Fe(CN)_6]$ was added to the membrane to give a final concentration of 6.7 mM. The electrochemical experiments for the composite membrane were performed at room temperature (30 ^oC). Electrochemical Impedance studies were performed with the same cell using an Autolab PGSTAT30(ECO CHEMIE) instrument equipped with Frequency Response Analyzer, immediately after adding equal proportions of $K_3[Fe(CN)_6]$ and

$K_4[Fe(CN)_6]$ (3.4 mM each) using a 10 mV rms ac signal in the frequency range 10 mHz to 100 kHz.

After the electrochemical investigations, the Nafion membranes were peeled off from the holder and analyzed using XPS, ESR, UV-Visible and IR spectral investigations. XP spectra of $K_3[Fe(CN)_6]$/Nafion (0.05 M) was recorded, one hour after the addition of ferricyanide to the membrane. XPS measurements were carried out on a VG MicroTech ESCA 3000 instrument at a pressure of > 1 x 10^{-9} Torr (pass energy of 50 eV, electron take-off angle 60^o, and overall resolution ~1 eV using monochromatic Al K_α source (hν = 1486.6 eV)). The core level spectra of the C 1s, O 1s, N 1s, F 1s, Fe 2p and S 2p signals were recorded with an overall instrumental resolution of ~1 eV. The alignment of binding energy (BE) was carried out using C 1s BE of 285 eV as the reference. The X-ray flux (70 W) was kept deliberately low to reduce beam-induced damage. The Spectra were fitted using a combined polynomial and Shirley type background function [21,22]. ESR spectra were recorded on a Bruker EMX spectrometer operated at X-band frequency (~ 9.784 Hz). The samples were analyzed both at 298 K and 77 K. The UV-Visible spectra of the solid membranes were recorded (in the transmittance mode), using a JASCO Model V-570 dual beam Spectrophotometer operating at a resolution of 2 nm and the solid state UV-Visible spectra of the potassium ferrocyanide and potassium ferricyanide were recorded (in the reflectance mode) using Perkin Elmer Lambda 650 instrument, operating at a resolution of 5 nm**.** For IR spectroscopy, Perkin-Elmer FTIR Spectrum One Spectrophotometer operated in the diffuse reflectance mode at a resolution of 4 cm^{-1} was used. All these studies were repeated for cyanoferrate-incorporated membranes prepared under identical conditions, without subjecting them to an electric field.

Electrochemistry of Hemoglobin

A thin film of Nafion (thickness 0.2 mm) was cast over the electrodes from a 5 wt% commercial dispersion. Then 70 µl of Methemoglobin (MetHb) solution (1mg/ml) in 50 mM phosphate buffer (made using Sodium dihydrogen phosphate and Sodium hydroxide; pH 7) was added to the film and enough time (~ 20 min) was given for the species to be absorbed in the membrane, confirmed by open circuit potential-time transients and the appearance of redox peaks in cyclic voltammograms (Figure 2.2).

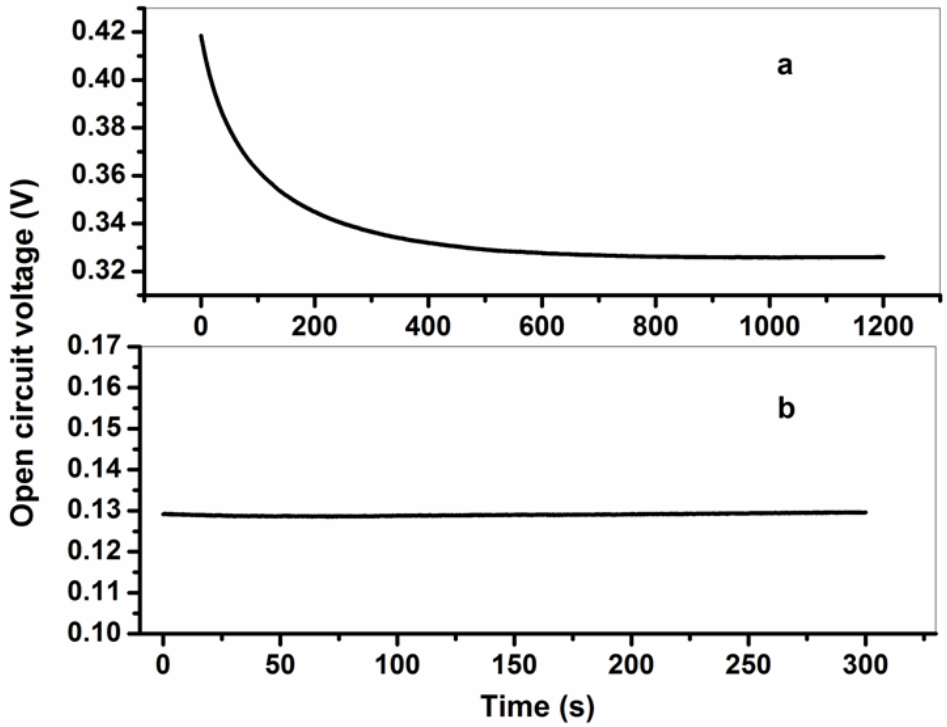

Figure 2.2. Open circuit voltage vs. time profiles for a) Nafion-Hb and b) pristine Nafion films at 30% relative humidity. A redox peak due to the $Fe^{3+/2+}$-heme couple is observed after OCV stabilization indicating that Hb is absorbed into the polymer electrolyte and becomes accessible to the working electrode.

Electrochemical experiments were performed using a Solartron SI 1287 Electrochemical Interface equipped with a 1255B Frequency Response Analyzer at

room temperature (25 ± 0.5 ^{o}C) in a N_2 atmosphere (humidified to retain the water content of Nafion, relative humidity 30%) unless otherwise specified and the Nafion-Hb films were stored at 4 ^{o}C when not under study. The cell resistance was 70-75 Ω and was electronically compensated to 10-15 Ω by a positive feedback circuitry available with the instrument. Relative humidity was measured using a Metravi HT-3005 humidity sensor.

UV-visible spectra were recorded using a Varian Cary50 double beam spectrophotometer with 1 nm resolution, with a MetHb concentration of 0.25 mg/ml in 50 mM phosphate buffer (pH 7) at a scan speed of 288 nm/min. Samples for solid-state UV-vis spectroscopy were prepared by casting a thin film (thickness 0.1 mm approx.) of 2 wt% Nafion on a quartz slide followed by the addition of 20 µl of Methemoglobin (MetHb) solution (1 mg/ml in 50 mM phosphate buffer, pH 7). Fluorescence emission scans and lifetime analysis were recorded using a FLS 900 (Edinburgh) instrument operated at a resolution of 7 nm at 18 ^{o}C, with a MetHb concentration of 0.25 mg/ml in 50 mM phosphate buffer (pH 7) before and after the addition of 10 µl of 5 wt% Nafion. IR spectra of the solid Nafion-Hb films were recorded using Perkin-Elmer FTIR Spectrum One Spectrophotometer operated in the Diffuse Reflectance mode at a resolution of 4 cm^{-1}.

2.3 Results and Discussion

2.3.1. Cyanoferrates in Nafion matrix

2.3.1.1. Cyclic Voltammetry

Pristine Nafion membrane shows an open circuit voltage (OCV) of +0.3 V, while the $K_4[Fe(CN)_6]$-incorporated membrane shows an OCV of + 0.2 V. Figure 2.3 shows the cyclic voltammograms of Nafion membranes with and without $K_4[Fe(CN)_6]$

(7 mM). The $K_4[Fe(CN)_6]$/Nafion membrane exhibits two anodic peaks, one at −3 mV (peak a) and another at +0.3 V (peak b) along with a cathodic peak at +0.2 V (peak c).

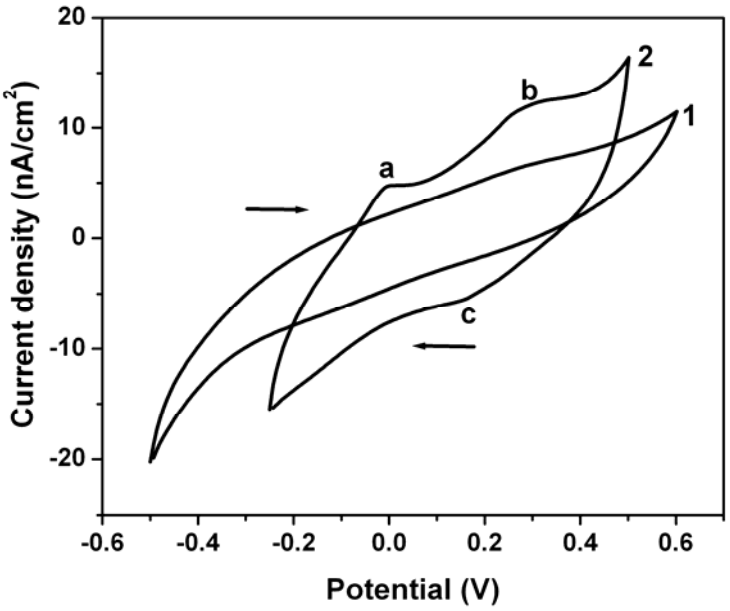

Figure 2.3. Cyclic voltammograms of 1) Pristine Nafion membrane; 2) $K_4[Fe(CN)_6]$/Nafion membrane (6.7 mM) at a scan rate of 100 mV/s using Pt disk working electrode (0.14 mm diameter), Ag/AgCl Reference and Pt counter electrode (Peak a: H_2 oxidation; Peak b: $[Fe(CN)_6]^{4-}$ oxidation; Peak c: $[Fe(CN)_6]^{3-}$ reduction).

Peak 'a' could be assigned to the oxidation of adsorbed H_2, since the peak current increases when the potential is held at - 0.25 V for 2 minutes. This is further confirmed by the increase in the peak current with increase in partial pressure of H_2 gas passed over the membrane (Fig. 2.4). The scaling of peak current with hydrogen partial pressure has implications for solid state H_2 sensing [23]. Voltammograms at different scan rates (10, 25, 50, 100, 200 mV/s) clearly indicate a shift in the peak potential, E_{pa} to more positive values as revealed in Figure 2.5. For an irreversible charge transfer process, E_p is supposed to shift in the positive direction (for oxidation) by $2.303RT/\alpha F$ (where, R is the gas constant, T is the Temperature in K, α is the charge transfer coefficient and F is Faraday's constant) for every ten-fold increase in the scan rate [24].

In this system, as the peak potential shifts by + 22 mV, on increasing the scan rate from 100 to 200 mV/s, the anodic charge transfer coefficient α for peak a, is calculated to be 0.3. The peak current, I_p of peak 'a' as a function of the square root of scan rate (V/s) (inset-Fig. 2.5), gives a straight line with a positive slope.

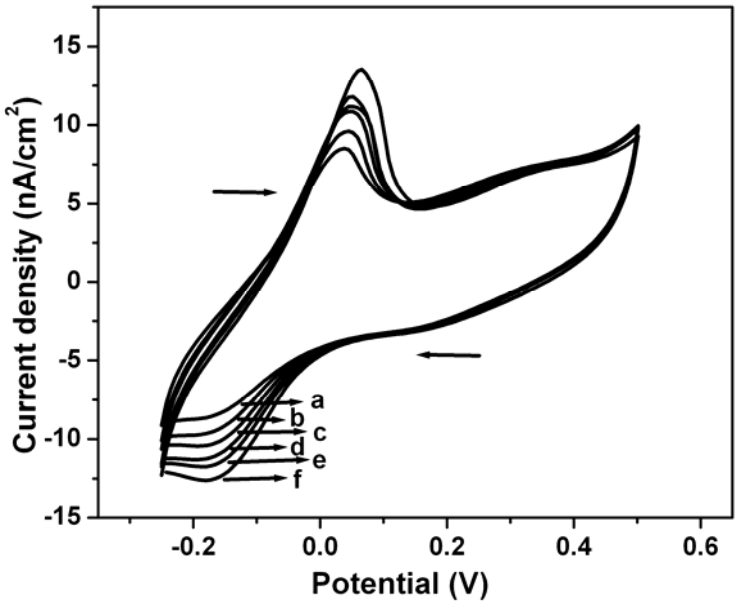

Figure 2.4. Hydrogen oxidation signal of $K_4[Fe(CN)_6]$/Nafion membrane at a scan rate of 100 mV/s indicating increase in peak current with partial pressure of H_2 (flow rate: 0.6 ml/min) from a-f.

Using the slope of the I_p versus $v^{1/2}$ plot, the diffusion coefficient of H_2 in the membrane is calculated to be 4 x 10^{-10} cm^2/s from the following expression for an irreversible electron transfer process,

$$i_p = \left(2.99 \times 10^5\right) \alpha^{1/2} A D_o^{1/2} C_0^* \nu^{1/2} \qquad (2.1)$$

where, i_p is the peak current (A), α is the charge transfer coefficient, A is the area of the working electrode (1.5 x 10^{-4} cm^2), D_O is the diffusion coefficient of hydrogen (cm^2/s), C_O^* is the bulk concentration of hydrogen in the recast Nafion membrane (1.4 x 10^{-6}

mol/cm^3 [25]), ν is the scan rate (V/s). The diffusion coefficient of hydrogen in ferrocyanide incorporated Nafion membrane is found to be five orders of magnitude lower than that in 0.5 M H_2SO_4 [26] (3.83 x 10^{-5} cm^2/s) and four orders of magnitude lower than that reported for the pristine Nafion membrane recast on a Pt electrode (8.7 x10^{-6} cm^2/s [25]).

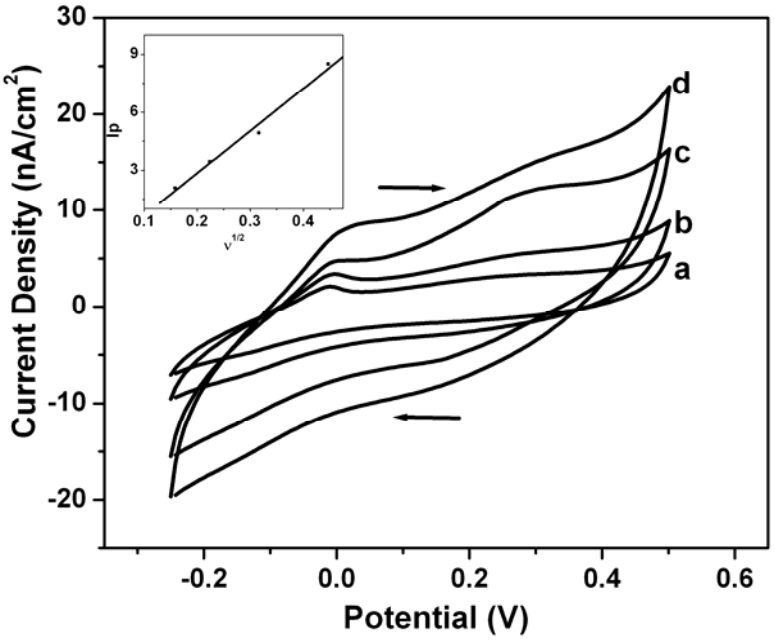

Figure 2.5. Cyclic voltammograms of $K_4[Fe(CN)_6]$/Nafion membrane at different scan rates a) 25 mV/s; b) 50 mV/s; c) 100 mV/s; d) 200 mV/s (Inset**:** Plot of $[Fe(CN)_6]^{4-}$ oxidation peak current (I_p) Vs square root of scan rate ($\nu^{1/2}$) (V/s).

A possible reason for the decrease in the rate of hydrogen diffusion in the present case could be that the membrane is not activated by peroxide pretreatment. Using the diffusion coefficient value, the apparent rate constant, k^o for the oxidation of adsorbed hydrogen is calculated to be 3x 10^{-4} cm/s using the expression [27],

$$E_p = E^{o'} - \frac{RT}{\alpha F}\left[0.78 + \ln\left(\frac{D_o^{1/2}}{k^o}\right) + \ln\left(\frac{\alpha F \nu}{RT}\right)^{1/2}\right] \qquad (2.2)$$

where, $E^{0'}$ is the formal potential (−0.05 V), ν is the scan rate (0.1 V/s), and E_p is the anodic peak potential (−3 mV). Hydrogen oxidation on Pt is a well-known electrocatalytic reaction that has been extensively studied using a number of techniques. While rate constant values above 1 cm/s have been reported for hydrogen oxidation on a polycrystalline Pt electrode using steady state techniques like SECM [28], the abnormally low value of rate constant in the present case could be partly due to the limitation imposed by cyclic voltammetry, which is a transient technique. Hence it is difficult to comment on the effect of the solid polymer matrix on the kinetics of hydrogen oxidation in the present case using cyclic voltammetry.

On the other hand, the reason for the hydrogen oxidation peak becoming prominent only after the addition of potassium ferrocyanide to the Nafion membrane is not clearly understood. However, it could be compared with a report on enhanced hydrogen sensitivity of Nafion membrane by incorporating Chromium species [29]. This observation probably implies that the rate of hydrogen oxidation could be modulated, by using composite polymer electrolytes. The origin of the quasi-reversible peaks 'b' & 'c' in Figure 2.3 could be easily attributed to the $[Fe(CN)_6]^{4-/3-}$ redox couple, since the peak currents increase with increase in concentration of potassium ferrocyanide. While $[Fe(CN)_6]^{4-/3-}$ is a well- known reversible couple in aqueous electrolytes, it shows a quasi-reversible behavior (as is evident from the shift in peak separation (ΔE_p) with change in the potential scan rate (Fig.2.5)) in the ionomer matrix, probably due to the phase separated structure of the polymer and its chemical interaction with the incorporated complex ions.

The $K_3[Fe(CN)_6]$/Nafion membrane (6.8×10^{-4} M) shows an open circuit potential of +0.1 V, which is lower than that for the $K_4[Fe(CN)_6]$/Nafion membrane by 60 mV. This implies that $[Fe(CN)_6]^{3-}$ ions are more reducible in Nafion environment than $[Fe(CN)_6]^{4-}$ ions. As the first sign of autoreduction, an anodic peak appears at

+0.15 V in the first cycle, on scanning the potential from its open circuit value in the anodic direction (Fig. 2.6), which shows the presence of $[Fe(CN)_6]^{4-}$ species in the system. The peak current increases in the second cycle due to $[Fe(CN)_6]^{4-}$ species electro-generated in the first cycle which then remains almost constant in subsequent cycles.

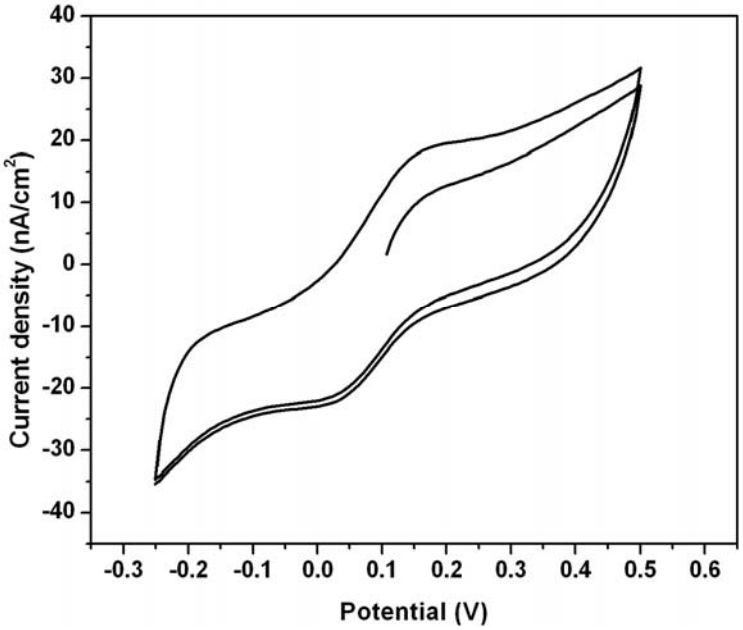

Figure 2.6. Cyclic voltammogram of $K_3[Fe(CN)_6$/Nafion membrane (6.83×10^{-4} M) at a scan rate of 100 mV/s, when the potential is scanned in the anodic direction from the open circuit potential (0.1 V) to 0.5 V and back to -0.25 V

This observation is in excellent agreement with the report on electron self-exchange dynamics of hexacyanoferrate, synthetically combined with a quarternary ammonium counter-cation connected to polyether chains [30]. This system is analogous to Nafion/hexacyanoferrate except that the pendant chains have a positive charge. On the other hand, Fe (III) ions are known to attack the pendant chains of Nafion resulting in the formation of membrane-derived radical species [31]. In addition, partial reduction of ferricyanide in anionic AOT (sodium bis(2-ethylhexyl) sulfosuccinate) micelles, which are structurally similar to Nafion, has been proposed in another report [32]. Also,

similar reports on the auto-reduction of Cu^{2+} to Cu^{+} on dithiol modified Copper electrodes [33] and spontaneous reduction of Cu^{2+} in Zeolites [34] are available.

2.3.1.2. Zero-current Chronopotentiometry

Figure 2.7 shows the plots of Open circuit voltage against time for Nafion membranes containing $K_3[Fe(CN)_6]$ at different concentrations (0.7, 1.3, 2.6 mM). It is found that at intermediate concentration (1.3 mM), there is an exponential increase in OCV from 0.31 V to 0.45 V for the first 13 minutes after which it starts decreasing. The

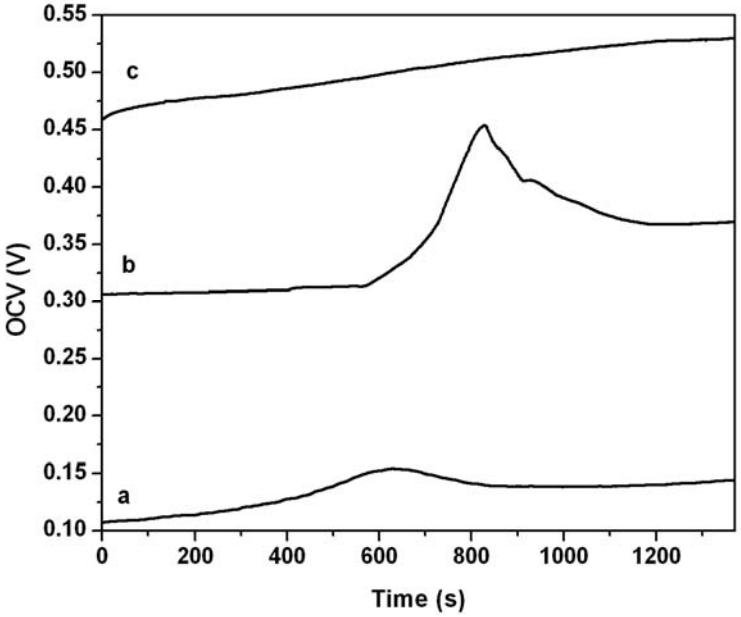

Figure 2.7. OCV Vs time plots for $K_3[Fe(CN)_6]$/Nafion with different concentrations of ferricyanide a) 0.7 mM; b) 1.3 mM; c) 2.6 mM.

initial increase could be ascribed to the exchange of potassium ions with protons in the membrane and the later decrease signifies the autoreduction of $[Fe(CN)_6]^{3-}$ in Nafion matrix. On the other hand, at lower concentration (6.8 mM), initially there is a slight increase in OCV, followed by a decrease, while at higher concentrations (2.7 mM), a steady increase is noticed. A possible explanation could be that in the former case, the anions present in the middle of the water pools enclosed by the sulfonate groups move

to the interface between the hydrophilic and hydrophobic domains to get partially reduced and in the latter case the exchange of potassium ions of the redox species with the protons in the ionomer matrix could be the predominant process. However, there could be other contributions to the observed concentration dependence like the dynamics and segmental mobility of the polymer chains which could accompany the mass transport of the redox species.

2.3.1.3. Electrochemical Impedance

Figure 2.8 shows the Nyquist plots (Z(Im) Vs Z(Re)) for the pristine Nafion membrane and Nafion membrane containing equal amounts of potassium ferrocyanide and potassium ferricyanide (0.34 mM in each) respectively . In the impedance plot of the modified membrane (Fig. 2.8), a curved portion is observed in the high frequency region whereas that of the unmodified membrane is almost linear (inset-Fig. 2.8). This allows us to assign the curved portion in the modified membrane to the redox process of the cyanoferrate species present in the polymer matrix and the linear region in the low frequency part could be assigned to the mass transport of the species.

The high frequency part in Figure 2.8 is then fitted with a semicircle using CNLS (Complex Non-linear Least Square fitting) method and fitting it with a simple Randles circuit, the resistance of the medium (R_s) is calculated to be 295 Ω/cm^2 and resistance for interfacial charge transfer (R_{ct}) is found to be 6.15 x 10^3 Ω/cm^2. From the R_{ct} value, the exchange current density for ferrocyanide oxidation in Nafion matrix is calculated to be 4.2 x 10^{-6} A/cm^2 which yields a value of 0.08 cm/s for apparent rate constant, k^o for $[Fe(CN)_6]^{4-}$ oxidation. From this, the diffusion coefficient, D_o of the complex anion is calculated to be 1.3 x 10^{-12} cm^2/s by adopting a treatment proposed by Nicholson [35] for quasi-reversible systems (assuming a value of 0.3 for the anodic charge transfer coefficient, α**).** When these values are compared with those obtained by dissolving the redox couple in 0.5M H_2SO_4 using a blank Pt electrode (Table 2.1), the

diffusion coefficient is found to be lower than the latter by six orders of magnitude and the exchange current density by one order of magnitude while the apparent rate constants are found to be of the same order. As the standard expressions for deriving the electrochemical parameters were originally developed for liquid electrolytes, which could have some contribution to the deviation of the calculated values from those of the aqueous systems. But such a difference of several orders of magnitude indicates the effect of the solid polymer electrolyte matrix on the charge transfer and mass transport of the incorporated redox species.

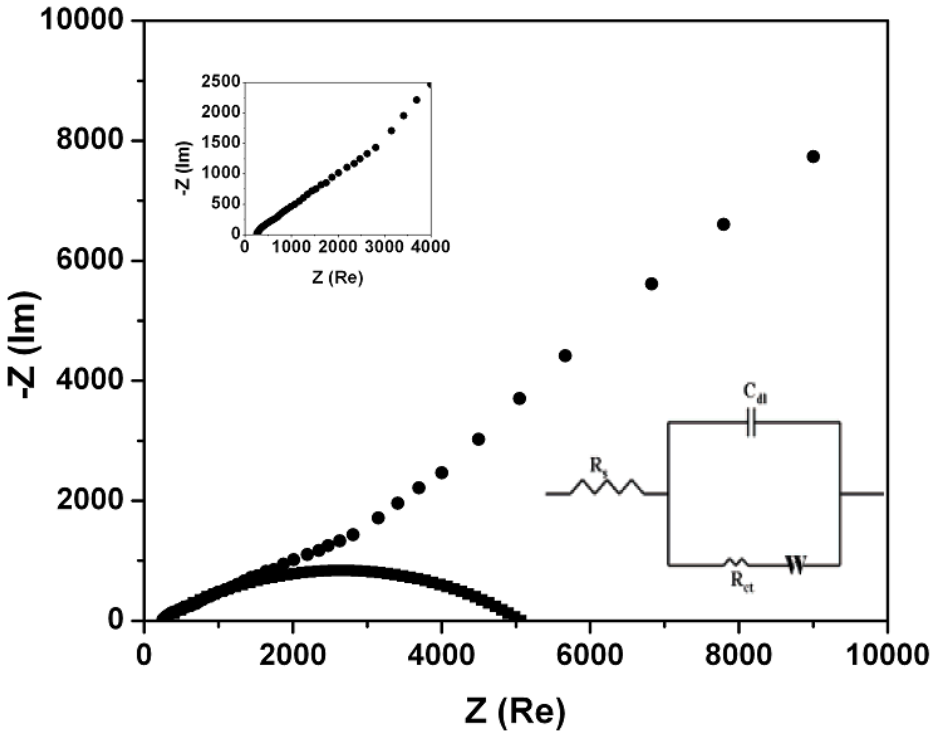

Figure 2.8. Impedance plot of Nafion membrane containing equal amounts of $K_3[Fe(CN)_6$ and $K_4[Fe(CN)_6]$ (3.4×10^{-4} M each) using a 10 mV rms AC signal in the frequency range, 10 mHz to 100 kHz. (**Inset bottom right:** Equivalent circuit corresponding to the semicircle fitted with the high frequency part; **inset top left**: Impedance plot of pristine (unmodified) Nafion membrane).

Table 2.1. Comparison of the thermodynamic and kinetic parameters for electrochemical $[Fe(CN)_6]^{4-}$ oxidation in a solid Nafion membrane (relative humidity 60%) with those in 0.5 M H_2SO_4.

Electrolyte	D_o (cm^2/s)	k^o (cm/s)	A	j_o (A/cm^2)
Nafion	1.3×10^{-12}	0.08	0.5	4.2×10^{-6}
0.5M H_2SO_4	4.7×10^{-6}	0.07	0.5	1.9×10^{-5}

In comparison, Murray and coworkers [10d] have observed a remarkable decrease in diffusion coefficient (2.5×10^{-10} cm^2/s) by four orders of magnitude in hexacyanoferrate-modified polyether compared to that in aqueous solution (4.7×10^{-6} cm^2/s), which has been attributed to the dominance of electron hopping over physical transport. However while deriving kinetic parameters from aqueous solutions, complications arising from adsorption of the redox species on electrode surface leading to an inner-sphere mechanism must also be considered [36]. In this context, solid-state electrochemistry is one of the most promising methods to evaluate pure outer-sphere electron transfer processes without any complications from adsorption. Also, these observations demonstrate the possibility to predict the charge transfer and mass transfer dynamics in catalyst-coated membranes - an alternate technology useful in fuel cells, wherein the catalyst material is coated directly on the polymer electrolyte membrane, instead of coating over the electrodes.

2.3.1.4. Diffuse Reflectance Infrared Spectroscopy

Figure 2.9 shows the Fourier Transform Infrared spectra (in diffuse reflectance mode) of $K_3[Fe(CN)_6]$/Nafion membrane (Fig. 2.9a) and $K_4[Fe(CN)_6]$/Nafion membrane (Fig. 2.9b). Compared to the ν_{CNstr} for aqueous solutions of potassium errocyanide [37] (2037 cm^{-1}) and ferricyanide (2115 cm^{-1}), those in the Nafion membrane (2090, 2122 cm^{-1}

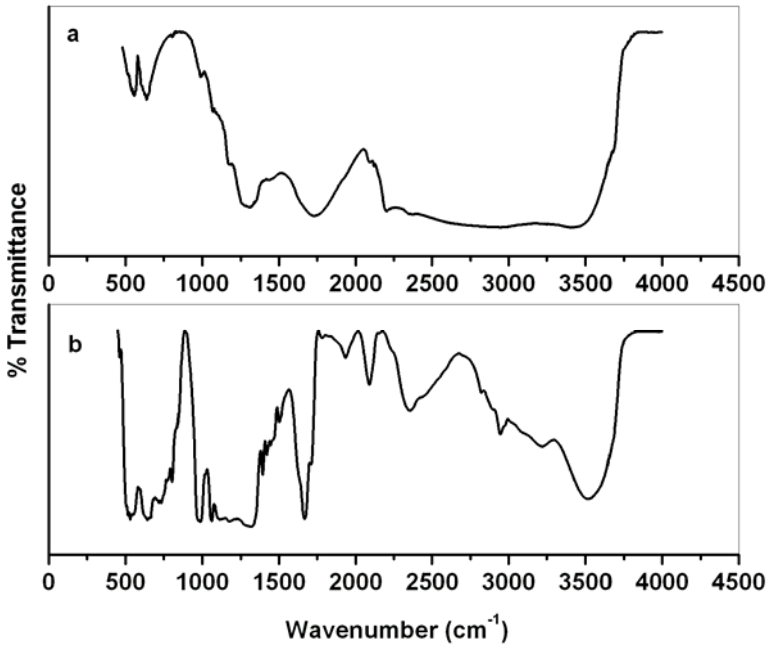

Figure 2.9. DRIFT spectra of a) $K_4[Fe(CN)_6]$/Nafion and b) $K_3[Fe(CN)_6]$/Nafion in the solid state recorded with a resolution of 4 cm^{-1}.

respectively) show a slight blue shift. The increase in the CN bond energy in the latter case implies an increase in the metal to ligand π-σ* back bonding, which in turn could be due to an increase in electron density at the metal center. This could be possible if the pendant sulfonate groups of the polymer interact with the Iron center forming a partial bond, thereby increasing the electron density in the vacant d orbitals of the metal. Such interactions play a crucial role in deciding the charge transfer dynamics and energetics of the redox couple in the polymer matrix. Interestingly, $K_3[Fe(CN)_6]$/Nafion membrane shows absorption at frequencies corresponding to ν_{CNstr} of both cyanoferrate (III) and cyanoferrate (II) (2122 cm^{-1} and 2090 cm^{-1} respectively), while $K_4[Fe(CN)_6]$/Nafion membrane shows no signature of cyanoferrate (III) after CV. Thus the autoreduction of ferricyanide to ferrocyanide in Nafion matrix is evident from the above results.

2.3.1.5. X-ray photoelectron Spectroscopy

Figure 2.10 shows the O 1s, S 2p and Fe 2p core level XP spectra of Nafion membranes containing potassium ferricyanide (Fig. 2.10a) and potassium ferrocyanide (Fig. 2.10b), along with the O 1s and S 2p spectra of the pristine membrane (Fig. 2.10c). In all the cases two peaks are observed in the O 1s spectra, of which, the peak appearing at higher binding energy (B.E.) could be attributed to the oxygen in the sulfonic acid group and the other component at a lower B.E. is due to the entrapped water molecules [38].

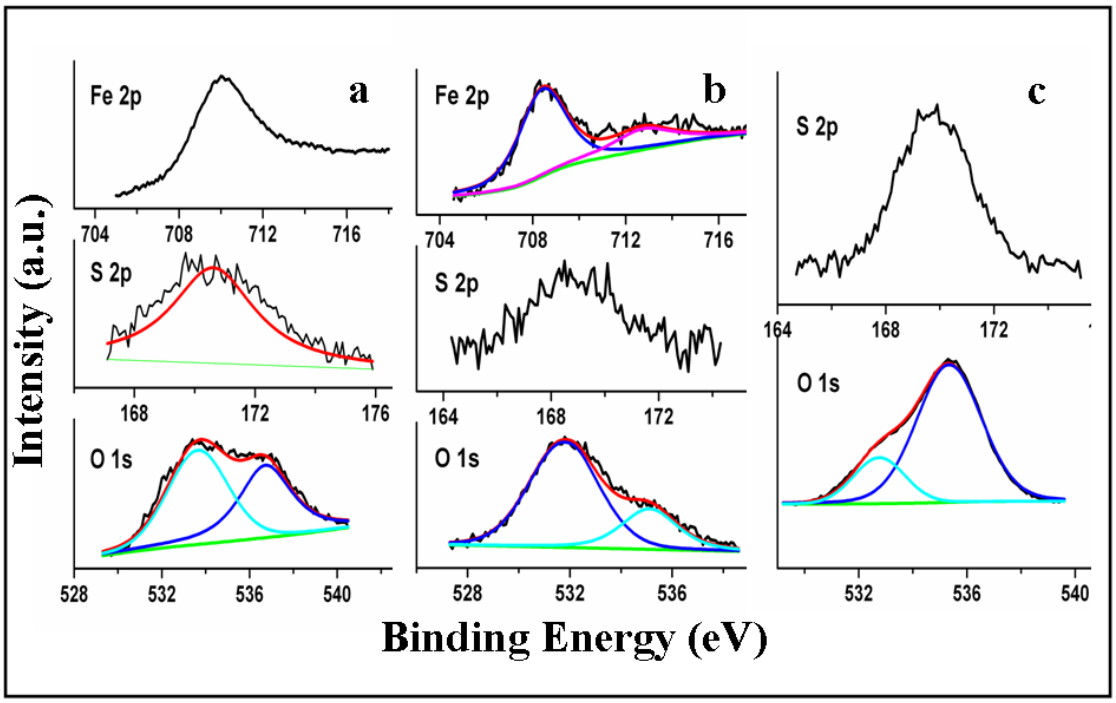

Figure 2.10. Fe 2p, S 2p, O 1s XP spectra of a) $K_3[Fe(CN)_6]$/Nafion; b) $K_4[Fe(CN)_6]$/Nafion and c) S 2p, O 1s XP spectra of pristine Nafion membrane (black lines show plots of raw data coloured lines show fitted data (wherever necessary) using a combined polynomial and Shirley type background function).

The increase in the B.E. of sulfonate oxygen (by 1.5 eV) in ferricyanide containing Nafion compared to that of the pristine membrane, could be due to the ligation of sulfonate oxygen to the Iron center in the ferricyanide ion. On the other

hand, no such increase in BE is observed after the addition of ferrocyanide ions. Similarly an increase in BE is observed for the S 2p level, confirming the validity of the explanation given above for the BE shift for O 1s level. The Fe 2p region of $K_4[Fe(CN)_6]$/Nafion membrane shows a main Fe $2p_{3/2}$ peak at 708.5 eV and associated satellites at 714 eV as expected for $[Fe(CN)_6]^{4-}$. On the other hand, the Fe 2p spectrum of $K_3[Fe(CN)_6]$/Nafion membrane shows Fe $2p_{3/2}$ peak at 710.1 eV, which is intermediate between the BE values expected for pure $K_4[Fe(CN)_6]$ (708-709 eV) and $K_3[Fe(CN)_6]$ (711 eV) [38, 39]. This shows the presence of a mixture of ferric and ferrous species that would have been formed during the autoreduction of potassium ferricyanide in Nafion matrix. Also, no $[Fe(CN)_6]^{3-}$ peak appears for $K_4[Fe(CN)_6]$/Nafion after cyclic voltammetry. The experimental B.E. values for C 1s, F 1s and N 1s core levels are found to be in close agreement with the reported values which are compiled in Table 2.2.

Table 2.2. Comparison of binding energies of various core level electrons in cyanoferrate-incorporated Nafion membranes with those in the pristine membrane along with BE values reported for closely related systems

Core level	**Pristine Nafion**	**$K_4[Fe(CN)_6]$/ Nafion**	**$K_3[Fe(CN)_6]$/ Nafion**	**Reported B.E. values [38] (Source)**
C 1s	284.6	283.8	285	284.8 (graphite)
C 1s	291.4	291.4	291.4	292.4 (Teflon)
O 1s	532.7	531.7	533.7	532.0 (RSO_3H)
O 1s	535.3	535.1	536.8	534.8 (polyamic acid)[a]
F 1s	688.9	689	690.5	690.0 (Teflon)
S 2p	169.8	168.8	170.7	169.0 ($F_3CSOOCH_3$)
Fe $2p_{3/2}$		708.5	710.1	709 711
N 1s		397.6	397.6	397.8

[a] This reference is given to indicate the appearance of a separate O 1s peak for entrapped water molecules in polymer chains. However, in the discussion, the O 1s peak at lower binding energy is assigned to entrapped water molecules in Nafion based on the chemical environment, which is different from that of polyamic acid.

Thus the above XPS investigations clearly demonstrate the autoreduction of $[Fe(CN)_6]^{3-}$ in Nafion environment, mediated by the oxidation of sulfonate groups.

2.3.1.6. Electron Spin Resonance Spectroscopy

Cyanoferrates belong to the class of low-spin metal complexes. In the native state, ferrocyanide is diamagnetic and ferricyanide is paramagnetic. Hence $[Fe(CN)_6]^{3-}$ /Nafion system is expected to be amenable for ESR studies. Surprisingly, this material is found to be ESR-silent, in the magnetic field region of 500 – 6500 G which covers also the region of the expected peaks at g = 4, indicating in agreement with the other characterization studies that the Fe center is reduced from +3 to +2 state, when present in the Nafion matrix.

2.3.1.7. UV-visible Spectroscopy

Figure 2.11 shows the UV-Visible spectra of cyanoferrate (II) (Fig. 11b) and cyanoferrate (III) (Fig. 11c) along with that of cyanoferrate (III) incorporated Nafion membrane (Fig. 2.11a) (6.7×10^{-3} M) – all recorded in the solid state.

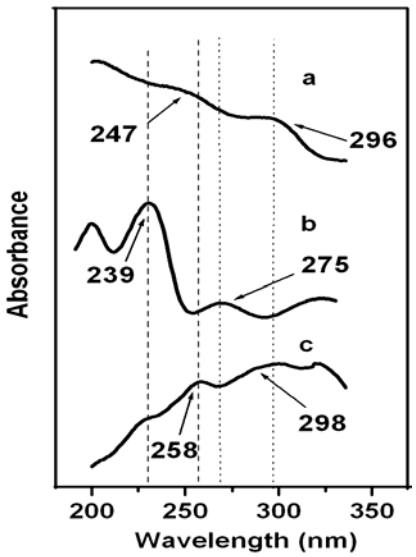

Figure 2.11. UV-Visible spectra of a) $K_3[Fe(CN)_6]$/Nafion; b) $K_4[Fe(CN)_6]$ and c) $K_3[Fe(CN)_6]$ recorded in the solid state

In the UV-Visible spectrum of $K_3[Fe(CN)_6]$ incorporated Nafion membrane, broad bands are seen at 247 nm and 296 nm, which are intermediate between the corresponding bands observed for $K_4[Fe(CN)_6]$ (239 and 275 nm) and $K_3[Fe(CN)_6]$ (258 and 298 nm) respectively. This is an obvious indication for the presence of both the species in the membrane in which only ferricyanide was added initially. Also it is worth mentioning here that the possibility of formation of mixed valence polynuclear complexes is very low at such low concentrations used in this study [40].

2.3.1.8. Mechanism of Autoreduction

Based on the above observations, a possible mechanism is proposed for the interaction of $K_3[Fe(CN)_6]$ with Nafion and its subsequent autoreduction (Fig. 2.12). The first step in the proposed mechanism is the exchange of potassium ions with protons in the sulfonate groups of the ionomer. This is supported by the decrease in OCV of pristine Nafion membrane by 116 mV after the addition of potassium ferrocyanide. Also the concentration dependent OCV-time plots indicate that the complex ion initially in the middle of the water pool move to the micellar interface where initially the potassium ions are exchanged with the protons in the membrane followed by its autoreduction (Fig. 2.12).

1) Proton Exchange:

$$K_3[Fe(CN)_6] + x\ RSO_3^-H^+ \longrightarrow K_{3-x}H_x[Fe(CN)_6]$$

2) Autoreduction:

$$[Fe(CN)_6]^{3-} + RSO_3^- \longrightarrow [Fe(CN)_6]^{4-} + RSO_3\cdot$$

Figure 2.12. Mechanism of $[Fe(CN)_6]^{3-}$ autoreduction in Nafion Membrane

Subsequent to this initial cation - exchange, the sulfonate groups (where S is in +4 state) are found to ligate (through the oxygen atom) to the Iron center and facilitate reduction

of $[Fe(CN)_6]^{3-}$ to $[Fe(CN)_6]^{4-}$ themselves getting oxidized probably to sulfonate radical as the attack of Fe (III) species on the sulfonate pendant groups in Nafion is known to produce membrane derived radical species [31]. The initial ligation of sulfonate oxygen to the Iron center, is evident from the increase in O 1s B.E. value of sulfonate oxygen on addition of ferricyanide to the polymer. In the case of ferrocyanide containing Nafion, such a shift is not observed which is expected in the light of the theory of Hard and Soft Acids and Bases (HSAB), since sulfonate oxygen would interact more strongly with Fe(III) center than with Fe(II). It is very exciting to note that a similar mechanism already exists in biological systems, wherein ferricytochrome C acts as the final electron acceptor in the oxidation of sulfite ions catalysed by sulfite oxidase enzyme present in the mitochondria of human cells [41]**.**

Thus a reasonable understanding of the interactions of the incorporated ions with polymer electrolytes at the molecular level could be attained by a judicious combination of complementary techniques, as demonstrated in this work. This property of the polymer electrolyte is broadly analogous (despite different mechanisms) to the role of the CeO_2 component in the solid electrolyte (CeO_2/ZrO_2) for Solid Oxide Fuel Cells, wherein, CeO_2 provides a better dispersion of the catalyst by tuning its redox potential, thereby enhancing the activity of the incorporated catalyst. This incorporated ion probe protocol may also provide valuable insights into the mechanism of membrane degradation caused by impurity generated radical intermediates under the operating conditions of fuel cells.

The above investigations demonstrate the inherent capability of Nafion membrane to tune the redox potential of the incorporated ions in addition to proton conduction, unlike the electrode potential-induced redox properties of Nafion, reported earlier. The similarity of diffusion coefficient (obtained from the electrochemical data) of $[Fe(CN)_6]^{4-}$ incorporated in Nafion membrane to that of protons allows us to surmise a proton coupled electron transfer mechanism for the $[Fe(CN)_6]^{4-}/[Fe(CN)_6]^{3-}$ couple.

Also, the dependence of OCV-time profiles on the concentration of ferricyanide ions incorporated in the membrane reveals the micellar nature of the interface between the hydrophilic and hydrophobic domains in the polymer. Thus the cyanoferrate anions incorporated in the anionic resin, are demonstrated to serve as effective probes in unfolding the structural, thermodynamic and charge-transport pathways of the ionomer. These results could be applied in the fabrication of catalyst-coated membranes, for choosing proper form of catalyst material having redox compatibility with the ionomer and in deciding their relative proportions to achieve optimum efficiency in fuel cells and supercapacitors. In addition to that, the hydrogen oxidation signal observed in the CV of $K_4[Fe(CN)_6]$/Nafion membrane, has direct implications for fuel cells, as an anodic process in H_2/O_2 PEFCs, as well as in solid state hydrogen sensing, since the peak current scales with hydrogen concentration.

2.3.2. Hemoglobin in Nafion matrix

2.3.2.1. Stability of hemoglobin in Nafion matrix

The biological function of a protein is highly dependent on its secondary and tertiary levels of organization in a given environment, which could be understood by various spectroscopic tools like circular dichroism, IR and Fluorescence spectroscopy. Subsequently, we have examined the stability of hemoglobin in the polymer electrolyte using fluorescence spectroscopy, which gives direct information about protein secondary structure and residual conformations along with UV-vis spectroscopy, which indicates whether the prosthetic group retains its electronic state and spin multiplicity after interacting with the polymer matrix. Accordingly, the fluorescence emission scans of MetHb solutions (1mg/ml in pH 7, 50 mM phosphate buffer) after the addition of Nafion (10 μl of 5 wt % resin in 1 ml of MetHb solution) at an excitation wavelength of 280 nm (which corresponds to Tyr fluorophores) and 295 nm (corresponding to that of Tryptophan [Trp] residues) result in emission maxima at 326 and 327 nm respectively,

indicating the retention of protein secondary structure in the polymer. On the other hand, the presence of Nafion is found to have an interesting effect on fluorescence relaxation dynamics of the native protein as understood from fluorescence-lifetime analysis shown in Figure 2.13.

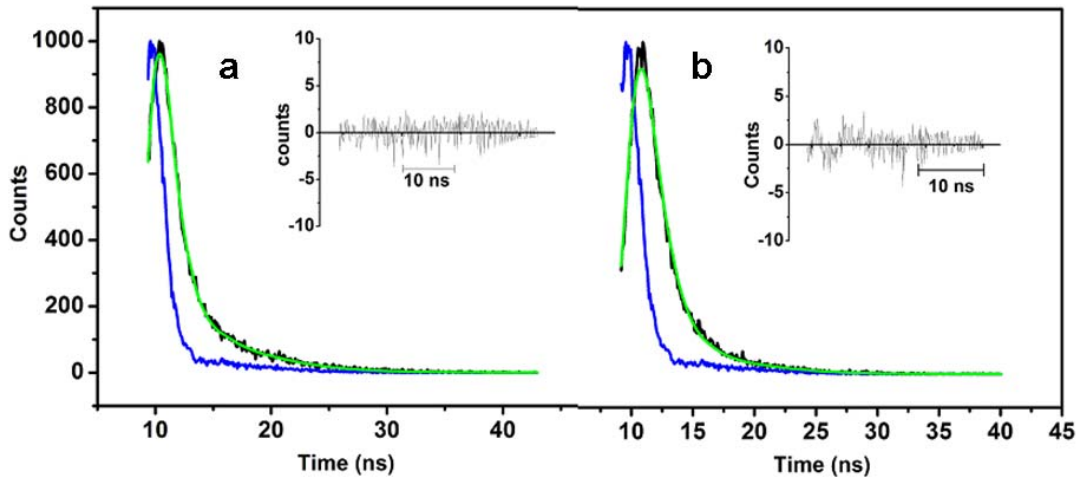

Figure 2.13. Nanosecond fluorescence relaxation spectra of MetHb solution in 50mM phosphate buffer (pH 7) a) before and b) after the addition of 10 µl of 5 wt% Nafion. (black curve: experimental data; green curve: fitted data; blue curve: Internal reference; inset shows the goodness of fit)

Surprisingly, the bi-exponential decay kinetics of Hb solution becomes single-exponential after the introduction of Nafion resin into the protein solution, indicating interesting restrictions in relaxation mechanisms of the protein imposed by the polymer matrix. This could be either due to direct interactions between the sulfonate groups in the polymer with the Tyr and Trp residues of the heme protein or an indirect effect on the quarternary structure arising from a change in the redox state of the heme moiety. It could be roughly compared with earlier reports on transitions between relaxed (R) and tense (T) states of hemoglobin accompanying ligand-binding/dissociation (although our present results do not provide a clear-cut evidence for R---T transitions and may require further experimentation), which mainly arise due to breaking of hydrogen bonds formed by the Trp and Tyr residues at the interface of α and β chains of hemoglobin [42]. A

similar type of transition in quarternary structure might be expected to follow redox changes because of correlations between ligand binding efficiency and redox activity at the prosthetic group [43].

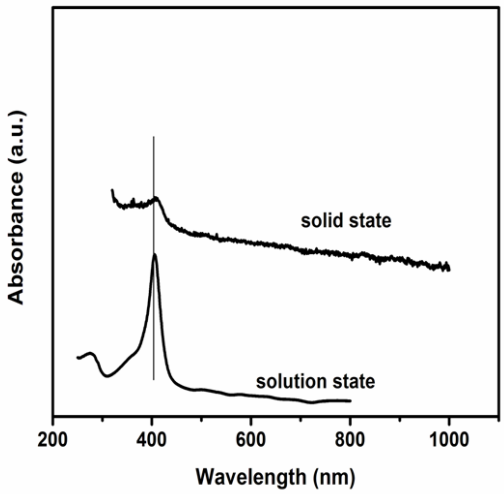

Figure 2.14. UV-visible spectra of Nafion/Hb system in the solid state with a film recast on a quartz slide and in the solution state with Hb dissolved in a 50mM phosphate buffer (pH 7) containing 10 μl of 5 wt% Nafion resin.

Further, the UV-vis spectrum of MetHb-entrapped Nafion film (thickness: 100 μm approx.) cast on a quartz slide (Fig. 2.14) shows a Soret band at 400 nm similar to that of MetHb solution in a pH 7 phosphate buffer (50 mM), which indicates a similarity in heme environment in the polymeric matrix. However, the differences in peak shapes and signal-to-noise ratio between the solid state and liquid state spectra could be attributed to restricted degrees of freedom and slower relaxation processes in the 100 μm thick polymer film used for the spectral studies.

2.3.2.2. Cyclic Voltammetry

A schematic representation of hemoglobin (Hb) molecules entrapped inside the hydrophilic pools of water clusters marked by the pendent sulfonate groups of the polymer electrolyte is shown in Figure 2.15, which also shows the cyclic voltammograms of MetHb-entrapped Nafion film (C_{Hb} = 5.6 x 10^{-7} mol cm^{-3}) under N_2 atmosphere (relative humidity: 30%) at room temperature with a set of redox peaks positioned at $E_{1/2}$ = - 0.057 V vs Ag/AgCl ($E_{1/2} = (E_{pa} + E_{pc})/2$, where E_{pa} and E_{pc} are the anodic and cathodic peak potentials respectively) due to the heme-$Fe^{2+/3+}$ couple [43].

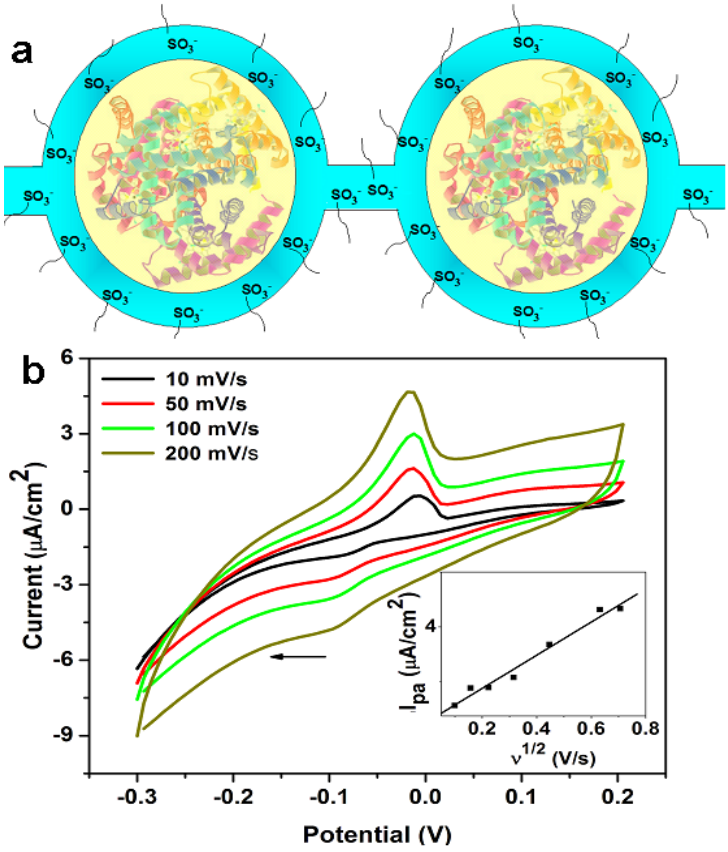

Figure 2.15. A) Schematic representation of hemoglobin molecules entrapped in the hydrophilic domains of Nafion; B) Cyclic voltammograms of Nafion/Hb films in the solid state at various scan rates ranging from 0.01 V/s to 0.2 V/s with 150 μm Pt wire as the working electrode, a Pt counter electrode and AgCl coated Ag wire as reference electrode. The cell briefly consists of a cylindrical Teflon block with a shallow trough housing the working, counter and the reference electrodes over which the polymer film is cast and electrochemical experiments are carried out in a humidified N_2 atmosphere using a special provision available in the cell. The voltammograms correspond to the second potential cycle and no changes were observed in subsequent cycling, indicating the absence of any coupled chemical reaction.

The appearance of redox peaks for the heme couple in the solid polymer electrolyte indicates that the heme protein is present in an environment with sufficient hydration to preserve its biological function, provided by water molecules associated with the hydrophilic pools of the polymer. In fact, the presence of enough amount of water in the matrix (i.e., humidification) is crucial for the functioning of the polymer as 'electrolyte', which could be ensured by a qualitative comparison of the cyclic voltammograms of completely dry and humidified Nafion films (Fig. 2.16). In addition, the difference in redox potential observed in the present case from that reported for hemin [44] (which is closely related to heme except for a few differences in substituents) indicates that the prosthetic group remains in tact in its protein cage and MetHb is considerably stable in the solid polymer electrolyte film.

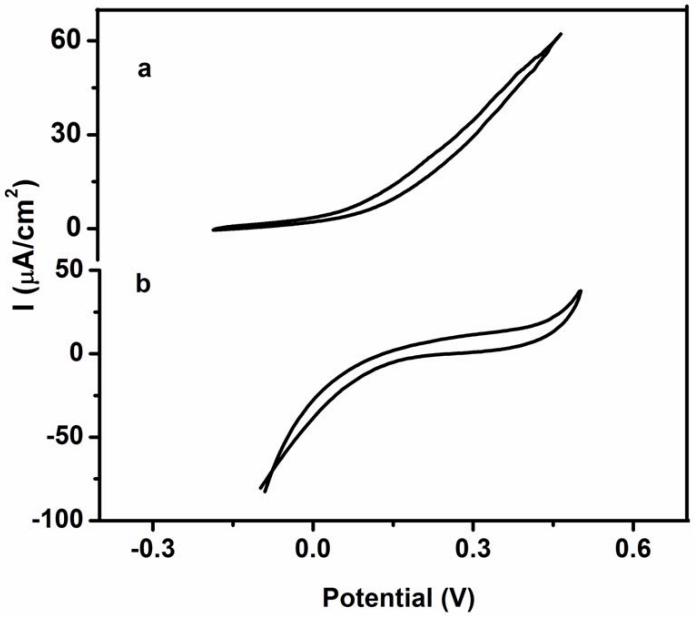

Figure 2.16. Cyclic voltammograms of pristine Nafion films (thickness 150 μm *ca.*) under a) almost completely dry and b) humidified (30% relative humidity) conditions with enough water content. As the proton conducting behavior of the polymer electrolyte depends on the water content, a dry membrane shows almost an Ohmic I-V behavior in the cyclic voltammograms. In addition the presence of water in the microstructural environment of the polymer confers enough stability for the incorporated biomolecules making it considerably biocompatible.

Further, the linear nature of the plot of anodic peak current (I_{pa}) against the square root of potential scan rate indicates that diffusion is the principal mode for transporting the Hb molecules from the bulk electrolyte to the electrode surface. Accordingly, the diffusion coefficient of Hb in the solid polymer electrolyte matrix is calculated to be 3.04 x 10^{-9} cm^2/s using the expression for quasi-reversible systems [27],

$$i_p = \left(2.69 \times 10^5\right) n^{3/2} A D_o^{1/2} C_o^* \nu^{1/2} \tag{2.3}$$

where, i_p is the peak current (after subtracting the non-faradaic contribution); 'n' is the number of electrons involved in the redox process (taken as 4 in the present case- one electron from each of the four heme groups in hemoglobin assuming that there is no intramolecular interaction between the heme groups); A is the area of the electrode; D_o is the diffusion coefficient of the electroactive species (cm^2/s); C_o^* is the bulk concentration and ν is the potential scan rate. The diffusion coefficient of hemoglobin in the polymer matrix is found to be of the same order as that reported for hemoglobin solutions [45] .More significantly, the solid state CVs show a quasi-reversible behavior (peak separation varies with scan rate; $I_{p,anodic} \neq I_{p,cathodic}$) in contrast to the reversible CVs often observed in the case of Electrode/Nafion film/liquid electrolyte systems [43]. In addition, the cathodic current is found to be lower than the anodic current despite the initial addition of the oxidized form i.e., MetHb. Though in the earlier section, ferricyanide ($[Fe(CN)_6]^{3-}$) species incorporated in Nafion films was found to undergo spontaneous reduction due to specific chemical interactions with the polymer matrix, such a situation is chemically unlikely in the case of hemoglobin. Hence the above voltammetric features could be attributed to the differences in transport rates between oxidized (MetHb) and native (Hb) forms of the protein, in the solid polymer matrix, as further clarified by electrochemical impedance studies. Subsequently, by employing Laviron formalism [46], apparent rate constants (k_{app}) for MetHb reduction and Hb oxidation in Nafion matrix have been found to be 0.5 s^{-1} and 0.7 s^{-1} respectively, using the expression [47],

$$\log k = \alpha \log(1-\alpha) + (1-\alpha) \log\alpha - \log(RT/nF\nu) - \alpha(1-\alpha)nF\Delta E_p/2.3RT \qquad (2.4)$$

where, α is the transfer coefficient (an average α value of 0.5 for the anodic process and 0.3 for the cathodic process has been determined from the slope of E_p vs log ν plots; the theoretical slopes being $-2.303RT/\alpha nF$ for the cathodic peak and $2.303RT/(1-\alpha)nF$ for the anodic peak); R is the universal gas constant; T is the temperature (298 K); n is the number of electrons involved in the redox process (here 'n' is taken as 4 with one electron from each heme group which are assumed to be non-interacting); ν is the scan rate (0.2 V/s); ΔE_p is the peak separation (V). The apparent rate constant for Hb oxidation is quite comparable to reported values in similar systems; for example, a value of 56 s^{-1} has been reported by Wang et al for Hb oxidation on PVS-modified pyrolytic graphite electrodes [43a] and a value of 42 s^{-1} for Hb/clay films [48]. Interestingly, the enhancement in Hb oxidation rates after immobilizing the protein on electrode surfaces compared to those obtained with Hb dissolved in the electrolyte (viz. 3.7×10^{-7} cm s^{-1}) [49], could be understood in the light of Marcus theory of electron transfer. In other words, formation of a precursor complex, docking the redox partners in mutually favorable configurations is extremely important to maximize electron transfer rates in biological macromolecules. On the other hand, precursor-complex formation is nearly insignificant and almost undetectable in the case of small outer sphere redox couples dissolved in liquid electrolytes [11]. Particularly, it is this feature of biological electron transfer that marks the efficacy of 'all solid-state' electrochemistry towards biomimetic investigations of physiological redox processes. However the theoretical treatments of electrochemical phenomena normally developed for liquid electrolytes may not always be valid in all respects in the case of solid electrolytes. For example, in the present case, contributions from the polymer matrix such as restrictions imposed on the degrees of freedom of the entrapped protein molecule, dielectric effects arising from the amphiphilicity of the polymeric matrix etc., are not considered while using Laviron's approach to extract rate constants for the redox process.

2.3.2.3. Oxygen Uptake studies

Having analyzed the redox behavior of hemoglobin entrapped inside the polymer electrolyte membrane, it would be more interesting to understand its oxygen-binding characteristics, which is the biological role of the protein. Accordingly, the oxygen uptake/release characteristics of the polymer-entrapped protein are shown in Figure 2.17a.

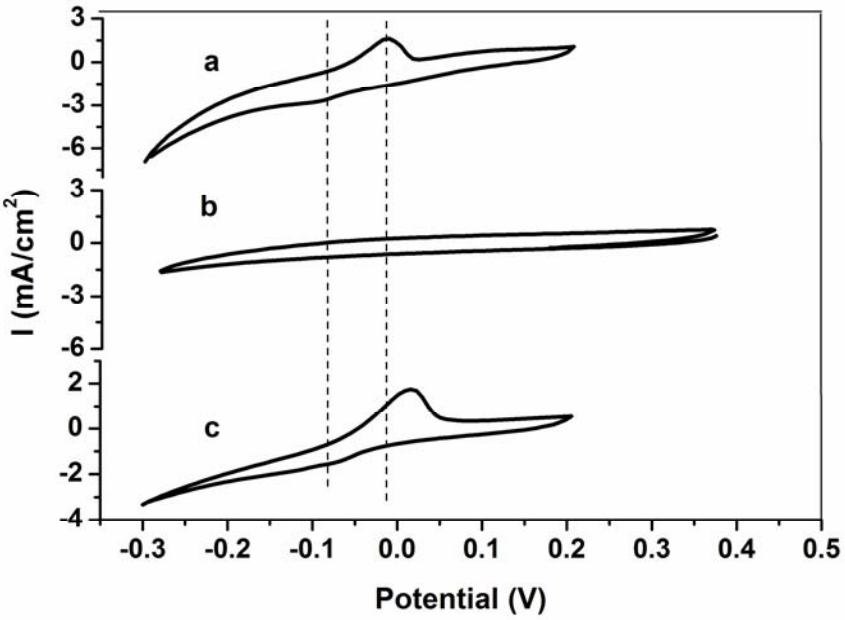

Figure 2.17. Cyclic voltammograms of a Nafion/Hb film in the solid state in a) N_2 ; b) after passing O_2 ; c) rejuvenation of the anodic peak after 2 days in N_2 at a scan rate of 25 mV/s with 150 μm Pt wire as the working electrode, a Pt counter electrode and AgCl coated Ag wire as reference electrode**.**

The anodic peak in the CV is found to vanish in O_2 atmosphere, which could be attributed to the formation of oxyhemoglobin, difficult to be oxidized electrochemically to the Fe^{3+} form. Another possibility could be that the anodic peak shifts beyond the experimental potential window accessible with the present system, because of

differences in redox potentials arising from the chemical transformation of Fe (II) to the Fe (II) ---O_2 state [50]. On the other hand, the cathodic peak could hardly be judged as vanishing owing to its insignificant shape. Surprisingly, in contradiction to earlier reports in which hemoglobin is found to release bound-oxygen instantaneously when the partial pressure of oxygen comes down in the atmosphere, the heme groups are found to bind oxygen very strongly in Nafion matrix, as evident from a slow rejuvenation of the anodic peak after 2 days. This could be possible because oxygen binding, unlike electron exchange process, is known to be sensitive to steric constraints [42b] that vary considerably when the protein is entrapped in a solid polymer membrane. In addition, the anodic peak is found to shift to a more positive value by 30 mV, indicating only a partial recovery of the deoxy state even after two days.

Further, we tried to trigger the release of bound oxygen by performing CV under SO_2 atmosphere, which is expected to bind to the metal center. However, the anodic peak did not reappear even after holding the potential at – 0.4 V for 30 min. On the contrary, an instantaneous release of oxygen shown by a rejuvenation of the anodic peak, again with a shift to a more positive potential by 43 mV, is observed when a small amount (5 μl) of 0.2 M NaOH solution is added to the membrane.

2.3.2.4. Electrochemical Impedance

Figure 2.18 shows the Nyquist plots (imaginary versus real part of impedance) of Nafion-Hb membrane. The high frequency part (100 kHz to 100 Hz) was fitted with a simple Randles equivalent circuit with a constant phase element (considering the shift in the center of the semicircle) to yield the following trend in electron transfer resistance (indicative of the feasibility of hemoglobin oxidation). A further analysis of the low frequency part of the impedance plots, results in a diffusion coefficient value of 4.82 x 10^{-6} cm^2/s, which is about three orders of magnitude higher than that estimated using cyclic voltammetry. This discrepancy could be arising from the assumption made while

simplifying the expressions for Warburg impedance, that the diffusion coefficients of Hb and MetHb are equal. This clearly indicates that the transport rates of Hb and MetHb in the polymer electrolyte film are entirely different which could also form the reason behind the quasi-reversible nature of the cyclic voltammograms.

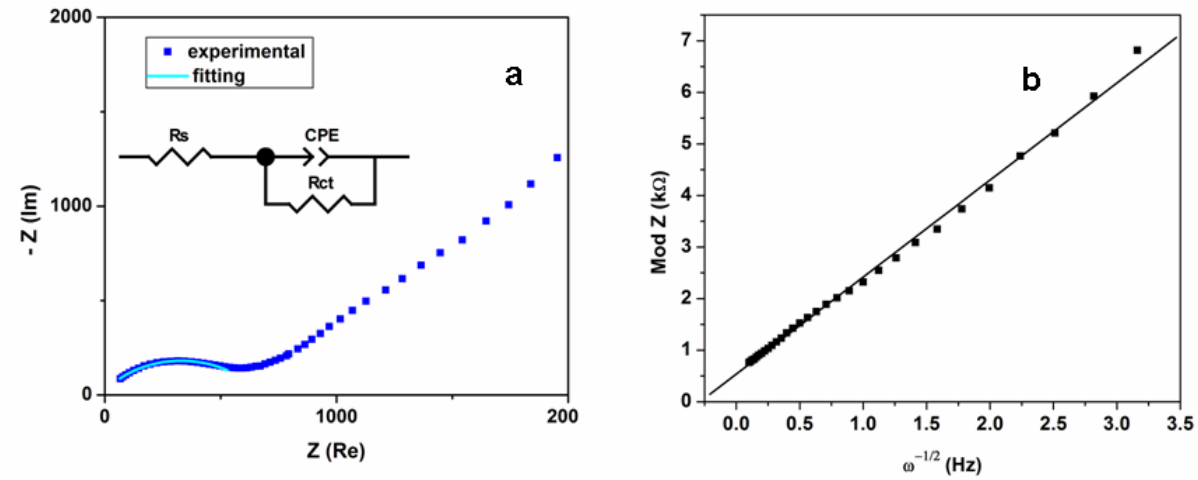

Figure 2.18. Electrochemical impedance Nyquist (-Z(Im) versus Z(Re)) plot of a Nafion/Hb membrane with a) the high frequency part fitted with a Randles electrical equivalent circuit; b) the low frequency part fitted with a straight line.

A further examination of the system in different gas atmospheres using the electrochemical impedance technique is shown in Figure 2.19. The Nyquist plots (imaginary versus real part of impedance) illustrate a semicircle in the high frequency region indicating the presence of a charge-transfer limited process followed by a linear behavior in the low frequency region corresponding to the diffusion of the species to the electrode surface. The R_{ct} values for the pristine Nafion membrane and for Nafion/Hb membranes in different gas atmospheres are tabulated below (Table 2.3)

Table 2.3. Comparison of charge transfer resistance values for pristine Nafion film with Nafion/Hb film at various atmospheres

Atmosphere	**R_{ct} (Nafion) kΩ/cm^2**	**R_{ct} (Nafion/Hb) kΩ/cm^2**
N_2	5	1
O_2	22	1.1
SO_2	7	1.2
Alkaline medium	2.4	0.7

The trend in the charge transfer resistance values is in agreement with the appearance and disappearance of heme oxidation peaks in cyclic voltammetry discussed above. While the pristine Nafion film shows the trend,

$$R_{alkaline} < R_{N_2} < R_{SO_2} < R_{O_2}$$

the Nafion/ Hb film exhibits the trend,

$$R_{alkaline} < R_{N_2} < R_{O_2} < R_{SO_2}$$

In addition, the higher R_{ct} observed in SO_2 atmosphere and a more negative open circuit voltage shown in the OCV-time profiles (Fig. 2.19) probably indicates the involvement of sulfonate groups of the polymer in the redox equilibrium of hemoglobin.

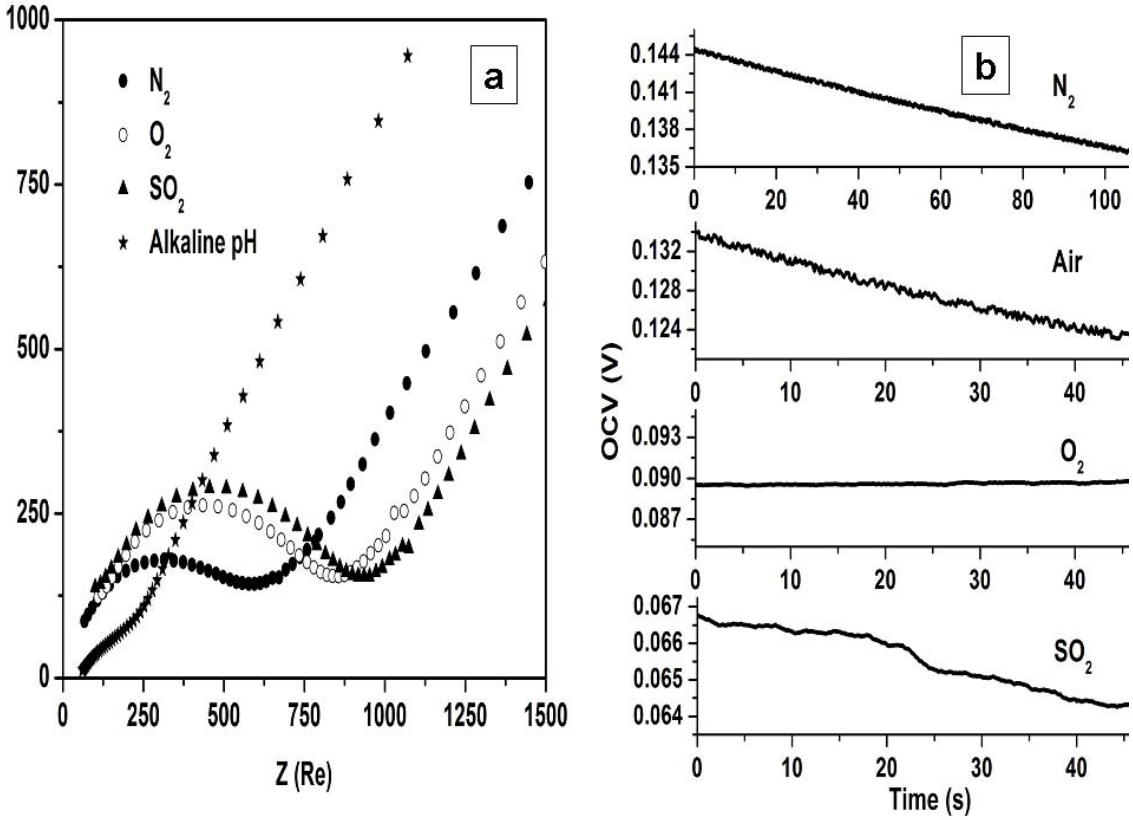

Figure 2.19 a) Electrochemical impedance Nyquist plots ($Impedance_{real}$, Z(Re) vs $Impedance_{imaginary}$ Z(Im)) for Nafion/Hb films successively under N_2, O_2, SO_2 atmospheres and after addition of 10 μl of 0.2 M NaOH solution to the film with 150 μm Pt wire as the working electrode, a Pt counter electrode and AgCl coated Ag wire as reference electrode. b) OCV-time profiles of the Nafion/Hb films in different atmospheres.

A subsequent calculation based on the electron-transfer resistance values in N_2 atmosphere yields an apparent heterogenous rate constant of 0.52 cm/s, which is closely related to the reported values [51].

Thus the effect of Nafion matrix on the redox behavior of cyanoferrates and heme proteins has been understood with the help of all-solid-state electrochemistry. Though, the present work needs more rigorous investigation to explore the exact mechanism of autoreduction, which could be achieved by modifying the

electrochemical cell to allow *in situ* spectroscopic examination and to understand the role of polymer chain dynamics on the transport of redox species.

2.4 Summary and Conclusions

Using "all-solid-state" electrochemical measurement on cyanoferrates incorporated in Nafion matrix, it is found that cyanoferrate (III) ions undergo autoreduction in the ionomer matrix. In addition to proposing a mechanism for the process, this chapter demonstrates the effectiveness of the polymer electrolyte interface in tuning the redox potential of the confined ions. A systematic analysis of the cyclic voltammograms and impedance data for the $[Fe(CN)_6]^{4-}$ containing Nafion membrane enables the estimation of standard rate constant for $[Fe(CN)_6]^{4-}$ oxidation, k^o, as 0.08 cm/s and diffusion coefficient, D_o as 1.3×10^{-12} cm^2/s. A similar calculation yields a value of 4×10^{-10} cm^2/s for diffusion coefficient of hydrogen in Nafion matrix and 3×10^{-4} cm/s for standard rate constant for hydrogen oxidation. The results of the above investigations could have direct technological relevance for choosing catalyst materials having redox compatibility with the polymer electrolyte. Also, the study may be helpful in the preparation of catalyst-coated membranes (wherein the fuel cell catalyst is directly coated onto the polymer membrane instead of on the carbon support). Solid state electrochemistry of hemoglobin performed in Nafion matrix following the studies of cyanoferrates. The protein is considerably stable in the polymer matrix, as confirmed by UV-visible, Fluorescence and FTIR spectroscopy. Interestingly, the Fe^{2+}-form of the polymer-confined protein is found to bind molecular oxygen more strongly than the native protein, which could be due to some specific interactions between the sulfonate groups and some of the amino acid residues of the protein part.

Hemoglobin and Nafion have been chosen for the present studies to demonstrate the all-solid-state methodology, as they are well characterized by other electrochemical techniques, thus allowing easier comparison of the present results with the reported

ones. However, this could be readily extended to any combination of redox protein-polymer electrolytes thereby providing a broader application in diverse fields like protein-based biotechnology and pharmaceutical industry.

2.5 References

1. Mauritz, K. A.; Moore, R. B. *Chem. Rev*. **2004**, *104*, 4535.
2. (a) Gyurcsanyi, R. E.; Pergel, E.; Nagy, R.; Kapui, I.; Lan, B. T. T.;. Toth, K.; Bitter, I.; Linder, E. *Anal. Chem*. **2001**, *73*, 2104. (b) Lee, C.; Anson, F. C. *Anal. Chem*. **1992**, *64*, 528. (c) Nugues, S.; Denuault, G. *J. Electroanal. Chem.* **1996**, *408*, 125. (d) Jeon, C.; Anson, F. C. *Anal. Chem.* **1982**, *84*, 2021. (e) Kwak, J.; Anson, F. C. *Anal. Chem*. **1992**, *64*, 250.
3. Neppel, A.; Butler, I. S.; Eisenberg, A. *Macromolecules*, **1979**, *12*, 948.
4. Schlick, S.; Gobel, G.; Pineri, M; Volino, F. *Macromolecules*, **1991**, *24*, 3517.
5. (a) Rex, G. C.; Schlick, S. *J. Phys. Chem*. **1985**, *89*, 3598. (b) Amigo, M.G. –A.; Schlick, S. *J. Phys. Chem* **1989**, *93*, 7526. (c) Bednarek, J.; Schlick, S. *J. Am. Chem. Soc.* **1990**, *112*, 5019. (d) Bednarek, J.; Schlick, S. *J. Am. Chem. Soc*. **1991**, *113*, 3303. (e) Maiti, B.; Schlick, S. *Chem. Mater*. **1992**, *4*, 458.
6. Amigo, M. G. –A.; Schlick, S. *J. Phys. Chem*. **1986**, *90*, 6353.
7. Che, C. M.;. Fu, W. F.; Lai, S. W.; Hou, Y. J.; Liu, Y. L. *Chem. Commun*. **2003**, 118.
8. (a) Moore, C. M.; Hackman, S.; Brennan, T.; Minteer, S. D. *J. Membr. Sci.* **2005**, *255*, 233. (b) Moore, C. M.; Hackman, S.; Brennan, T.; Minteer, S. D. *J. Membr. Sci.* **2005**, *254*, 63.
9. (a) Maruyama, J.; Abe, I. *J. Electroanal. Chem*. **2002**, *527*, 65. (b) Kalj, B.; Dryfe, R. A. W. *Phys. Chem. Chem. Phys*, **2001**, *3*, 3156.

10. (a) Riess, I. *Solid State Ionics* **2005**, *176*, 1667. (b) Claye, A. S.; Fischer, J. E.; Huffman, C. B.; Rinzler, A. G.; Smalley, R. E. *J. Electrochem. Soc.* **2000**, *147*, 2845. (c) Basura, V. I.; Beattie, P. D.; Holdcroft, S. *J. Electroanal. Chem*. **1998**, *458*, 1. (d) Kulesza, P. J.; Dickinson, E. V.; Williams, M. E.; Hendrickson S. M.; Malik, M. A.; Miecznikowski, K.; Murray, R. W. *J. Phys. Chem. B* **2001**, *105*, 5833.
11. Armstrong, F. A.; Hill, H. A. O.; Walton, N. J. *Acc. Chem. Res.* **1988**, *21*, 407.
12. Niki, K. et al. *J. Phys. Chem. B* **2003**, 107, 9947
13. (a) Armstrong, F. A.; Heering, H. A.; Hirst, J. *Chem. Soc. Rev.* **1997**, *26*, 169. (b) McEvoy, J. P.; Armstrong, F. A. *Chem. Commun.* **1999**, 1635. (c) Hirst, J.; Ackrell, B.A. C.; Armstrong, F. A. *J. Am. Chem. Soc.* **1997**, *119*, 7434.
14. Rusling, J. F. *Acc. Chem. Res.* **1998**, *31*, 363.
15. (a) Degani, Y.; Heller, A. *J. Am. Chem. Soc.* **1988**, *110*, 2615. (b) Degani, Y.; Heller, A. *J. Am. Chem. Soc.* **1989**, *111*, 2357. (c) Heller, A. *Acc. Chem. Res.* **1990**, *23*, 128. (d) Degani, Y.; Heller, A. *J. Phys. Chem.* **1987**, *91*, 1285
16. (a) Fan, Z.; Harrison, J. D. *Anal. Chem.* **1992**, *64*, 1304. (b) Moussy, F.; Jakeway, S.; Harrison, J. D.; Rajotte, R. V. *Anal. Chem.* **1994**, *66*, 3882 – 3888. (c) Valdes, T. I.; Moussy, F. *Biosens. Bioelectron.* **1999**, *14*, 579.
17. Allen, P. M.; Hill, H. A. O.; Walton, N. J. *J. Electroanal. Chem*. **1984**, *178*, 69
18. Safranj, A.; Gershuni, S.; Rabani, J. *Langmuir* **1993**, *9*. 3676.
19. Bertoncello, P.; Ciani, I.; Li, F.; Unwin, P. R. *Langmuir* **2006**, *22*, 10380.
20. Navati, M. S.; Friedman, J. M. *J. Biol. Chem.* **2006**, *281*, 36021.
21. Borchert, H.; Talapiin, D. V.; Goponik, N.; McGinley, C.; Adam, S.; Lobo. A.; Moller, T.; Weller, H. *J. Phys. Chem. B* **2003**, *107*, 9662.
22. The spectra were fitted using the software XPSPEAK4.1 available free on

the website, http:\\www.uksaf.org/software.html#7.

23. Lu, X.; Wu, S.; Wang, L.; Su, Z. *Sensors and Actuators B*, **2005**, *107*, 812.
24. Bard, A. J.; Faulkner, L. R., 'Electrochemical Methods: Fundamentals and Applications' 2nd ed. **2004**, p. 99.
25. Maruyama, J.; Inaba, M.; Katakura, K.; Ogumi, Z.; Takehara, Z. I. *J. Electroanal. Chem*. **1998**, *447*, 201.
26. Seeliger, D.; Hartnig, C.; Spohr, E. *Electrochim. Acta*, **2005**, *50*, 4234.
27. Bard, A. J.; Faulkner, L. R., 'Electrochemical Methods: Fundamentals and Applications' 2nd ed. **2004**, p. 236.
28. Jambunathan, K.; Shah, B. C.; Hudson, J. L.; Hiller, A. C. *J. Electroanal. Chem.* **2001**, *500*, 279.
29. Liu, Y.; Huang, B.; Tzeng, I. *J. Electroanal. Chem.* **2002**, *533*, 85.
30. Kulesza, P. J.; Dickinson, E. V.; Williams, M. E.; Hendrickson S. M.; Malik, M. A.; Miecznikowski, K.; Murray, R. W. *J. Phys. Chem. B* **2001**, *105*, 5833.
31. Kadirov, M. K.; Bosnjakovic, Admira; Schlick, S. *J. Phys. Chem. B* **2005**, *109*, 7664.
32. Sando, G. M.; Dahl, K.; Owrutsky, J. C. *J. Phys. Chem. B* **2005**, *109*, 4084.
33. Brust, M.; Blass, P. M.; Bard, A. J. *Langmuir*, **1997**, *13*, 5602.
34. Jacobs, P. A.; De Wilde, W.; Schoonheydt, R. A.; Uytterhoeven, J. B. *J. Chem. Soc. Faraday Transactions*, **1976**, *72*, 1221.
35. Nicholson, R. S. *Anal.Chem.***1965**, *37*, 1351.
36. Kitamura, F.; Nanbu, N.; Ohsaka, T.; Tokuda, K. *J. Electroanal. Chem.* **1998,** *456*, 113.
37. Dobson, K. D.; McQuillan, A. J. *Phys. Chem. Chem. Phys*. **2000**, *2*, 5180.
38. Binding energy values of the reference compounds were obtained from NIST website, http://srdata.nist.gov/xps/bind_e_detail
39. 'Handbook of X-Ray Photoelectron Spectroscopy, Ed. C. D. Wagner, W. M. Riggs, L. E. Davis, J. F. Moulder, G. E. Mullenberg, 1979, Perkin Elmer

Corporation.

40. (a) Hush, N. S. *Electrochim. Acta* **1968**, *13*, 1005. (b) Glauser, M.; Hauser, U.; Herren, F.; Ludi, A.; Roder, P.; Schmidt, E.; Siegenthaler, H.; Wenk, F. *J. Am. Chem. Soc* **1973**, *95*, 8457. (c) Khostariya, D. E.; Kjaer, A. M.; Marsagishvili, T. A.; Ulstrup, J. *J. Phys. Chem*. **1992**, *96*, 4154.
41. Details about sulfite oxidase are available in the website, http://www.metallo.scripps.edu
42. (a) Rodgers, K. R.; Spiro, T. G. *Science* **1994**, *265*, 1697. (b) Nagai, M.; Kaminaka, S.; Ohba, Y.; Nagai, Y.; Mizutani, Y.; Kitagawa, T. *J. Biol. Chem.* **1995**, *270*, 1636.
43. (a) Wang, L.; Hu, N. *Bioelectrochemistry* **2001**, *53*, 205. (b) Ye, J.; Baldwin, R. P. *Anal. Chem.* **1988**, *60*, 2263. (c) Schelereth, D. D.; Mantele, W. *Biochemistry* **1992**, *31*, 7494.
44. (a) Gao, Y.; Chen, J. *J. Electroanal.Chem.* **2005**, *578*, 129. (b) Nan, C. G. *Anal. Chim. Acta* **2002**, *452*, 245.
45. Bouwer, S. T.; Hoofd, L.; Kreuzer, F. *Biochim. Biophys. Acta* **1997,** *338*, 127.
46. Laviron, E. *J. Electroanal. Chem.* **1979**, *101*, 19.
47. Huang, Q.; Lu, Z.; Rusling, J. F. *Langmuir* **1996**, *12*, 5472.
48. Zhen, L.; Li, Z.; Hu, N.; Zeng, Y. *Langmuir*, **2002**, *18*, 8573.
49. Dong, S.; Zhu, Y.; Song, S. *Bioelectrochem.Bioenerg.***1989**, *21*, 233.
50. Blankman, J. I.; Shahzad, N.; Miller, C. J.; Guiles, R. D. *Biochemistry* **2000**, *39*, 14806.
51. Zhang, L.; Jiang, X.; Wang, E.; Dong, S. *Biosens. Bioelectron.* **2005**, *21*, 337.

Nafion/Polyoxyethylene bis (amine) Polyelectrolyte Complexes

This chapter deals with the transport properties of aqueous solutions of Nafion and redox behavior of ions dissolved in them with an objective to correlate the solution properties of Nafion with those of the membranes discussed in the previous chapter. The strategy is to introduce a second polymer electrolyte, polyoxyethylene bis (amine), capable of developing a charge opposite (positive) to that of Nafion by acid-base interactions with the latter. The amino polymer electrolyte acts not only as a probe to unravel the conformational manifestations of dissolved Nafion but also helps to tune its transport properties when added in different proportions. Interestingly, polyoxyethylene bis (amine), is found to hinder the autoreduction of cyanoferrate(III) in Nafion, by forming stable 'polyelectrolyte complexes' through electrostatic association. However, the poor mechanical stability of the resulting membranes precludes their direct application as solid electrolyte in polymer electrolyte fuel cells and further investigations are required in this direction.

* A part of the work discussed in this chapter has been published in: *Macromolecules* 2008, *41*, 3653.

3.1 Introduction

Polymer electrolytes exhibit interesting properties not only in the solid state, but also in the solution form depending on the nature of the solvent. The ionic groups distributed along the macromolecule lead to non-covalent interactions between the polymer chains including electrostatic, hydrogen bonding, Van der Waals and hydrophobic interactions. The intermolecular 'cross-talk' arising from these interactions results in interesting outcomes, especially in terms of solvation, self-assembly and aggregation dynamics of the polymer electrolyte molecules in their respective solutions. One of the most interesting aspects of polymer electrolyte solutions is their excellent sensitivity to variations in parameters like ionic strength, pH, shear stress and temperature, which qualifies them as potential candidates for the fabrication of stimuli-responsive polymer systems [1].

Especially, solutions of amphiphilic polymer electrolytes (containing hydrophobic as well as hydrophilic domains) exhibit interesting rheological properties and phase behavior, attributed to their characteristic self-assembling nature. The aggregate structure depends on the relationship between the polymer backbone and the solvent based on which polymer electrolyte solutions can be classified broadly into three types as follows [2].

1. Solutions in non-polar solvents, characterized by a concentration-dependent aggregation due to electrostatic interactions between the ionic groups attached to the solvated polymer backbone,
2. Solutions in polar solvents capable of dissolving the polymer backbone, which form extended polymer chains similar to weakly charged polymer electrolytes,

3. Solutions in polar solvents, in which the neutral counterpart of the polymer electrolyte is insoluble, characterized by phase separation between the polymer and the solvent resulting in a colloidal dispersion.

The behavior of polymer electrolyte solutions is not only interesting from a fundamental viewpoint but also provides useful insight into the properties of the membranes cast from the respective solutions. In this respect, Nafion solution is among the most studied systems mainly owing to its importance as ionomer binder in the catalyst layer of membrane electrode assemblies constituting polymer electrolyte fuel cells (PEFCs) [3]. For instance, self-assembly and aggregation of Nafion molecules in different solvents has been studied extensively to understand the poorer proton conductivity, chemical and thermal stability of recast and solution-cast Nafion membranes compared to those of the commercial membranes [2]. More specifically, solutions of Nafion in solvents like water, methanol, ethanol, triethyl phosphate, formamide, *N*-methyl formamide, *N,N*-dimethyl formamide and *N,N*-dimethyl acetamide have been studied using small angle x-ray and neutron scattering [4]. Rod-like structures arranged in a planar hexagonal array or mutually orthogonal rods are observed for Nafion in most of the solvents. In these structures, the perfluoro backbone constitutes the core of the rods, while the ionic groups sit at the rod/solvent interface. In another report, the aggregate structure of Nafion solutions in aqueous and non-aqueous solvents has been studied using electron spin resonance with spin probes [5].

Thus the aggregate structure of polymer electrolyte solutions can be controlled by varying the solvent. In line with the sensitivity of these systems to solvent, temperature, ionic strength and pH, another method for tuning the transport properties of polymer electrolyte solutions is to modify the local ionic environment by introducing an oppositely charged polymer electrolyte. Aggregates formed by the interaction between the two polymer electrolytes fall under a class of systems known as “polyelectrolyte complexes” (PECs), which in fact comprises complexes of polymer electrolytes as well as those of polyelectrolytes. Studies on PECs date back to 1896 when Kossel precipitated

egg albumin with protamine [6]. Complexes between synthetic polymer electrolytes began in 1961 with a report on the association of poly(4-vinylbenzyltrimethylammonium chloride) with poly(sodiumstyrenesulfonate) [7].

The driving force for the formation of polyelectrolyte complexes (PECs) is the strong Coulombic interaction between oppositely charged polymer electrolytes, which leads to inter-polymer ionic condensation. In addition, inter-macromolecular interactions like hydrogen bonding, Van der Waals forces, hydrophobic and dipole interactions also play a role in PEC formation. PECs are more attractive than simple polymer electrolytes, as they could yield synergistic properties different from those of the individual components [8,9]. For example, quite recently Cayre *et al* observed diode characteristics at the junction of two oppositely charged polymer electrolytes [9a]. Similarly, PECs in the form of continuous thin films and membranes have been successfully applied for membrane separation processes [10] and dehydration of alcohols [11] respectively. More recently, PEC membranes of chitosan and poly(acrylic acid) were synthesized for application as polymer electrolytes in direct methanol fuel cells [12]. Despite such considerable advances in the field of PECs, their potential utility in a wide range of applications has not gained much attention, probably due to the limited choice of effective combinations of the polymer electrolyte constituents. For instance, the microstructure and the size of the ionic domains of an amphiphilic polymer electrolyte could be tuned by electrostatic interaction with a counter macro-ion. Such variations can have significant impact on the transport properties of the individual components, as they could also affect the local dielectric distribution along the polymer chains [13].

In the previous chapter, the effect of microphase separation in Nafion membranes on the redox behavior of incorporated electroactive ions has been studied towards answering the question: *How does the polymer matrix alter the fate of the ions ensued in it?* Subsequently, the present chapter aims to address its corollary: *How does the presence of ions affect the properties of a polymer?* In this context, electrostatic interaction between Nafion and another polymer electrolyte viz., polyoxyethylene bis (amine) (will

be designated hereafter as polyox), which develops an opposite (positive) charge in acidic conditions, is investigated to follow its manifestations on the properties of either of the polymers.

More specifically, we describe in this chapter, the unique transport properties of novel PECs of polyox and Nafion, electrochemically using $K_3[Fe(CN)_6]/K_4[Fe(CN)_6]$ couple as redox probe. polyox is a neutral polymer electrolyte in its native state, which possesses a basic character by virtue of the presence of amino groups that can interact with the sulfonic acid groups of the former. More significantly, the chemical similarity between the side chains of Nafion (with $–O-CF_2-$ repeat units) and the backbone of polyox (with $–O-CH_2-CH_2-$ repeat units) together with the possible electrostatic interactions between the oppositely charged functional groups could offer excellent compliance between the polymer electrolyte partners. Further, since the average molecular weight of both the polymers are of the same order of magnitude ($\sim 10^3$ g/mol), the relative orientation of the individual polymeric chains (especially at higher concentrations) could have interesting consequences on their transport properties. Hence the results presented in this chapter would be useful to understand the impact of polymer electrolyte aggregation in solution on its electrochemical properties.

3.2 Experimental Section

Nafion ion-exchange resin (5 wt% dispersion in water and lower alcohols; equivalent weight 1000), polyoxyethylene bis (amine) (molecular weight 2000) and Potassium ferricyanide were procured from Aldrich chemicals. Millipore de-ionized water (18 MΩ resistance) was used for preparing the solutions.

PEC preparation Salt-free aqueous solutions of Nafion (2.5 wt% approx.) were ultrasonicated for 15 min followed by the addition of appropriate amounts of polyox to obtain different proportions as explained in Table 3.1. The resulting mixture was

ultrasonicated for further 30 min to yield a clear solution. Blend designated as N8020 indicates that the resulting solution contains 80 % Nafion and 20 % polyox.

Table 3.1. Composition of Nafion/polyox blends and their corresponding designations

Weight ratio (%) [Nafion : polyox]	**Designation**	**Percentage by weight of Nafion**	**Percentage by weight of polyox**	**Ionic strength (x 10^{-2} M) (w.r.t. ionic groups in the polyelectrolytes)**
100/0	Nafion	3	-	9.0
90/10	N9010	2.8	0.3	8.8
80/20	N8020	2.7	0.68	8.9
70/30	N7030	2.5	1.27	9.2
60/40	N6040	2.5	1.5	9.1
50/50	N5050	2.2	2.2	8.9

FTIR studies FTIR spectra were recorded in Diffuse Reflectance mode with a Perkin-Elmer Spectrum One Spectrophotometer, by casting the blends on clean Si wafers (cleaned thoroughly by treating with Piranha solution to form thin films and subsequently dried in air for 24 h). The response of blank Si wafer was subtracted from the resultant spectra before analysis.

UV-visible spectroscopy Mordant Brown, a sulfonic acid containing chromophoric molecule was dissolved (2mM) in Nafion dispersions with varying amounts of polyox and analyzed using UV-visible spectroscopy with a Cary 50 model Varian dual beam spectrometer operating at a resolution of 1 nm.

Viscosity measurements The blends were diluted 100 times with de-ionized water and their relative viscosity (with respect to water) was measured using a Schott AVS 350 viscometer with a Schott CK160-CT1650 Temperature controller, at 303 K. The flow

time was measured five times for each sample, averaged out and then used for calculating the relative viscosity.

pH measurements were performed using a pH meter purchased from Eutech instruments at room temperature (30 ^{o}C) (error in pH measurements ± 0.1).

Potentiometric titrations The pKa of protonated polyox in water (in the absence of Nafion-H^{+}) was determined by pH-metric titrations. In brief, an aqueous solution of pristine polyox (0.5 wt%; 5 mM in terms of the concentration of $–NH_2$ groups) was protonated by titrating first with 10 mM HCl. The resulting solution containing protonated polyox and excess acid was back-titrated with 5 mM NaOH. In this step, the excess HCl in the analyte solution was neutralized first followed by the de-protonation of protonated polyox. Assuming independent titration of the $–NH_2$ groups in each polyox chain (a two-step protonation/deprotonation equilibria, corresponding to two $–NH_2$ groups per polyox chain, was not observed during the titrations probably because the individual pKa values were too close to be detected within our experimental limits) the pKa of protonated polyox was found to be 7.7 (approx.) from three replicate titrations.

Contact angle measurements In order to evaluate the liquid/air surface tension of the blend solutions, the contact angle of the blend droplets on a clean, dry glass plate was measured. All contact angle measurements were performed using a GBX model DIGIDROP contact angle instrument controlled by Windrop software at room temperature 30 ^{o}C and constant humidity (RH 40-50%) with a standard deviation of ± 2 degrees. For each sample, the measurement was repeated 5 times by sessile drop method at different parts of the glass slide and the average value of the contact angle was noted.

Surface Tension calculation Surface tension of the blends at the liquid-air interface were calculated from contact angle-sessile drop measurements on plain glass substrates followed by independent capillary rise measurements using the expression,

$$h = \left(\frac{2\gamma \cos\theta}{\rho g r} \right) \tag{3.1}$$

where, h = height of the liquid lifted in the capillary; γ = liquid-air surface tension; ρ = density of the liquid; r = inner radius of the capillary; g = acceleration due to gravity; θ = contact angle.

Cyclic Voltammetry was performed using Solartron SI 1287 Electrochemical Interface operated through Corrware software and **Electrochemical Impedance** was performed using Solartron 1255B instrument coupled to a Frequency Response Analyzer, operated through a Zplot software. A three-electrode cell consisting of a Pt working electrode, Pt counter electrode and an Ag wire quasi-reference electrode was used for the electrochemical measurements. The blend solutions were used electrolytes and the measurements were performed at room temperature (30 ^{o}C).

3.3 Results and Discussion

3.3.1. Viscosity

Concentration-dependence of the reduced viscosity, η_r, of a neutral polymer solution is given by the expression [14],

$$\eta_r = \frac{(\eta - \eta_o)}{\eta_o C} = [\eta] + k_h [\eta]^2 C \tag{3.2}$$

where, η_o is the solvent viscosity, η is the intrinsic viscosity of the polymer, C is the concentration, and k_h is the Huggins coefficient, corresponding to the free-draining and

non-draining limits varying between 0.4 and 0.76 [15]. On the contrary, in the case of polymer electrolyte solutions, the reduced viscosity exhibits a peculiar behavior as a function of concentration, often described by Fuoss law [16],

$$\eta_r = \frac{A}{\left(1 + B\sqrt{C}\right)} \tag{3.3}$$

Thus the reduced viscosity passes through a maximum at a particular concentration of the polymer electrolyte which is considered as a manifestation of the 'polyelectrolyte effect'. As the position of the maximum is independent of the concentration, its origin is ascribed to electrostatic interactions. Hence, viscosity measurements have been frequently employed to understand polyion-counter ion and polyion-polyion association. For example, the reduced viscosity (η_{sp}/C, where η_{sp} = η-η_o/η_o) of a salt-free polymer electrolyte solution increases markedly on dilution and passes through a maximum at low ionic strengths at zero shear rate [17]. Earlier, this has been attributed to chain expansion at lower polymer electrolyte concentrations, but the concentration-dependent viscosity profiles of rigid and flexible ionic polymer electrolytes have been later found to be similar indicating that conformation effects are not of primary importance. On the contrary, it has been suggested that counterion-mediated attraction between polyions may play a crucial role [18]. The extent of electrostatic interactions and the consequent viscosity changes have been found to depend on the electrostatic persistence length of the polymer electrolyte, defined as [19],

$$l_e = l_B/4\kappa^2 b^2 \tag{3.4}$$

where, l_e is the electrostatic persistence length (discussed in section 1.2.1); l_B is the Bjerrum length (defined as the distance at which the Coulomb interaction between two unscreened elementary charges equals the thermal energy given by the expression, $e^2/\varepsilon k_B T$, where, ε is the dielectric constant of the solvent and k_B is the Boltzmann

constant); κ^{-1} is the Debye-Huckel screening length (defined as the geometrical dimension around a point charge which screens the electrostatic interactions, given by the expression, $(\varepsilon\varepsilon_o kT/2N_A e^2 I)^{1/2}$, where I is the ionic strength of the medium) and b is the average charge separation on the contour of the polymer electrolyte chain. Accordingly, Figure 3.1 shows the variation of viscosity with the composition of Nafion/polyox blend solutions. As the concentrations of the individual polymer electrolytes in the blend solutions are high enough to show the polymer electrolyte effects corresponding to the electrostatic persistence lengths of the individual polymers [20]. Hence, the maximum observed in Figure 3.1 could be attributed to the electrostatic association of Nafion and polyox probably resulting in the formation of polymer electrolyte complexes.

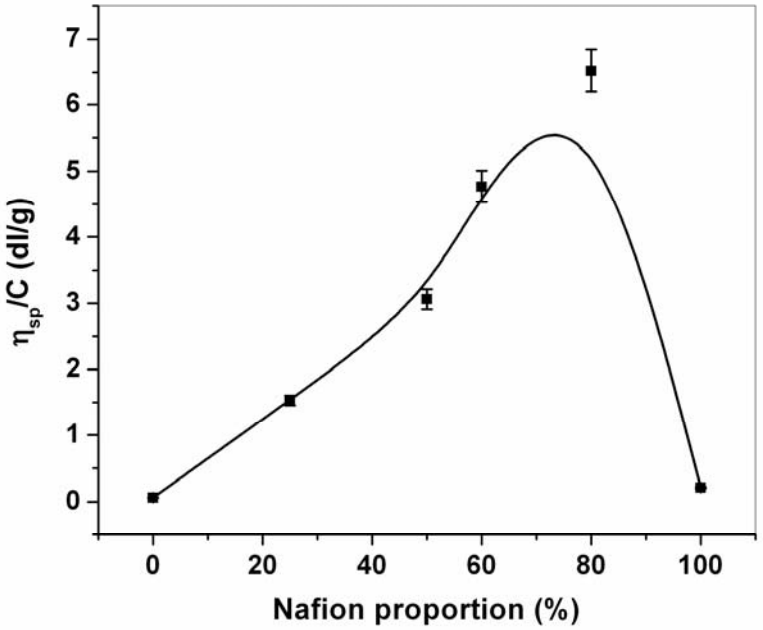

Figure 3.1. Variation of reduced viscosity (η_{sp}/c) with composition of Nafion/polyox blends at 303 K

3.3.2. Surface Tension

In order to verify independently, the electrostatic association of the polymer electrolytes, surface tension measurements at varying concentrations of polymer

electrolyte solutions is a classical method for the determination of critical micelle concentrations. Figure 3.2 shows the variation of surface tension (calculated by independent capillary rise measurements and sessile drop method) of the polymer electrolyte blends with composition, whose values are found to be of the same order as that reported for pristine Nafion dispersions [21]. A clear maximum is observed in the plot of surface tension (polymer electrolyte-air interface) with blend composition, probably indicating that the electrostatic interaction between the polymer electrolyte components is maximum at a composition of 50:50.

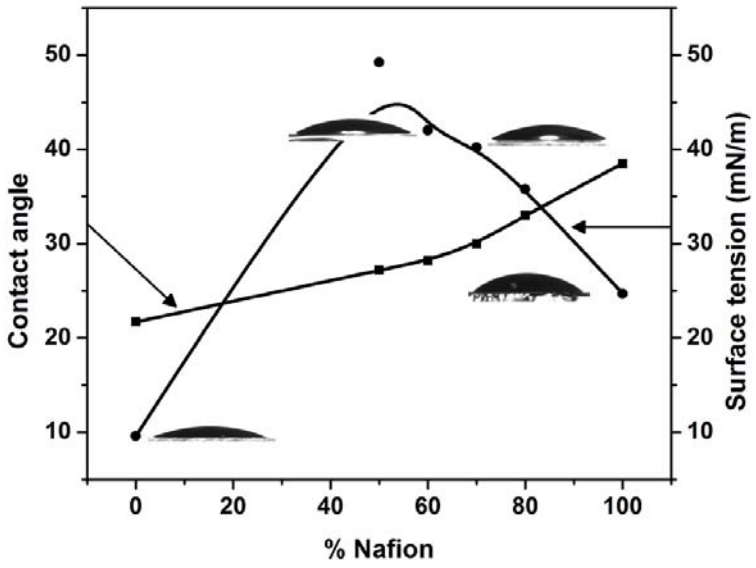

Figure 3.2. Variation of contact angle and surface tension at the liquid/air interface with composition

A more convincing evidence for the acid-base interaction between Nafion and polyox is the variation in the pH of the blend solutions with composition as shown in Figure 3.3. The pH of the blend solutions is found to vary from 8.0 (approx.) for an aqueous solution of pristine polyox to pH 2 (approx.) for an aqueous dispersion of Nafion similar to an acid-base potentiometric titration with the neutralization point falling approximately at a composition of 50:50 in accordance with the surface tension measurements, indicating salt formation. In addition, the excess polyox added after the neutralization point does not disrupt the stability of the PECs by de-protonation of

polyox-NH_3^+ in the range of blend composition under investigation, as the pH of the blend solutions is considerably below the pKa of protonated polyox (7.7) determined independently (described in the experimental section).

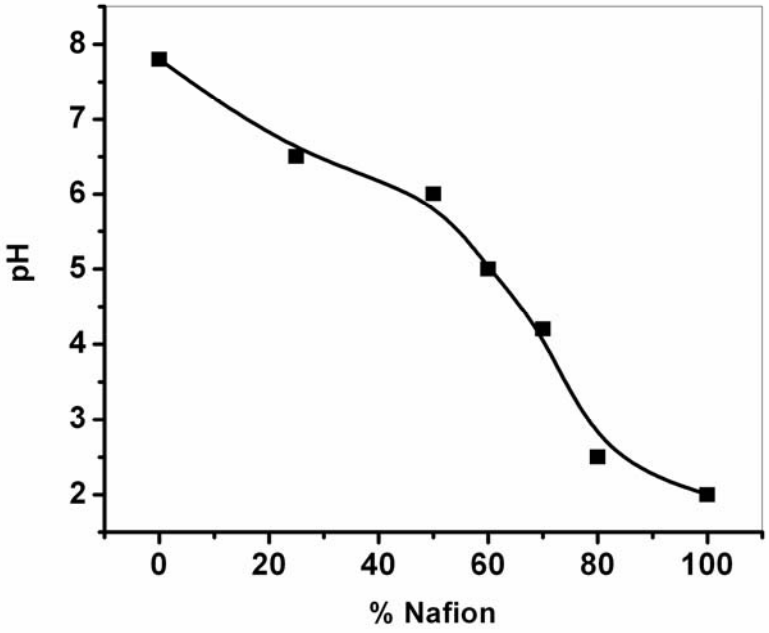

Figure 3.3. Variation of pH with increasing proportions of polyox in Nafion dispersions

For pendent-type polyions with charges residing in their side chains like Nafion, it is found that an equilibrium salt structure is easily formed due to interactions of adjacent reactive sites that follows immediately after atleast one ionic bond is formed [20]. In the present case, the salt formation could occur in two steps viz., i) the initial protonation of the amine groups of polyox by the protons originally associated with the sulfonate groups of Nafion followed by, ii) the electrostatic interactions between the -NH_3^+ and -SO_3^- groups of polyox and Nafion respectively. This could also be compared with the acid-base interactions observed between 2-amino benzimidazole (a basic polymer) and sulfonated poly(ether ether ketone) (an acidic polymer) [22]. Although there could be concomitant changes in the respective conformations of both the polymer electrolytes, we could make a fair assumption that the contribution of conformational changes may be negligible compared to that of the electrostatic forces. For example, Wei and Hudson

have studied the binding of SDS to Chitosan of various degrees of acetylation to demonstrate that the initial binding constant is unchanged, indicating that the contribution of charge density-induced conformational changes of the individual polymer electrolytes may not be high enough to influence the effective potential at the polymer electrolyte interface [23]. Hence, we consider here mainly the changes in the solution structure of the polymer electrolytes occurring after the second step of salt formation viz., coulombic interaction between the charged functional groups and attribute the changes in the properties of the blend solutions to the same.

3.3.3. DRIFT Analysis

Diffuse reflectance Infrared spectra of the polymer electrolyte complex membranes prepared by blending Nafion and polyox in different proportions are presented in Figure 3.4. In the case of perfluorosulfonic acid ionomers, whenever the sulfonate groups of the ionic clusters interact electrostatically with counterions, water molecules bound to them are expected to be expelled away. For example, a similar decrease in water content is observed in Nafion as a consequence of its electrostatic interactions with alkali metal ions [24].

Accordingly, Figure 3.4A shows a transition from a state of medium hydration (3452, 1566 cm^{-1}) in the case of pristine Nafion to a partially dehydrated state (3202, 2881 and 1715 cm^{-1}) with increasing polyox content [25]. This could have interesting consequences for PEM fuel cells, as one could envision polymer electrolyte membranes which could sustain lower humidity conditions. However, the poor mechanical stability of the Nafion/polyox blend membranes in the present work has precluded the verification of their solid-state proton conductivity, which is an important requirement for fuel cell applications. Additionally, the peak at 1058 cm^{-1} corresponding to the symmetric stretching mode of the sulfonate groups, gets broadened and becomes almost undetectable with increasing polyox content in the films. More interestingly, there is a gradual change in the 1100-1400 cm^{-1} region with increasing polyox proportion (Figure

3.4B). Although the asymmetric stretching vibration of the sulfonate groups is expected to absorb in this region, the peak assignment often becomes uncertain due to interference from the C-F vibrational modes of Nafion [12]. Nevertheless, in the present case, despite the invariance in the shape and position of other peaks in this region (1170, 1290 cm^{-1}), the relative intensity of the peaks at 1267 and 1303 cm^{-1} show an interesting variation with polyox proportion. Hence, the latter peaks could be probably due to the asymmetric stretching vibrations of the sulfonate groups, which are known to split into doublet depending on the environment and water structure in the ionic clusters [25].

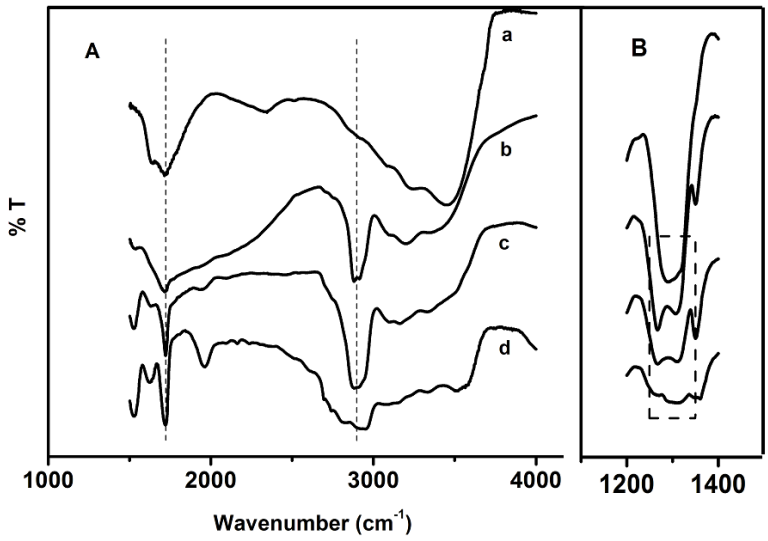

Figure 3.4. Diffuse reflectance FTIR spectra of a) pristine Nafion; b) N8020; c) N6040; d) N5050 films (cast on a clean Si wafer) at 30 ^{o}C (A and B correspond to two different regions of the same spectra).

3.3.4. UV-visible spectroscopy

UV-visible spectroscopy is a convenient technique to study chromophoric polymer electrolytes like poly(styrene sulfonate) [26], where the repeat unit itself is UV-active. However, in the case of polymer electrolytes which do not/contain very low concentration of chromophoric moieties, addition of an oppositely charged dye molecule

to the analyte solution allows to follow changes in the charge density on the polymer electrolyte chain [20]. Accordingly, the electrostatic interaction between Nafion and polyox is followed by UV-visible spectroscopy by adding a few amount of a sulfonated dye, Mordant brown (MB), to the solution. Figure 3.5 shows the UV-visible spectra of MB dissolved in water and dispersions containing various proportions of Nafion and polyox.

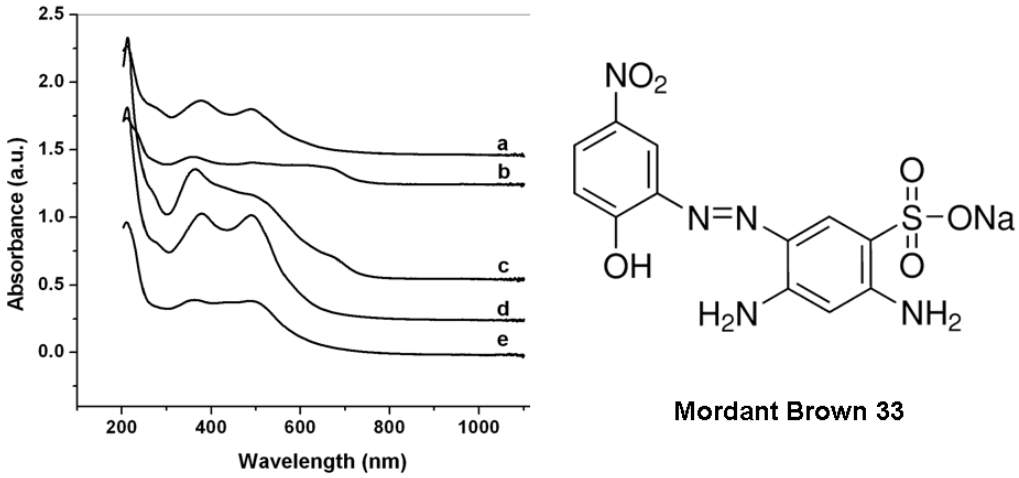

Figure 3.5. Molecular structure of mordant brown 33 (right); UV-visible spectra of mordant brown dissolved in a) water; b) pristine polyox solution in water; c) N2080; d) N4060; e) pristine Nafion dispersion.

The spectral features of the dye get distorted when pristine polyox is added to the solution, which could be due to acid-base interactions between the sulfonic acid groups of the dye and the amine groups of the polymer. Interestingly, the original spectral features of the dye start reappearing when Nafion is progressively introduced into this solution, indicating that there is an electrostatic interaction between the two polymer molecules which in turn releases the dye molecules bound to polyox. However, the dye does not exhibit prominent spectral features even when dissolved in a pristine Nafion dispersion though the peak positions are not very different from those in the aqueous solution. This could be due to some non-specific adsorption of the dye molecules along the polymer chain.

3.3.5. Electrochemical Impedance

Having analyzed the interactions between Nafion and polyox, the electrochemical transport properties of the blend solutions are investigated using electrochemical impedance spectroscopy (EIS) and cyclic voltammetry using $K_3[Fe(CN)_6]$ as a redox probe, which is known to have specific interactions with the pendent sulfonate groups of Nafion-H^+ [27]. Figure 3.6 shows an interesting trend in the complex plane impedance plots [Z (Im) versus Z(Re)] of ferricyanide-dissolved solutions with varying compositions of the polymer electrolyte blends.

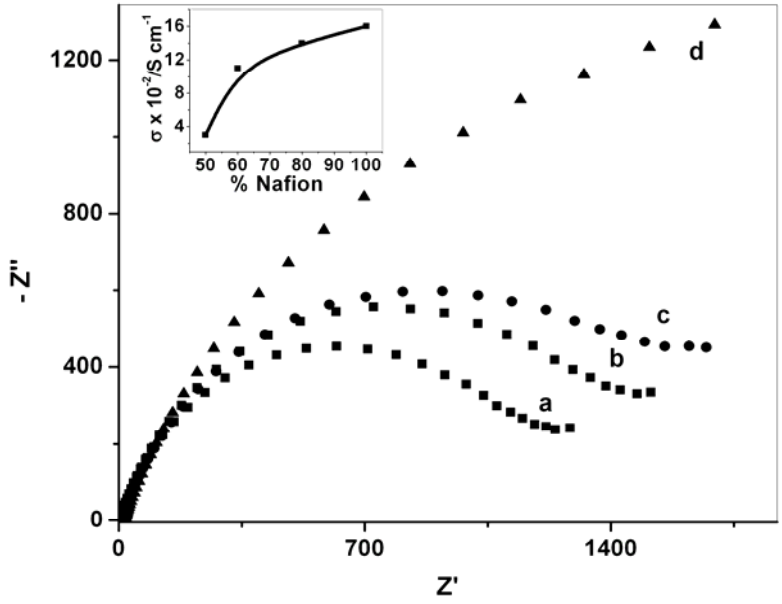

Figure 3.6. Electrochemical impedance of $[Fe(CN)_6]^{3-}$solutions in a) Pristine Nafion (2.5 wt%), b) N8020, c) N6040 and d) N5050 blends under open circuit conditions. Inset shows variation in the proton conductivity calculated from the solution resistance (R_s) values

Usually, when the mass transport of a dissolved redox species is very fast compared to the rate of interfacial electron transfer, a semicircle appears in the high frequency part, the diameter of which is proportional to the rate of electron transfer to the

redox couple. Here, the semicircle spans the whole frequency range (10 mHz to 100 kHz) indicating that the electron transfer rate is considerably high compared to the mass transport rate (Figure 3.6a). When each of the plots is fitted into a semicircle, a gradual increase in its diameter with increasing polyox content could be observed. This indicates important differences in the dielectric constant distribution in the light of the Hubbard-Onsager model [13] for solvation in macroion systems that could probably arise from changes in the solution structure of Nafion due to electrostatic interactions with polyox as depicted in Figure 3.7.

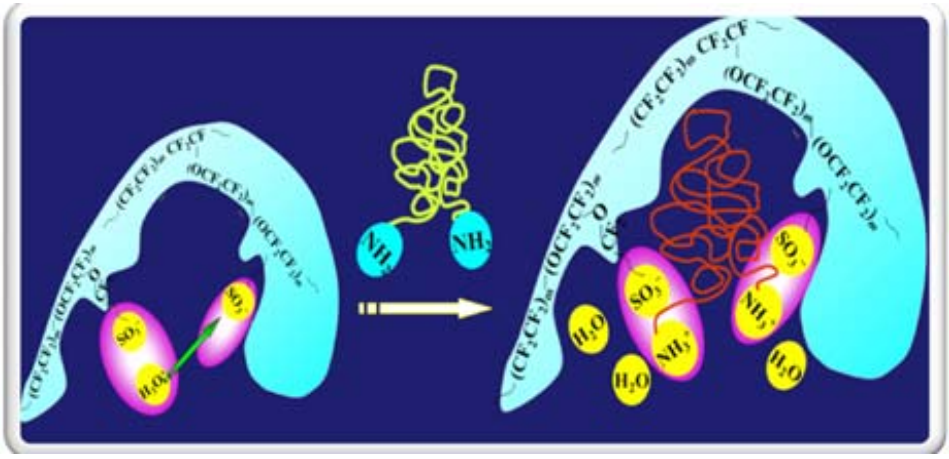

Figure 3.7. Formation of polyelectrolyte complex between poly(oxyethylene bis amine) and Nafion-H^+ involving (i) the protonation of the amine groups of the former by the protons originally associated with the sulfonate groups of Nafion-H^+ followed by (ii) the association of the -NH_3^+ groups of polyox with the sulfonate groups (-SO_3^-) of Nafion. Consequently, some of the hydronium ions present originally in the water clusters of Nafion-H^+ are expelled as water molecules resulting in a secondary solvation shell

Thus, the dielectric constant distribution in an ionomer could be manipulated by deliberately introducing an oppositely charged polymer electrolyte. Accordingly, the proton conductivity of the PEC solutions decreases exponentially with increasing content of polyox as shown in the inset of Figure 3.6. This could be compared with the ion cluster-channel model, according to which, even in solid polymer electrolyte membranes, minor changes in the cluster sizes could lead to significant changes in proton conductivity [28]. Further, Figure 3.8b shows a remarkable variation of ferricyanide diffusion

coefficients (calculated from the peak current variation with square root of scan rate from cyclic voltammograms) with increasing polyox content in the blends.

However, compared to that expected on the basis of viscosity changes shown in Figure 3.1 the variations in the diffusion coefficients are somewhat subtle, indicating that the effect of inter-polymer interactions is more pronounced than that of the viscosity changes with composition. Another possibility is the involvement of polymer conformation effects in addition to electrostatic effects analogous to polyion-counter ion condensation explained by the dynamical scaling theory of polymer electrolyte conductivity [29].

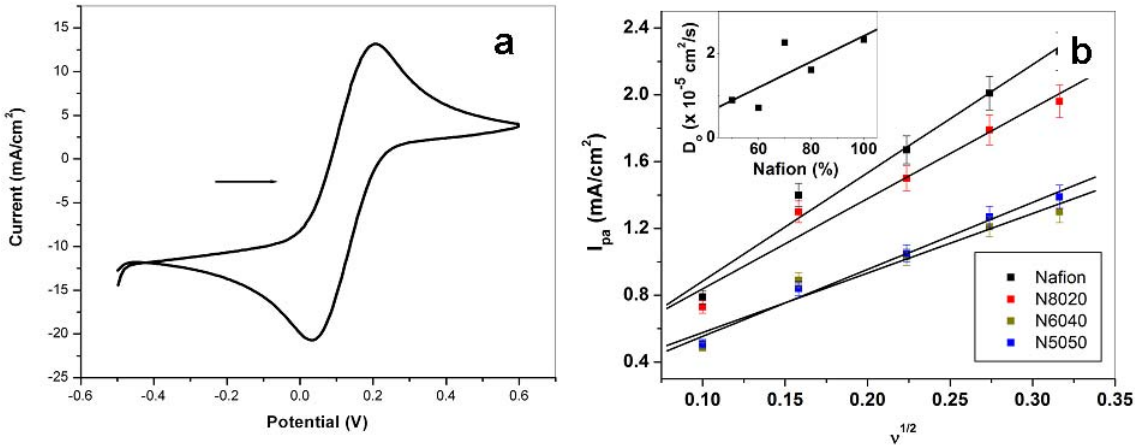

Figure 3.8. a) Cyclic voltammogram of a N8020 blend solution containing $K_3[Fe(CN)_6]$ as the redox probe at a scan rate of 25 mV/s. b) Anodic peak current versus square root of scan rate from cyclic voltammograms of $[Fe(CN)_6]^{3-}$-dissolved blend solutions ($C_{[Fe(CN)6]3-}$= 5 mM ;Ionic strength of the pristine blends was maintained constant at 90 ± 0.5 mM) at 303 K Inset shows the variation in $[Fe(CN)_6]^{3-}$ diffusion coefficient with blend composition.

3.3.6. Cyclic voltammetry

More interesting evidences for the Coulombic interactions between Nafion-H^+ and polyox is obtained by a comparison of the first cyclic voltammeric scan of ferricyanide-

containing pristine Nafion dispersions with that of the N6040 blend solution (Figure 3.9). The sulfonate-containing pendent chains of the perfluorosulfonic acid ionomer, Nafion are known to interact chemically with $[Fe(CN)_6]^{3-}$ and Fe^{3+} species resulting in a release of sulfonate radicals from our earlier studies and independent reports from other groups respectively [27]. However, here polyox is found to minimize such degradation reactions, as evident from the cyclic voltammograms. When the potential is swept in the positive direction starting from the open circuit potential, an anodic peak is noticed in ferricyanide-dissolved pristine Nafion dispersion, which does not appear in the case of similar dispersions with Nafion/polyox blends. The appearance of such an anodic peak indicates that some amount of ferricyanide added initially into the polymer electrolyte dispersion is converted chemically to the ferrocyanide form.

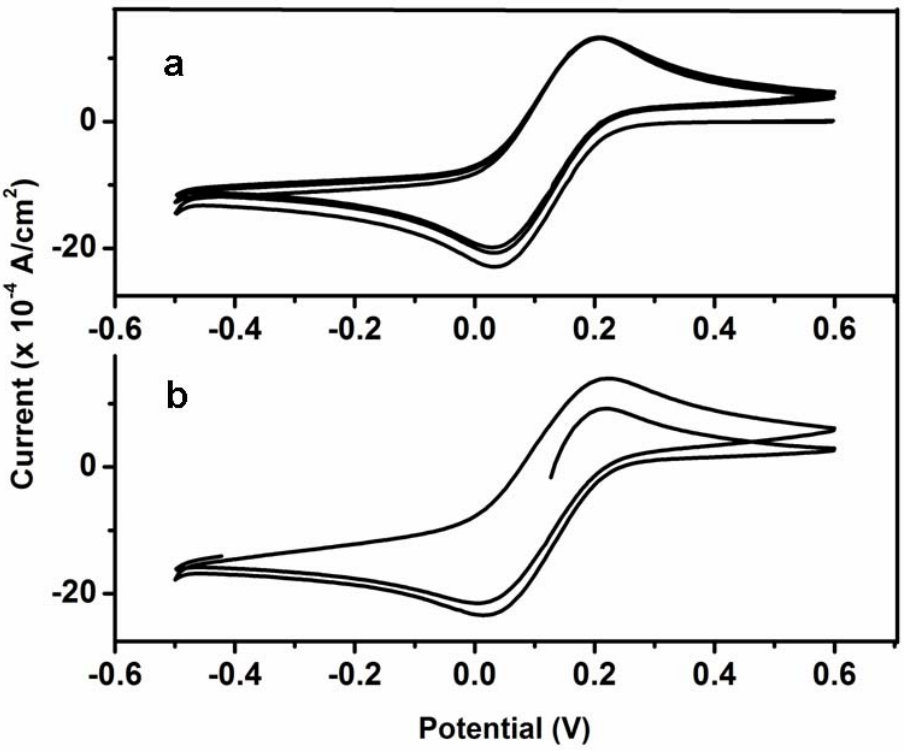

Figure 3.9. Cyclic voltammograms of aqueous solutions of a) N60/40 blend and b) pristine Nafion containing dissolved $K_3[Fe(CN)_6]$, at a scan rate of 25 mV/s

This is further supported by the open circuit potential (OCP)-time profiles, which shows a larger decrease in OCP for pristine Nafion solutions compared to the N6040 blend solution (Figure 3.10). In many circumstances, employing a charged chromophore that interacts specifically (or more selectively) with one of the polymer electrolytes, has been an efficient method for confirming the formation of PECs [20].

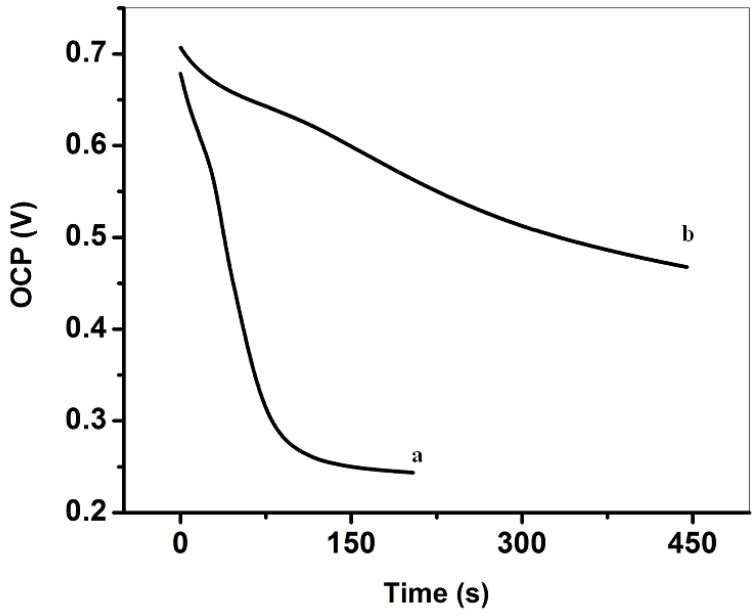

Figure 3.10. Evolution of the Open circuit potential (OCP) with time for $K_3[Fe(CN)_6]$ solutions of a) pristine Nafion (2.5 wt%) and b) N6040 blend indicating the better oxidative stability of the latter towards $[Fe(CN)_6]^{3-}$ species

By a similar argument, the formation of PEC between Nafion and polyox by Coulombic attraction possibly minimizes the interaction of the former with the ferricyanide species, improving the oxidative stability of Nafion. Many of the properties investigated in the present work, arising due to specific interactions between the polymer electrolyte components could be reflected in the respective membranes as the conformations of Nafion molecules in the casting solutions are known to have a significant effect on the morphology of membranes prepared by casting them [30].

However, the oxidative stability and proton conductivity of the blend solutions may not necessarily be observed in the case of solid membranes, in which case it would have a significant impact for different applications utilizing solid polymer electrolytes like PEM fuel cells, supercapacitors and membrane-based separation systems.

3.4 Summary and Conclusions

Polymer electrolyte complexes of Nafion-H^+ and polyoxyethylene bis (amine) were synthesized and characterized using a combination of spectroscopic and electrochemical techniques. The formation of PECs was confirmed by FTIR, pH measurements and cyclic voltammetry using $[Fe(CN)_6]^{3-}$ species, a redox active chromophore as an internal probe. More specifically, considerable changes in the diffusion coefficient of the $[Fe(CN)_6]^{3-}$ as a function of blend composition, indicating the effect of PEC formation on the transport properties, is noticed in the EIS as well as the CV results. Interestingly, $[Fe(CN)_6]^{3-}$ species, is found to have minimum interaction with the sulfonate groups of Nafion after blending with polyox, signifying polymer electrolyte - polymer electrolyte association. In addition, plots of viscosity ad surface tension versus blend composition pass through a maximum, indicating specific interaction between the polymer electrolytes. These results demonstrate that a wide range of properties of a polymer electrolyte could be tuned by complexation with an oppositely charged polymer electrolyte, which could be utilized in developing stimuli-responsive polymer systems for targeted drug-delivery, rheology modifiers and environmental applications.

3.5. References

1. Harada, A.; Kataoka, K. *Macromolecules* **1995,** *28*, 5294.
2. Jiang, S.; Xia, K. –Q.; Xu, G. *Macromolecules* **2001**, *34*, 7783.
3. (a) Wilson, M. S.; Gottesfeld, S. *J. Appl. Electrochem.* **1992**, *22*, 1. (b) Ren, X. M.; Wilson, M. S.; Gottesfeld, S. *J. Electrochem. Soc.,* **1996**, *143*, L12.

4. (a) Aldebert, P.; Dreyfus, B.; Pineri, M. *Macromolecules* **1986**, *19*, 2651. (b) Williams, C. E. *J. Phys. Chem. B* **1997**, *101*, 1884.
5. Szadjzinska-Pietek, E.; Schlick, S.; Plonka, A. *Langmuir* **1994**, *10*, 2188.
6. Kossel, A. *J. Phys. Chem.* **1896**, *22*, 178.
7. Michaels, A. S; Miekka, R. G. *J. Phys. Chem.* **1961,** *65*, 1765.
8. (a) Costa, L. T.; Ribeiro, M. C. C. *J. Chem. Phys.* **2006,** *124*, 184902. (b) Choi, J. –W.; Cheruvally, G.; Kim, Y. –H.; Kim, J. –K.; Manuel, J.; Raghaven, P.; Ahn, J. –H.; Kim, K. –W.; Ahn, H. –J.; Choi, D. S.; Song, C. E. *Solid State Ionics* **2007,** *178*, 1235. (c) Thunemann, A. F.; Muller, M.; Dautzenberg, H.; Joanny, J. –F.; Lowen, H. *Adv. Polym. Sci.* **2004,** *166*, 113.
9. (a) Cayre, O. J.; Chang, S. T.; Velev, O. D. *J. Am. Chem Soc.* **2007,** *129*, 10801. (b) Smitha, B.; Sridhar, S.; Khan, A. A. *Macromolecules* , **2004,** *37*, 22339.
10. Michaels, A. S. *Ind. Eng. Chem.* **1965,** *57*, 32.
11. Shieh, J. –J.; Huang, R. Y. M.; *J. Membr. Sci.* **1997,** *127*, 185.
12. Smitha, B.; Sridhar, S.; Khan, A. A. *Macromolecules* **2004,** *37*, 2233.
13. Schmitz, K. S. In *Handbook of Polyelectrolytes and their Applications*; Tripathy, S. K., Kumar, J., Nalwa, H. S. Eds.; American Scientific Publishers: California, USA, 2002; Vol. 3, pp 203.
14. Borsali, R. In *Handbook of Polyelectrolytes and their Applications*; Tripathy, S. K., Kumar, J., Nalwa, H. S. Eds.; American Scientific Publishers: California, USA, 2002; Vol.2, pp 250.
15. Freed, K. F.; Edwards, S. F. *J. Chem. Phys.* **1975**, *62*, 4032.
16. Fuoss, R. M. *Discuss. Faraday Soc.* **1951**, *11*, 125.
17. Yamanaka, J.; Matsuoka, H.; Kitano, H.;Hasegawa, M.; Ise, N. *J. Am. Chem. Soc.* **1990,** *112*, 587. Yamanaka, J.; Araie, H.; Matsuoka, H.; Kitano, N.; Ise, N. *Macromolecules* **1991,** *24*, 3206
18. Yamanaka, J.; Araie, H.; Matsuoka, H.; Kitano, H.; Ise, N.; Yamaguchi, T.;

Saeki, S.; Tsubokawa, M. *Macromolecules* **1991,** *24*, 6156.

19. Bohidar, H. B. In *Handbook of Polyelectrolytes and their Applications*; Tripathy, S. K., Kumar, J., Nalwa, H. S. Eds.; American Scientific Publishers: California, USA, 2002; Vol. 2, pp 131.
20. Koetz, J.; Kosmella, S. *Polyelectrolytes and Nanoparticles*; Springer Berlin Heidelberg, 2007.
21. Curtin, D. E.; Lousenberg, R. D.; Henry, T. J.; Tangeman, P. C.; Tisack, M. E. *J. Power Sources* **2004**, *131*, 41.
22. Fu, Y.; Manthiram, A.; Guiver, M. D. *Electrochem. Commun.* **2007,** *9*, 905.
23. Wei, Y. C.; Hudson, S. M. *Macromolecules* **1993,** *26*, 4151.
24. Lowry, S. R.; Mauritz, K. A. *J. Am. Chem. Soc.* **1980,** *102*, 4665.
25. Gruger, A.; Regis, A.; Schmatko, T.; Colomban, P. *Vibrational Spectroscopy* **2001,** *26*, 215.
26. Major, M. D.; Torkelson, J. M. *Macromolecules* **1986**, *19*, 2801.
27. (a) Kadirov, M. K.; Bosnjakovic, A.; Schlick, S. *J. Phys. Chem. B* **2005,** *109*, 7664. (b) Sando, G. M.; Dahl, K.; Owrutsky, J. C. *J. Phys. Chem. B* **2005,** *109*, 4084.
28. Hsu, W. Y.; Gierke, T. D. *J. Membr. Sci.* **1983,** *13*, 307.
29. Bordi, F.; Cametti, C.; Gili, T. *Phys. Rev. E* **2002,** *66*, 021803.
30. Lin, H. –L.; Yu, T. L; Huang, C. –H; Lin, T. –L. *J. Polymer Sci. Part B: Polymer Physics*, **2005,** *43*, 3044.

4

Biocomposites of Nafion

Composites of Nafion with a class of biomolecules viz., plant hormones are explored as potential polymer electrolytes for improving the performance of H_2/O_2 Fuel Cells. Specifically, four nitrogenous plant hormones, two each from the class of auxins and cytokinins have been investigated, following preliminary characterization of the composite dispersions and membranes. Interestingly, indole-3-acetic acid (an auxin) in the catalyst layer, reveals a 30 % enhancement in Pt catalyst utilization and improves fuel cell performance by 150 mW/cm^2. The effect of these biomolecules on the kinetic and mass transport parameters has been analyzed systematically using a combination of electrochemical and spectroscopic techniques.

* A part of the work discussed in this chapter has been communicated.

4.1. Introduction

Polymer electrolyte fuel cells (PEFCs) are one of the major options for achieving sustainable energy conversion for portable, stationary and automobile applications [1]. Critical challenges in making medium temperature PEFCs affordable include the replacement of expensive catalyst materials with cheaper ones, overcoming the poor kinetics of oxygen reduction reaction (ORR), eliminating CO poisoning of the Pt catalyst and improving the life of the components which normally degrade after several thousand cycles of operation. The cost factor arises mainly due to the use of Pt as catalyst, which has been addressed by various research groups by reducing the amount of Pt using bimetallic catalysts instead of pure Pt [2] and by improving the utilization of Pt in the catalyst layer. An interesting breakthrough in this area is the recent demonstration of the catalytic efficiency of a conducting polymer, poly(3,4-ethylenedioxythiophene) (PEDOT) [3] to replace Pt altogether in the catalyst layer. However, the current densities obtained with PEDOT electrodes are very low (~ 6mA/cm^2) suitable only for microfuel cells and its performance is significantly lower than that of Pt at acidic pH (pH=1) of relevance to fuel cells involving proton exchange membranes. Another major breakthrough in this area is the reduction in Pt loading by depositing a monolayer of Pt on non-nobel metal cores [4]. On the other hand, improving catalyst utilization requires careful engineering of the complicated microstructure of the carbon support which consists of micropores that trap the catalyst particles leading eventually to poor interfacing with the polymer electrolyte membrane [5]. For instance, graded-porosity electrodes have been introduced recently for improving water management and gas diffusion in PEFCs [6]. Some of the most important factors related to the catalyst layer include, dissolution and diffusion of protons, H_2 and O_2 through the polymer electrolyte layer encapsulating the catalyst agglomerates, electronic conduction through the carbon support, partial pressure of O_2, ionomer loading and Pt loading. Most of these parameters have been optimized especially in the case of Nafion based PEFCs operating at medium temperatures (60 to 80 ^oC), by

improving the engineering aspects of MEA fabrication [7]. Hence a further improvement in the ORR kinetics and the fuel cell performance requires a rationale different from the existing approaches.

Increased attention is being given nowadays to bio-inspired strategies, exploiting the similarities in the functional aspects of biological systems with some of the fuel cell components [8]. For instance, a number of metalloenzymes catalyzing the oxygen reduction reaction (ORR), which is the most common pathway for O_2 metabolism in aerobic organisms [9], have been successfully investigated as cathode catalysts in H_2/O_2 PEFCs. However, their performance is suitable only for small power requirements like that of pacemakers. As an alternative approach, addition of metalloenzymes or their active sites to the state-of-the-art fuel cell cathodes is emerging rapidly. For example, alternate assemblies of metallo-porphyrins with platinum nanoparticles have been identified as tunable electrocatalysts for ORR [10]. On the other hand, Cobalt phthalocyanin is found to increase the solubility of O_2 in the ionomer layer encapsulating the Pt particles in the cathode [11]. Similarly, the effect of adsorbing Uracil, a nitrogenous base found in ribonucleic acids, on the ORR activity of Pt electrodes has been investigated [12]. However, almost all of the bio-inspired strategies discussed above, despite their fundamental interest, result in performance lower than that of the conventional PEFCs. Nevertheless, the scenario of bio-inspired electrodes could be improved by choosing a different class of molecules other than the porphyrins, nucleobases and metalloenzymes, which take part in physiological pathways more relevant to H_2/O_2 fuel cells.

In this context, plant hormones constitute one of the least explored classes of biomolecules for fuel cell applications probably due to the diversity in their molecular structures and comparatively less understood biochemical pathways unlike those in animal systems. Hormones, in general, are growth substances produced in one region of a multicellular organism, which upon transfer in very small quantities to other parts induce

developmental processes in plants and animals [7]. The definition is in fact, less succinct for plant hormones, because specific physiological effects are not often associated uniquely with a specific class of hormones. Thus, based on a combination of physiological functions and molecular structure, plant hormones are broadly classified as auxins, cytokinins and gibberellins. However, the whole class of hormones does not come under a specific chemical family and there are many sub-classes based on the differences in molecular structures. As the objective of the present work is to improve the proton conductivity of Nafion for fuel cell applications, only those hormones which are involved in proton transport related processes in biological systems will be considered (figure 4.1).

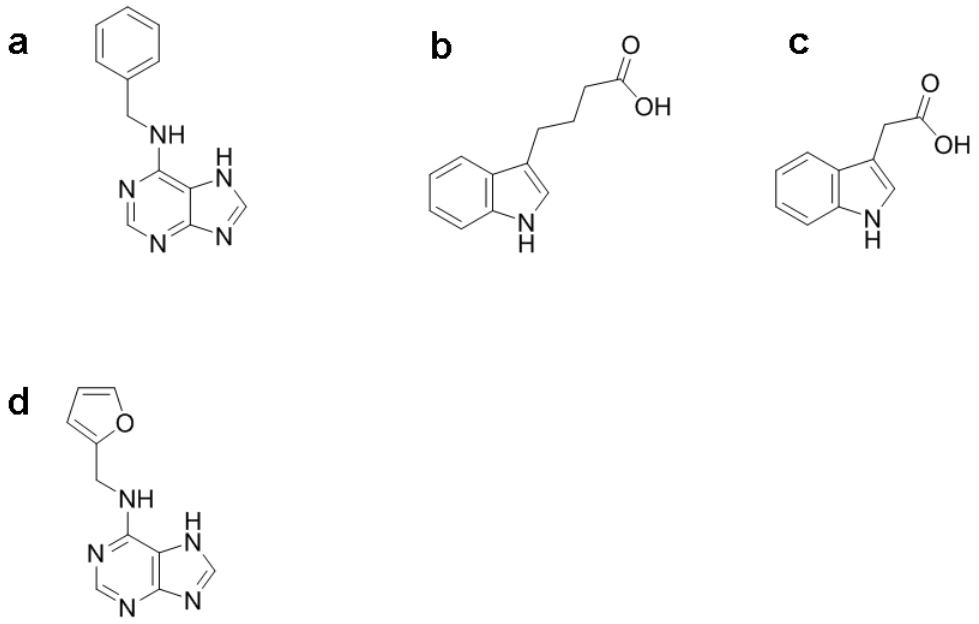

Figure 4.1. Molecular structures of plant hormones used in the present study a) 6-Benzylamino purine (BAP); b) Indole-3-butyric acid (IBA); c) Indole-3-acetic acid (IAA); d) Kinetin among which (a) and (d) are cytokinins whereas (b) and (c) are cytokinins.

In this context, special mention is to be made of the auxin, Indole-3-acetic acid (IAA), a powerful plant hormone capable of stimulating a number of functions at *in vivo* concentrations as low as 10^{-8} M [13]. There is an astonishing correspondence of its

physiological activity with the critical functional aspects of the catalyst layer [8a]. More specifically, IAA is known to trigger proton pumps across plasma membranes resulting in the acidification of protoplasts to effect cell elongation [14]; reduce molecular oxygen to superoxide radical ion and disintegrate hydrogen peroxide (H_2O_2) to hydroxyl radical to create oxidative stress [15] and impart better permeability of ions through the cell membranes [16]. It should be noted that the disintegration of H_2O_2 -intermediate is the rate-determining factor in the two-step O_2 reduction mechanism at fuel cell cathodes. Nevertheless, the indole-derivative, IAA, is quite different in its reactivity compared to *N*-heterocycles such as imidazole, pyrazole and benzimidazole, deployed frequently as electrolytes in PEMs due to the presence of both proton-donor as well as acceptor nitrogen atoms [16].

The past two chapters (Chapter 2 and 3) have been dealing with the mutual interaction between ions and polymer chains in a polymer electrolyte. The present chapter is focused on *How to improve the transport properties of polymer electrolytes using biomolecules?* Thus it is aimed at improving the proton conductivity and the net performance of Nafion-based fuel cells in continuation with the investigation on improving the oxidative stability of Nafion by complexation with an oppositely charged polymer electrolyte discussed in the previous chapter. More specifically, the scheme involves the characterization of Nafion dispersions and films containing the hormones viz., Indole-3-acetic acid, Indole-3-butyric acid, 6-benzylamino purine and kinetin using spectroscopic and electrochemical techniques to understand the interfacial interactions between Nafion and the biomolecules. Following the preliminary studies, membrane-electrode assemblies with hormones in the catalyst layer are investigated using the electrochemical impedance technique and the performance of the corresponding H_2/O_2 PEFCs is tested. Thus the present investigation validates the interesting option of using plant hormones for boosting the performance of PEFCs. Moreover, this investigation may pave way to the deployment of more natural products or even plant extracts directly to improve the performance of PEFCs.

4.2. Experimental Section

Nafion (5 wt% dispersion in lower aliphatic alcohols), Indole-3-acetic acid, Indole-3-butyric acid, 6-Benzylamino purine and Kinetin were procured from Sigma-Aldrich chemicals Ltd. Vulcan XC-72 and 20 wt% Pt/C were procured from Arora Matthey Ltd. De-ionized water from Millipore (18 MΩ.cm) was used for external humidification of the MEAs and for preparing electrolyte solutions. The Nafion/hormone composite dispersions were prepared by dissolving appropriate amount of the hormones in the commercial Nafion dispersion. The membranes were cast from the solution at a temperature of 60 ^{o}C in an air-oven. UV-visible spectra were recorded at room temperature (25 ^{o}C) using a Varian Cary50 model dual beam spectrophotometer. Diffuse reflectance FTIR spectra were recorded using a Perkin-Elmer Spectrum One spectrophotometer operating at a resolution of 4 cm^{-1}. Solid-state cyclic voltammetry of the composite membranes was conducted using the setup described in the experimental section of chapter 2 with a Solartron SI 1287 electrochemical interface operated through Corrware software; pH measurements were carried out using a glass electrode purchased from Eutech instruments.

The fuel cell tested was a single cell with a geometric area of 5 cm^2 with Nafion 115 as the polymer electrolyte membrane. The gas diffusion layer (GDL) was prepared by brushing a slurry of Vulcan XC-72, PTFE, water and cyclohexane until a carbon loading of 4 mg/cm^2 was achieved. The GDL was heat treated at 350 ^{o}C for 30 minutes. Then the catalyst ink was prepared by mixing 20 wt % Pt/C, Nafion, water and isopropyl alcohol in a homogenizer for 2 min at intervals of 20 seconds. The catalyst ink was then applied on the GDL by brushing so that Pt and Nafion loading were 0.5 and 0.6 mg/cm^2 respectively for both of the electrodes. After applying a thin layer of Nafion over the

catalyst layer for achieving optimum Pt catalyst utilization and mass transport of reactants to the catalyst layer [17], the membrane-electrode assembly (MEA) was obtained by pressing the two electrodes uniaxially with the Nafion 115 membrane in between at 110 ^{o}C at a pressure of 1 ton for 4 min. Hormone-modified MEAs were fabricated by introducing different amounts of Indole-3-acetic acid (IAA) in the catalyst layer by dissolving it in the catalyst ink. Proportions (by weight) of IAA with respect to the weight of Pt in the catalyst layer include W_{Pt}:W_{IAA} – 1:0, 3:1, 2:1, 1:1, 2:3, 1:2. The MEAs were used to form single fuel cells by passing humidified H_2 on one electrode and humidified O_2 on the other at 0.2 slpm through serpentine flow fields designed by Electrochem Inc., The fuel cells were conditioned at 0.2 V for 30 min and polarization measurements were carried out using an Arbin fuel cell test station (Model: Arbin-001 MITS Pro-FCTS 5.0-FCTS) at 60 ^{o}C. The single cells were further analyzed using electrochemical impedance with a 10 mV rms signal in the frequency range 100 mHz-100 kHz and solid state cyclic voltammetry by passing H_2 in the anode and N_2 in the cathode.

ORR activity of the catalyst was analyzed independently in 0.5 M H_2SO_4 by coating a 7 μl of the catalyst dispersion (in ethanol:water 2:4 v/v) on a 1.5 mm diameter Glassy carbon electrode (purchased form Microdevices Ltd.,) using cyclic voltammetry. The electroactive Pt area was determined by integrating the area under the hydrogen adsorption peaks based on the assumption of a charge of 210 μC/cm^2 on polycrystalline Pt. Based on the electroactive Pt area and the geometric area of Pt on the carbon support obtained from manufacturer's specifications, the catalyst utilization factor was calculated. In the same electrochemical cell, rotating disk electrode experiments were constructed using an Autolab controller coupled to the Autolab PGSTAT30 bipotentiostat.

4.3. Results and Discussion

4.3.1. Nafion/Hormone Composite Membranes

5 wt% Nafion dispersions containing dissolved hormones analyzed using UV-visible spectroscopy reveal that there is no specific chemical interaction between Nafion and the hormone molecule. Specifically, the UV-visible spectra of the pristine hormone solutions (in ethanol) are similar to those in the presence of Nafion which have also been checked once in every 24 h for a period of 1 week at various hormone concentrations (2.5, 0.5, 0.1 mg/ml). However, the pH of Nafion dispersion is found to increase after the addition of each of the hormones, probably due to acidification of the hormone molecules by Nafion (Table 4.1).

Table 4.1. Effect of adding plant hormones at a concentration of 2.5 mg/ml on the pH of a 5 wt % commercial dispersion of Nafion in water and lower aliphatic alcohols

Sample	**pH**
Pristine Nafion	2
IAA/Nafion	4.2
IBA/Nafion	4
BAP/Nafion	5
Kinetin/Nafion	5

Subsequent analysis of the composite membranes cast from the respective dispersions using FTIR spectroscopy indicates that the spectra are almost similar to that of the pristine Nafion membrane in the case of IBA, BAP and kinetin-modified membranes (Figure 4.2). However, the FTIR spectrum of the Nafion/IAA composite membrane

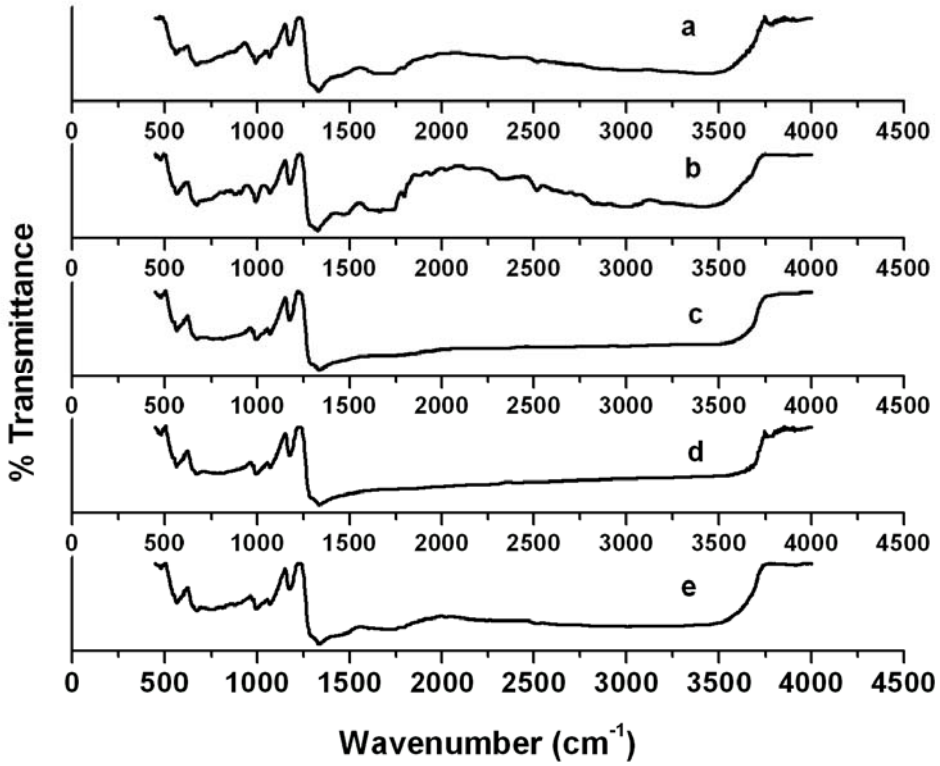

Figure 4.2. Diffuse reflectance infrared spectra of a) Nafion/Kinetin; b) Nafion/BAP; c) Nafion/IBA; d) Nafion/IAA with a hormone loading of 2.5 mg/ml e) Pristine Nafion membranes

indicates many subtle changes in the characteristic frequencies of the sulfonic acid groups (1067 and 1332 cm^{-1}) [18] present in the pendant chains of Nafion with a red shift of 7 cm^{-1} and 3 cm^{-1} for the symmetric and asymmetric stretching vibrations respectively. In addition, the C-C_{str} frequency is found to be lower than that of pristine Nafion by 17 cm^{-1}, indicating a weakening of the C-C bonds, which could also be one of the probable reasons for the poor mechanical stability observed in the case of the composite membranes compared to that of pristine Nafion membrane. Thus it is evident from the FTIR spectra that the hormones do not disrupt the chemical structure of Nafion. This is also supported by the results of thermal analysis, in which there is no significant effect of hormone incorporation on the thermal stability of Nafion membrane.

Further, the electrochemical stability of the composite membranes is understood from solid state cyclic voltammetry performed using the home-made all-solid-state electrochemical cell described in Chapter 2. Accordingly, Figure 4.3 shows the solid state cyclic voltammograms of the composite membranes, with all of them exhibiting a considerably wide electrochemical potential window except for the Nafion/kinetin membrane, which shows a small anodic wave at about – 0.5 V vs. Ag/AgCl probably due to the oxidation of kinetin [19]. This could also be compared to the observation that the Nafion/kinetin composite membrane, which is originally colorless, turns black when aged for 2 days.

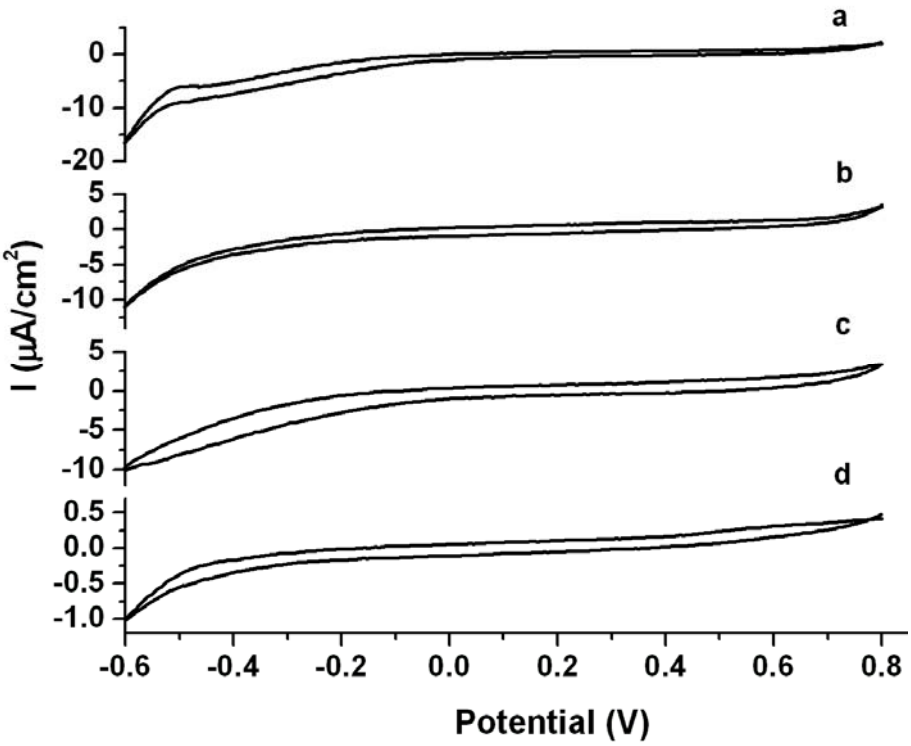

Figure 4.3. Solid-state cyclic voltammograms of a) Nafion/Kinetin; b) Nafion/IBA; c) Nafion/BAP; d) Nafion/IAA membranes with a hormone loading of 2.5 mg/ml. Working electrode: Pt disk; counter electrode: Pt wire; reference electrode: AgCl coated Ag wire.

Following the preliminary characterization of the Nafion/hormone interfaces, the next objective is to verify whether the hormone molecules have any impact on the transport properties of Nafion. Accordingly, the composite membranes in the dry state are investigated using the electrochemical impedance technique (Figure 4.4). The inset in the

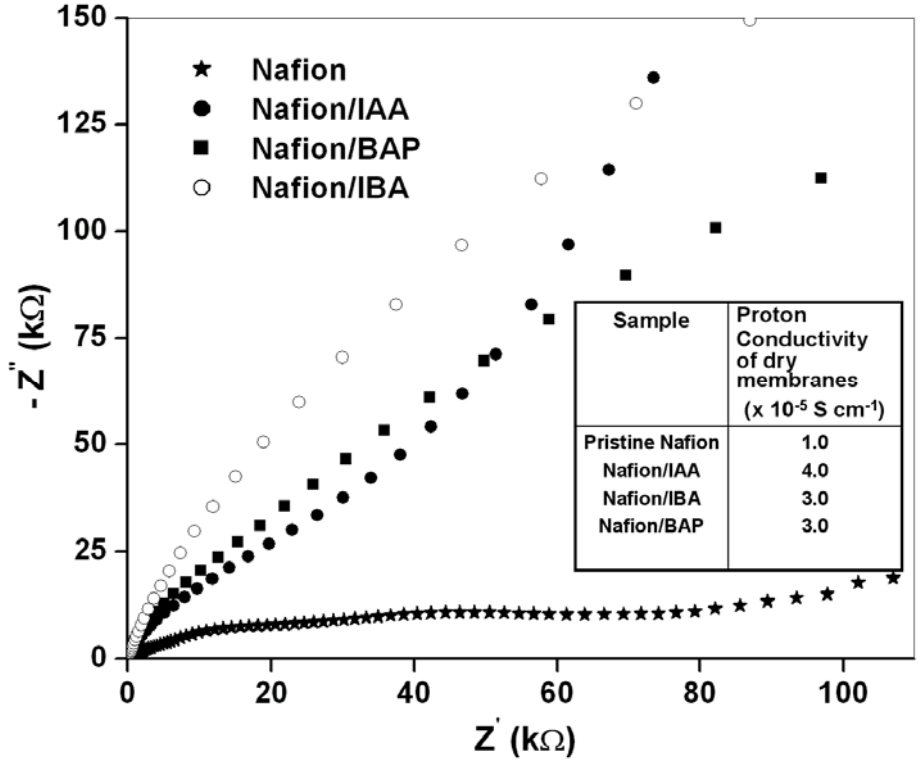

Figure 4.4. Electrochemical impedance-Nyquist (Z(Im) versus Z(Re)) plots of the composite membranes using a 10 mV rms ac signal in the frequency range of 10 mHz to 1 MHz at 25 ^{o}C at 50 % relative humidity. Inset shows the proton conductivity values of the composite membranes.

figure shows the proton conductivity values of the membranes in the dry state calculated from the intercept of the impedance plot on the real axis in the high frequency region. The proton conductivity of Nafion membrane cast from a 5 wt% commercial dispersion is found to be 10^{-5} S/cm at 25 ^{o}C. Although commercial Nafion membranes exhibit proton conductivity of about 0.1 S/cm (*cf.* Table 1.1), those cast from solutions and recast from solutions of dissolved membranes are known to have proton conductivity about 4 orders of magnitude lower than that of the former [20]. The inferior proton conductivity,

thermal and chemical stability of the recast membranes has been ascribed to the partial decrease on crystallinity of the membranes due to self-aggregation of polymer chains in Nafion solutions [21]. Thus the proton conductivity values obtained here are in accordance with the literature reports. Interestingly, about a 2 to 4 fold increase in proton conductivity is observed after modifying the membranes with different hormones. The enhancement in conductivity could be due to the hormone molecules acting as proton acceptors.

Thus the above preliminary investigations reveal that the hormones can serve as proton conducting conduits in the Nafion matrix without significant impact on the chemical structure and thermal stability of the polymer electrolyte membrane, indicating their possible application in PEFCs. However, the poor mechanical stability of the resulting membrane precludes the deployment of the composite membranes directly as electrolytes in fuel cells. Hence, as an alternative approach, we proceed further by employing the Nafion/hormone composite dispersions as a binder in the catalyst layer of the fuel cells.

4.3.2. Hormone-modified Catalyst layers for H_2/O_2 Fuel cells

4.3.2.1. Fuel Cell Polarization

Figure 4.5 shows the superimposed steady state polarization plots of H_2/O_2 fuel cells (at 60 ^oC) containing Nafion115 membrane as the polymer electrolyte with different hormones in the catalyst layer. While the maximum performance reported for the system built with state-of-the-art technology is 600 mW/cm^2, the performance obtained with the fuel cell design and testing procedures employed in the present study is 250 mW/cm^2 , which is used as the benchmark for this study and will be denoted as the 'Reference system'. An interesting enhancement in the fuel cell performance (by 100 mW/cm^2) is

observed for the MEA containing IAA in the catalyst layer compared to the reference system. On the other hand, the rest of the hormones exhibit only poor performance

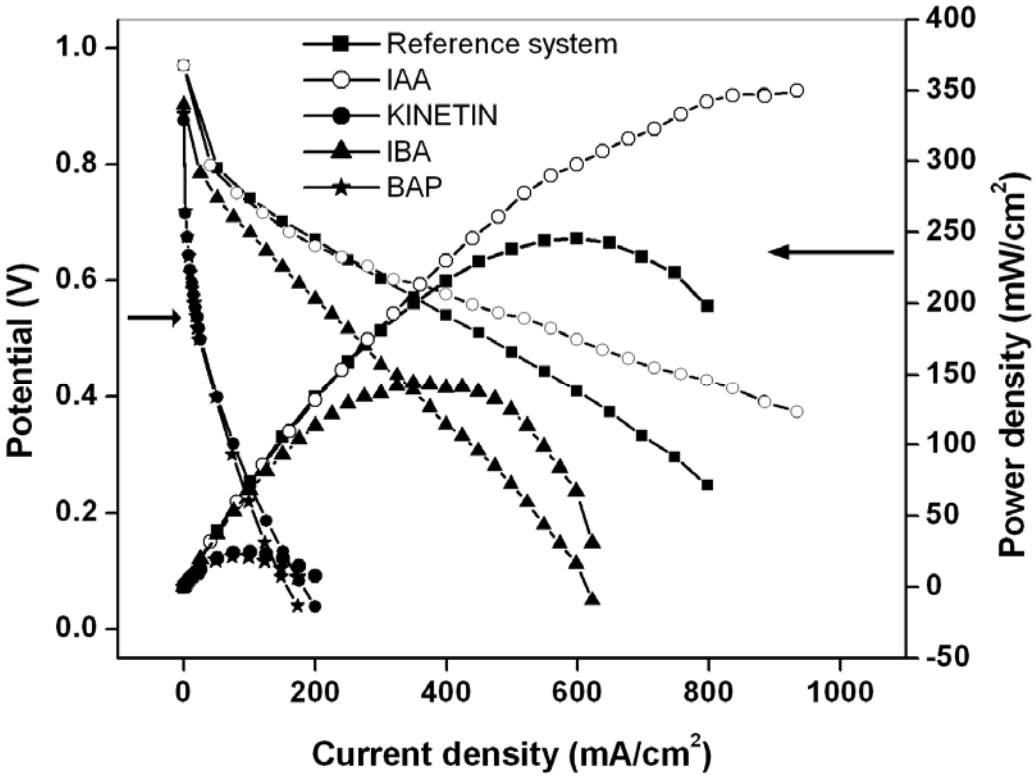

Figure 4.5. Single cell polarization plots of MEAs with and without different hormones in the catalyst layer measured at 60^{o}C using Nafion 115 as the polymer electrolyte membrane. Humidified H_2 and O_2 gases were passed at a rate of 0.2 slpm and the cells were conditioned at 0.2 V for 30 minutes before recording the polarization plots. An excellent increase in power density in the case of IAA-containing cell can be seen (350 mW/cm^2) compared to the reference system (245 mW/cm^2).

compared to the reference system with the cytokinins (BAP and Kinetin) showing very poor performance compared to that with the auxin, IBA. While the pH of the composite dispersions and the electrochemical stability window of the corresponding membranes are almost similar, only IAA is capable of enhancing the performance of the PEFC. Although specific reasons for this discrimination could not be identified which may require *in situ* spectroscopic examination of the fuel cell under operation, a probable

reason could be the difference in chemical stability of the hormones in the presence of the reactive intermediates produced during the fuel cell reactions.

Having identified IAA as the potential candidate to improve fuel cell performance, the rest of the study is focused on exploring its effect on the various performance parameters. Accordingly, Figure 4.6 shows superimposed steady state polarization plots of H_2/O_2 fuel cells (at 60 ^oC) containing Nafion115 membrane as the polymer electrolyte with different concentrations of IAA in the catalyst layer. The amount of IAA is expressed as its ratio by weight to the amount of Pt loaded in the catalyst layer. Thus the catalyst composition of the MEAs represented in the present figure involves Pt:IAA ratios, 1:0, 3:1, 1:1 and 2:3.

It is obvious from the figure that the 1:1 MEA shows an excellent enhancement in performance compared to that of the 1:0 MEA, by 150 mW/cm^2 as verified by three replicate measurements with 20-25 cycles of operation in each measurement. The fuel cell performance (i.e., power density and current density) is found to increase with increasing proportions of IAA in the catalyst layer, attain a maximum at 1:1 ratio and fall back below the performance of the 1:0 cell by 15 mW/cm^2 in the case of 2:3 Pt:IAA composition. In addition, the extension of the ohmic polarization region to offer higher current densities in IAA-modified cells signifies faster mass transport of species (viz., H^+, O_2, H_2) to the Pt catalyst, which is interestingly in accordance with the well-known ability of IAA to trigger the transport of ions across cell membrane [14]. On the other hand, there is not much change in the open circuit potentials indicating that the incorporation of IAA does not alter the redox equilibrium of the cell.

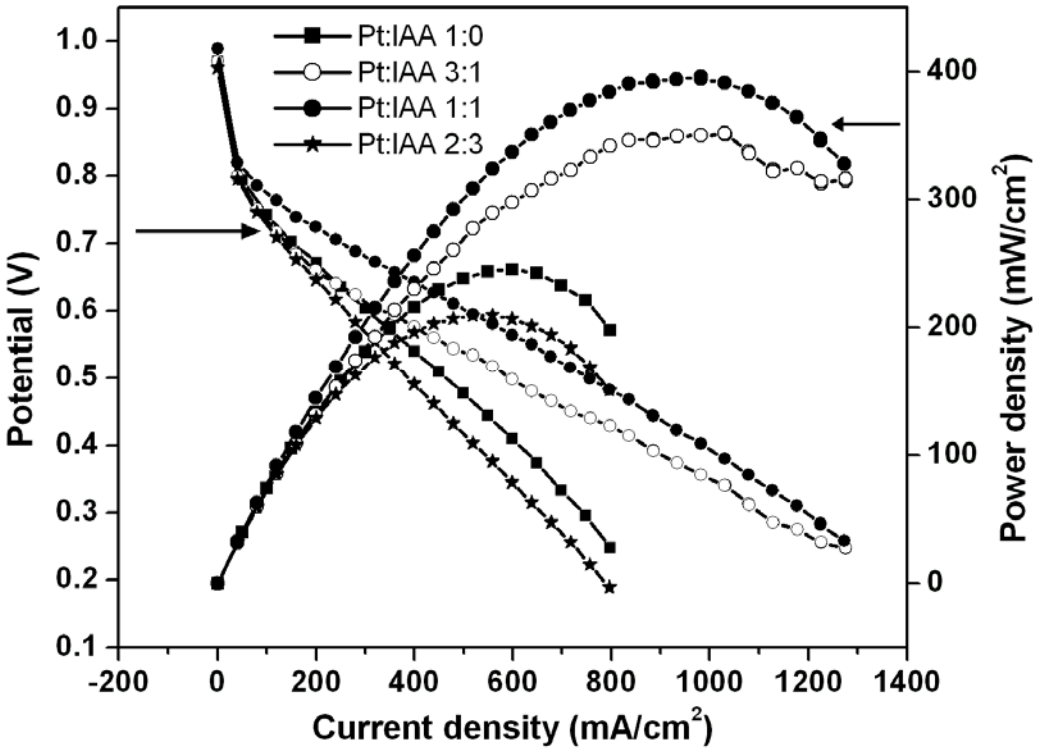

Figure 4.6. Single cell polarization plots of MEAs with varying amounts of IAA in the catalyst layer measured at 60 ^{o}C using Nafion 115 as the polymer electrolyte membrane. Humidified H2 and O2 gases were passed at a rate of 0.2 slpm and the cells were conditioned at 0.2 V for 30 minutes before recording the polarization plots. An excellent increase in power density in the case of 1:1 cell can be seen (395 mW/cm2) compared to the reference cell (245 mW/cm2).

4.3.2.2. Electrochemical Impedance of MEAs

Subsequently, to discriminate the influence of IAA on the mass transport and charge transport parameters, the MEAs are further examined by the electrochemical impedance technique in the frequency range, 100 mHz to 100 kHz by simultaneously passing humidified H_2 and O_2 gases in the anode and the cathode compartments respectively at 60 ^{o}C (Figure 4.7a). As previous reports have clearly demonstrated that the cell impedance under similar conditions is essentially influenced by ORR [22], the impedance measurements in this work involve two-electrode systems with the anode serving as both auxiliary and reference electrode while the cathode serves as the working electrode. The intercept at the real axis in the high frequency part of the Nyquist (-Z(Im)

Vs Z(Re)) plots shows that the overall cell resistance decreases with increasing IAA content from an R_s value of 84 mΩ/cm^2 for MEA without IAA to 55 mΩ/cm^2 for 1:1 MEA after which it starts decreasing with further increase in IAA concentration (inset top left-figure 4.7a). While the Nyquist plots at open circuit potential do not exhibit any semicircular behavior corresponding to charge transfer control, those at overpotentials ($\eta = E_{applied}-E_{equilibrium}$) higher than 60 mV indicate a semicircular behavior at lower frequencies. The overall impedance behavior at η = 180 mV shown in Figure 4.7a, signifies a charge transfer process with a single time constant similar to that reported for similar systems controlled predominantly by ORR at low overpotentials (η < 200 mV $=E_{applied}-E_{equilibrium}$) [22].

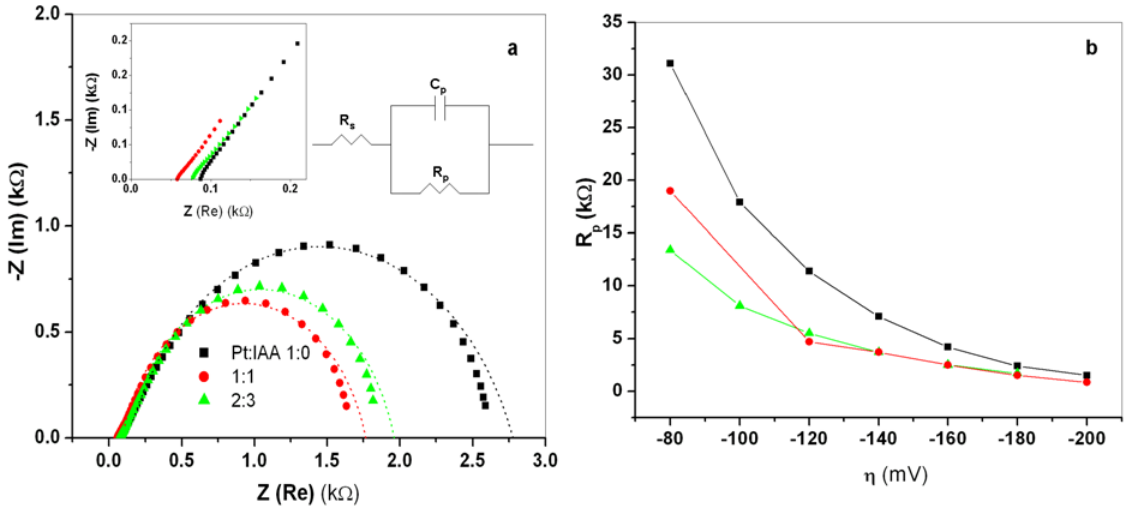

Figure 4.7. a) Electrochemical impedance Nyquist (-Z(Im) versus Z(Re)) plots for MEAs with and without IAA in the catalyst layer at a polarization of 180 mV, obtained by passing humidified H_2 and O_2 gases at the anode and the cathode compartment respectively at 25 ^oC. The symbols (—●—,—■—,—▶—) represent experimental data and dotted lines correspond to the fitted curve using an equivalent circuit consisting of a single resistor in series with a parallel RC component. **Inset top right:** Electrical equivalent circuit used for fitting the impedance data. **Inset top left:** Comparison of overall cell resistance by examining the low frequency part of the impedance plots at open circuit potential; **b)** Variation of $R_{parallel}$ (R_p) with polarization with IAA content in the catalyst layer which is indicative of the variation of the charge transfer resistance and hence the ORR kinetics due to the incorporation of IAA in the catalyst layer

This indeed corresponds to the activation polarization region in steady-state polarization plots. When the semicircular region is fitted using the complex non-linear least squares (CNLS) method, with a simple equivalent circuit shown in the inset of Figure 4.7a, an interesting decrease in the parallel resistance (R_p) with increasing IAA content is observed. The same trend in R_p is found at a range of overpotentials ranging from 80 mV to 200 mV (Figure 4.7b).

4.3.2.3. Cyclic Voltammetry of Catalyst Layers

Following the studies on the effect of incorporating IAA on the overall performance and electrochemical impedance behavior of the fuel cell, we proceed now to explore its influence on ORR kinetics. The catalyst slurries with various ratios of Pt:IAA (1:0, 3:1, 2:1, 1:1, 2:3, 1:2) have been examined using cyclic voltammetry at a glassy carbon electrode in 0.5 M H_2SO_4. Accordingly, Figure 4.8 shows representative cyclic voltammograms (CVs) of a 1:0 catalyst slurry (without IAA) and 1:1 slurry superimposed on the CV of IAA. The absence of significant redox peaks in the case of IAA (designated as 0:1 in Figure 4.8) and the stability of the response with subsequent potential scans indicate that the hormone is considerably stable under the experimental conditions.

This could be verified with reference to earlier detailed reports on the stability of IAA in aqueous systems [13]. Significant enhancement (by a factor of 2) in the areas under the O_2 reduction and H_2 adsorption peaks for the same amount of Pt on the electrode is evident in the case of 1:1 catalyst layer compared to that without IAA (1:0) (Figure 4.8). This observation is in sharp contrast to that reported in the literature [23], in which the area under the H_2 adsorption/desorption and O_2 reduction peaks on a Pt electrode decreases, corresponding to a decrease in the electroactive Pt area by 15 to 20%, after coating it with a thin film of Nafion (3 μm thick) as the latter hinders the

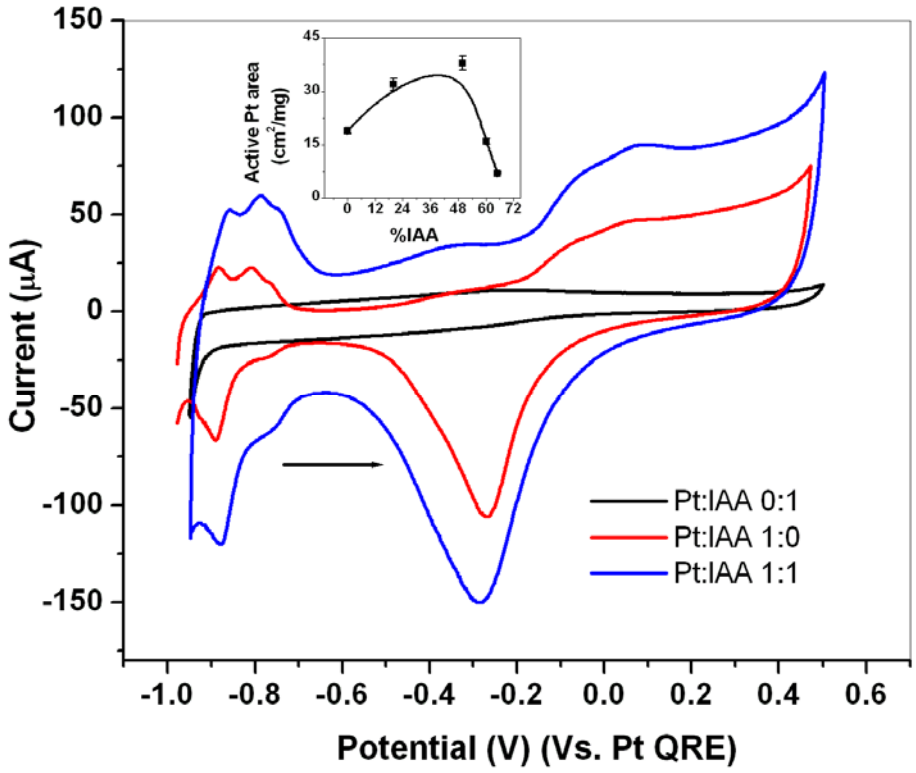

Figure 4.8. Cyclic voltammograms of catalyst slurries coated on a 1.5 mm diameter glassy carbon working electrode in N_2 saturated 0.5 M H_2SO_4 at a scan rate of 50 mV/s. A Pt wire was used as the quasi reference electrode and a Pt foil was used as the auxiliary electrode. While IAA alone does not show any redox peaks, its presence in the catalyst slurry leads to a remarkable enhancement in the areas under the O_2 reduction and the H_2 adsorption/desorption peaks. **Inset:** The electroactive Pt area calculated from the area under the H_2 adsorption peak assuming 210 μC charge per cm^2 of a polycrystalline Pt surface, passes through a maximum value at a W_{Pt}:W_{IAA} ratio of 1:1.

transport of reactant species to the catalyst surface. Nevertheless, the scenario is entirely different in a solid PEFC, wherein the Nafion layer on the catalyst particles is essential to ensure better interfacing with the solid polymer electrolyte membrane [23]. Conversely, thus, the enormous enhancement in peak area in the present case clearly reveals that IAA remarkably facilitates the mass transport of species to the catalyst surface, in addition to possibly minimizing peroxide-induced degradation of Nafion [15]. Accordingly, a calculation based on the area under H_2 adsorption peaks on a polycrystalline Pt surface indicates that the electroactive Pt area is doubled after the addition of IAA to the catalyst

layer (peak area$_{Pt:IAA\ 1:0}$ = 19 m^2/g; peak area$_{Pt:IAA\ 1:1}$ = 38 m^2/g). Most importantly, this enhancement in electroactive Pt area amounts to an increase in catalyst utilization from 30% to 60% calculated with respect to the geometrical surface area of Pt. Interestingly, this implies that the Pt loading in fuel cells can be reduced by 30% by the mere addition of a few milligrams of the plant hormone in the catalyst layer. Moreover, the effect of increasing IAA concentration in the catalyst layer (inset-figure 4.8) follows a trend similar to that observed in the polarization and impedance behavior of the corresponding MEAs. The reason for the peak-shaped variation of all these parameters with increasing IAA concentration could be the blocking of pores in the carbon support hindering the mass transport. In addition, the increase in double layer capacitance (calculated from the non-Faradaic part of the CVs) by 50 F/g in the 1:1 slurry compared to that without IAA indicates that there may not be a significant adsorption of IAA on the catalyst surface.

The enhancement in catalyst utilization after adding IAA to the catalyst layer can be explained based on improved mass transport to the catalyst surface as follows. The carbon support used in the catalyst layer has a complicated microstructure with pores of two different sizes namely the 'macro' pores (diameter > 0.1 μm) formed between a group of agglomerates of catalyst particles and the 'micro' pores (diameter < 0.1 μm) representing the spaces between the particles constituting each agglomerate [5b]. Uninterrupted network of protons between the catalyst particles and the polymer electrolyte membrane (PEM) is a crucial factor, discrepancy in which is known to result in a marked polarization limiting cell performance [12]. Continuous proton transport between the catalyst layers and the PEM is ensured usually by using a solution of the ionomer as binder in the catalyst layers. The high molecular weight of the ionomer (~6000 to 7000 $gmol^{-1}$), however, precludes it from entering the 'micro' pores to access catalyst particles struck up in them. For example, Kim *et al* have demonstrated significant changes in the pore structure of the catalyst layer, upon manipulating the aggregate size of polymer electrolyte, poly(benzimidazole) in different solvents [24]. Nevertheless, this problem could be effectively overcome if a low-molecular weight proton conductor (~

100-300 g/mol) is used along with the ionomer dispersions as binders in the catalyst layer, as depicted in Figure 4.9.

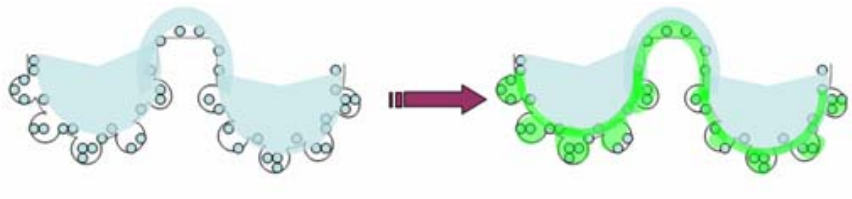

Figure 4.9. The effect of incorporating a low molecular weight proton conductor on the catalyst utilization. The two big bowl-shaped features represent the macropores in the catalyst layer and the smaller dips in each bowl represent the micropores in the carbon support; the blue filling indicates the polymer electrolyte solution used as binder and the green component is the plant hormone. When Pt catalyst particles (shown here as small blue circles) are struck up in the micropores, they become inaccessible to the high molecular weight ionomer filling, which is the reason for inefficient catalyst utilization. This is overcome by introducing hormones as low molecular weight proton conductors into the micropores.

4.3.2.4. Rotating Disk Voltammetry of Catalyst Layers

Having identified the beneficial role of IAA due to several factors like Pt catalyst utilization, electroactive Pt area, enhanced mass transport of the reactant gases and thermodynamic efficiency of the cell the next step is to investigate its specific effect on ORR kinetics. The objective now is to clarify whether the improvement in fuel cell performance by IAA is only due to improved mass transport features in the catalyst layers or it affects the kinetics of charge transport at the electrode/electrolyte interfaces as hinted earlier by the electrochemical impedance investigations. Accordingly, the catalyst/electrolyte interface has been studied using the rotating disk electrode (RDE) method, which offers one of the best means for kinetic investigations devoid of mass transport limitations. Linear sweep voltammograms (LSV) of the catalyst layers with (W_{Pt}:W_{IAA} 1:1) and without IAA in O_2 saturated 0.5 M H_2SO_4, superimposed with the LSV of IAA at an electrode rotation speed of 900 rpm are shown in Figure 4.10.

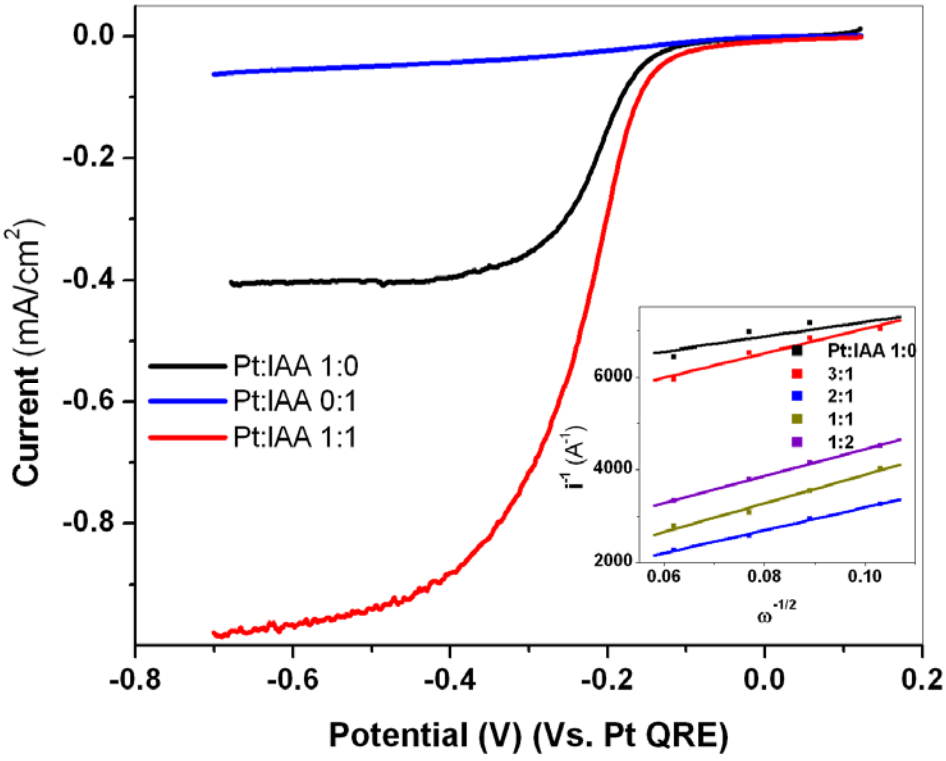

Figure 4.10. Steady state voltammograms of the catalyst slurries coated on a glassy carbon working electrode (1.5 mm diameter) in O_2 saturated 0.5 M H_2SO_4 at a scan rate of 10 mV/s obtained by rotating the electrode at a speed of 900 rpm. Excellent enhancement in the limiting current for ORR is observed after introducing IAA in the catalyst layer. **Inset:** Koutecky-Levich plots of limiting currents versus electrode rotation speeds for various amounts of IAA in the catalyst layer.

The absence of a significant redox response in the case of IAA probably indicates that the molecule itself does not catalyze oxygen reduction in the absence of Platinum. A remarkable enhancement in the limiting current for O_2 reduction is observed in the presence of IAA in the catalyst layer ($j_{L(1:0)} = 0.4$ mA/cm^2 ; $j_{L(1:1)} = 1$ mA/cm^2), clearly indicating the positive impact of IAA on ORR kinetics. It should be noted that previous RDE studies under similar conditions have clearly revealed that the polymer electrolyte film on Pt surface does not affect the kinetics or mechanism of ORR except for its effect on reducing the diffusion coefficient of O_2 by 2.5 times compared to that in 0.1 M H_2SO_4 [23,25]. Hence the remarkable enhancement in the limiting current density is clearly due

to the presence of IAA. This is further confirmed by varying its concentration in the catalyst layer, when the limiting current density increases with increasing IAA content upto 1:1 (Pt:IAA) after which it decreases.

The improvement in limiting current is augmented by a corresponding increase in kinetic current densities (j_k) with increasing IAA content, derived from the variation of limiting currents with rotation speeds (inset figure 4.10) using the Levich-Koutecky expression [26],

$$\frac{1}{j} = \frac{1}{j_k} + \left[\frac{1.613\nu^{1/6}}{nFC_{O_2} D_o^{2/3} \omega^{1/2}} \right] \qquad (4.1)$$

where, $j_k = nFkC_{O_2}$ in which, n = number of electrons transferred, F is the Faraday constant (96485 C/mol), k is the apparent rate constant (cm/s), C_{O_2} is the concentration of dissolved oxygen (1.26 x 10^{-6} mol/cm^3) [27,28], D_o is the diffusion coefficient of oxygen (1.93 x 10^{-5} cm^2/s), ω is the angular rotation speed of the electrode (radians/s) and ν is the kinematic viscosity of the electrolyte (1.009 x 10^{-2} cm^2/s) [28]. In addition, the apparent rate constants (k) for O_2 reduction calculated from the intercepts of j^{-1} versus $\omega^{-1/2}$ (Koutecky-Levich) plots using the values reported for the solubility of O_2 i.e., 1.22 x 10^{-6} mol/cm^3 [27] reveal an interesting four-fold enhancement in the case of 1:1 composition compared to that of 1:0. The rate constant values are comparable to the reported ones in similar systems [29,30]. Further calculation yields a value of 5.2 x 10^{-11} A/cm^2 for the exchange current density (j_o) for oxygen reduction in the absence of IAA compared to a value of 1.9 x 10^{-10} A/cm^2 the catalyst layer with W_{Pt}:W_{IAA} corresponding to 1:1 composition (Table 4.2). The j_o values are comparable to those reported for oxygen reduction in similar systems [31,32].

Table 4.2. Comparison of thermodynamic and kinetic parameters of MEAs and catalyst slurries with varying proportions of IAA with respect to Pt loading.

W_{Pt}:W_{IAA}	Open circuit potential$_{cell}$ (V)	Electro-active Pt area[a] (m^2/g)	Catalyst utilization [a] (%)	Apparent rate constant for ORR[b] (x10^{-4} cm/s)	R_s[c] (mΩ/cm^2 electrode geometric area)	J_o[b] (A/cm^2 Active Pt)
1:0	0.96	19	30	0.4	17	5.2 x 10^{-11}
3:1	0.92	32	50	0.3	15	3.4 x 10^{-11}
1:1	0.97	38	60	1.6	11	1.9 x 10^{-10}
2:3	0.97	16	25	3.2	15	3.9 x 10^{-10}

[a] Calculated from cyclic voltammetry of catalyst slurries in 0.5 M H_2SO_4

[b] Calculated from Koutecky-Levich plots derived from rotating disk electrode measurements of catalyst slurries in O_2-saturated 0.5 M H_2SO_4 at a potential of 0.17 V vs. Hg/Hg_2SO_4.

[c] Calculated from Electrochemical impedance measurements of the MEAs by passing humidified H_2 and O_2 gases in the anode and the cathode compartments respectively

The effect of IAA on ORR kinetics could be understood with respect to its functional similarities in biological systems. One of the major roles of IAA in plant tissues is the elongation of cell walls by triggering proton pumps across the plasma membrane [13]. The principal step in this process involves the binding of IAA to molecular O_2 in the presence of plant peroxidases followed by the reduction of O_2 to $O_2^{\bullet-}$, which further reacts with H_2O_2 (which is also a metabolite) to produce hydroxyl radicals [15]. Meanwhile IAA is oxidized to a cation radical. Also it is known that even in the absence of a suitable auxin-binding protein, IAA can reduce O_2 in the presence of H_2O_2 [15]. This could be the probable reason for IAA not showing any voltammetric peak for ORR in the absence of Pt as it requires H_2O_2 for showing its activity which will be

supplied by the electrocatalytic O_2 reduction at the Pt surface. Thus the plant hormone enhances ORR kinetics probably by facilitating the cleavage of the peroxide intermediate formed in the two-step mechanism of oxygen reduction on Pt.

Thus the present investigation demonstrates the promising role of auxins and cytokinins as additives in the catalyst layer to enhance the performance of PEFCs with reduced Pt loading. However, it should be noted that the mode of action of the hormones in the catalyst layer is not clearly understood from the above results, which may require *in situ* spectroscopic monitoring of the fuel cell electrodes. Also, the effect of hormones on peroxide-induced degradation of Nafion, Pt dissolution and redeposition, the poisoning of Pt surface by carbon monoxide when reformed hydrogen is used as the fuel and the durability of electrode materials need to be investigated more rigorously. Although the results of only a few hormones are shown here, there are many other biomolecules, especially indole derivatives like Tryptophan and Melatonin which are known to follow biological pathways of relevance to fuel cells [33,34].

4.4. Summary and Conclusions

In summary, the beneficial role of plant hormones viz., auxins and cytokinins in enhancing the performance of low temperature H_2/O_2 PEFCs has been demonstrated in terms of ORR kinetics, catalyst utilization and fuel cell performance parameters. More specifically, the auxin, IAA is found to provide a realistic enhancement in performance compared to that of the well-established systems employing Pt catalyst, while majority of the reports on bio-inspired approaches have shown only nominal improvements in performance, despite their novelty and scientific interest. Thus the results of this investigation are *en route* to improving fuel cell performance using natural products extracted from plants and other biological systems as vital ingredients to boost the performance of fuel cells. Though the present study is concerned with H_2/O_2 PEFCs, the strategy is expected to be valid for other reactants like methanol and ethanol and the

formulation may serve effective in polymer electrolyte-based systems other than fuel cells like biosensors. More significant will be the extension of these results for microbial and other types of bio-fuel cells.

4.5. References

1. Steele, B. C. H.; Heinze, A. *Nature* **2001**, *47*, 345.
2. (a) Stamenkovic, V. R.; Moon, B. S.; Mayrhofer, K. J. J.; Ross, P. N. Markovic, N. M. *J. Am. Chem. Soc.* **2006**, *128*, 8813. (b) Zhang, J.; Vakmirovik, M. B.; Xu, Y.; Mavrikakis, M.; Adzik, R. R. *Angew. Chem. Int. Ed.,* **2005**, *117*, 2170.
3. Jensen, B. –W.; Jensen, O. –W.; Forsyth, M.; MacFarlane, D. R. *Science* **2008**, *321*, 671.
4. Zhang, J.; Lima, F.; Shao, M.; Sasaki, K.; Wang, J.; Hanson, J.; Adzik, R. R. *J. Phys. Chem.* **2005**, *109*, 22701.
5. (a) Song, J. M.; Suzuki, S.; Uchida, H.; Watanabe, M. *Langmuir* **2006**, *22*, 6422. (b) Paulus, U. A.; Veziridis, Z.; Schnyder, B.; Khunke, M.; Scherer, G. G.; Wokaun, A. *J. Electroanal. Chem.* **2003**, *541*, 77.
6. Tang, H.; Wang, S.; Pan, M.; Yuan, R. *J. Power Sources* **2007**, *166*, 41.
7. Phillips, I. D. J. "Introduction to the biochemistry and physiology of plant growth hormones" Mc Graw Hill Book company, New York, 1971.
8. (a) Sun, W.; Peppley, B. A.; Karan, K. *Electrochim. Acta.* **2005**, *50*, 3359. (b) Yamada, M.; Honma, I. *Fuel Cells Bulletin* **2006**, *5,* 11.
9. Malmstrom, B. G. *Annu. Rev. Biochem.* **1981**, *51*, 21.
10. Huang, M.; Shao, Y.; Sun, X.; Chen, H.; Liu, B.; Dong, S. *Langmuir* **2005**, *21*, 323.
11. Shoji, M.; Oyaizu, K.;Nishide, H. *Polymer* **2008**, *49*, 5659.
12. Saffarian, H. M.; Srinivasan, R.; Chu, D.; Gilman, S. *J. Electroanal. Chem.* **2001**, *504*, 217.

13. Gazaryan, I. G.; Lagrimini, L. M.; Ashby, G. A.; Thorneley, R. N. F. *Biochem. J.* **1996**, *313*, 841.
14. Tamimoto, E. *Critical Rev. Plant Sci.* **2005**, *24*, 249.
15. Kawano, T. *Plant Cell Rep.* **2003**, *21*, 829.
16. Kreuer, K. D.; Fuchs, A.; Ise, M.; Spaeth, M.; Maier, J. *Electrochim. Acta* **1998**, *43*, 1281.
17. Ticianelli, T. A.; Derouin, C. R.; Srinivasan, S. *J. Electroanal. Chem.* **1988**, *251*, 275.
18. Gruger, A.; Regis, A.; Schmatko, T.; Colomban, P. *Vib. Spectrosc.* **2001**, *26*, 215.
19. Ballesteros, Y.; Gonzalez de La Huebra, M. J.; Hernandez, P.; Hernandez, L. *Microchem. J.* **2003**, *74*, 193.
20. (a) Wilson, M. S.; Gottesfeld, S. *J. Appl. Electrochem.* **1992**, *22*, 1. (b) Ren, X. M.; Wilson, M. S.; Gottesfeld, S. *J. Electrochem. Soc.,* **1996**, *143*, L12.
21. Jiang, S.; Xia, K. –Q.; Xu, G. *Macromolecules* **2001**, *34*, 7783.
22. Ciureanu, M.; Roberge, R. *J. Phys. C hem.* **2001**, *17*, 105.
23. Zecevic, S. K.; Wainright, J. S.; Litt, M. H.; Gojkovic, S. Lj.; Savinell, R. F. *J. Electrochem. Soc.* **1997**, *144*, 2973.
24. Kim, J. –H.; Kim, H. –J.; Lim, T. –H.; Lee, H. –I. *J. Ind. Eng. Chem.,* **2007**, *13*, 850.
25. Gottesfeld, S.; Rasitrick, I. D.; Srinivasan, S. *J. Electrochem. Soc.,* **1987**, *134*, 1455.
26. Bard, A. J.; Faulkner, L. R. *Electrochemical Methods: Fundamentals and Applications*, second edition, Wiley; New York 2004.
27. Itoe, R. N.; Wesson, G. D.; Kalu, E. E. *J. Electrochem. Soc.* **2000**, *147*, 2445.
28. Chen, W.; Kim, J.; Sun, S.; Chen, S. *J. Phys. Chem. C* **2008**, *112*, 3891.
29. Shaijumon, M. M.; Ramaprabhu, S. *Appl. Phys. Lett.* **2006**, *88*, 253105.
30. Prakash, J.; Tryk, D. A.; Yeager, E. B. *J. Electrochem. Soc.* **1999**, *146*,

4145.

31. Parthasarathy, A.; Srinivasan, S.; Appleby, J. *J. Electrochem. Soc.* **1992**, *139,* 2530.
32. Beattie, P. D. *et al J. Electroanal. Chem.* **1999**, *468*, 180.
33. Chung, L. W.; Li, X.; Sugimoto, H.; Shiro, Y.; Morukama, K. *J. Am. Chem. Soc.* **2008**, *130*, 12299.
34. Reiter, R. J.; Tan, D. –X.; Manchester, L. C.; Qi, W. *Cell Biochem. Biophys.* **2001**, *34*, 237.

5 Carbon nanotube Composite Electrolytes

The effect of incorporating carbon nanotubes on the microstructure and transport properties of polymer electrolytes is investigated in this chapter. Electrochemical and spectroscopic properties of Nafion/Multiwalled CNT composite membranes are presented. This is followed by studies on Polyacrylamide/CNT composites and their subsequent application as matrices in gel electrophoresis. Interestingly, single-walled and multi-walled CNT-modified polyacrylamide gels exhibit better separation efficiency of low molecular weight proteins (14-97 kDa) than the pristine polymer. These results are promising to enable new methodology for the selective separation of low molecular weight proteins and for determining the molecular weight of newly isolated proteins.

5.1 Introduction

Graphite is the thermodynamically stable allotrope of carbon. When graphite crystallites become very small (nanosize), the high density of dangling bonds (i.e., carbon atoms with unsaturated valencies) forces the individual graphene sheets to form closed structures like rings and shells. Fullerene (C_{60}) is the first closed allotrope of carbon to be discovered in the 1980s [1], after which, carbon nanotube (CNT) has been identified as its elongated form, built of pentagons and hexagons [2]. CNT can also be envisioned as a sheet of graphene folded into a cylinder such that the open edges match perfectly to form a seamless structure, which are closed with pentagons at a later stage of the growth process. The structural subtlety of the nanotubes is explained by their symmetry arising from the way the graphene sheets are rolled, described as the 'helicity' of the nanotubes. Thus they can be classified as chiral, armchair and zigzag nanotubes based on the symmetry of rolling. The superior and exotic properties of CNTs stem from a combination of their dimension, structure and topology. More specifically, the perfect alignment of the carbon lattice along the tube axis together with the closed topology endows the CNTs with high electrical and thermal conductivity, mechanical strength, stiffness, chemical specificity and inertness [3]. In addition, quantum confinement of electrons in the radial direction of the nanotubes results in exotic electronic conduction mechanisms.

CNTs have found tremendous application in a number of domains ranging from electronics to space technology. Especially, they are among the most investigated nanomaterials for the separation of DNAs and proteins [4], mainly due to the unique and selective adsorptive power of CNTs towards these biomolecules [5]. More significantly, the adsorptive power of CNTs has been deployed at different levels of proteomics. For example, CNT-peptide conjugates have been employed to selectively destroy the anthrax toxin [6]. On the other hand, CNTs have been used as the stationary phase for protein separation using capillary electrophoresis [7]. Tunable diameter, ease of functionalization

(by covalent, electrostatic and other interactions) to create desired biocompatible functional groups in a selective manner both at the tips as well as along the sidewalls are additional advantages of CNTs.

A gallery of hybrid materials with improved properties can be prepared by incorporating CNTs in a matrix of another material, thereby exploiting the advantages of synergistic interactions between the matrix and the nanotubes. In this context, CNT/polymer composites constitute one of the most widely studied hybrid materials, wherein the role of the nanotube can be either to reinforce the structural properties of the polymer matrix or to improve its functional behavior [8]. In many cases, the mechanical properties of the polymer matrix are found to improve dramatically after reinforcement with CNTs [9], even with an insignificant amount of the nanotubes, than the loading expected as per the percolation theory [10]. However, the incorporation of CNTs does not always 'improve' the mechanical properties of the polymer as the reverse situation has been observed in certain cases [2c]. Similarly, the nanotubes can also tune the function of a polymer electrolyte, especially when the former are functionalized appropriately. For example, single-walled carbon nanotubes functionalized with sulfonic acid groups on the surface can enhance the proton conductivity of Nafion membranes and the performance of H_2/O_2 fuel cells incorporating the composite electrolytes [11].

In view of their compliance with many polymers and specific interactions with biomolecules like DNA and proteins, CNTs can be combined with polymers used as matrices for the electrophoretic separation of proteins. Polyacrylamide (PAM) is one of the most widely studied polymers for protein separation in a technique commonly called Polyacrylamide Gel Electrophoresis (PAGE) [12]. It briefly involves the separation of proteins and peptides in a porous gel matrix, which offers a sieving action in the presence of an external electric field. Protein separation by PAGE is normally based on the differences in charge density, size and shape of the protein molecules, which is commonly referred to as Native-PAGE. However, the effect of charge density and shape

could be virtually eliminated by denaturing the proteins by a suitable surfactant viz., sodium dodecyl sulfate (SDS) so that the separation is exclusively based on their molecular weight (referred to as SDS-PAGE). In this technique, prior to electrophoresis, the protein mixture is treated with SDS, which coats all proteins in proportion to their mass (1.4 g SDS/g protein) and ensures that they all have a net negative charge on the surface. As the SDS-coated proteins assume linear structures like rods or random coils, a linear relationship between their molecular weight and the logarithm of their relative electrophoretic mobility (R_f) is achieved at a given gel concentration [12,13], so that the proteins are separated based on their sizes. More significantly, this procedure is found to be more precise and reproducible than the contemporary techniques such as gel filtration for the molecular weight determination of proteins [12,14].

A number of attempts have been made for improving the efficiency of protein separation by SDS-PAGE and also for achieving unanimous applicability in the whole range of protein size from a few to several hundred Daltons. It is particularly challenging to separate low molecular weight proteins (1- 100 kDa) [12]. This limitation arises from the 'pores' (defined as the separation between two successive crosslinks) in a PAM gel [15] not being uniform in size (ranges from 0.5 to 3 nm [12]) and shape. The pore size is found to follow a slightly skewed non-Gaussian distribution [16,17] as explained by the Ogston theory of gel electrophoresis, which considers the gel as a random meshwork of fibers [17]. Recently, gel electrophoresis has been used successfully to separate gold nanoparticles (15 ± 2.7 nm) loaded in an agarose gel based on the differences in their size and shape [18]. In this context, composites of PAM with high aspect ratio nanomaterials could be essentially effective for protein separations owing to the unique features of the latter like flexibility due to self-organization, dynamics of assembly, adsorption and percolation behavior in the polymer matrix [19]. For example, multiwalled CNTs (MWCNTs) modified polyacrylamide gels have been used for the separation of apolipoprotein and complement C3 of human serum using Native-PAGE [20]. However the above study employs a very high loading of the nanotubes (upto 0.1 wt%) in the gel

matrix and uses the differential adsorption of the two proteins on CNTs. Nonetheless, CNT matrices with very low loading could work well for SDS-PAGE as the SDS-denatured proteins may not interact with CNTs as strongly and specifically as the native proteins [21], although the SDS added to the buffer solutions (anode as well as cathode buffers) may have subtle adsorptive interactions with the nanotubes present in the gel matrix by virtue of its long alkyl (C_{12}) chain. Also, SDS is capable of displacing proteins adsorbed on CNT surfaces [22] to ensure that the nanotubes affect protein separation mainly by altering gel morphology instead of interacting with the proteins directly.

The previous chapters (Chapters 2, 3 and 4) have been discussing the effect of incorporating water-soluble moieties viz., cyanoferrates, hemoglobin and plant hormones on the microstructure and ionic transport properties of Nafion. This chapter involves the modification of the polymer electrolytes, Nafion and polyacrylamide with partially hydrophobic carbon nanotubes (CNTs). Polyacrylamide is chosen because of its similarities with Nafion in terms of amphiphilic microstructure and network topology. Subtle changes in the morphology of polyacrylamide gels induced by CNTs are found to affect the electrophoretic mobility of protein molecules. Further, we demonstrate how to achieve better separation of proteins using CNT-modified PAM gels, which would help in the application of CNT composites for gel electrophoresis of various classes of biomolecules like DNA, proteins and peptides.

5.2 Experimental Section

Multi-walled carbon nanotubes (MWCNTs) were synthesized using Chemical Vapor Deposition (CVD) with methane as the source, at 950 ^{o}C using a trimetallic catalyst (1000 sccm methane; 200 sccm H_2) for 30 min. Then the MWCNTs were purified by continuous stirring at room temperature in a 1:3 solution of Conc. HNO_3 in water for 48 hours and SWCNTs were procured commercially.

Nafion/MWCNT Composites

Required amount of acid-treated carbon nanotubes were dispersed in 1 wt% Nafion solution in deionised water by sonication for 15 min at a frequency of 33 kHz. The composite films were prepared by subsequent casting of these homogeneous dispersions on a glass disc followed by air-drying until the films could be peeled off from the holder. Scanning Electron Microscopy was done using A Leica stereoscan 440 model SEM with a Kevex model EDAX system. The micrographs were recorded using a 20 kV electrical high tension and a 25 pA camera attached on the high resolution recording unit. The purified carbon nanotubes were coated on a flat substrate and subjected to EDX analysis (K_α lines) with a Leica model instrument operating at a take off angle of 22.8 at a pressure of 10^{-9} torr. Transmission Electron Microscopy was performed using a JEOL model 1200 EX instrument equipped with a field emission gun at an accelerating voltage of 200 kV, magnification 389,000x and coefficient of spherical aberration 1.5 mm. Electronic (dc) conductivity of the films was recorded in a parallel configuration by sandwiching them in between two brass discs using a 6514 Keithley system electrometer. Dielectric relaxation and electrochemical impedance spectroscopy were recorded in a parallel configuration with a Solartron biptentiostat equipped with a frequency response analyzer (FRA) and interfaced to the computer. The instrument is associated with a *SMART* software for dielectric studies and *ZPlot* software for impedance analysis.

Polyacrylamide/CNT Composites

Polyacrylamide/CNT composite gels were prepared by dispersing CNTs by ultrasonication (33 kHz, 25 min, 30 ^{O}C) in a gel buffer solution for Laemmli's SDS-PAGE [23] at pH 8.8 followed by *in situ* radical polymerization using TEMED (*N, N, N′, N′*- tetramethylethylene diamine) as the initiator and ammonium persulfate as the catalyst. While PAM wrapped CNTs are known to be water-soluble [24], the presence of a cross linker viz., bisacrylamide ensures the formation of gels. Electrophoresis was performed

for 14- 97 kDa marker proteins procured from GE health care (Code No. 17-0446-01) reconstituted with an appropriate buffer of composition specified by the manufacturers and 2.5 – 17 kDa marker proteins from (Product No. MW-SDS-17S), with a protein loading of 7 μg. A stacking gel (5 %T, pH 6.8) was employed to concentrate the protein sample into a thin band before it enters the resolving gel, with a dc voltage of 120 V and 20 mA current using a constant power supply and the average running time was 2 to 2.5 h, judged visually from the mobility of a tracking dye (bromophenol blue for 14 – 97 kDa proteins and coomassie brilliant blue in the case of 2.5 – 17 kDa proteins) added to the protein mixture.

5.3 Results and Discussion

5.3.1. Nafion/CNT Composites

The poor solubility/dispersibility of CNTs in almost all solvents often precludes the synthesis of homogeneous polymer/CNT composites. Protocols normally used for solubilizing CNTs include, functionalization of CNTs with polar end groups [25], physical wrapping of the nanotubes in polymers [26] and *in situ* polymerization strategy in which a monomer entity chemically bonded to the CNTs is polymerized along the carbon scaffold [27]. Recently it has been found that Nafion, a perfluoro sulfonic acid ionomer could improve the stability of carbon nanotube dispersions in a range of solvents [28]. The advent of this unique property of Nafion has led to enormous developments in the fabrication of devices based on highly transparent CNT-Nafion composites for applications like, biosensors, PEM fuel cells, supercapacitors and electrochemical hydrogen storage [29]. Notwithstanding their importance in technological applications, these composites are also good candidates to understand the fundamental interfacial properties of the carbon nanostructures and the amphiphilic polymeric domains confining them. In this context, a fair amount of understanding, especially in the case of CNT composites with electronically conducting polymers like polyaniline [30] has been

attained by investigating their electrical, electrochemical, mechanical and thermal properties. On the other hand, CNT-composites involving polymer electrolytes are often explored with the objective of revealing the effect of the polymeric matrix on the CNTs. However it is equally important to analyze the reverse case i.e., the effect of CNT percolation on the domain structure and microscopic properties of the polymer electrolyte, because the whole range of functions exhibited by polyelectrolytes, especially in the case of Nafion, is attributed to the phase-separated domain structure. In this connection, we have investigated the effect of multi-walled carbon nanotube incorporation on the micro-structural properties of Nafion particularly in terms of its dielectric relaxation, dc conductivity and spectroscopic behavior along with a morphological characterization using Scanning Electron Microscopy (SEM).

Figure 5.1 shows the electron micrographs along with the EDAX spectra of the MWCNTs after purification by acid-treatment indicating good quality and excellent purity (90 %) of the carbon nanotube samples used in the present work. Subsequently, figure 5.2 shows a comparison of the optical clarity of the dispersions of MWCNTs in Nafion with varying amounts of CNTs (a) and with different densities of Nafion dispersions (b). Having understood the dispersibility of MWCNTs in Nafion solutions, it would be interesting to analyze their electrical properties.

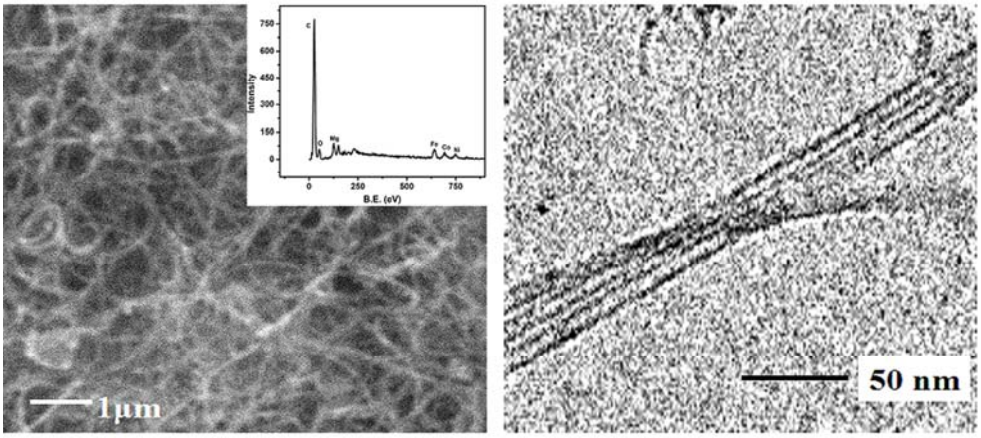

Figure 5.1. Scanning electron micrograph (left) and Transmission electron micrograph (TEM) of MWCNTs after purification by acid treatment. The inset (left) shows the EDAX spectrum of the purified MWCNTs

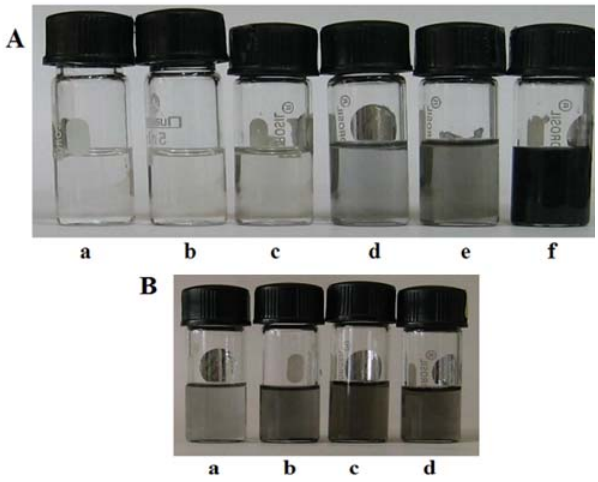

Figure 5.2. A) Dispersion of purified MWCNTs in 0.5 wt% Nafion in Ethanol with different proportions of MWCNTs: 24 hr after sonication (a-f) 0.01, 0.025, 0.1, 0.25, 0.5 wt%; **B)** Dispersions of MWCNTs (0.2 mg/ml) in (a-d) 0.05 wt%, 0.1 wt%, 1 wt%, 2.5 wt% Nafion.

The composite films cast from the above dispersions show variations in electrical (dc) conductivity with the proportion of MWCNTs (figure 5.3). The conductivity values are found to be of the order of 10^{-5} S/m, which is significantly higher than that of the pristine Nafion film measured under identical conditions (~10^{-12} S/m) by almost seven orders of

magnitude, probably indicating the formation of inter-connecting networks of nanotubes in the polymer matrix [31]. This could also be compared with the SEM images shown in the inset of Fig. 5.3, which illustrates the formation of networks of nanotubes in the polymer matrix.

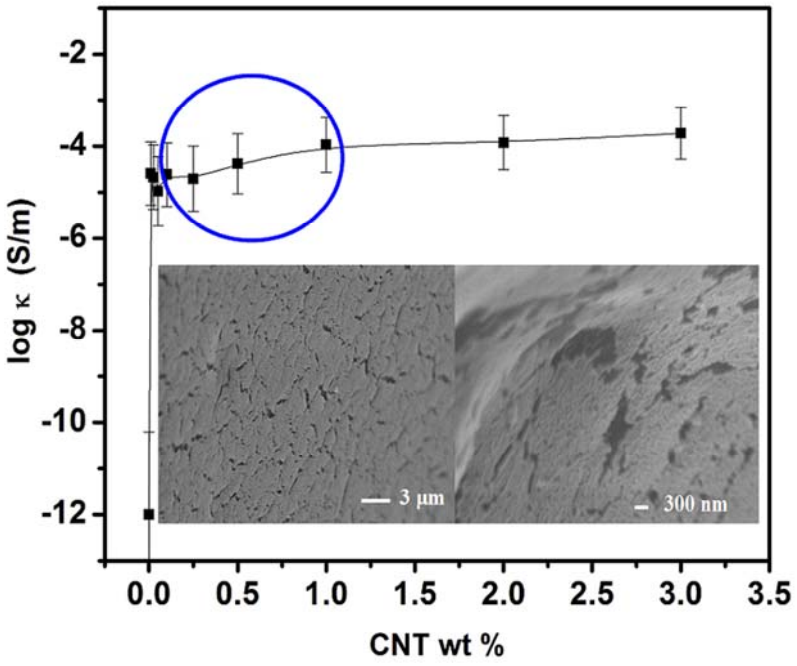

Figure 5.3. Variation of electronic (dc) conductivity with varying proportions of MWCNTs in Nafion- MWCNTs films (average thickness: 60 μm approx.). The sharp inflection at around 0.01 % CNT indicates the percolation threshold for the composites (the error bars refer to the standard deviation in the conductivity values observed in five repetitive measurements). Another inflection is noticed at 0.4 % (encircled portion) The inset shows the SEM images of a 0.5 wt% Nafion-CNT film indicating the formation of interconnecting networks of MWCNT bundles in the polymer matrix

A further analysis based on percolation theory [10] yields a threshold of 0.01 wt % (approx.). However, in the case of electronically conducting polymers with conjugated π systems, percolation threshold below 0.1 wt% has been reported earlier [32]. Particularly, Windle and coworkers have achieved an ultralow electrical percolation threshold of 0.0025 wt% in epoxy-based composites of aligned MWCNTs [33]. In addition, their pioneering contributions in understanding the interactions responsible for

the formation of percolating networks in CNT/polymer composites [34] have added momentum to several further advances. More interestingly, in addition to the sharp inflection at 0.01 wt% CNT, another inflection is clearly observed at around 0.4 wt%, signaling changes in the microstructure of the ionomer matrix induced by the percolation of carbon nanotubes. Usually analyses based on percolation phenomena are focussed mainly on the sharp inflection region and the fate of the polymeric matrix, particularly in terms of its morphological changes, after incorporation of carbon nanotubes is yet to be explored. In this context, the present work is an attempt to analyze the forces responsible for the morphological changes in the ionomer, induced by interpenetrating carbon nanotube bundles. Nafion, in particular, would be an interesting choice for such investigations because of its tunable amphiphilic morphology, which in turn allows its applicability in a diverse range of technologies.

Having observed the percolation of CNTs into the ionomer matrix, interesting effect of the nanometric ingredient on the microstructure of Nafion is unraveled from the DRIFT (Diffuse Reflectance Infrared Fourier Transform) spectra of the composite membranes recorded at room temperature shown in figure 5.4.

Interestingly, both sulfonate stretching vibrations (Fig. 5.4A) as well as the vibrations of the bound water molecules (Fig. 5.4B) in the Nafion membrane vary significantly with a gradual increase in CNT content in the composites. In the sulfonate stretching region (900-1500 cm^{-1}), a band at 1239 cm^{-1} (insignificant in the pristine membrane) which appears after incorporation of MWCNTs, transforms gradually into a doublet at higher proportions. This band could be assigned to the asymmetric stretching vibrations of SO_3^- groups in the pendent chains pointing into the hydrophilic pools of the polymer, the splitting of which could be attributed to the squeezing of the hydrophilic pools with increasing proportions of CNTs in the hydrophobic part. This is not unlikely since the $\upsilon_{SO_3^-}$ asymmetric stretching vibrations in Nafion are known to become doubly degenerate depending on its environment [35]. Although these bands are generally

masked by intense CF_2 stretching vibrations in Nafion, they become prominent in the present case, probably because of pronounced entropic constraints imposed by CNT

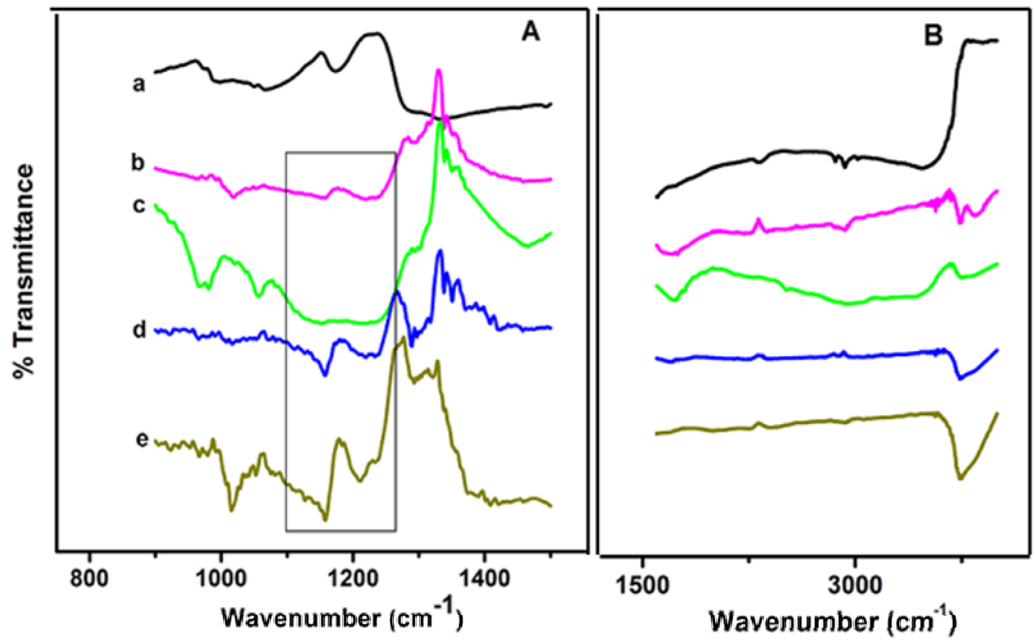

Figure 5.4. DRIFT spectra of a) Recast film of pristine Nafion and composite Nafion films with b) 0.05 wt%; c) 0.1 wt%; d) 0.5 wt% and e) 1 wt% MWCNTs. Significant changes in the sulfonate stretching frequencies (Region **A**) as well as the vibrational frequencies of bound water molecules (Region **B**) are observed with increasing proportions of CNTs.

on the minority hydrophilic phase of the ionomer. In addition, the $\upsilon_{SO_3^-}$ symmetric stretching vibrations at 1056 cm^{-1} in the pristine film, gets sharpened with increasing proportion of CNTs in accordance with the above explanation. Similarly significant changes in the second region (1500-4000 cm^{-1}) corresponding to the bound water molecules in the ionomer could be observed. For example, i) a doublet appears at 3718 cm^{-1} after introducing CNTs into the membrane which becomes a singlet with increasing proportions of CNTs in the composite and ii) The band at 2916 cm^{-1} in the pristine membrane disappears after incorporating CNTs, indicating changes in the degrees of freedom induced by the hydrophobic ingredients.

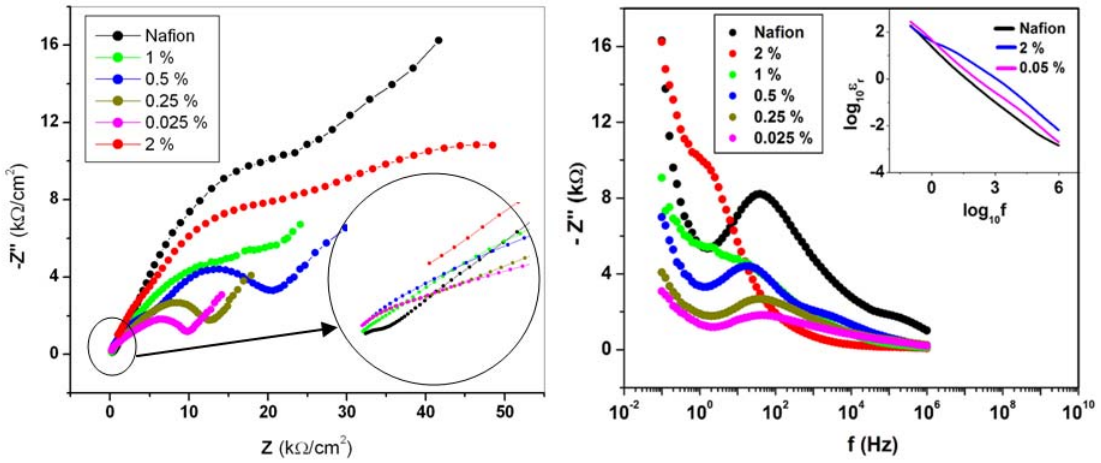

Figure 5.5. Variation of the imaginary part of electrochemical impedance (Z´´) with the real part of impedance (Z´) (left) and variation of Z´´ with the frequency (f) (right) of an applied ac signal (10 mV rms amplitude) from 10 mHz to 1 MHz at room temperature. The inset in the left shows the expanded view of the low frequency part of the Nyquist plots and the inset in the right shows a comparison of the dielectric relaxation spectra (DRS) of Nafion-MWCNT composites with that of pristine Nafion (ε_r denotes dielectric constant). The introduction of CNTs into Nafion matrix results in a hump in the DRS at lower frequencies (~ kHz).

More interestingly, the effect of CNTs on the degrees of freedom of the polymeric chains is also noticed in the dielectric relaxation spectra of the Nafion-MWCNT films at room temperature (Fig. 5.5 inset-right). While the high frequency part of the Nyquist plots (Fig. 5.5. left) shows a decrease in proton conductivity of Nafion with increasing CNT content, the variation of ε_r with the frequency of the applied ac signal (10 mV rms amplitude; 10 mHz to 1 MHz) for the 2 wt % composite film shows a hump nearly at 10 kHz, which is absent in the case of pristine Nafion film and almost insignificant for composite films with lower proportions of CNTs. This could be compared with reports on composites based on epoxy resins and functionalized carbon nanotubes, wherein the dielectric relaxation is found to shift to higher frequencies with increasing CNT content indicating a decrease in charge carrier mobility of the nanotubes due to the formation of polymer networks [36]. Thus, such chemical modifications have always been found to hamper the inherent properties of the CNTs [37]. On the other hand, the DRS results presented here, clearly indicate a decrease in internal degrees of freedom in the minority

phase of the phase-separated ionomer, the entropic penalty being compensated by pushing the nanotubes into the majority hydrophobic phase, something like a 'cushioning' effect. However, this is not surprising because a combined effect of weak long range Van der Waals interactions could overcome short range inter-tube attraction [38], despite the contact energy between individual CNTs being 40,000 times the thermal energy [37]. Further examination of the dependence of the imaginary part of electrochemical impedance with frequency (Fig. 5.5) shows a similar effect of CNTs on the electrical phase change of the polymer. A considerable shift in the impedance maximum associated with changes in peak shape towards the lower frequency side is observed with increasing proportions of CNTs in the composite, which again shows the formation of nanotube-networks with higher proportions. It indicates that CNTs could act as 'entropic modifiers' for Nafion, thereby enabling the analysis of its bound water molecules at lower frequencies under ambient conditions.

Thus the results of the present investigation could help in improving the efficiency of PEM fuel cells as the nanotubes introduced into the electrolyte would facilitate the monitoring of changes in its local water content due to 'electro-osmotic drag' generated during the fuel cell operation. On the other hand, when the CNTs are coupled with metal nanoparticles like Pt which could offer catalytic sites for the combination of H_2 and O_2 to produce water, it could result in efficient self-humidifying polymer membranes for application in PEMFCs [39].

5.3.2. Polyacrylamide/CNT Composites

This section discusses the synthesis and application of carbon nanotube (CNT)/polyacrylamide (PAM) composite gels for the electrophoretic separation of proteins. Figure 5.6 shows the transmission electron micrographs of the single-walled and multi-walled carbon nanotubes used in this study and figure 5.7 demonstrates the quality

of the polyacrylamide composite gels with single-walled and multi-walled carbon nanotubes, which will be used for separation of proteins by gel electrophoresis.

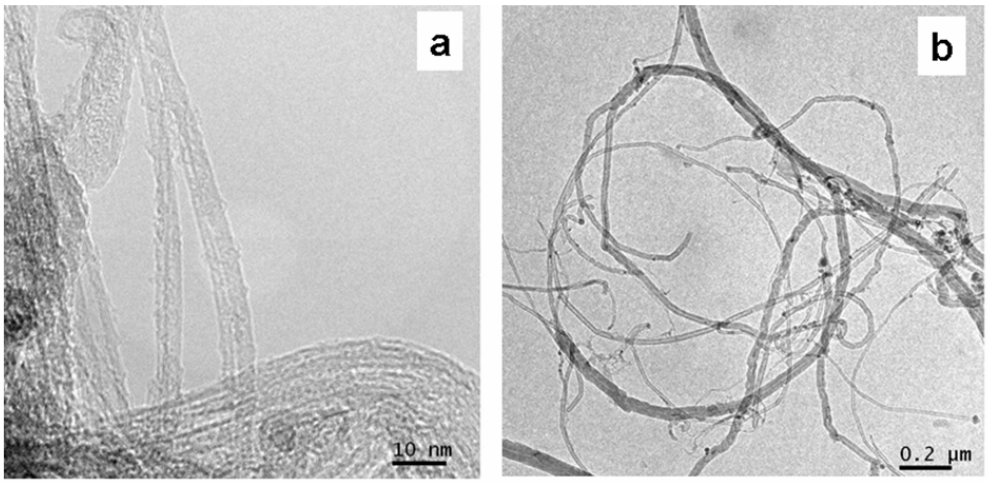

Figure 5.6. Transmission electron micrographs of a) SWCNTs and b) MWCNTs after purification by acid treatment

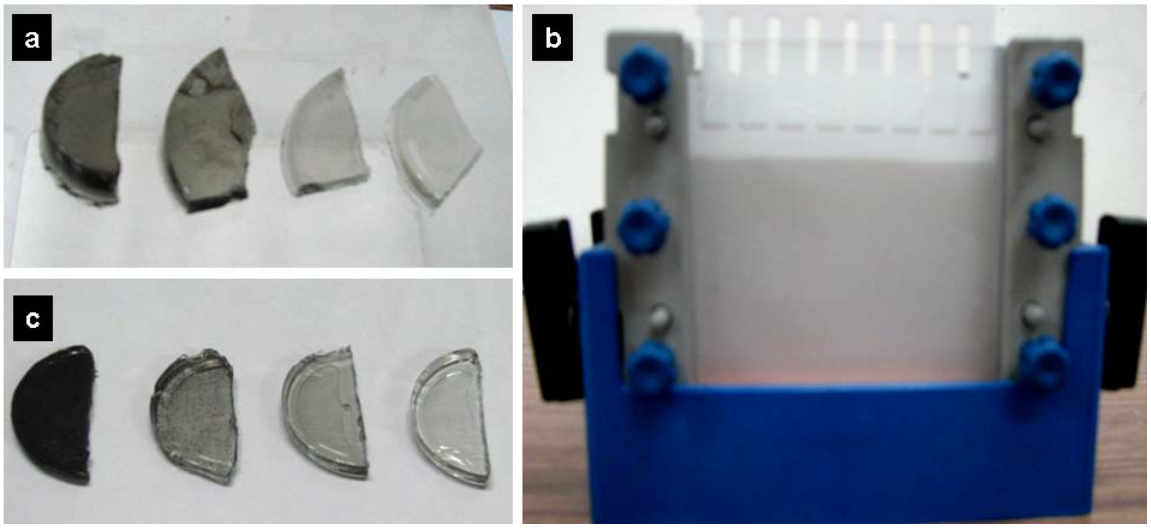

Figure 5.7. a) SWCNT/PAM gels of composition (wt %) from right to left: 0.0015 %, 0.0025 %, 0.005 %, and 0.01 %; b) Homogeneous SWCNT/PAM gel in the casting unit before electrophoresis; c) MWCNT/PAM gels of composition (wt %) from right to left: 0.0015 %, 0.0025 %, 0.005 %, and 0.01 %.

The relative mobility of a protein during gel electrophoresis (defined as its absolute mobility, *M*, divided by the mobility of the tracking dye), depends on parameters of the protein, gel and buffer system as expressed below [12].

$$R_f = \frac{M}{u_f} = \frac{M_o}{u_f}\left[\exp\left(K_R T\left(\log_c 10\right)\right)\right] \tag{5.1}$$

$$K_R = \frac{\pi\left(R + r\right)^2 l'}{\log_c 10} \tag{5.2}$$

where, M_o is the free electrophoretic mobility of the protein, u_f is the mobility of the tracking dye, R and r are the radii of the protein and counter ion(s) respectively, l' is a parameter characteristic of the gel and K_R is the retardation coefficient, characteristic of the molecular size of the protein. The expression remains essentially valid for any gel electrophoresis experiment despite the basic assumptions involved in its derivation. Among the various parameters, those corresponding to the resolving gel, especially, the pore size and its distribution, play a key role in achieving good separation as well as reproducibility. In this regard, the incorporation of high aspect ratio nanostructures like carbon nanotubes could have a significant impact on the gel parameters due to their unique adsorptive capabilities. For example, SWCNTs have been used in the run buffer to separate the homologues - caffeine and theobromine using capillary electrophoresis by virtue of the unique network formation capabilities [6].

The morphology of the CNT/PAM composite gels can be understood qualitatively from figure 5.8. In brief, the acrylamide monomer molecules as well as the bisacrylamide

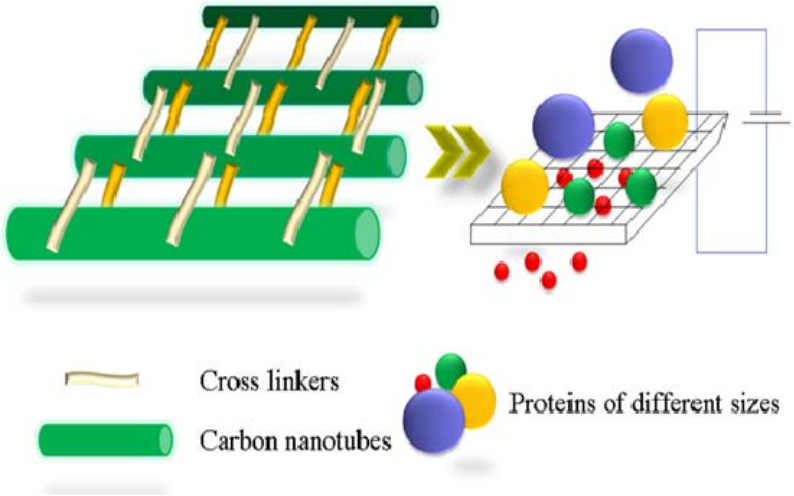

Figure 5.8. *In situ* radical polymerization of acrylamide monomers adsorbed on carbon nanotubes result in composite gels proposed to have uniform pore sizes. The CNT/PAM composite gel could be visualized as a mesh with uniform pores which can effectively separate surfactant-denatured proteins, based on their molecular weight differences by a sieving action in presence of an externally applied electric field and hence could be applied for molecular weight estimation of new proteins.

(cross linker) molecules can adsorb on nanotube sidewalls due to π-π interactions between their vinyl groups and the sp^2 hybridized carbons in CNTs. As the diameter of the nanotubes is far higher than the molecular dimensions of the monomer and cross linker, polymerization could occur also along the nanotubes and the cross linkers could bridge the nanotubes to form networks resulting in gelation. This is evident from the clear quality of dispersions and gels of the CNT/PAM composites which would not be possible unless there is a considerable debundling of the nanotubes to overcome the strong van der Waals and $\pi - \pi$ interactions between them. Also, difference in pore size distribution is expected between the pristine PAM and CNT/PAM gels. In the former case, there is hardly any control on the regularity in the cross linking intervals (i.e., the pores) due to the kinetic control during the polymerization of the free monomer molecules. Conversely in the CNT/PAM gels, the polymerization of pre-adsorbed monomer molecules probably ensures sufficient cross-linking at regular intervals forming a network of uniform pores.

On the other hand, protein adsorption on CNTs cannot be overruled altogether. The adsorptive interactions of proteins with CNT surfaces could be broadly categorized as specific and non-specific, depending on the selectivity of the nanotubes to the proteins. While the major driving force for the former is hydrophobic interaction, the latter could arise either due to hydrogen bonding interaction between the –COOH groups on the nanotube surfaces and the –NH and –OH groups of proteins and/or van der Waals interactions. These interactions could be arranged in the order of the associated free energy changes as [22,39],

Hydrophobic (0.1 eV) < van der Waals (0.27 eV) < hydrogen bonding (0.36 eV)*

In the present case, the hydrophobic and hydrogen bonding interactions between the nanotubes and the proteins have been largely overcome, as SDS renders the protein surface highly hydrophilic, simultaneously masking the functional groups from getting exposed to the nanotube surface. Nevertheless, the van der Waals interactions between the proteins and CNTs cannot be totally precluded, which is dictated by the surface energy of the respective nanotubes. Accordingly, the SWCNTs are expected to adsorb the proteins more strongly than the MWCNTs, which are indeed reflected in the experimental observations too.

5.3.2.1. Single-walled versus Multi-walled Nanotube Gels: Protein Separation

Figure 5.9 shows a comparison of SDS-PAGE results for the separation of 14 – 97 kDa marker proteins using pristine polyacrylamide gels (12% *T*) with those of SWCNT/PAM and MWCNT/PAM gels (containing 0.001 wt% CNT). The absence of any

* Calculated for a 20-layered MWCNT of 10 nm diameter with 2000 dangling bonds available for hydrogen bonding interaction

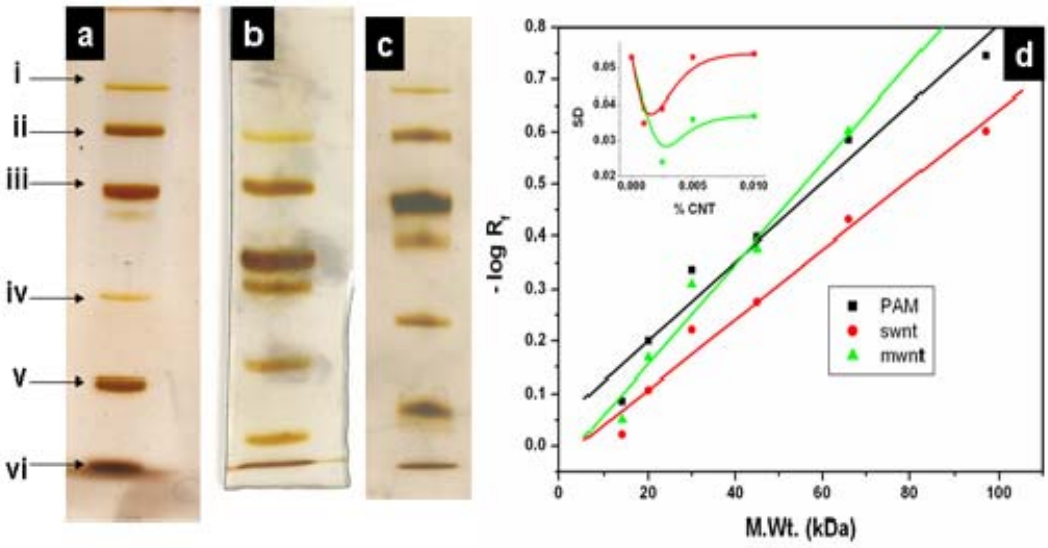

Figure 5.9. Separation of 14-97 kDa marker proteins by electrophoresis in a) Polyacrylamide gel (12% T); b) Single walled carbon nanotube/polyacrylamide composite gel; c) Multi walled carbon nanotube/polyacrylamide composite gel each with 0.001 wt% CNT content, after silver staining; the protein mixture consists of i) Phosphorylase b (97 kDa); ii) Albumin (66 kDa); iii) Ovalbumin (45 kDa); iv) Carbonic anhydrase (30 kDa); v) Trypsin inhibitor (20.1 kDa) and vi) Lactalbumin (14.4 kDa); d) Variation of R_f values (logarithm) of the individual proteins with their molecular weight : inset shows the dependence of standard deviations from linearity in these plots on CNT content for both SWCNTs and MWCNTs.

obvious differences in the number of bands in both the nanotube gels indicates that there is no specific adsorption of any of the SDS-denatured proteins on the nanotubes. This could be compared with a report by Huang *et al*, wherein bovine serum albumin exhibits multiple bands in PAGE due to differential/non-quantitative adsorption on CNT surfaces [37]. It also indicates that possibly, CNTs cannot be used instead of SDS for denaturing the proteins, since they may not ensure a purely molecular weight-dependent mobility unlike SDS, which binds to proteins in a quantitative and an essentially non-specific fashion (binding all the proteins) simply in proportion to their molecular weights. Hence our present approach of using CNT matrices for SDS-PAGE could be appropriate to improve protein separation by selectively modifying the gel morphology without any

specific interaction with the proteins. Furthermore, both the nanotube gels exhibit excellent linearity when the logarithm of R_f is plotted against the molecular weight of proteins. Surprisingly, Figure 5.9d shows that the standard deviation from linearity compared to that of the pristine polyacrylamide gels is reduced by 55 % in the case of multi walled carbon nanotube (MWCNT) gels and 34 % in the case of single walled carbon nanotube (SWCNT) gels, in agreement with the narrower pore size distribution in the case of nanotube gels proposed in Figure 5.8. Figure 5.9 also indicates that the SWCNT gels enhance the mobility of higher molecular weight proteins while the MWCNT gels facilitate the movement of the lower molecular weight ones, which could be due to the differences in pore sizes between the single and multi-walled nanotube modified gels.

5.3.2.2. Separation of 2.5 – 17 kDa proteins

In order to understand the molecular weight range of proteins in which CNT-PAGE is effective, electrophoretic separation of shorter peptide markers (2.5 – 17 kDa) has also been attempted (Fig. 5.10). Usually, separation of shorter peptides is performed with tricine buffer system (instead of tris-HCl employed in the above studies) for about 18 hrs. Here, we have used the same separation in the routine tris-HCl buffer to investigate whether the CNT matrix offers any advantage over the polyacrylamide gel.

Although there is some qualitative improvement in comparison to the latter, it is difficult to quantify the results probably due to the adsorption of shorter peptides on the nanotubes. Nevertheless, the method works fairly well for a certain choice of shorter peptides with appropriately functionalized CNTs.

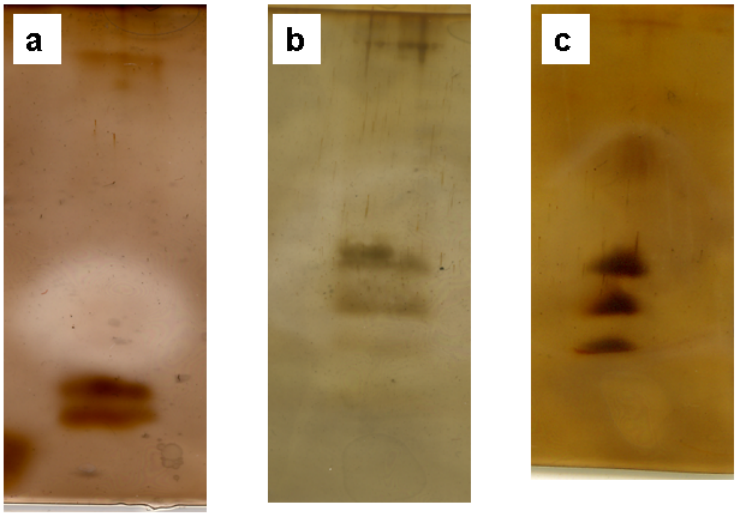

Figure 5.10. Separation of 2.5-17 kDa peptides by a) Polyacrylamide gel (12 % T); b) Single-walled carbon nanotube/polyacrylamide composite gel; c) Multi-walled carbon nanotube/polyacrylamide composite gel after silver staining.

5.3.2.3. Effect of Nanotube Loading

Further, in order to understand the effect of both CNT loading and dispersion on the separation efficiency of 14-97 kDa proteins, separate experiments have been carried out with different amounts of CNTs in the matrix ranging from 0.001 wt % to 0.01 wt %. Accordingly, Figures 5.11 and 5.12 show the effect of MWCNT and SWCNT loading on the separation efficiency. A common feature in both the cases is that the separation becomes less efficient with increasing CNT content, though the gels with the lowest CNT content significantly enhance the efficiency compared to that of pristine polyacrylamide.

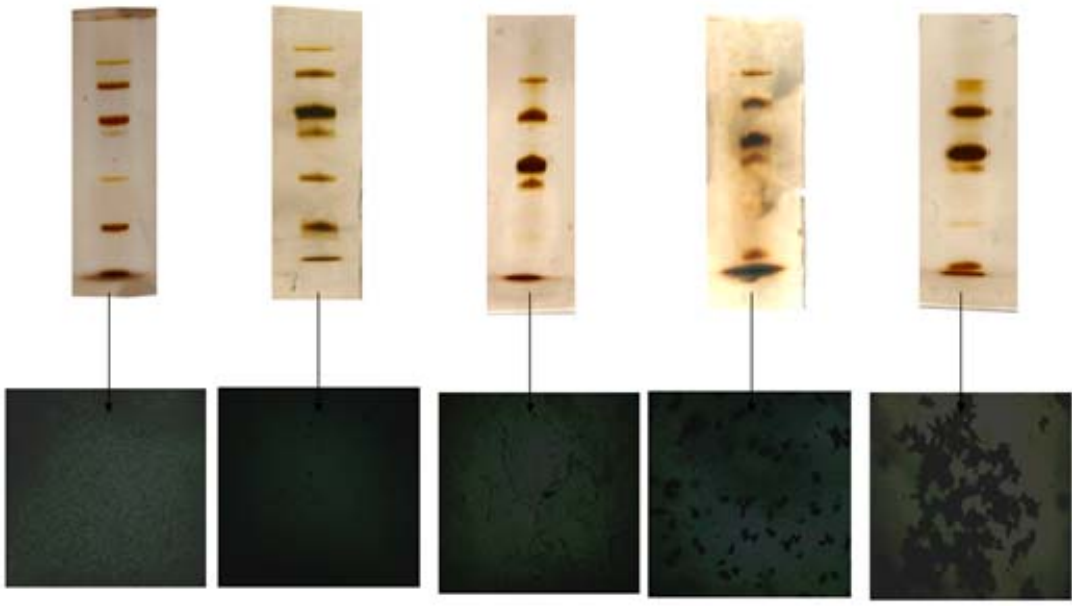

Figure 5.11. Effect of MWCNT content on the separation of 14 – 97 kDa proteins: top row: (from left to right) pristine PAM, 0.001, 0.0025, 0.005 and 0.01 wt% MWCNT; bottom row represents Optical Micrographs of the corresponding gels.

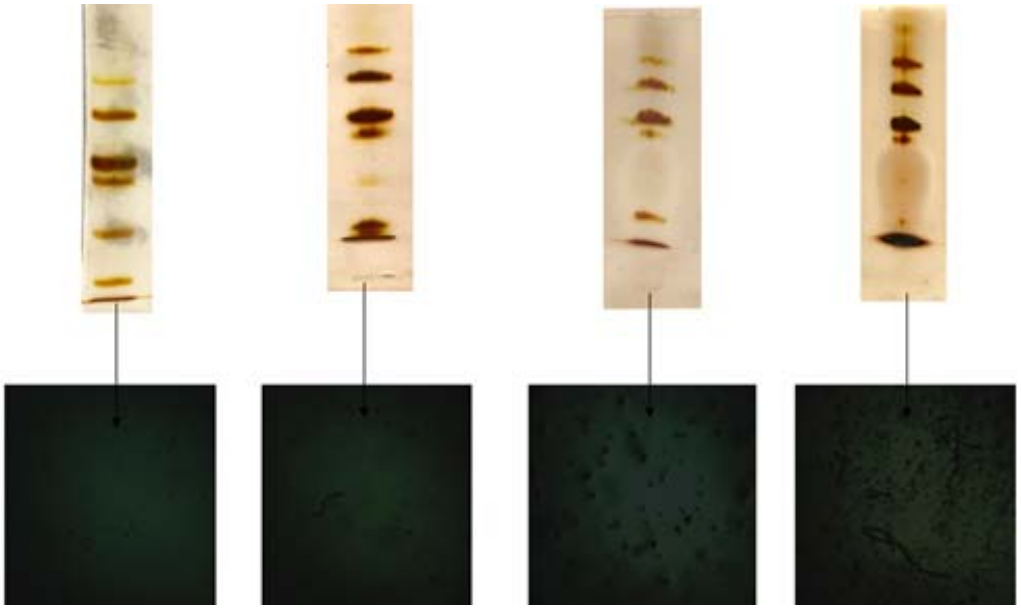

Figure 5.12. Effect of SWCNT content on the separation of 14 – 97 kDa proteins: top row: (from left to right) 0.001, 0.0025, 0.005 and 0.01 wt% SWCNT; bottom row represents optical micrographs of the corresponding gels

The deterioration in separation efficiency with increasing CNT content could be readily explained in terms of nanotube dispersion in the polyacrylamide matrix, with reference to the optical micrographs of the respective gels presented in the figures. The main difference between the SWCNT and MWCNT gels is in terms of the sharpness of the protein bands, with those in the latter being sharper than those in the former. A plausible reason for this could be the difference in adsorptive interactions between the single-walled and multi-walled nanotube surfaces towards the proteins [43,44]. The mode of adsorption, however, could be mainly van der Waals interaction rather than the specific hydrophobic interaction between the SDS-bound proteins and the CNTs as evident from the higher mobility of lysozyme (M.Wt. 14.3 kDa), a protein which is well-known to interact specifically with SWCNTs, in 0.01 wt% SWCNT compared to that of the 0.005 wt % SWCNT gel (Figure 5.13).

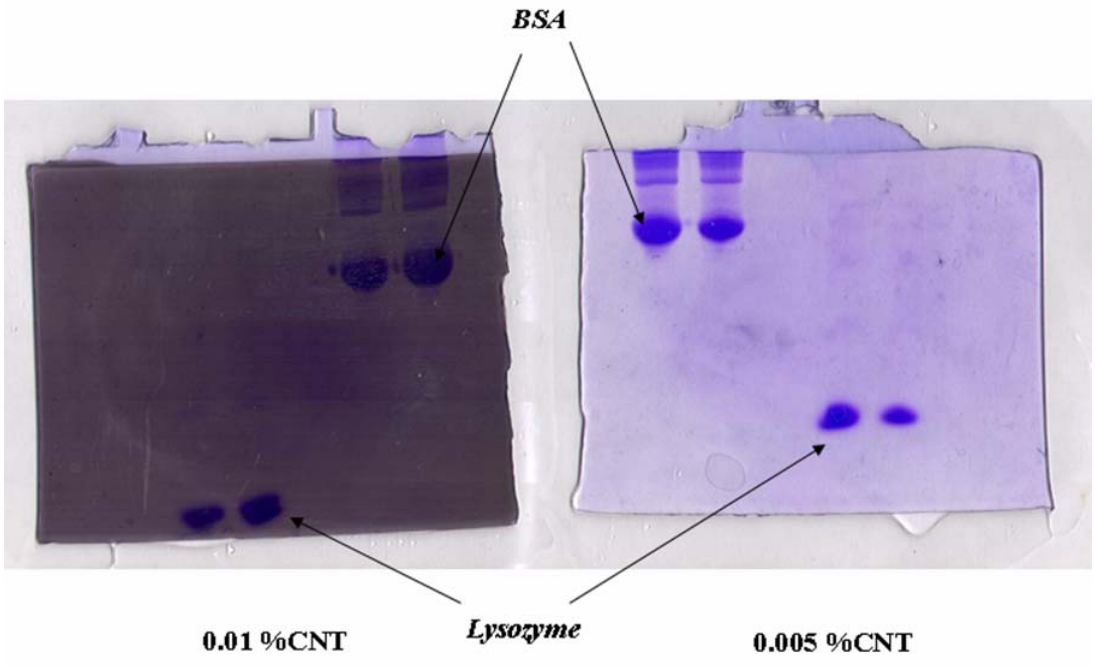

Figure 5.13. CNT/PAM gels stained with coomassie brilliant blue after electrophoresis of Bovine serum albumin (M. Wt. 97 kDa) and Lysozyme (M. Wt. 14.3 kDa) in 7.5 %T PAM gels containing SWCNTs 0.01 wt% (left) and 0.005 wt% (right). Lysozyme is known to undergo specific adsorption on SWCNTs. Its increased mobility with increasing SWCNT content indicates that the SDS-bound protein does not undergo specific adsorption on the CNTs present in the gel matrix

Thus, the effect of carbon nanotube incorporation on the microstructure and transport properties of the polymer electrolytes, Nafion and polyacrylamide has been systematically demonstrated in this chapter. Although the analysis has been based mostly on the resulting properties of the polymer electrolytes instead of direct microscopic evidences, the results of the investigation provide a considerable appreciation of the correlation between the microstructure and the net properties of the polymer electrolytes.

5.4 Summary and Conclusions

In summary, we demonstrate in this chapter, the electrical, microstructural and morphological properties of homogeneous Nafion-MWCNT composite films yielding a low percolation threshold. This is followed by the investigations on carbon nanotube composites of polyacrylamide and their further application for the electrophoretic separation of proteins. A systematic comparison of the protein separation efficiency by SWCNT with MWCNT/PAM composite gels reveals that the latter is more efficient in terms of resolution mainly due to weaker van der Waals interactions with proteins. Nevertheless, both types of CNT/PAM composites show exceptionally better protein separation compared to the pristine PAM, which is attributed to the improved pore size distribution in the CNT/PAMs in the light of a proposed qualitative model based on the adsorptive power of the nanotubes. Further, the differences in protein mobilities between SWCNT and MWCNT, at a given acrylamide concentration, renders the composite gel matrix tunable according to the molecular weight range of the proteins. It would be more interesting in future to investigate the effect of nanotube surface chemistry on the efficiency of CNT-PAGE.

5.5 References

1. Kroto, H. W.; Heath, J. R.; O'Brien, S. C.; Curl, S. C.; Smalley, R. E.

Nature **1985**, *318*, 162.

2. (a) Iijima, S. *Nature,* 1991, *354*, 56. (b) Iijima, S.; Ichihashi, T. *Nature*, **1993**, *363*, 603. (c) Ajayan, P. M. *Chem. Rev.* **1999**, *99*, 1787.
3. Dresselhaus, M. S.; Dresselhaus, G.; Avouris, Ph. "*Carbon nanotubes: Synthesis, structure, properties and applications*" **2001**, Springer.
4. Du, Z.; Yu, Y. –L.; Chen, X. –W.; Wang, J. –H. *Chem. Eur. J.* **2007**, *13*, 9679.
5. Morales, C. S.; Flahaut, E.; Sim, E.; Sloan, J.; Green, M. L. H.; Sim, R. B.; *Mol. Immunol.* **2006**, *43*, 193.
6. Joshi, A.; Punyani, S.; Bale, S. S.; Yang, H.; Tasciuc, T. B.; Kane, R. S. *Nature Nanotech.* **2008**, *3*, 41.
7. Wang, Z.; Luo, G.; Chen, J.; Xiao, S.; Wang, Y. *Electrophoresis* **2003**, *24*, 4181.
8. Liu, P. *Eur. Polym. J.* **2005**, *41*, 2693.
9. Wagner, H. D.; Lowry, O.; Feldman, Y.; Tenne, R. *Appl. Phys. Lett.* **1998**, *72*, 188.
10. Kirkpatrick, S. *Rev. Mod. Phys.* **1973**, *45*, 574.
11. Kannan, R.; Kakade, B. A.; Pillai, V. K. *Angew. Chem. Int. Ed.,* **2008**, *47*, 2653.
12. Chrambach, A.; Rodbard, D. *Science* **1971**, *172*, 440.
13. Shapiro, A. L.; Maizel, J. V. *Anal. Biochem.* **1969**, *29*, 505.
14. Rodbard, D.; Chrambach, A. *Anal. Biochem.* **1971**, *40*, 95.
15. Tanaka, T. *Sci. Am.* **1981**, *244*, 124.
16. Chrambach, A.; Rodbard, D. *Proc. Natl. Acad. Sci. U.S.* **1970**, *65*, 970.
17. Ogston, A. G. *Faraday Soc. Trans.* **1958**, *54*, 1754.
18. Xu, X.; Caswell, K. K.; Tucker, E.; Kabispathy, S.; Brodhacker, K. L.; Scrivens, W. A. *J. Chromatography A* **2007**, *35*, 1167.
19. Bauer, L. A.; Birenbaum, N. S.; Meyer, G. J. *J. Mater. Chem.* **2004**, *14*, 517.

20. Huang, G.; Zhang, Y.; Ouyang, J.; Baeyens, W. R. G.; Delanghe, J. R. *Anal. Chim. Acta* **2006**, *557*, 137.
21. Matsuura, K.; Saito, T.; Okasaki, T.; Ohshima, S.; Yumura, M.; Iijima, S. *Chem. Phys. Lett.* **2006**, *429*, 497.
22. Valenti, L. E.; Fiorito, P. A.; Garcia, C. D.; Giacomelli, C. E. *J. Colloid Interface Sci.* **2007**, *307*, 349.
23. Laemmli, U. K. *Nature*, **1970**, *227*, 680.
24. Liu, Y.; Guan, W.; Li, X.; Huang, M. *J. Appl. Polym. Sci.* **2007**, *106*, 1.
25. Salzmann, C. G.; Llewellyn, S. A.; Tobias, G. *Adv. Mater.* **2007**, *19*, 883.
26. Liu, J. Q.; Xiao, T.; Liao, K. *Nanotechnology* **2007**, *18*, 165701.
27. Kang, M.; Myung, S. J., Jin, H. J. *Polymer* **2006**, *47*, 3961.
28. Lee, J. –H. *et al. J. Phys. Chem. C* **2007**, *111*, 2477.
29. Landi, B. J.; Raffaell, R. P.; Heben, M. J.; Alleman, J. L.; Vanderweer, W.; Gennett, T. *Nano Lett.* **2002**, *2*, 1329.
30. Ramamurthy, P. C.; Harrell, W. R.; Gregory, R. V. *J. Electrochem. Soc.* **2007**, *154*, H495.
31. Yang, B.; Fu, Y. Z. Manthiram, A. *J. Power Sources* **2005**, *139*, 170.
32. Grunlan, J. C.; Mehrabi, A. R.; Bannon, M. V.; Bahr, J. L. *Adv. Mater.* **2004**, *16*, 150.
33. Sandler, J. K. W.; Kirk, J. E.; Kinloch, I. A.; Shaffer, M. S. P.; Windle, A. H. *Polymer* **2003**, *44*, 5893.
34. (a) Martin, C. A.; Sandler, J. K.W.; Windle, A. H.; Schwarz, M. –K.; Bauhofer, W.; Schulte, K.; Shaffer, M. S. P. *Polymer*, **2005**, *46*, 877. (b) Hughes, M.; Shaffer, M. S. P.; Renuof, A. C.; Singh, C.; Chen, G. Z.; Fray, D. J.; Windle, A. H. *Adv. Mater.* **2002**, *14*, 382.
35. Gruger, A.; Regis, A.; Schmatko, T.; Colombon, P. *Vibrational Spectroscopy* **2001**, *26*, 215.
36. Valentini, L.; Armentano, I.; Puglia, D.; Kenny, J. M. *Carbon*, **2004**, *42*, 323.

37. Szleifer, I.; Rozen, R. Y. *Polymer*, **2005**, *46*, 7803.
38. Girifalco, L. A.; Hodak, L. M.; Lee, R. S. *Phys. Rev. B* **2000**, *62*, 13104.
39. Liu, Y. H.; Yi, B.; Shao, Z. G.; Wang, L.; Xing, D.; Zhang, H. *J. Power Sources* **2007**, *163*, 807.

Electrochemical Imaging of Proton Transport & Related Processes

This chapter demonstrates the application of Scanning Electrochemical Microscopy (SECM) for imaging the morphology of Nafion membranes impregnated with Pt catalyst. The (feedback) imaging principle involves the H^+/H_2 couple as the redox mediator to map the reactivity gradients of Pt catalyst incorporated in Nafion membrane towards hydrogen oxidation reaction. Vital information on the effect of oxide formation on the catalytic activity of the Pt particles present in the polymer electrolyte matrix is obtained. This is followed by the application of SECM imaging in the Generation/Collection mode to understand the role of proton fluxes on the mechanism of stomatal opening/closure in peanut plants. In addition, interesting variation in the distribution of stomata and their photosynthetic activity is observed by coupling the tissue culture protocol, Somatic Embryogenesis with SECM. The results presented in this chapter could be helpful to explore the application of SECM to understand processes ranging from catalytic activity in fuel cells to ion fluxes in biological systems.

* A part of the work discussed in this chapter has been published in *Anal. Bioanal. Chem.* 2008, *391*, 2227.

6.1 Introduction

Understanding the properties of matter at a molecular level is essential for the fabrication of hybrid materials with controlled functions. A number of imaging techniques capable of analyzing and manipulating materials in the nanoscale have been developed since many years. With the emergence of newer fabrication methods and theoretical models, the principle of imaging has been changing from one generation of microscopes to another. For instance, the conventional microscopes are mostly based upon the interaction of electromagnetic radiation with the sample. These are followed by Scanning Probe Microscopes which are capable of forming images by moving a small tip on a surface by sensing the changes in tip position or some other tip variable.

While the resolution of images obtained with the conventional microscopes is often limited by the wavelength of the incident radiation, the image resolution of Scanning Probe Microscopy (SPM), is limited by the size of the tip and its distance from the substrate [1]. For example, in Scanning Tunneling Microscopy (STM), when an atomically sharp metal tip is scanned within 1 nm of the surface, the tunneling current flowing between the tip and the substrate enables even the visualization of 'atoms'. But, STM cannot be used with insulating substrates and it does not yield information about the chemical nature of the surface [2]. On the other hand, contemporary scanning techniques such as the atomic force and the ion-conductance microscopy can image insulators but are not 'chemically sensitive'. One of the most noticeable developments in this area is electrochemical imaging, which broadly involves the interaction of the substrate with a species electro-generated at the tip. The key advantage of electrochemical imaging over other imaging techniques is its 'chemical sensitivity' which allows envisaging pathways and kinetics of interfacial processes viz., corrosion, electro-catalysis, dissolution of compounds and biological processes like photosynthesis and ion transport through cell membranes with spatial resolution.

Electrochemical imaging of reactive surfaces, especially biological specimens like roots and tissues, using a tip capable of recording potential differences along the surfaces has been known since 1960s [3]. Later, Bard and coworkers invented Scanning Electrochemical Microscopy (SECM) [2,4], which provides a higher resolution than the potentiometric imaging methods. The success of SECM relies on the advantages offered by the ultramicroelectrode (UME) used as the imaging probe. UME as the name implies is smaller than the conventional electrode, which has dimensions of the order of meters, centimeters or millimeters. When the size of the electrode becomes smaller or comparable to the diffusion layer thickness at the electrode/electrolyte interface, several advantages over the conventional electrode can be realized as given below [5].

- **Fast Double-layer Charging** – Electrochemical measurements at conventional electrodes are restricted to millisecond or larger time scales mainly due to the intervention of double layer charging. As many events like electron/proton transfer, ligand exchange and isomerization occur on the micro and nano second time scales, an important objective in transient electrochemical measurements is to minimize the charging time ($RC = (\pi r_o C)/4\kappa$, where, r_o is the electrode radius, C is the double layer capacitance, R is the interfacial resistance and κ is the conductivity of the electrolyte.). Since the charging time constant, RC, is proportional to electrode dimension, UME has the advantage of very fast double layer charging.
- **Reduced Ohmic Losses** – The actual potential realized at the interface is often lower than the applied potential by a quantity, iR, which is called the 'Ohmic drop'. Although the interfacial resistance increases with the decrease in electrode radius, the faradaic current, i, decreases with electrode area, resulting in a net reduction in the Ohmic drop at an UME. For example, if the Ohmic drop at an electrode of radius 1 mm is 5-10

mV, it will be only a few μV at an UME. Thus UME enables transient measurements even in the absence of a supporting electrolyte and in highly resistive media.

- **High Mass Transport Rates** – The small size of the UMEs makes diffusional mass transport extremely efficient. For example, the rate of mass transport to a 1 μm diameter UME disk is higher than the rate of convective mass transport at a 1 mm electrode rotated at a speed of 10^4 rpm. Thus the diffusion layer thickness easily exceeds electrode dimension at time scales shorter than that at conventional electrodes allowing the investigation of fast heterogeneous kinetics.

Combining the unique advantages of UMEs and the ability to raster the UME tip over the surface of a substrate electrode, SECM can offer a spectrum of information on different types of samples. Its basic instrumentation is depicted in Figure 6.1.

In brief, the SECM instrument consists of an UME fixed to a nanopositioner controlled by XYZ piezo stages, which can move the tip over a substrate electrode. Both the tip as well as the substrate electrodes are dipped in a solution containing an electroactive species like $[Fe(CN)_6]^{3-}$ and a supporting electrolyte to minimize solution resistance. The potential of the electrodes is controlled using a bipotentiostat and the speed and direction of tip movement can be controlled by a personal computer, which records the tip current as a function of its position as well as the applied potential. The SECM tip is usually a Pt or Carbon microwire or fiber (0.2 – 50 μm in diameter) sealed in a glass capillary as shown in Figure 6.2. The end of the glass is etched to expose a disk shaped electrode. However, tip geometries other than 'disk' can also be designed such as spherical, cone and band electrodes. Methods of designing UMEs are documented elsewhere [4b]. One of the main advantages of SECM is that in many cases, the substrate electrode, whether an insulator or a conductor need not be connected to the potentiostat.

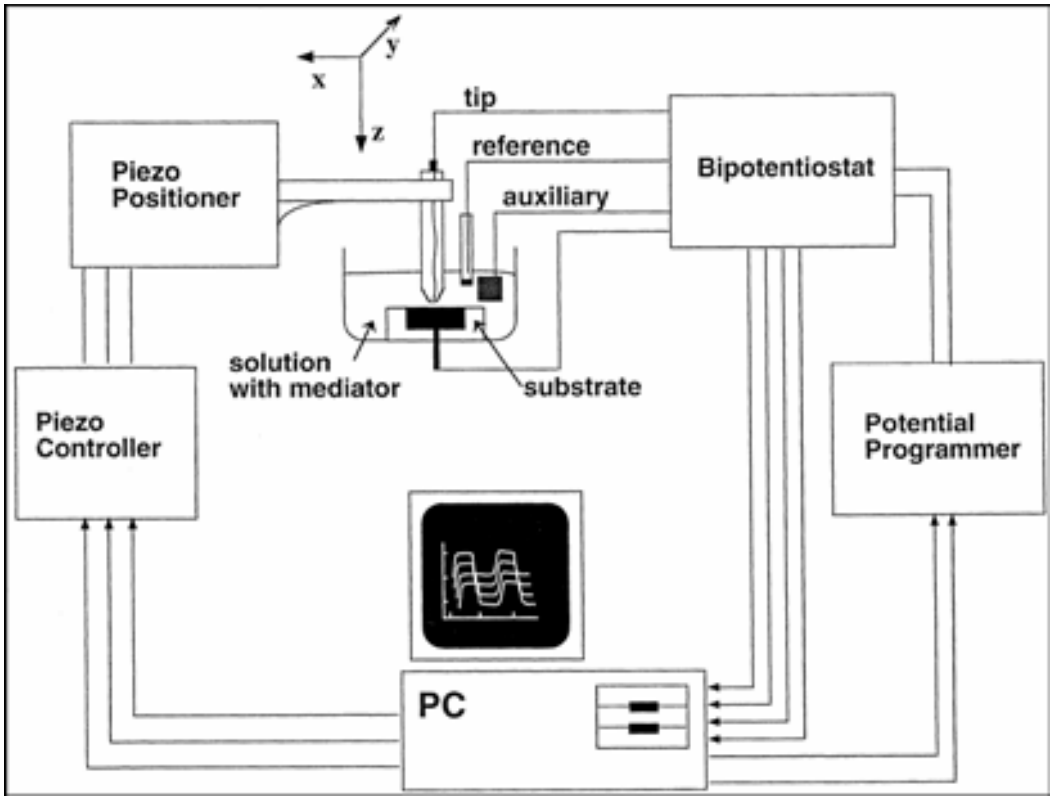

Figure 6.1. Schematic representation of the basic instrumentation of a Scanning Electrochemical Microscope. *Reproduced from Ref.* [*6*]

The imaging signal in SECM arises when the diffusion layer at the tip corresponding to the dissolved redox species is perturbed by the substrate as illustrated in Figure 6.3. More specifically, when the tip is kept far away (10-15 times the radius of the tip) from the substrate surface, the diffusion layer at the tip is nearly hemispherical as shown in Figure 6.3a. When the tip is brought closer to the substrate, diffusion of electroactive species to the tip electrode is either hindered or reinforced depending on whether the substrate is insulating or conducting respectively. For instance, if we consider the simple one-step one-electron redox process,

$$O + ne^{-} \rightarrow R$$

If the substrate is an insulator, part of the diffusion layer will be blocked and the tip current decreases (Fig. 6.3c). If the substrate is a conductor and is held at a potential where it can oxidize R back to O, the tip current will increase due to 'recycling' of O when the tip is close to the substrate (Fig. 6.3b). This phenomenon forms the basis for the most common imaging mode used in SECM known as the 'feedback' mode. The direction of the current feedback indicates whether the substrate is electrically insulating or conducting while the magnitude of current change indicates the distance of separation between the tip and the substrate or in other words, the rate of species turnover at the substrate.

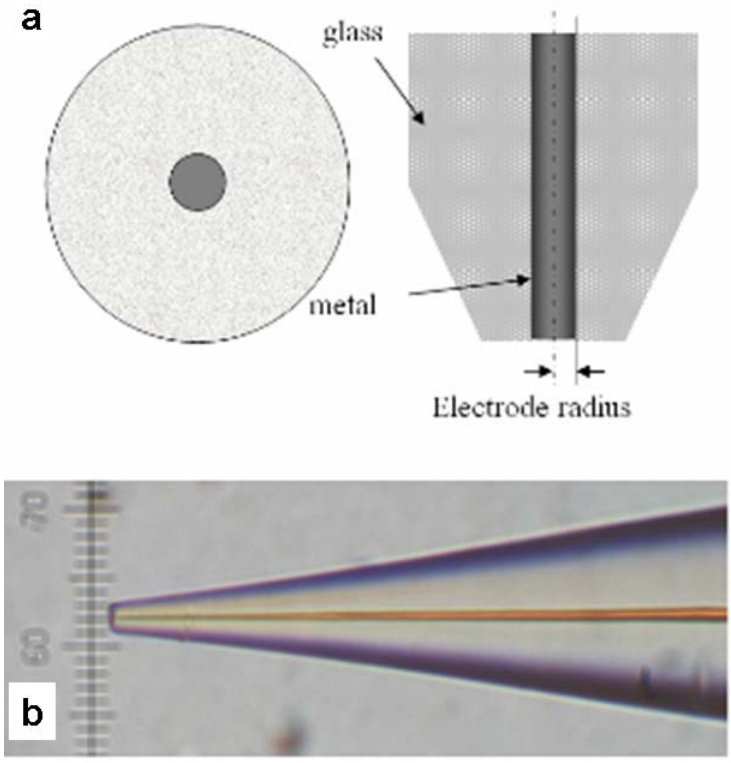

Figure 6.2. a) Cross-sectional and b) lateral views of a disk-type ultramicroelectrode sealed in a glass capillary. *Reproduced from Ref.* [*6*]

SECM imaging can be done either by monitoring the current response at the tip as a function of the redox reactions occurring at the substrate (amperometric) or by using ion-selective electrodes as probes to detect specific ions on the substrate (potentiometric). While potentiometric imaging is commonly used for locating ions in specific samples like biological cell membranes, the amperometric mode is the most widely employed for kinetic investigations. The latter can be further classified as the feedback and the generation/collection modes based on whether the tip-generated species is recycled by a counter redox reaction at the substrate or the species generated at one of the electrodes are just collected at the other electrode respectively. Both the modes of amperometric imaging have their own merits and demerits.

For instance, the feedback mode is one of the best ways for evaluating the radius and geometry of the SECM tip and to calculate tip-substrate separation. Prior to imaging, the separation between the tip and the substrate is estimated by recording the tip current as a function of its distance perpendicular to the substrate in a typical 'probe approach experiment'. The tip current either increases or decreases when it is close enough (a few tip diameters) to the substrate, depending on whether the substrate is a conductor or insulator resulting in a positive or a negative feedback respectively. While it is customary to provide a potential bias to the substrate electrode for positive feedback, sometimes large conductive substrates are known to regenerate the mediator by a process called 'substrate-potential driven feedback' [7]. Analytical approximations of the approach curves based on more efficient algorithms to describe SECM theory are available in the literature [8]. These analytical expressions can be used to fit the experimental approach curves to determine the actual tip-substrate separation. Thus, the amperometric feedback

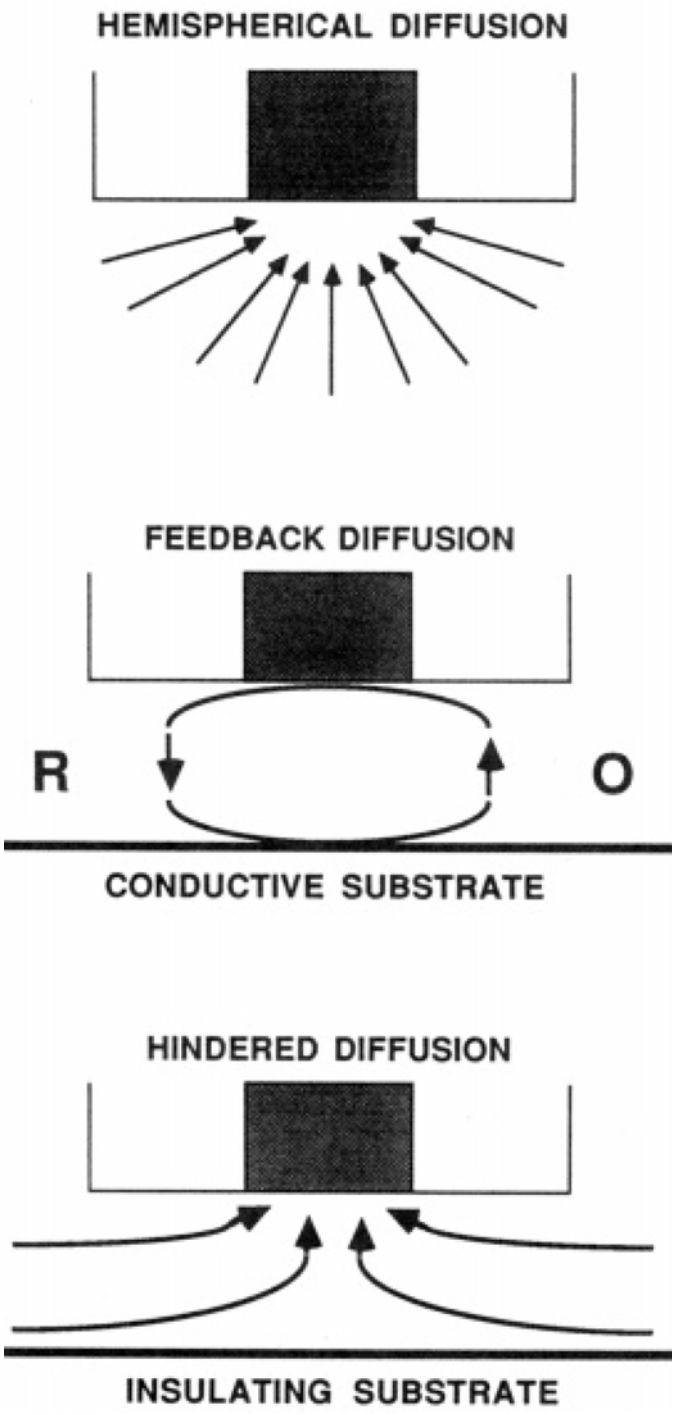

Figure 6.3. Principles of operation of a Scanning Electrochemical Microscope. a) Tip is far from the substrate – diffusion leads to a steady state current, $i_{T,\infty}$. b) Tip is close to a conductive substrate, feedback diffusion leads to $i_T > i_{T,\infty}$ c) Tip is close to an insulating substrate, hindered diffusion leads to $i_T < i_{T,\infty}$. *Reproduced from Ref.*[*2*]

mode can be used to achieve precise positioning of the tip, accurate estimates of local heterogeneous kinetics of a reactive surface and excellent spatial and temporal resolution in a typical 'reactivity imaging'. However, the feedback mode suffers from major drawbacks, which restrict its application to a narrow range of samples.

For instance, the feedback mode is one of the best ways for evaluating the radius and geometry of the SECM tip and to calculate tip-substrate separation. Prior to imaging, the separation between the tip and the substrate is estimated by recording the tip current as a function of its distance perpendicular to the substrate in a typical 'probe approach experiment'. The tip current either increases or decreases when it is close enough (a few tip diameters) to the substrate, depending on whether the substrate is a conductor or insulator resulting in a positive or a negative feedback respectively. While it is customary to provide a potential bias to the substrate electrode for positive feedback, sometimes large conductive substrates are known to regenerate the mediator by a process called 'substrate-potential driven feedback' [7]. Analytical approximations of the approach curves based on more efficient algorithms to describe SECM theory are available in the literature [8]. These analytical expressions can be used to fit the experimental approach curves to determine the actual tip-substrate separation. Thus, the amperometric feedback mode can be used to achieve precise positioning of the tip, accurate estimates of local heterogeneous kinetics of a reactive surface and excellent spatial and temporal resolution in a typical 'reactivity imaging'. However, the feedback mode suffers from major drawbacks, which restrict its application to a narrow range of samples.

- Necessity to use low mediator concentration
- As the tip current is sensitive to both the activity of the substrate as well the tip-substrate separation, the catalytic surfaces should be morphologically smooth to obtain reactivity images.

- The redox process at the substrate electrode should be diffusion-controlled.
- The tilt of the sample especially while imaging large areas should be properly controlled.

Another common mode of imaging is the generation/collection (G/C) mode, which offers important advantages, especially for reactivity imaging, as it is insensitive to morphological effects and is independent of feedback restrictions. Although the resolution of images obtained in the G/C mode is inferior to that obtained by the feedback mode, its capabilities to induce and evaluate processes in the micro and nanometer domains make it very attractive for localized studies. Interestingly, G/C experiments can be performed at significant separations (up to L = d/a ~ 20, where, d is the tip-substrate separation and a is the electrode radius.), which is advantageous especially in studies involving the reactivity of surfaces with significant topographical geometry. In this mode, the tip behaves as a passive sensor probing the concentration profile of the product of a process occurring at the substrate. The sensing electrode can be either the tip or the substrate and the corresponding imaging methods are known as the substrate generation/tip collection (SG/TC) or tip generation/substrate collection (TG/SC) modes respectively. The SG/TC mode has been successfully employed to image activity of biological materials (microorganisms, enzymes), corrosion and transport processes across membranes [4b, 9]. It has also been used to image the concentration profile of oxygen photosynthetically generated from plant leaves [10].

However, both feedback and G/C imaging modes have their own experimental and theoretical limitations. The feedback mode is extremely useful to quantify the tip-substrate separation in both biological and chemical samples. However, during imaging the feedback mode does not yield much information about the biological activity of the substrate. On the other hand, the G/C mode differs widely from the feedback mode where the tip-generated species are actively involved in the substrate reaction. As the G/C mode

is governed by the uncontrolled mass transport of species from the biological specimen, unlike the feedback mode, it does not localize the reaction under the electrode. This implies that the feedback imaging provides greater lateral resolution. Nevertheless, the G/C mode can detect lower analyte concentrations than the feedback mode because it does not have a significant background current arising from the dissolved mediator in solution. For example, the G/C experiments could measure a rate constant three orders of magnitude higher than that via the feedback investigations. Thus the choice of a particular mode of SECM imaging depends on whether the image resolution or detection limit is important for a specific sample.

The investigations on hybrid polymer electrolytes described in Chapters, 2, 3, 4 and 5, indicate the importance of the domain structure of Nafion, emphasizing the necessity to map the local proton fluxes in PEMs. In this context, here we demonstrate the importance of SECM imaging in the feedback and generation/collection modes to monitor the proton conduction domains of polymer electrolyte membranes and ion fluxes in biological systems respectively. The results obtained here by feedback imaging of catalyst particles embedded in polymer electrolyte membranes relate to the real situation present in the catalyst layer of PEM fuel cells. This study could be useful to analyze critical factors like catalyst utilization in fuel cell electrodes. The next objective is to extend the applicability of SECM for imaging proton transport related processes in biological systems. Specifically, the photosynthetic activity of stomatal guard cells in peanut (*Arachis Hypogaea* L.) leaves is investigated using SECM, the results of which can be extended to achieve many new insights into various areas of biochemistry including cell fate/differentiation, signal transduction and developmental biology of plants.

6.2 Experimental Section

Nafion (5 wt% solution in a mixture of lower aliphatic alcohols and water (eq. wt. 1000), Lithium perchlorate, Potassium chloride, ferrocenemethanol and ammonium metavanadate were procured from Aldrich chemicals. Perchloric acid (70 vol% in water) was obtained from Loba chemicals, India. All the solutions were prepared in Millipore de-ionized water (18.2 MΩ.cm). Savlon (an antiseptic liquid of composition: Chlorhexidine gluconate solution 1.5 % v/v, Strong cetrimide solution 3.0 % w/v) was procured from Johnson and Johnson Ltd., Mumbai, India. 25 μm (diameter) Pt UME and all other electrodes were purchased from CH Instruments. Pt catalyst (~100 nm size, 20 wt%) supported on Vulcan XC-72 carbon was procured from Arora Matthey Ltd.

6.2.1. UME Standardization

Prior to imaging, the SECM tip was characterized by cyclic voltammetry to ensure that the electrode has reasonable current amplitude, low capacitive current and steady-state behavior. The cyclic voltammograms were recorded in 0.1 M KCl containing 1 mM ferrocenemethanol, with Ag/AgCl reference electrode and a Pt counter electrode from which the steady state current was found to be 3.8 nA, similar to that expected (3.1 nA) from the expression,

$$i_{tip,\infty} = 4nFaDC_o^* \qquad (6.1)$$

where, $i_{tip,\infty}$ is the steady-state limiting current of the tip, n is the number of electrons involved in the redox process, F is the Faraday constant (96500 C), 'a' is the radius of the UME tip, D is the diffusion coefficient of the electroactive species (taken as 7.8 x 10^{-6} cm^2/s for ferrocenemethanol [11] and C_o^* is the concentration of the species in the bulk of the electrolyte. Further, CVs in 0.1 M KCl, yield a steady state current of 7.9 nA for oxygen reduction from which the concentration of dissolved oxygen in the electrolyte

was calculated to be 0.16 mM using equation (1), assuming a diffusion coefficient of 2.5 x 10^{-5} cm^2/s for oxygen [12].

6.2.2. SECM Conditions

The SECM measurements were carried out using a model 900B CH Instrument. The electrochemical cell consists of circular Teflon trough mounted on a flat platform housing the counter (Pt wire) and reference (Ag/AgCl, sat. KCl) electrodes. The SECM probe was a 25 μm Pt disk ultramicroelectrode (UME) purchased from CH Instruments with an RG (ratio of the diameter of the UME tip to that of the insulating glass sheath) value of 7 (approx.).

For evaluating catalyst containing Nafion films, the substrate electrode was polished with a 0.3 μm alumina slurry and the tip electrode with a 0.05 μm alumina slurry. A solution of 0.1 M $LiClO_4$ in 10 mM $HClO_4$ was used as the electrolyte and the experiments were performed at room temperature. A 5 μl dispersion of Pt/C in 5 wt% Nafion solution was drop coated on the substrate electrode. The separation between the tip and the substrate was determined using few preliminary probe approach experiments, when the tip biased to a potential of – 0.7 V corresponding to steady state H_2 evolution approached the catalyst film. Subsequently a region of 100 x 500 μm^2 area of the catalyst coated films was imaged by setting the tip at a distance of 10 μm above the substrate and rastering it at a speed of 0.3 μm/s over the film surface. To discriminate the images from artifacts, the same area was scanned repeatedly atleast twice after performing independent probe approach experiments and also with another SECM tip with same dimensions.

For imaging peanut leaves, the electrolyte was 0.1 M KCl. Then the tip-substrate separation is determined from approach curves in the feedback mode, obtained by moving the SECM tip at a speed of 1 μm s^{-1} at a potential of – 0.5 V, the diffusion

limited region for dissolved - oxygen reduction. Before imaging, the leaves were kept immersed in de-ionized water for 2 hours, to open the stomata, under uniform illumination by white light. Subsequently, the abaxial surface (500 μm x 500 μm) was scanned by setting the SECM tip potential at – 0.5 V at a speed of 50 μm s^{-1} at a distance of 10 μm above the leaf surface.

6.2.3. Plant Tissue Culture Conditions

Mature pods of a peanut cultivar SB-11 were collected from the local market. Embryo axes were excised from the cotyledons, and somatic embryos were produced using the protocol described [13] for the cultivar JL-24. The somatic embryos germinated and converted into plantlets (3-4% only) in 8-12 weeks in the Murashige and Skoog (MS) [14] basal medium with 2% sucrose. Leaves of these plants were used for SECM. All cultures were incubated in 16 h photoperiod at 25 ± 2°C. Somatic embryo derived plantlets were transferred to green house after hardening for 2 weeks. Hardened plants were transferred to greenhouse and were grown for 10-12 weeks prior to sampling for SECM analysis.

For *in vitro* raised seedling derived leaves, the seeds were washed with detergent for 10 minutes followed by repeated washing with distilled water. Thereafter the seeds were treated with 4% savlon for 10 minutes. On removing savlon with repeated washing with sterile water, the seeds were disinfected by 0.1 % $HgCl_2$ treatment for 10-12 minutes. Repeated washing with double distilled water eliminated the adhering $HgCl_2$. The testa of these seeds was removed aseptically and the seeds were cultured in tubes containing 20 ml MS basal medium supplemented with 2 % sucrose. After 4 days incubation in dark for radical emergence, the cultures were transferred in 16 hr photoperiod at 25 ± 2°C and incubated for 4weeks prior to sampling of leaves for SECM. The pH of the media was adjusted to 5.8 prior to autoclaving. For ex vitro plant derived leaves the seeds were germinated and grown in sand:soil - 1:1 mixture in the greenhouse

for 10-12 weeks. Chlorophyll distribution was analyzed by taking green and yellow leaves from an aged SE plant (15 weeks old with part of the leaves turned yellow).

6.3 Results and Discussion

6.3.1. Feedback imaging of catalyst-containing Nafion membranes

SECM has been successfully applied for investigating liquid/membrane interfaces to understand the transport and distribution of ions and molecules through porous [15], small recast [16] and biological membranes [17]. The technique has been fruitful especially to understand the morphology of proton exchange membranes used in polymer electrolyte fuel cells. Different strategies have been demonstrated to perform SECM investigations on proton exchange membranes including monitoring of counter ion injection/ejection [18] and iontophoretic studies of molecular fluxes across the membranes [16a]. Recently, the H^+/H_2 couple has been shown to be a better redox mediator devoid of complications arising due to the ingress/egress of foreign ions at the polymer/liquid interface [19]. On the other hand, the H^+/H_2 mediator system has been used to evaluate hydrogen oxidation electrocatalysts for fuel cells [20]. Combining the advantage of the sensitivity of the H^+/H_2 couple to the activity of the electrocatalyst as well as the proton transport properties of the membrane, here we examine Pt catalyst-modified recast Nafion membranes using SECM in the feedback mode.

Figure 6.4 shows a typical cyclic voltammogram of Pt/C catalyst (20 wt% Pt on Vulcan XC-72 carbon) coated on a glassy carbon disk electrode in 0.5 M H_2SO_4. A simple calculation based on the area under the hydrogen adsorption peaks between - 0.3 and - 0.6 V and further comparison with the theoretically expected area, indicates that only 50% (approx.) of the catalyst in the slurry is utilized effectively.

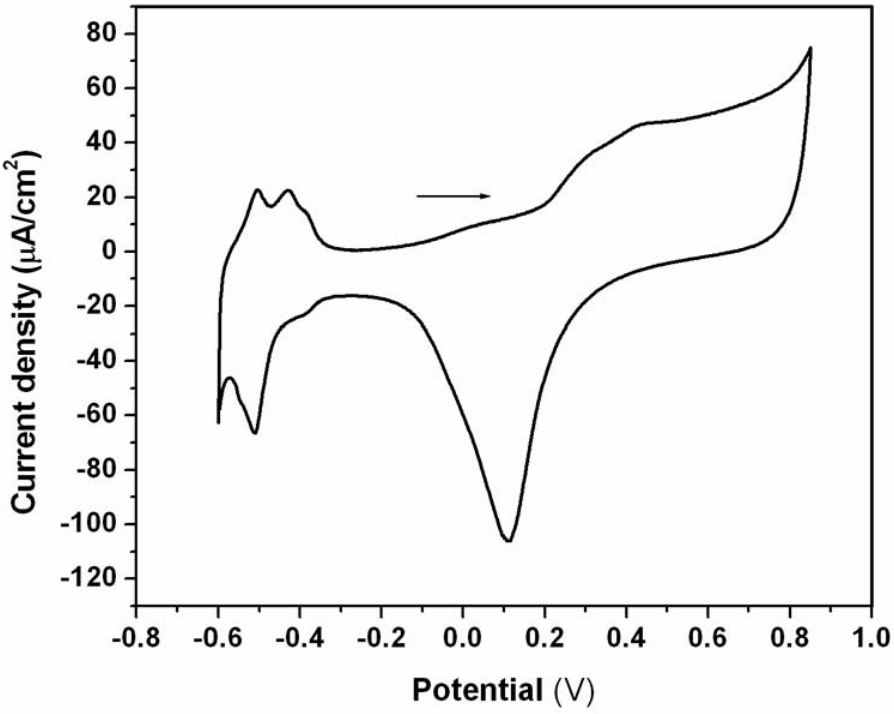

Figure 6.4. Cyclic voltammograms of Pt/C in 0.5M H_2SO_4 (a), Pt disk UME (b) and Pt/C-Nafion film coated substrate electrode (c) in 0.1 M $LiClO_4$ containing 10 mM $HClO_4$ at a scan rate of 25 mV/s. Reference electrode: Ag/AgCl

Figures 6.5a and 6.5b show the cyclic voltammograms of 25 μm Pt UME used as the SECM tip and the Pt disk substrate electrode (1.5 mm diameter) coated with Pt/C-Nafion film, after cycling the potential between 0.8 to - 0.8 V (vs. Ag/AgCl ref) to obtain reproducible behavior. Figure 6.5a indicates that H_2 is evolved after revealing characteristic adsorption/desorption peaks at the UME tip at potentials more negative than -0.6 V, from the reduction of protons present in the electrolyte.

$$2H^+ + 2e^- \longrightarrow H_2$$

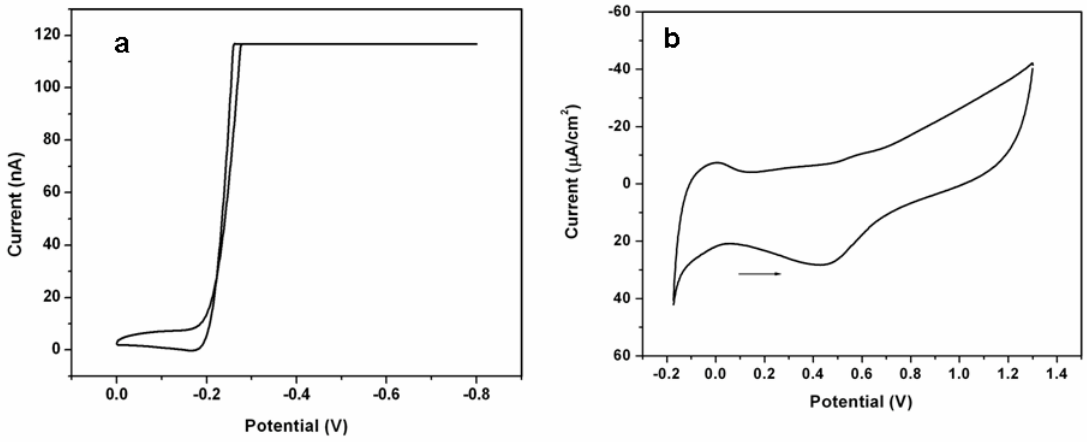

Figure 6.5. a) Probe approach curve showing the variation of dimensionless tip current ($i_T/ i_{T,\infty}$) versus normalized tip substrate distance (d/a, where d is the actual tip-substrate separation and a is the tip radius) as the SECM tip biased to a potential of – 0.6 V approaches the film surface at a speed of 50 μm/s.

The principle of feedback imaging used in this work is depicted in Figure 6.6. The imaging experiments involve the H^+/H_2 couple as the mediator to establish feedback currents by reoxidizing H_2 evolved at the tip by the substrate electrode [4a]. The low acid concentration in the electrolyte (10 mM) particularly avoids the formation of H_2 bubbles which may otherwise disrupt the steady state response, by creating fluctuations in current [4a].

The separation between the tip and the substrate is determined by monitoring the tip current at H_2 evolution potential as a function of the distance normal to the substrate electrode in a typical probe approach experiment. Accordingly, Figure 6.7a shows the probe approach curve of the UME tip biased to a potential of – 0.7 V. Although an increase in tip current (positive feedback) as it approaches the Pt/C film surface is expected, the negative feedback in the present case is attributed to the effect of the polymer film on the surface of the catalyst. This could be compared with similar observations in polymer film-coated substrate electrodes reported earlier [19,20]. More interesting information about the effect of Pt oxide formation on the catalytic activity is

obtained by plotting the ratio of tip currents at closest tip-substrate separation to those at infinity as a function of the substrate potential (Fig. 6.7b). As the substrate potential is made more and more positive, the tip current ratio decreases probably due to the formation of oxide on Pt surface. Nevertheless, the possibility of poisoning of the UME surface by ions present in the electrolyte medium has been ruled out by cycling the tip between potentials corresponding to water oxidation and hydrogen evolution after each probe approach experiment.

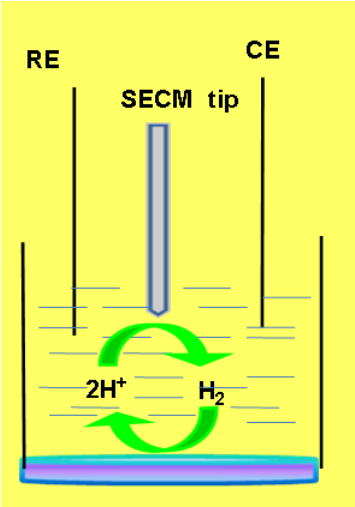

Figure 6.6. Schematic representation of the feedback imaging principle used in this investigation. The SECM probe is a 25 μm Pt disk electrode embedded in an insulating glass sheath, so that the ratio of the diameter of the sheath to that of the electrode (RG) is 7. RE and CE refer to the reference (Ag/AgCl sat. KCl) and counter electrodes respectively.

Having analyzed the electrochemical activity of the Pt UME and the Pt/C-Nafion film, the next step is to map the local reactivity gradients along the surface of the catalyst coated film, which is one of the principal objectives of the work. After determining the tip-substrate separation from the probe approach experiments, the tip is positioned at a constant distance of 10 μm above the film and rastered in the XY plane while monitoring the tip current. Accordingly, Figure 6.8 shows the electrochemical images of a catalyst coated film as a function of hydrogen oxidation reactivity of the Pt catalyst. More specifically, the images representing the same area of the film, indicate that the whole area seems to be homogeneous when there is no hydrogen evolution at the tip.

Interestingly, when the tip is biased to a potential appropriate for H_2 evolution (-0.7 V) regions of varying reactivity can be observed for the same area of the film.

Subsequently, more images are recorded by making the substrate potential more and more positive, which indicate critical variations in the reactivity profile as the catalyst surface gets oxidized. However, one of the major limitations of this study is the inability to access quantitative information due to the negative current feedback behavior at the metal/polymer electrolyte interface. Despite being semi-quantitative, the results presented are important since this illustrates the efficacy of SECM in understanding gradients in electrochemical activity of fuel cell catalysts in contact with a polymer electrolyte membrane. These results are also valid for analyzing many other polymer-modified electrodes since a similar approach could be effectively used for understanding electrocatalytic behavior for other applications like biosensors.

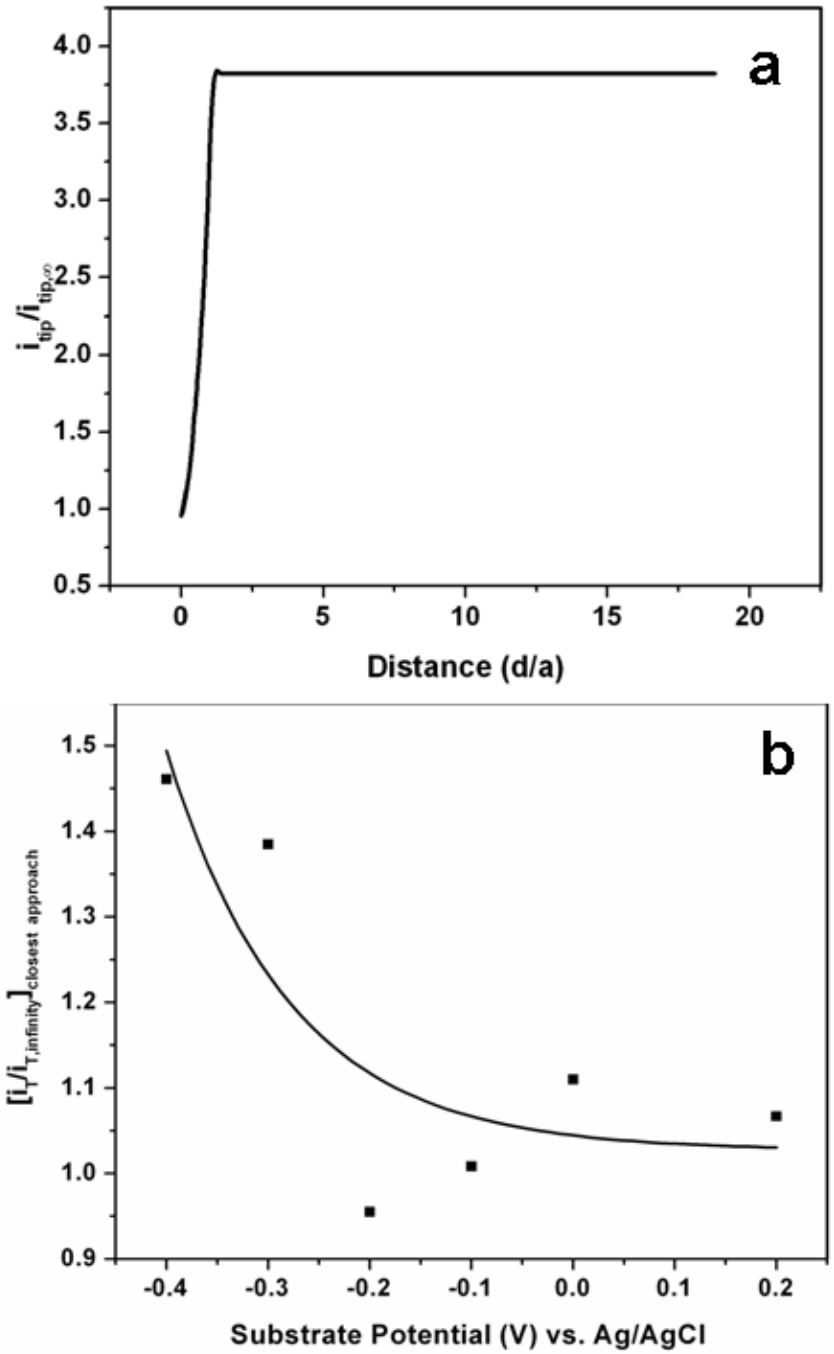

Figure 6.7. (a) Probe approach curve showing the variation of dimensionless tip current ($i_T/ i_{T,\infty}$) versus normalized tip substrate distance (d/a, where d is the actual tip-substrate separation and a is the tip radius) as the SECM tip biased to a potential of – 0.6 V approaches the film surface at a speed of 50 μm/s. (b) Variation of dimensionless tip current at the closest tip-substrate separation with substrate potential: the decrease in tip current at more positive substrate potentials indicates the effect of Pt oxide formation on its catalytic activity

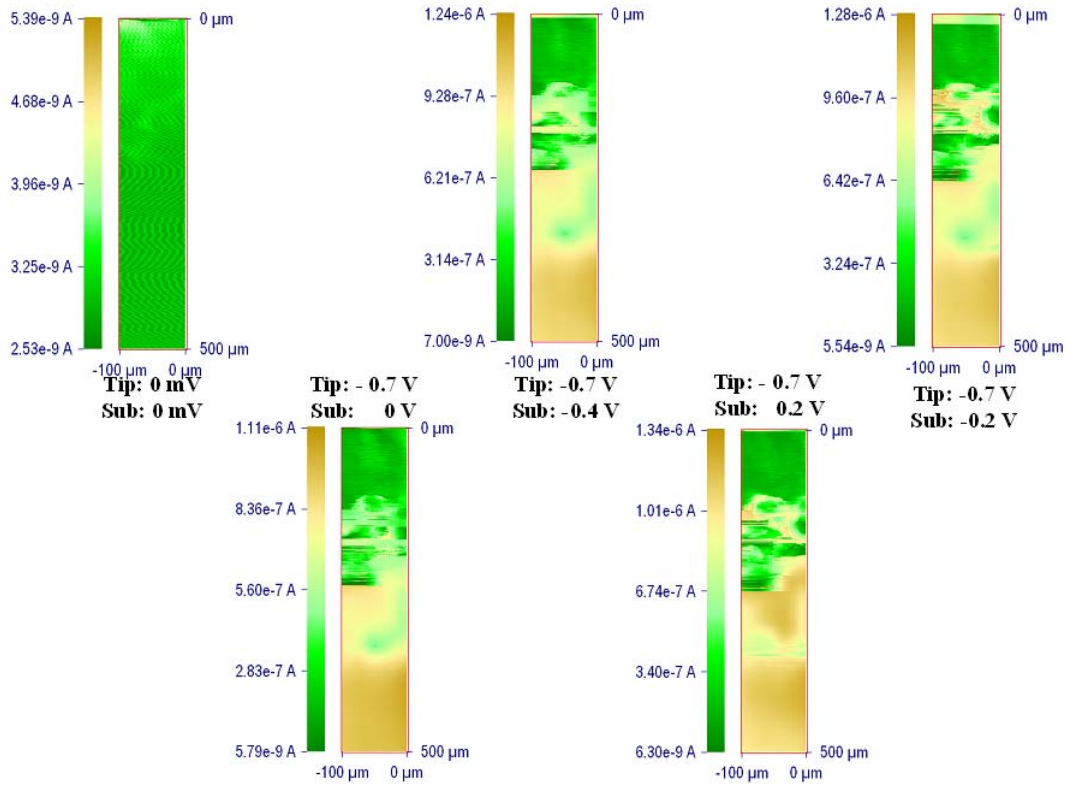

Figure 6.8. SECM images of the same area (100 x 500 µm) of a Pt/C-Nafion film as a function of tip and substrate potentials. The colour changes correspond to changes in current arising in turn from changes in the hydrogen oxidation activity of the catalyst film. The effect of Pt oxide formation is manifested in the relative current intensities with more positive substrate potentials.

6.3.2. Stomatal Physiology of Peanut Leaves – Substrate Generation/Tip Collection Imaging

SECM is an excellent technique to understand ion-transport, molecular fluexes across membranes and electron transfer in biological systems. Especially, it has been demonstrated to be an adaptable tool to study stomatal distribution in plants [10, 21] as it is impervious to most of the difficulties (e.g., sample preparation) haunting the contemporary techniques like fluorescence imaging and patch-clamp analysis [22].

However, the efficacy of SECM in revealing deeper aspects of plant physiology has not been realized completely, perhaps, due to the lack of combining it with rigorous biochemical experiments. Here, we couple this unique technique to a standard protocol in plant tissue culture viz. Somatic embryogenesis and validate the efficiency of the methodology in revealing deeper aspects of plant physiology by investigating the functioning of stomata in peanut (*Arachis Hypogaea* L.) leaves. Somatic Embryogenesis based micro-propagation technology is of paramount importance in plant tissue culture to achieve mass production of plants as well as to understand the fundamental biological processes. The success of the protocol depends largely on the ability of the *in vitro* (test tube-grown) raised plants to survive *extra vitrum* (soil-grown), which in turn depends on the photosynthetic ability of the propagules. In this context, SECM serves as a simple means to assess the photosynthetic activity prior to transferring the plants to soil. The peanut plant is chosen for this study, as we have been frequently using this system to understand the process of *in vitro* morphogenesis [23].

Here, we employ this methodology to achieve a systematic correlation between the intrinsic nutrient levels of peanut plants grown under different conditions and the stomatal physiology of their leaves. Accordingly, samples studied in the present investigation include leaves obtained from Somatic Embryo (SE) derived emblings grown *in vitro* and *extra vitrum,* seedlings germinated and cultured *in vitro,* and seedlings germinated and grown e*x vitro*, which have important physiological differences as explained below. The somatic embryos do not have well-developed cotyledons. Thus the germination of the somatic embryos and growth of the emblings depend largely on the support of the medium during germination and conversion *in vitro*. On the contrary, the seed germination and seedling growth *in vitro* gets the benefit of both rich storage products of the cotyledons and the nutrition from medium. Germination of seed, *ex vitro* is supported by the storage product of the cotyledons in the initial phase and thereafter on the natural soil conditions. One major difference between the plants grown *in vitro* and *ex vitro* is that, in the former case, the culture medium contains a carbon source whereas the

ex vitro grown plants depend on photosynthesis once the storage products of the seeds are exhausted. Further, by a judicious combination of SECM imaging using oxygen evolution and chlorophyll distribution (lateral and cross-sectional), we here unravel interesting information on stomatal physiology, which could be extended in future to understand more specific processes related to plant morphogenesis and acclimatization.

The principle of SECM imaging used in this work (Fig. 6.9) briefly involves the mapping of oxygen evolution profile as well as the lateral and cross-sectional distribution of chlorophyll 'a' pigment by rastering the SECM tip, biased to appropriate potentials, over the abaxial surface of the leaves dipped in the electrolyte.

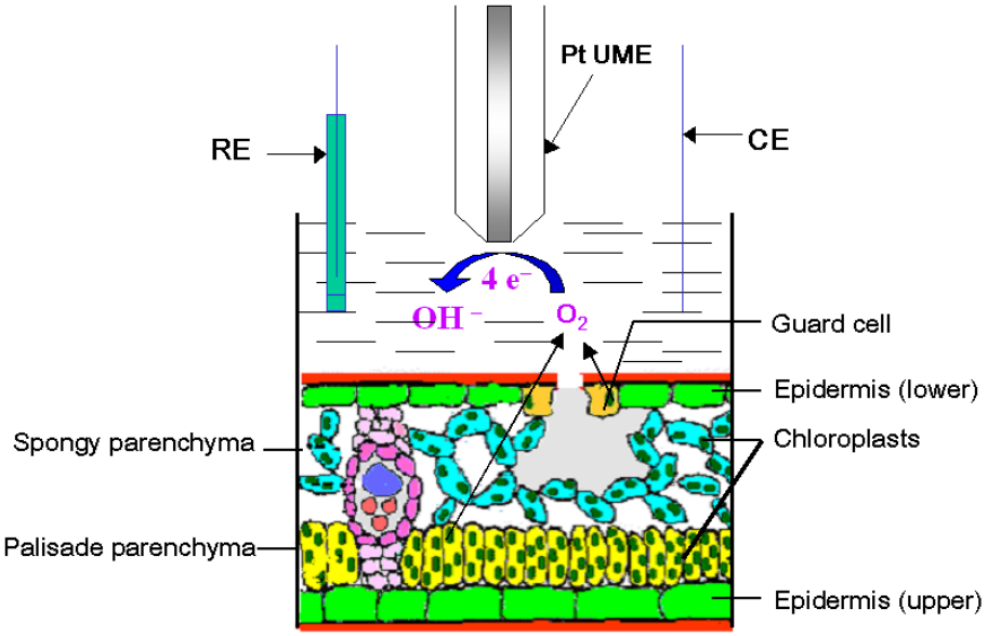

Figure 6.9. Schematic of SECM imaging in Substrate-Generation/Tip-Collection mode. The SECM probe is a 25 µm Pt UME disk. Oxygen evolving from the leaf surface during photosynthesis diffuses into the electrolyte (0.1 M KCl) and gets reduced at the Pt UME biased to a potential of -0.5 V at a diffusion-limited rate to produce a change in the tip-current.

Figure 6.10 shows a typical probe approach curve obtained by poising the SECM tip to – 0.5 V Vs. Ag/ AgCl, the potential at which oxygen reduction occurs at a

diffusion-controlled rate [21b]. The current decreases resulting in a negative feedback behavior when the tip approaches the epidermis indicating that the leaf surface acts as an insulator hindering the diffusion of dissolved oxygen in the electrolyte to the SECM tip in accordance with a report by Zhu *et al* [21b].

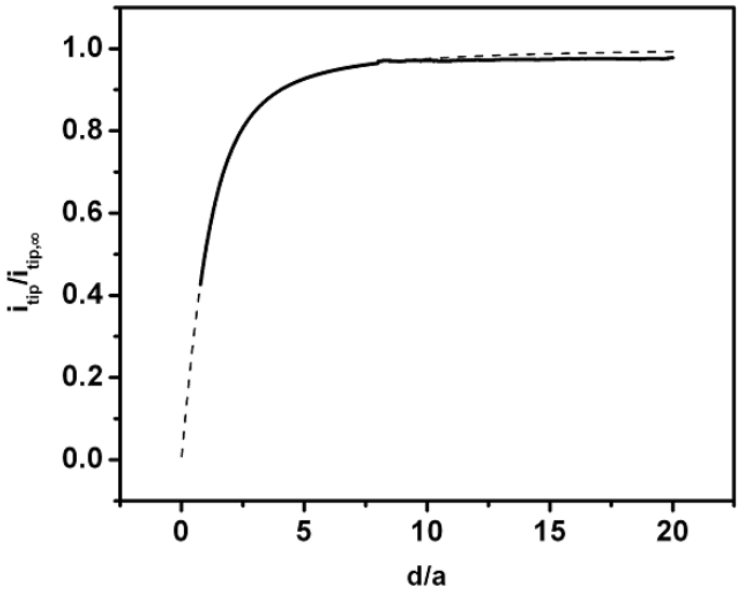

Figure 6.10. SECM approach curves showing a plot of dimensionless tip current ($i_{tip}/i_{tip,\infty}$) versus the normalized tip-substrate distance (d/a, where, 'd' is the actual tip-substrate distance and 'a' is the tip radius) as the UME tip biased to a potential of – 0.5 V approaches the substarte (the abaxial surface of an SE leaf) dipped in 0.1 M KCl at a speed of 50 μm/s. The dotted lines indicate the theoretical fit to the approach curve and the continuous line shows the experimental plot.

In addition, it implies that the amount of oxygen evolving from the leaf is well below that of the dissolved oxygen in the electrolyte. To confirm this, the approach curve is further fitted with theoretical curves described in earlier reports [24] using the analytical expression developed for SECM approach curve for an insulating substrate (i.e., current-distance curve controlled by hindered diffusion).

$$\frac{i_{tip}}{i_{tip,\infty}} = 1 \Big/ \left[a + \left(\frac{b}{L} \right) + c \exp\left(\frac{d}{L} \right) \right] \tag{6.2}$$

where, i_{tip} and $i_{tip,\infty}$ are the tip currents at a given tip-substrate distance, d and in the bulk respectively; a, b, c, and d are constants which depend on the RG value of the tip (i.e. the ratio of the tip radius to the insulating sheath radius; the RG value is 7 in the present case) and *L* denotes the dimensionless tip-substrate distance given by d/a ('d' is the tip-substrate distance and 'a' is the tip radius). However, as the diffusion of dissolved oxygen toward the SECM tip is hindered near the leaf surface, the variation in the tip current during lateral (x, y) - scans near the leaf surface could be essentially attributed to the differences in photosynthetic activity along the leaf surface.

6.3.2.1. SECM of *in vitro* Plants

Figure 6.11 shows a comparison of SECM images of *in vitro* Somatic Embryo-derived (SE) leaves (a) and seedling-derived leaves (b) with a tip bias of – 0.5 V (right) and 0 V (left), for the same area of the leaf, indicating stomatal complexes of size ca. 27 ± 5 μm. Significant differences between the SE and seedling-derived leaves due to the physiological differences could be noticed, in terms of both stomatal density (shown in the left panel) as well as the oxygen evolution profile (right panel), arising from photosynthesis. Nonetheless, the relative age of the plants could not be neglected altogether, as it is not easy to determine the exact age of the somatic embryo-raised plants. However, in both the cases, the stomatal complexes are randomly distributed without any obvious patterning as normally expected from dicotyledonous leaves. Interestingly, in the right panel of Figure 6.11, the SECM tip current (proportional to the amount of oxygen evolved) above the stomatal complexes in the SE-derived leaf surface is found to be lower than that on the seedling-derived leaf surface. This is in accordance with the higher stomatal density in the latter case (left panel), thereby demonstrating the relationship between the oxygen evolution profile and the photosynthetic activity. Moreover, the rate of photosynthesis is also a complex function of the developmental state of the leaf and thus there may be variation within the leaves of the same plant. Hence, the above results need not essentially mean that the photosynthetic yield differs

with tissue culture conditions. Surprisingly, in the seedling-derived leaves, the oxygen evolution current over the guard cells is found to be more than that over the mesophyll cells (Fig. 6.11B-right) whereas it is just the reverse in the case of SE-derived leaves. The former is in contradiction to the fact that the guard cells contain lesser number of chloroplasts than the palisade mesophyll cells [25]. It should also be mentioned that the role of guard cell-chloroplasts in photosynthesis itself is a controversial research topic [26]. However, the higher oxygen evolution current over the guard cells (Fig. 6.11B-right) could be a consequence of the leaf anatomy shown in Figure 6.9. In brief, the oxygen evolving from the guard cells in the abaxial leaf surface would be more accessible to the SECM tip than that from the palisade mesophyll cells buried below by a layer of spongy parenchyma cells and air gaps. In this context, the actually 'inverted' oxygen evolution current profile observed in the case of SE-derived leaves (Fig 6.11A-right) could be probably signalling important changes in the leaf anatomy with tissue culture conditions. One could clearly conclude from these observations that the SE-derived leaves have a thinner spongy parenchyma layer compared to that of the seedling-derived leaves.

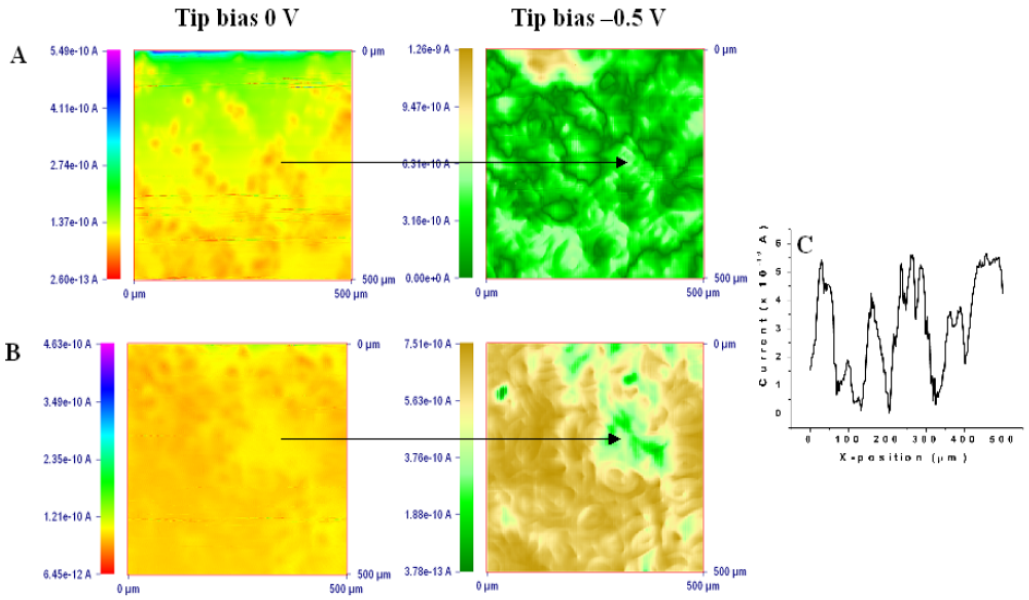

Figure 6.11. SECM images of (A) Somatic embryo-derived; (B) Seedling-derived peanut leaves (grown *in vitro*) with a tip bias of 0 V (left) showing the individual stomata (size ca. 27 ± 5 µm) and tip bias of – 0.5 V (right) displaying the Oxygen evolution profile on the leaf surface; (C) A cross-sectional scan in the x-direction across a group of stomata in (A) with a tip bias of – 0.5 V at a Y-position of 356 µm. The colour changes in the images indicate the variation in tip current, as it is rastered over the leaf surface at a scan speed of 50 µm/s. (arrows indicate the correspondence between the images in the left and the right panels to show that they belong to the same area of the leaf).

6.3.2.2. SECM of *ex vitro* Plants

Further, to understand the effect of growth conditions (*in vitro* Vs. *ex vitro*) on stomatal distribution, the SECM images of SE-derived (a) and seedling-derived (b) leaves obtained from *ex vitro* plants at a tip bias of – 0.5 V (right) and 0 V (left) are compared in Figure 6.12. It is difficult to explain the less prominent stomatal features in the *ex vitro* plants with the present state of knowledge.

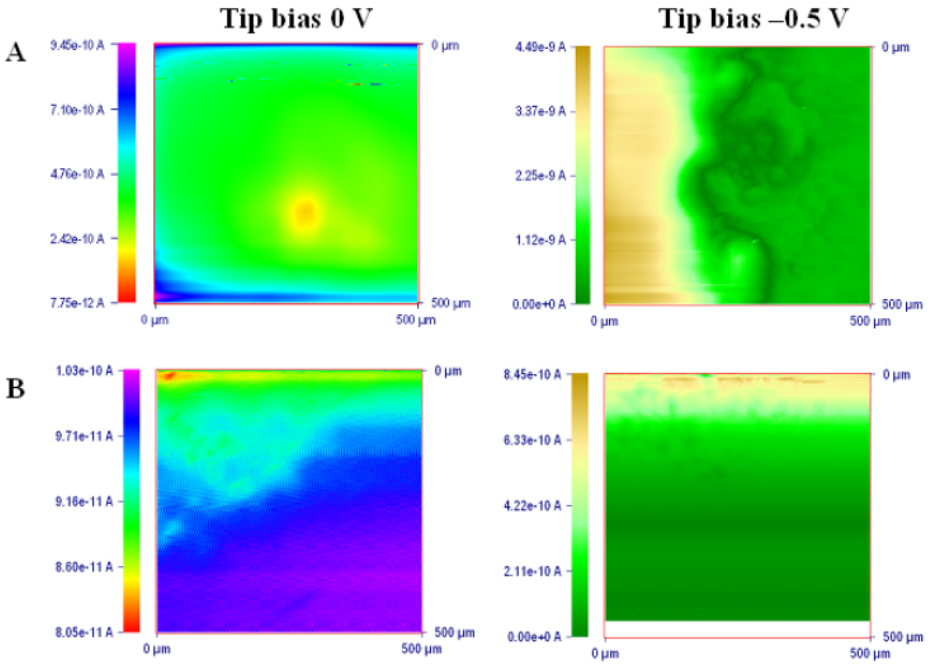

Figure 6.12. SECM images of (A) Somatic embryo-derived and (B) Seedling-derived peanut leaves (grown *ex vitro*) with a tip bias of 0 V (left) showing the individual stomata (size ca. 27 ± 5 µm) and tip bias of – 0.5 V (right) displaying the Oxygen evolution profile on the leaf surface

However, the possible influence of the different light conditions and nutritional conditions between the *in vitro* and *ex vitro* raised plants cannot be ruled out. Nevertheless, in Figure 6.12A, a double-bean shaped topographical feature housing a group of stomatal complexes could be seen and a few stomata could also be observed in the seedling-derived leaves in Figure 6.12B.

In addition, interesting insights into the role of proton fluxes on the mechanism of stomatal opening are obtained by imaging in the presence of vanadate ions (by adding ammonium vanadate to the electrolyte), which are known to inhibit plasma membrane H^+-ATPase activity [27], and close the stomata. Accordingly, Figure 6.13 shows the effect of ammonium vanadate addition (1 mM) on the SECM images of seedling-derived leaves, demonstrating an interesting inversion in the relative oxygen evolution current profiles. Stomatal opening/closure in plant leaves is effected by ATP-dependent

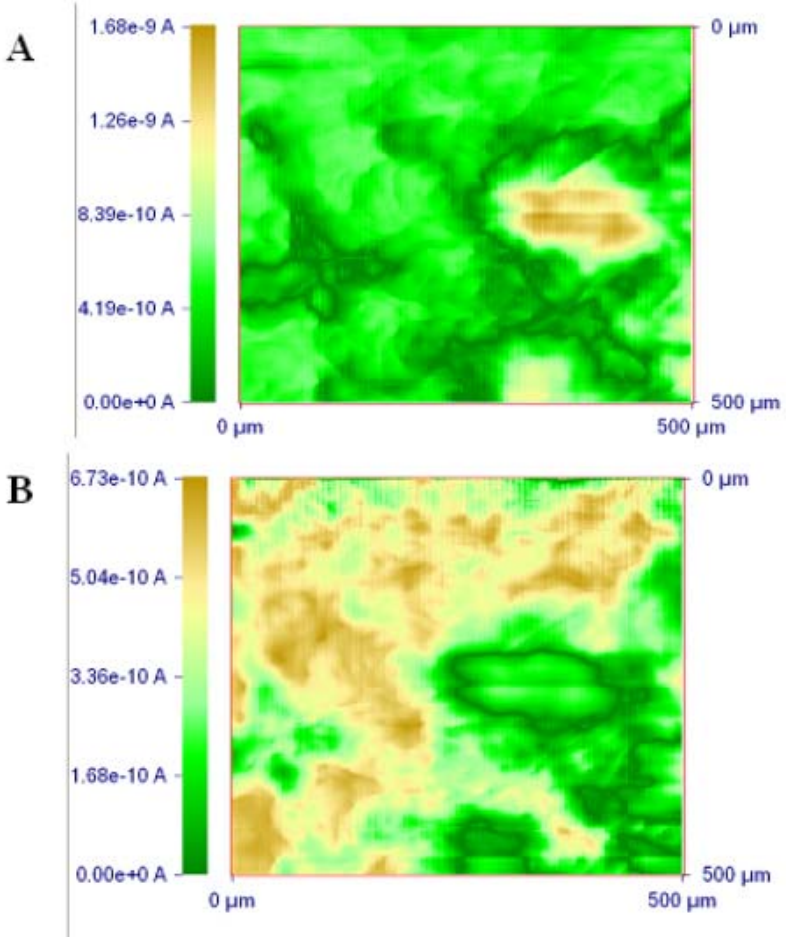

Figure 6.13. Effect of vanadate addition in the electrolyte (1 mM) on the turgor pressure in the stomatal complexes in an SE leaf grown *ex vitro*. SECM image (A) before and (B) after the addition of vanadate. The SECM images are recorded at a tip bias of – 0.5 V showing the oxygen evolution profile in 0.1M KCl. The sudden inversion in the current profile indicates that the group of stomata in the double-bean shaped feature close in the presence of vanadate ions, as they inhibit the plasma membrane H^+-ATPase responsible for apoplastic acidification and stomatal opening.

transport of solutes across the guard cell membranes resulting in an influx of potassium ions from the cytosol into the guard cell by inward potassium ion-channels and apoplastic acidification caused by ATPase-induced release of protons from inside the cells. In understanding this mechanism, one of the challenges that remains unresolved till date (up to the knowledge of the authors) is whether the proton efflux precedes/follows potassium influx during stomatal opening [28]. Because in the present case, the stomatal complexes

close as soon as the vanadate ions are added, even in the presence of excess potassium ions in the electrolyte, it is clearly evident that proton efflux precedes potassium influx during stomatal opening. It resolves yet another controversy about the involvement of plasma membrane H^+-ATPase in stomatal movements. For instance, it has been reported that the stomatal apertures of *Vicia Faba* L. do not close in presence of vanadate ions and concluded that ATPase inhibition does not effect stomatal closure [29]. Although the stomatal movements would differ from species to species, the choice of a sodium salt of vanadate (here we have used ammonium vanadate) might have influenced the results in the above report, as it is known that stomata once opened by sodium ions cannot be closed [30].

6.3.2.3. Imaging Chlorophyll Distribution

One of the most interesting challenges of this work is to understand the electrochemical process that generates the current distribution when the SECM tip is biased to 0 V (Vs. Ag/AgCl ref.) resulting in the images in the left panels of Figures 6.11 and 6.12. The earlier SECM investigations of stomata involved the imaging of oxygen evolution profiles by biasing the tip to –0.5 V or –0.6 V [10,21b] corresponding to the diffusion-limited region of oxygen reduction. However the variation in tip-currents during lateral scans at 0 V indicates that some other electroactive component on the leaf surface probably interacts with the tip. Consequently, in order to check whether the electron transfer components present in the chloroplasts (viz., chlorophyll pigment or proteins associated with the photosystem complexes) are responsible for these SECM images, yellow leaves from old peanut plants (*ex* vitro) were chosen due to the following reasons. Green leaves turn yellow when considerably mature due to the loss of total chlorophyll content in a process called ‘senescence’ which involves a sequential dismantling of their cellular components indicating the last phase of the organ’s development [31]. In many cases, as a result of leaf senescence, the chlorophyll pigment is found to undergo catabolic degradation to non-fluorescent end products resulting in a decreased photosynthetic activity [32]. Before falling off from the plant, a senescing leaf

is essentially viable and active as it has to carry out processes like transport of nutrients and degraded proteins/nucleic acids in an ordered fashion to new leaves and other developing organs of the plant [33]. Hence, SECM investigations of a senescing leaf detached from the plant is expected to provide valuable information about the relative contribution of the various leaf components to the current profiles. Accordingly, noticeable changes are observed in the SECM images as well as in the current-potential curves recorded by keeping the tip at a close proximity to a senescing SE leaf obtained from a mature plant (about 15 weeks old with part of the leaves turned yellow) as shown in Figure 6.14.

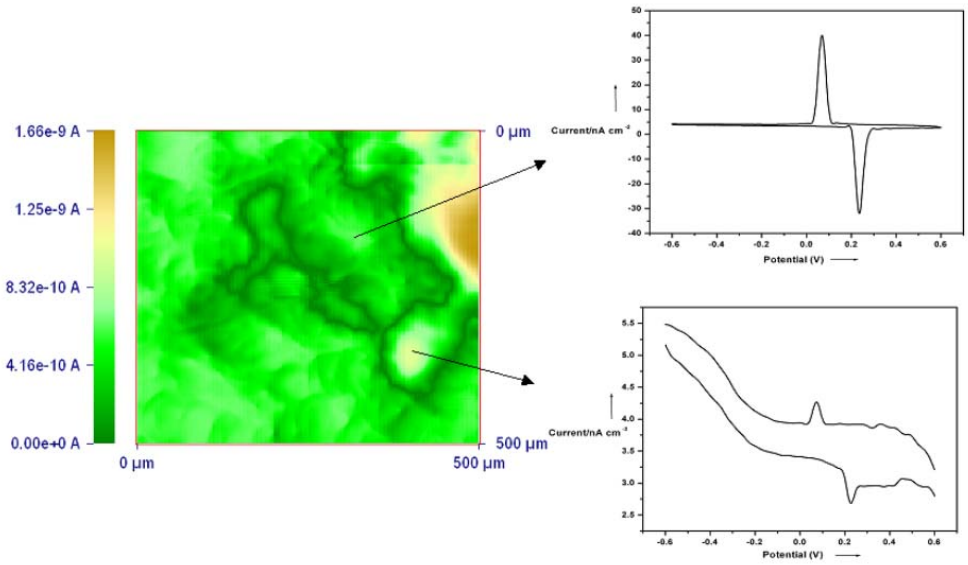

Figure 6.14. SECM image of an SE leaf from an *ex vitro* aged plant (15 weeks old) at a tip bias of – 0.5 V (left) and cyclic voltammograms at 25 mv/s scan rate on two different regions viz., above the stomatal complexes and the mesophyll cells. The redox couple has a half-wave potential, $E_{1/2}$ of 0.1 V vs. Ag/AgCl sat. KCl corresponding to that of chlorophyll 'a' pigment present in the chloroplasts of green leaves.

It is surprising to notice the appearance of a redox couple in the cyclic voltammogram (with a formal redox potential, $E^{o'}$ of 0.1 V) when the tip is closer to the leaf surface. As the redox peaks do not appear in the case of younger green leaves of 8-12 weeks old plants, the redox process could be attributed to that of chlorophyll 'a' pigment in the chloroplasts by comparison with earlier reports on chlorophyll-electrochemistry

[34]. In addition, the peak-shaped voltammograms in the present case in contrast to the sigmoid behavior expected with ultramicroelectrodes implies that the redox species are not freely diffusing to the SECM tip, since ultramicroelectrodes are expected to behave as conventional electrodes when the diffusion layer thickness is made smaller than the electrode dimensions either by altering the hydrodynamics/viscosity of the solvent or by reducing the time scale of the experiment [35]. For example, a peak shaped voltammogram for the $[Fe(CN)_6]^{3-/4-}$ redox process has been reported at a 25 μm diameter Pt disk microelectrode, even when the diffusion layer formation is obstructed by ultrasonication-induced cavitation at the electrode surface [36]. Similarly, in the present case, the diffusion layer formation could be slow probably due to the release of electroactive metabolites from chlorophyll breakdown, which is very slow (takes a few days) compared to their heterogeneous electron transfer rate [32b]. Another remarkable observation is the variation in the voltammetric peak shapes and currents with the region scanned on the leaf surface. For instance, Figure 6.14 shows the CVs at two different regions viz., above the stomatal complexes and over the surrounding tissues, as indicated by arrows in the adjacent SECM image. However, the higher peak current over the stomatal complexes compared to that over the surrounding tissues does not mean that the chlorophyll concentration is more in the stomatal complexes as discussed above. On the other hand, the difference in voltammetric peak shape and current between the two regions could be due to the localization of the chlorophyll pigment in different depths across the leaf cross-section as explained in Figure 6.9. Further, the cyclic voltammograms of the SECM tip as a function of its displacement perpendicular to the leaf surface (not shown here) indicate a decrease in peak current with increasing tip-to-leaf separation signifying the slow release of the electroactive metabolite from the senescing leaf, consistent with the above arguments. Thus, the results of the present investigation are expected to provide many new insights into various areas of plant bio-electrochemistry including cell fate/differentiation, signal transduction and developmental biology.

6.4 Summary and Conclusions

This chapter demonstrates the importance of SECM imaging to understand the morphology of Nafion membranes impregnated with catalyst particles and to reveal the importance of proton fluxes across guard cells in the mechanism of stomatal opening and closure in peanut leaves. The catalyst-coated Nafion membranes are studied in the feedback mode of SECM, the results of which are expected to be useful for analyzing reactivity gradients in catalyst layers employed in fuel cell electrodes. Though we have used H_2 oxidation reaction for imaging, the studies can be extended to other electrochemical reactions also. In the case of irreversible electron transfer reactions, SECM imaging could be done in the G/C mode. Subsequently, we have employed the G/C mode of SECM imaging to map the Oxygen evolution profiles and chlorophyll distribution on peanut leaves as a function of tissue culture conditions. While the Oxygen evolution profiles reveal interesting changes in the morphology of the leaves with changes in the intrinsic nutrient levels of the plants, localization of chlorophyll pigment unravels the effect of aging of the leaves on their photosynthetic activity. More interestingly, important information about the role of proton fluxes on the mechanism of stomatal opening has been obtained. Although the results may vary from species to species and even within different grades of peanut plant, they are believed to be of significance to explore the advantages of SECM imaging of biological systems.

6.5 References

1. Loos, J. *Adv. Mater.* **2005**, *17*, 1821.
2. Bard, A. J.; Denuault, G.; Lee, C.; Mandler, D.; Wipf, D. O. *Acc. Chem. Res.* **1990**, *23*, 357.
3. (a) Isaacs, H. S.; Kendig, M. W. *Corrosion* **1980**, *36*, 269. (b) Rosenfeld, I. L.; Danilov, I. S. *Corros. Sci.* **1967**, *7*, 129. (c) S. Mancuso; A. M. Marras,

V. Magnus; F. Baluska *Anal. Biochem.* **2005**, *341*, 344.

4. (a) Bard, A. J.; Fan, F. –R. F.; Pierce, D. T.; Unwin, P. R.; Wipf, D. O. Zhou, F. *Science* **1991**, *254*, 68. (b) Bard, A. J.; Mirkin, M. V. Ed., "*Scanning Electrochemical Microscopy*" Marcel Dekker Inc., New York (2001).
5. (a) Zoski, C. G. *Electroanalysis* **2002**, *14*, 1041. (b) Forster, R. J. *Chem. Soc. Rev.* **1994**, 289.
6. http://electrochem.cwru.edu/ed/encycl
7. Macpherson, J. V.; Slevin, C. J.; Unwin, P. R. *J. Chem. Soc., Faraday Trans.* **1996**, *92*, 3799.
8. (a) Fulian, Q.; Fisher, A. C. Denuault, G. *J. Phys. Chem. B* **1999**, *103*, 4393. (b) Sklyar, O.; Wittstock, G. *J. Phys. Chem. B* **2002**, *106*, 7499. (c) Nann, T.; Heinze, J. *Electrochim. Acta* **2003**, *48*, 3975. (d) Galceran, J.; Cecilia, J.; Companys, E.; Salvador, J.; Puy, J. *J. Phys. Chem. B* **2000**, *104*, 7993. (e) Zoski, C. G.; Aguilar, J. C.; Bard, A. J. *Anal. Chem.* **2003**, *75*, 2959. (f) Rajendran, L.; Ananthi, S. P. *J. Electroanal. Chem.* **2004**, *56*, 113.
9. (a) Shiku, H. *et al*. *Anal. Chim. Acta* **2004**, *522*, 51. (b) Wilhelm, T.; Wittstock, G. *Angew. Chem. Int. Ed.,* **2003**, *42*, 2248. (c) Zhao, C.; Sinha, J. K.; Wijayavardhana, C. A.; Wittstock, G. *J. Electroanal. Chem.* **2004**, *561*, 83. (d) Liu, B.; Cheng, W.; Rotenberg, S. A.; Mirkin, M. V. *J. Electroanal. Chem.* **2001**, *500*, 590. (e) Basame, S. B.; White, H. S. *J. Phys. Chem. B* **1998**, *102*, 9812.
10. Tsionsky, M.; Cardon, Z. G.; Bard, A. J.; Jackson, R. B. *Plant Physiol.* **1997**, *113*, 895.
11. Miao, W. J.; Ding, Z. F.; Bard, A. J. *J. Phys. Chem. B* **2002**, *106*, 1392.
12. Mancuso, S.; Papeschi, G.; Marras, A. M. *Planta* **2000**, *211*, 384.
13. Chengalrayan, K.; Sathaye, S. S.; Hazra, S. *Plant Cell Rep.* **1994**, *13*, 578.
14. Murashige, T.; Skoog, F. *Physiol. Plant* **1962**, *15*, 473.
15. (a) Scott, E. R.; White, H. S.; Phipps, J. B. *Anal. Chem.* **1993**, *65*, 1537. (b)

Bath, B. D.; Lee, R. D.; White, H. S.; Scott, E. R. *Anal. Chem.* **1998**, *70*, 1047. (c) Uitto, O. D.; White, H. S. *Anal. Chem.* **2001**, *73*, 533.

16. (a) Bath, B. D.; White, H. S.; Scott, E. R. *Anal. Chem.* **2000**, *72*, 433. (b) Gyurcsanyi, R. E. *et al. Anal. Chem.* **2001**, *73*, 2104.
17. Gonsalves, M.; Macpherson, J. V.; Hare, D. O'; Winlove, C. P.; Unwin, P. R. *Biochim. Biophys. Acta* **2000**, *66*, 1524.
18. Jeon, C.; Anson, F. C. *Anal. Chem.* **1992**, *64*, 2021.
19. Kallio, T.; Slevin, C.; Sundholm, C.; Holmlund, P.; Kontturi, K. *Electrochem. Commun.* **2003**, *5*, 561.
20. Zoski, C. G. *J. Phys. Chem. B* **2003**, *107*, 6401.
21. (a) Lee, C.; Kwak, J.; Bard, A. J.; *Proc. Nat. Acad. Sci.* **1990**, *87*, 2740. (b) Zhu, R.; Macfie, S. M.; Ding, Z. *J. Exp. Bot.* **2005**, *56*, 2831.
22. Hetherington, A. M.; Woodward, F. I. *Nature* **2003**, *424*, 901.
23. (a) Hazra, S.; Sathaye, S. S.; Mascarenhas, A. F. *Nat. Biotechnol.* **1989**, *7*, 949. (b) Chengalrayan, K.; Hazra, S.; Meagher, M. –G. *Plant Sci.* **2001**, *161*, 415. (c) Joshi, M. V.; Sahasrabudhe, N. A.; Hazra, S. *Biologia Plantarum* **2003**, *46*, 187.
24. (a) Shao, Y.; Mirkin, M. V. *J. Phys. Chem. B* **1998**, *102*, 9915. (b) Amphlett, J. L.; Denuault, G. *J. Phys. Chem. B* **1998**, *102*, 9946.
25. Bergmann, D. C. *Curr. Opin. Plant Biol.* **2004**, *7*, 26.
26. Zeiger, E.; Talbott, L. D.; Frechilla, S.; Srivastava, S.; Zhu, J. *New Phytol.* **2002**, *153*, 415.
27. Goh, C. –H.; Schreiber, U.; Hedrich, R. *Plant Cell Environ.* **1999**, *22*, 1057.
28. Fan, L. –M.; Zhao, Z.; Assmann, S. M. *Curr. Opin. Plant Biol.* **2004**, *7*, 537.
29. Shi, W. –L.; Liu, X.; Jia, W. –S.; Zhang, S. –Q. *J. Integ. Plant Biol.* **2005**, *47*, 319.
30. Robinson, M. F.; Very, A. –A.; Sanders, D.; Mansfield, T. A. *Annals Bot.* **1997**, *80*, 387.

31. Biswal, U. C.; Biswal, B. *Photochem. Photobiol.* **1984**, *39*, 875.
32. (a) Holloway, P. J.; Maclean, D. J.; Scott, K. J. *New Phytol.* **1992**, *120*, 145. (b) Maunders, M. J.; Brown, S. B. *Planta*, **1983**, *158*, 309.
33. Biswal, B.; Biswal, U. C. *Curr. Sci.* **1999**, *77*, 775.
34. (a) Cosma, P.; Longobardi, F.; Agosiano, A. *J. Electroanal. Chem.* **2004**, *564*, 35. (b) Ferryra, R. A.; Pachepsky, L. B.; Collino, D.; Acock, B. *Ecol. Model.* **2000**, *131*, 285.
35. Rubinstein, I. "*Physical Electrochemistry: Principles, Methods and Applications"* Marcel Dekker Inc., New York (1995).
36. Maisonhaute, E.; Campo, F. J. D.; Compton, R. G. *Ultrasonic. Sonochem.* **2002**, *9*, 275.

7 Conclusions & Future Prospects

The present chapter summarizes the important observations and conclusions of this thesis. The relevance of the strategy of hybrid polymer electrolytes for developing more efficient materials towards cleaner energy generation has been discussed. It also outlines some of the limitations of the studies. Finally, future perspectives of polymer electrolyte research are identified based on some of the theoretical and experimental observations.

With increasing population and advances in technology, energy and climate change have become the common concerns of science, engineering and society. While environmental issues like pollution, global warming and resource depletion necessitate the upsurge of cleaner technologies from renewable resources, the ever-increasing energy demands anticipate more 'efficient' methods of energy conversion. It is broadly agreed that there is hardly any single solution to address the dual problems of tackling future energy demands and managing the environmental consequences. Mainly as a result of the urgency to alleviate these problems, the research scenario has almost been shifted from doing something '*rationally new*' to something '*soon*'. Though it is imperative to work out immediate large-scale solutions for these problems, the unimaginable technologies about to emerge in the next 100 years will rely on the fundamental research and innovative strategies developed today. For example, the redox chemistry of oxygen has been a subject of active research since several decades, though the development of an efficient oxygen electrode to realize hydrogen economy requires innovative strategies. Similarly, a deeper understanding of the mysterious steps involved in photosynthesis will lead to excellent progress in solar energy conversion.

In this context, this thesis attempts to explore the possibility of achieving different strategies of modifying well-established materials like Nafion, a perfluorosulfonic acid polymer electrolyte, which have been consistently successful in the commercial market for several applications ranging from analytical separations to energy systems like polymer electrolyte fuel cells (PEFCs). However, Nafion suffers from a number of limitations including poor oxidative stability of the perfluorinate side chains in the presence of specific oxidants like peroxides, humidity-dependent proton conductivity, inability to function with hydrogen-rich reformate especially above 80 ^{o}C, permeability to molecules/species of interest to fuel cells (viz., methanol, ethanol, hydrogen and borohydride), poor mechanical stability, high cost, environmental hazards and issues related to disposal. Also, many of its fundamental properties like morphology and its relationship to mechanical properties, structure of confined water, chain dynamics and

proton transport mechanism require a deeper understanding to achieve better modifications and design more efficient polymer electrolytes in future.

We have addressed some of these issues in the present thesis and the major accomplishments are summarized below:

- **Development of an all-solid-state electrochemical methodology to investigate polymer electrolyte membranes**

  An all-solid-state electrochemical cell has been designed, to understand the effect of Nafion matrix on the redox behavior of cyanoferrates and heme proteins (Chapter 2). While cyanoferrate (III) undergoes spontaneous reduction to cyanoferrate (II) in the polymer matrix, the heme-iron of hemoglobin is protected from autoreduction by the protein chains encaging the heme center. However, the Nafion matrix is effective in tuning the biological activity (oxygen uptake) by hemoglobin, indicating the promise of the methodology for biomimetic investigations of enzyme/substrate interactions. Nevertheless, further modifications of the method to enable *in situ* spectroscopic investigations, high temperature measurements and experiments under controlled humidification would allow its application to a wide range of polymer electrolytes. Also, a number of proteins can be investigated in biocompatible polymer electrolyte matrices.

- **Controlling the oxidative stability and physical properties of Nafion by electrostatic association with an oppositely charged polymer electrolyte**

  As the mechanism of autoreduction of cyanoferrate (III) in Nafion is found to involve the sulfonate groups present in the pendant chains of the polymer, the next focus is to improve the oxidative stability of Nafion by engaging the

sulfonate group with an oppositely charged functional group. Instead of using freely diffusing ions of opposite charge, it is desirable to have the oppositely charged ionic groups fixed in another polymer, to make use of favorable inter-chain interactions (Chapter 3). Accordingly, when Nafion is allowed to interact with an oppositely charged polymer electrolyte, polyoxyethylene bis (amine), the sulfonate groups of the former get electrostatically associated with the protonated amino groups of the latter to form 'polyelectrolyte complexes'. Interestingly, electrostatic association of these two polymer electrolytes hinders the autoreduction of cyanoferrate (III) in Nafion. However, the poor mechanical stability of the corresponding membranes in the present case has precluded their examination in solid state, which may be overcome by optimizing the solvent or by using suitable reinforcing additives.

- **Enhancing the proton conductivity and performance of Nafion-based H_2/O_2 PEFCs by introducing small molecules active in biological proton transport**

The sensitivity of Nafion to interactions with electroactive complexes and other polymer electrolytes has been explored in another dimension by introducing small molecules involved in biological proton transport (Chapter 4). Specifically, the effect of two classes of plant hormones viz., auxins and cytokinins on the proton conductivity of Nafion and the net performance of H_2/O_2 PEFCs involving the composite ionomer as an active ingredient in the catalyst layer has been interrogated. One of the auxins, viz., indole-3-acetic acid exhibits an astonishing improvement both in the proton conductivity of Nafion as well in the fuel cell performance by improving the kinetics of oxygen reduction. Though, many more rigorous studies on the durability and cycle life of the bio-inspired electrodes, mode of action of the plant hormone and its effect on carbon monoxide poisoning of Pt (when reformed hydrogen is used as the fuel) are required before commercializing this strategy.

- **Improving the protein separation efficiency of polyacrylamide gels by incorporating single-walled and multi-walled carbon nanotubes**

  Remarkable flexibility of Nafion chains has been exploited since the past few years to achieve homogeneous composites with one-dimensional nanostructures like carbon nanotubes. In continuation, the approach has been applied to develop polyacrylamide/CNT composites, which has a similar amphiphilic microstructure like that of Nafion (Chapter 5). Interesting manifestations of single-walled and multi-walled CNTs on the morphology of polyacrylamide gels have been utilized to improve the electrophoretic separation efficiency of low molecular weight (14-97 kDa) proteins. In addition, excellent reduction in the standard deviation of protein mobility with respect to its molecular size implies that the polyacrylamide/CNT composite gels can be used for the molecular weight determination of newly extracted proteins. Nonetheless, detailed understanding of the effect of CNT incorporation on polymer morphology is required for the successful implementation of the composites for applications. Also, the effect of functionalizing the nanotubes on the protein separation efficiency needs to be explored.

- **Understanding the importance of proton fluxes in the mechanism of stomatal movements by electrochemical imaging of peanut leaves**

  Following the studies on the interesting proton conducting properties of Nafion discussed in the past four Chapters, our next curiosity has been to monitor the protons in real time as they get distributed in the hydrophilic domains and move through the ion channels in polymer electrolyte membranes (Chapter 6). Electrochemical Imaging of proton distribution in pristine Nafion membrane and its composites containing platinized carbon unravels exciting insights into

the morphology of the polymer electrolyte. Drawing inspirations from the behavior of polymer electrolytes, electrochemical imaging of biological proton transport has been performed to obtain critical information about proton pumping mechanisms across the guard cells constituting the stomatal pores of peanut leaves. However, further confirmation based on membrane morphology from contemporary techniques like small angle x-ray scattering could be vital.

The results presented in this thesis are believed to be useful for the development of hybrid polymer electrolytes with tailor-made properties by incorporating key species and biomolecules, which can effect critical changes in their microenvironments. Although more detailed investigations in terms of microscopic information about the polymer morphology and molecular modeling of interfacial interactions may shed more light into the importance of these investigations, the implications can be easily adapted to a number of bio- and nanocomposites of polymer electrolytes.

Future research on polymer electrolytes will be focused on developing alternative membranes with better stability at high temperatures (~ 200 ^{o}C), improved CO tolerance, high corrosion resistance in fuel cell environment, high conductivity at low water content and better water management, which may even lead to the realization of membranes with water replaced by an inorganic phase/phosphoric acid/small nitrogenous organic molecules or polymer electrolytes with water ‘traps’ in the sol-gel phase. These objectives may be achieved either by synthesizing novel systems or by preparing hybrids of existing polymer electrolytes. Also, future research in polymer electrolytes may benefit greatly from organic/inorganic hybrids and nanocomposites. However, to custom-design a polymer electrolyte with desirable conductivity, thermal and mechanical properties, it is important to develop rigorous multi-scale theoretical models which can simulate its long range structure over different levels of hierarchy.

List of Publications

1. "Autoreduction of Cyanoferrate (III) ions in a polymer electrolyte membrane: All solid state electrochemical and spectroscopic investigations" **Meera Parthasarathy**, Chinnakonda S. Gopinath, Vijayamohanan K. Pillai, *Chem. Mater.* (**2006**) *18*, 22, 5244-5252.

2. "Surface State-mediated Electron Transfer at nanostructured ZnO multipod/Electrolyte Interfaces" **Meera Parthasarathy**, Niranjan S. Ramgir, Bhaskar R. Sathe, Imtiaz S. Mulla, Vijayamohanan K. Pillai, *J. Phys. Chem. C* (**2007**) *111*, 13092-13102.

3. "All-Solid-State electrochemistry of a protein-confined polymer electrolyte film" **Meera Parthasarathy**, Vijayamohanan K. Pillai, Imtiaz S. Mulla, Mohammed Shabab, M. I. Khan, *Biochem. Biophys. Res. Commun.* (**2007**) *364*, 86-91.

4. "Tuning the transport properties of Poly(oxyethylene)bis amine-Nafion Polyelectrolyte Complexes by dielectric manipulation" **Meera Parthasarathy,** Bhalchandra Kakade, Vijayamohanan K. Pillai, *Macromolecules* (**2008)** 41, 3653-3658.

5. "Imaging stomatal physiology of somatic embryo-derived peanut leaves by Scanning Electrochemical Microscopy" **Meera Parthasarathy,** Shweta Singh, Sulekha Hazra, Vijayamohanan K. Pillai, *Anal. Bioanal. Chem.* (**2008**) 391, 2227-2233.

6. “Can plant-hormones enhance oxygen reduction kinetics in polymer electrolyte fuel cells?”
   Meera Parthasarathy, Ramaiyyan Kannan, Kurungot Sreekumar, Vijayamohanan K. Pillai, *Communicated.*

7. “Domain size manipulation of perfluorinated polymer electrolytes by sulfonic acid functionalized MWCNTs to enhance fuel cell performance”
   Ramaiyyan Kannan, **Meera Parthasarathy**, Sreekuttan U. Maaraveedu, Sreekumar Kurungot, Vijayamohanan K. Pillai, *Communicated.*

List of Publications

1. "Autoreduction of Cyanoferrate (III) ions in a polymer electrolyte membrane: All solid state electrochemical and spectroscopic investigations" **Meera Parthasarathy**, Chinnakonda S. Gopinath, Vijayamohanan K. Pillai, *Chem. Mater.* (**2006**) *18*, 22, 5244-5252.

2. "Surface State-mediated Electron Transfer at nanostructured ZnO multipod/Electrolyte Interfaces" **Meera Parthasarathy**, Niranjan S. Ramgir, Bhaskar R. Sathe, Imtiaz S. Mulla, Vijayamohanan K. Pillai, *J. Phys. Chem. C* (**2007**) *111*, 13092-13102.

3. "All-Solid-State electrochemistry of a protein-confined polymer electrolyte film" **Meera Parthasarathy**, Vijayamohanan K. Pillai, Imtiaz S. Mulla, Mohammed Shabab, M. I. Khan, *Biochem. Biophys. Res. Commun.* (**2007**) *364*, 86-91.

4. "Tuning the transport properties of Poly(oxyethylene)bis amine-Nafion Polyelectrolyte Complexes by dielectric manipulation" **Meera Parthasarathy,** Bhalchandra Kakade, Vijayamohanan K. Pillai, *Macromolecules* (**2008)** 41, 3653-3658.

5. "Imaging stomatal physiology of somatic embryo-derived peanut leaves by Scanning Electrochemical Microscopy" **Meera Parthasarathy,** Shweta Singh, Sulekha Hazra, Vijayamohanan K. Pillai, *Anal. Bioanal. Chem.* (**2008**) 391, 2227-2233.

6. “Can plant-hormones enhance oxygen reduction kinetics in polymer electrolyte fuel cells?”
   Meera Parthasarathy, Ramaiyyan Kannan, Kurungot Sreekumar, Vijayamohanan K. Pillai, *Communicated.*

7. “Domain size manipulation of perfluorinated polymer electrolytes by sulfonic acid functionalized MWCNTs to enhance fuel cell performance”
   Ramaiyyan Kannan, **Meera Parthasarathy**, Sreekuttan U. Maaraveedu, Sreekumar Kurungot, Vijayamohanan K. Pillai, *Communicated.*